# High-temperature resistant sprayed UHPC based on PC-CAC-C$ system

Jia He

Bouwstenen 431

# High-temperature resistant sprayed UHPC based on PC-CAC-C$ system

**Jia He**



CIP-DATA LIBRARY TECHNISCHE UNIVERSITEIT EINDHOVEN

High-temperature resistant sprayed UHPC based on PC-CAC-C$ system / by Jia He

A catalogue record is available from the Eindhoven University of Technology Library

ISBN: 978-90-386-6591-7

Bouwstenen 431

NUR 955



Cover design: Jia He

Ph.D. thesis, Eindhoven University of Technology, the Netherlands

# High-temperature resistant sprayed UHPC based on PC-CAC-C$ system

PROEFSCHRIFT

ter verkrijging van de graad van doctor
aan de Technische Universiteit Eindhoven,
op gezag van de rector magnificus, prof. dr. S.K. Lenaerts,
voor een commissie aangewezen door het College voor Promoties,
in het openbaar te verdedigen op woensdag 14 januari 2026 om 16:00 uur

door

**Jia He**

geboren te Hubei, China

Dit proefschrift is goedgekeurd door de promotoren en de samenstelling van de promotiecommissie is als volgt:

| | |
|---|---|
| Voorzitter: | prof.dr.ir. A.S.J. Suiker |
| Promotoren: | dr. Q.L. Yu |
| | prof.dr.ir. H.J.H. Brouwers |
| Leden: | prof.dr. C.J. Shi (Hunan University) |
| | prof.dr. P. Kinnunen (University of Oulu) |
| | prof.dr. M.C. Bignozzi (University of Bologna) |
| | prof.dr.ir. D.M.J. Smeulders |
| | dr. E. Bosco |
| Adviseur: | dr.ir. R.J.M. Wolfs |

*Het onderzoek of ontwerp dat in dit proefschrift wordt beschreven is uitgevoerd in overeenstemming met de TU/e Gedragscode Wetenschapsbeoefening.*

# Contents

# Chapter 1 Introduction

## 1.1 Research background

Fire safety requirements in large-scale infrastructure, such as tunnels and long-span bridges, are of paramount importance to ensure the safety of both structural systems and occupants [1]. As illustrated in Fig. 1.1(a-b), tunnel fires can cause severe high-temperature spalling and collapse of the lining, highlighting the urgent need to develop fire-resistant concrete materials that are easy to apply for both new construction and post-fire repair [2]. Conventional shotcrete, while advantageous for its rapid construction, exhibits relatively low strength and insufficient fire resistance, as illustrated in Fig. 1.1(c). In contrast, ultra-high-performance concrete (UHPC) possesses exceptionally high strength but is highly susceptible to explosive spalling at elevated temperatures and exhibits poor rheological properties, which make it unsuitable for spraying.

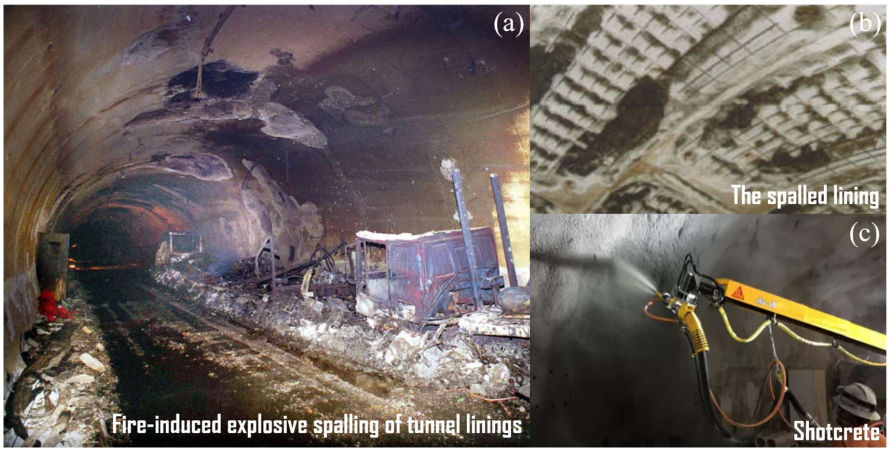


Fig. 1.1. Fire-induced explosive spalling of tunnel linings (a, adapted from [3]); The spalled lining (b, adapted from [3]); And conventional shotcrete used for construction and repair (c, adapted from [4]).

Therefore, developing a fire-resistant and sprayable UHPC (referred to as sprayed UHPC, abbreviated as SUHPC) is of critical significance for enhancing the fire safety, structural reliability, and rapid constructability of infrastructure systems. This novel SUHPC would not only need to meet stringent fire safety requirements, but also provide excellent adaptability for the rapid construction and repair of geometrically complex structures. The development of fire-resistant SUHPC has the potential to substantially broaden the applicability of UHPC in rapid structural repair and fire-resilient engineering.

However, the development of novel fire-resistant SUHPC still faces several major challenges:

- Preventing or alleviating explosive spalling at elevated temperatures.
- Achieving adequate early-age performance, including rheological behavior, early strength development, and dimensional stability.
- Ensuring sufficient mechanical performance at later ages.

To address the aforementioned challenges, it is essential to develop appropriate strategies that can simultaneously prevent explosive spalling at elevated temperatures while ensuring excellent early-age behaviors and later-age mechanical performance. In this thesis, successive approaches were explored, including the incorporation of supplementary cementitious materials (SCMs), the use of steel fibers, and the development of a novel ternary binder system, with the aim of enhancing the performance of SUHPC across multiple stages.

### 1.1.1 Characteristics of conventional UHPC

Ultra-High-Performance Concrete (UHPC) is an advanced cement-based composite material distinguished by its superior mechanical properties, enhanced ductility, and excellent long-term durability. In contrast to Normal Strength Concrete (NSC), UHPC offers the following significant advantages:

- An extremely low water-to-binder ratio combined with a high binder content contributes to the formation of a highly dense microstructure.
- An optimized particle size distribution significantly enhances the packing density of the microstructure.
- Ultra-high compressive strength, typically exceeding 120 MPa.
- Superior toughness, which effectively inhibits the propagation of cracks.
- Outstanding durability, characterized by extremely low permeability and strong resistance to chemical attack.

Despite the outstanding performance of UHPC, several issues still require urgent improvement:

- The high binder content combined with a low cement hydration rate results in low resource utilization efficiency, high carbon emissions, and poor environmental sustainability.
- UHPC has limited high-temperature resistance. Its dense pore structure prevents the release of internal steam pressure at elevated temperatures, making it prone to explosive spalling and posing serious risks to structural integrity and human safety.

### 1.1.2 Effect of SCMs on the explosive spalling resistance of UHPC at elevated temperatures

Sustainable development is a pressing global issue. The high material cost, energy consumption, and carbon dioxide emissions of UHPC are typical drawbacks that limit its widespread application. According to the literature [5], the unit volume cost of UHPC in engineering practice can reach as high as €750/m³, which is significantly higher than that of NSC, typically around €90/m³. Meanwhile, the carbon dioxide emissions generated during the production of UHPC are approximately 877 kg $CO_2$/m³, nearly twice that of NSC, which emits around 348.3 kg $CO_2$/m³. This highlights the economic and environmental disadvantages of UHPC.

Numerous studies have explored the use of supplementary cementitious materials (SCMs) as partial replacements for cement to reduce both production costs and carbon emissions. Common SCMs include fly ash (FA), ground granulated blast-furnace slag (GGBS), metakaolin (MK), and silica fume (microsilica, MS), among others. Recent studies have increasingly focused on the role of SCMs in modifying the performance of UHPC, particularly regarding strength development, hydration mechanisms, and microstructure refinement. For instance, partially

replacing cement with 10% metakaolin has been reported to notably enhance the compressive and flexural strengths of UHPC, along with improvements in its elastic modulus and resistance to permeability [6]. Both GGBS and MK contribute to the development of long-term strength and improved matrix densification, whereas FA is beneficial in enhancing the workability of fresh mixtures [7, 8]. In addition, the synergistic use of multiple SCMs, such as the combined application of MK with GGBS or red mud with limestone powder, can accelerate the hydration process, promoting the formation of C-S-H gel [6]. This also enhances the interfacial bonding between steel fibers and the cementitious matrix, thereby improving the overall toughness and impact resistance of UHPC [9].

Among various SCMs, GGBS is considered one of the most promising cement replacements for UHPC, owing to its relatively low carbon footprint and high pozzolanic reactivity. GGBS has the potential to accelerate the hydration process, which in turn contributes to pore structure refinement and improvements in impermeability and durability [10-14]. In addition, limestone powder (LP) has attracted considerable attention due to its filler effect and nucleation effects [15, 16]. Its incorporation is considered beneficial for refining the pore structure and potentially enhancing the durability of UHPC. Although the use of SCMs in UHPC has attracted growing research interest [17, 18], comprehensive investigations into their effects on hydration kinetics, pore structure evolution, and durability-related mechanisms remain limited.

In addition to its high carbon emissions, the risk of explosive spalling of UHPC under elevated temperatures has increasingly emerged as a critical research and engineering concern. Due to the low porosity and high packing density, UHPC significantly restricts the diffusion and release of water vapor. This can lead to the accumulation of internal steam pressure, which can readily trigger severe explosive spalling at elevated temperatures. To mitigate such damage, modifying the pore structure of concrete has been regarded as an effective strategy for reducing the risk of spalling. The incorporation of SCMs not only alters the pore structure but also affects the characteristics of the interfacial transition zone (ITZ) between fibers and the surrounding matrix. These changes may further influence the spalling behavior of UHPC when exposed to elevated temperatures. Therefore, optimizing the binder system through the incorporation of SCMs represents a promising approach for performance enhancement. However, systematic investigations are still lacking to clarify the intrinsic relationships among SCM dosage, pore structure modification, and resistance to spalling at elevated temperatures.

### 1.1.3 Evolution of mechanical properties of UHPC at elevated temperatures

Fire remains a non-negligible threat to civil infrastructure, with severe implications for both structural performance and occupant safety. UHPC exhibits excellent performance under ambient conditions due to its high strength, dense microstructure, and extremely low permeability. However, these same characteristics can increase its susceptibility to spalling at elevated temperatures, thereby undermining its reliability in fire-exposed applications. The incorporation of polypropylene (PP) fibers has been extensively investigated for enhancing the fire resistance of UHPC. Upon exposure to high temperatures, PP fibers melt and generate macro-channels within the matrix, facilitating the release of steam pressure and thereby effectively reducing or even preventing explosive spalling [19, 20]. The addition of steel fibers primarily contributes to the improvement of mechanical properties and overall toughness of

UHPC after exposure to high temperatures [20]. Hybrid fiber reinforcement strategies have been widely investigated to enhance the thermal stability and spalling resistance of UHPC. The combination of PP fibers with steel fibers or natural fibers such as sisal and jute has been shown to significantly enhance the spalling resistance and residual mechanical properties of UHPC under elevated temperature conditions [21, 22]. In addition, synthetic fibers such as nylon, polyvinyl alcohol (PVA), and polyethylene terephthalate (PET) are generally less effective than PP fibers in preventing spalling. However, they can help improve the toughness and impact resistance of UHPC at elevated temperatures [23, 24].

Although numerous studies have focused on evaluating the basic mechanical performance of UHPC under high-temperature conditions, most have emphasized the dominant role of fiber type in determining residual strength and spalling resistance. However, systematic investigations into the post-heating fracture behavior of UHPC remain limited. Fracture energy is a fundamental measure of the resistance of materials to crack initiation and propagation, reflecting the total energy absorbed during the fracture process. It plays a critical role in evaluating whether UHPC retains sufficient load-bearing capacity after exposure to elevated temperatures. Current research on UHPC has largely focused on its performance at discrete temperature levels, while systematic studies examining the temperature-dependent evolution of its properties remain scarce. Therefore, establishing a correlation model between fracture performance and temperature under high-temperature conditions holds significant theoretical value. Such a model can contribute to a deeper understanding of the post-heating failure mechanisms of UHPC and support efforts to enhance its structural safety.

### 1.1.4 Mix design of SUHPC with superior early-age performance

In emergencies such as fire, collapse, water ingress, or localized impact affecting major load-bearing structures like tunnel linings and bridge piers, repair materials are required to respond rapidly. It is essential that repair materials harden rapidly and offer immediate support to maintain structural stability and protect occupant safety. In recent years, sprayed ultra-high-performance concrete (SUHPC) has emerged as a focal point of research in the field of rapid repair materials due to its high strength, excellent durability, and strong adaptability to complex structural interfaces. SUHPC integrates the advantages of conventional UHPC and shotcrete techniques, offering superior mechanical strength along with the capability for thinner layer application during spraying. Despite its numerous advantages, SUHPC still faces critical challenges in terms of rheological properties, early-age shrinkage, and early-age strength, which require further breakthroughs.

Current research on SUHPC is still in its early developmental stage and remains largely exploratory in nature. To improve the sprayability of SUHPC, some studies have investigated the use of viscosity-enhancing admixtures (VEAs) to increase its yield stress and thixotropic behavior [25]. However, the incorporation of VEAs tends to increase the porosity of SUHPC, which in turn compromises its mechanical performance [26]. In addition, $Al_2(SO_4)_3$-based alkali-free accelerators have been applied in shotcrete systems to shorten the setting time of SUHPC and enhance its early-age strength [27, 28]. Despite these benefits, the use of accelerators also presents certain limitations, including increased macroscopic porosity, intensified long-term shrinkage, and relatively high cost. Developing alternative approaches for

SUHPC to accelerate setting and enhance early-age strength, while reducing reliance on alkali-free accelerators, remains an urgent research priority.

Binder optimization in SUHPC may serve as an effective means of reducing or eliminating the reliance on alkali-free accelerators. This dissertation introduces a ternary binder system (PC–CAC–C$), composed of Portland cement (PC), calcium aluminate cement (CAC), and gypsum (C$), aiming to improve the rheological performance, shrinkage resistance, and early-age strength of SUHPC. The underlying mechanism lies in the formation of ettringite, which serves as the primary expansive phase in the PC–CAC–C$ system. Its presence not only helps mitigate autogenous shrinkage but also accelerates the setting process [29]. Theoretically, the application of the PC–CAC–C$ system in SUHPC has the potential to partially or even completely offset the shrinkage induced by accelerators, thereby enabling the replacement of alkali-free accelerators. However, the PC–CAC–C$ system has not been applied in SUHPC, and the role of the gypsum-to-CAC ratio (C$/CAC) in governing hydration mechanisms remains unexplored.

### 1.1.5 Performance of SUHPC with different cementitious materials and accelerators at later age

The previous section (Section 1.1.4) focused on the early-age performance of SUHPC, highlighting the use of various binder systems composed of different cementitious materials to improve rheological properties, shrinkage resistance, and early-age strength, while also reducing reliance on alkali-free accelerators. In contrast, this section addresses the lack of systematic research on the effects of cementitious materials and accelerators on the later-age mechanical properties of SUHPC.

The various binder systems investigated in this study, composed of different cementitious materials, include a PC-based binder system, a binary system (PC–CAC), and a ternary system (PC–CAC–C$). The PC-based system consists solely of Portland cement and serves as the control group. In the binary binder system (PC–CAC), the formation of ettringite, along with $CAH_{10}$ and/or $C_2AH_8$, is likely to accelerate the setting process, thereby contributing to the enhancement of early-age strength. The hydration behavior of the ternary binder system (PC–CAC–C$) becomes more complex, as it is further influenced by the proportions of PC to CAC and CAC to gypsum [30, 31]. Studies reported that an appropriate ratio of CAC to gypsum (CAC/C$) promotes the rapid formation of ettringite, which can significantly reduce autogenous shrinkage and accelerate the setting process [32-34]. Therefore, in theory, the incorporation of a PC–CAC–C$ system in SUHPC may partially or even fully offset the shrinkage induced by alkali-free accelerators, offering a potential sustainable solution for accelerators.

Although various studies have investigated the effects of different binder systems on concrete performance, most of them have focused on early-age properties (such as hydration behavior, early strength development, and setting time). However, there is a lack of systematic research that thoroughly evaluates the combined effects of different binder systems and alkali-free accelerators on the later-age mechanical properties of SUHPC. Detailed investigations into comprehensive mechanical performance indicators such as flexural strength, compressive

strength, flexural toughness, compressive toughness, fracture energy, and compressive energy absorption remain limited. A comprehensive understanding of these mechanical parameters is essential for informing the practical use and design optimization of SUHPC in structural engineering.

### 1.1.6 Spalling resistance of SUHPC under elevated temperatures

Civil infrastructure such as tunnels and bridges must be designed to withstand potential fire and other high-temperature extremes during the service life. SUHPC, characterized by its exceptional mechanical strength and suitability for rapid application on complex geometries, presents significant potential for structural repair and tunnel lining applications. However, its spalling behavior and the associated mechanisms under high-temperature exposure have yet to be systematically investigated.

SUHPC is characterized by an extremely low porosity and a highly compact microstructure, resembling that of conventional UHPC [35]. At elevated temperatures, this dense matrix inhibits vapor escape, leading to a rapid buildup of internal steam pressure and a greater susceptibility to explosive spalling than ordinary shotcrete. Incorporating polypropylene (PP) fibers into concrete is a commonly adopted and effective method for mitigating high-temperature-induced spalling. PP fibers melt and generate macropores within the UHPC matrix at elevated temperatures. These pores provide pathways for steam release and thereby mitigate spalling; however, the resulting voids can also compromise residual strength and long-term durability [36-38]. Due to their high thermal conductivity, steel fibers can intensify temperature gradients within concrete, thereby promoting local thermal stresses and elevating the risk of explosive spalling [39]. Nevertheless, steel fibers maintain effective crack-bridging capacity at elevated temperatures, which enhances the residual strength and toughness of UHPC [40]. A hybrid reinforcement approach incorporating steel and PP fibres can further mitigate strength degradation and spalling under elevated temperatures [38]. Nevertheless, the macropores created by melted PP fibres continue to adversely affect the residual strength of UHPC, and this structural issue remains fundamentally unresolved. To address this limitation, binder optimization aimed at introducing a greater number of uniformly distributed fine pores has emerged as a promising alternative strategy for enhancing the high-temperature spalling resistance of SUHPC.

CAC exhibits excellent high-temperature resistance, particularly at temperatures of 800°C or even above 1000°C, and is widely used in refractory concrete applications [41, 42]. Its hydration products, such as $CAH_{10}$ and $C_2AH_8$, tend to transform into stable $C_3AH_6$ under elevated temperatures, increasing the porosity of the matrix. This increased porosity facilitates the release of internal vapor pressure, thus enhancing the spalling resistance of the concrete. However, excessive incorporation of CAC may lead to a significant reduction in strength and an increase in material costs. Existing studies recommend limiting the CAC content to below 400 kg/m³ and maintaining the water-to-binder ratio below 0.40 to mitigate these adverse effects [43]. In this context, the use of a ternary binder system (PC–CAC–C$) with a controlled CAC dosage holds promise for enhancing the overall performance of SUHPC under low water-to-binder ratios and elevated temperature conditions. The ternary binder system exhibited excellent mechanical performance when the gypsum-to-CAC ratio (C$/CAC) was maintained

at 0.5 [44]. However, research on the high-temperature spalling resistance of ternary binder system (PC–CAC–C$) remains scarce, especially in the context of SUHPC, where systematic investigations have yet to be conducted.

## 1.2 Research motivation and aim

Driven by the concepts of green construction and low-carbon development strategies, SCMs play a crucial role in the sustainable advancement of UHPC. The appropriate incorporation of SCMs can substantially reduce cement usage and associated carbon emissions, while simultaneously enhance strength development and refine the microstructure of UHPC. However, systematic investigations into the underlying mechanisms by which SCMs enhance the durability of UHPC remain scarce. Specifically, comprehensive investigations into the evolution of hydration products and the fundamental mechanisms governing chloride ion transport at the microstructural level remain limited. Moreover, the introduction of SCMs alters the pore structure and the fiber-matrix interfacial bonding, potentially influencing the explosive spalling behavior of UHPC. However, systematic research exploring the relationship between SCM content and hydration, pore structure, durability, and high-temperature spalling resistance of UHPC remains scarce, highlighting an urgent need for further investigation.

Furthermore, fire events constitute a common extreme condition and pose a critical safety challenge during the service life of concrete structures, potentially compromising their structural integrity and service lifespan. Although UHPC exhibits outstanding mechanical performance and durability, its pronounced susceptibility to explosive spalling at elevated temperatures severely limits its use in high temperature environments. Although compressive and flexural strengths have been widely studied after high-temperature exposure [36, 45-48], research on fracture energy remains limited. Fracture energy, a critical parameter reflecting crack propagation resistance, is essential for evaluating structural safety after high-temperature exposure. Nevertheless, systematic investigations into the fracture behavior of UHPC following exposure to high temperatures, particularly the influence of varying steel fiber contents on fracture energy and crack propagation resistance, remain limited. Current research on the fracture performance of concrete, including UHPC, is largely limited to discrete temperature levels [36, 49, 50], with few studies providing a comprehensive temperature-fracture energy relationship. A clear understanding of the temperature–fracture energy relationship is essential for enhancing the structural safety of UHPC under high-temperature conditions.

When large-scale concrete structures are subjected to localized impacts or fire, rapid repair materials capable of providing immediate structural support are essential for maintaining structural safety. SUHPC, characterized by its high strength and the ability to be rapidly sprayed without formwork over complex geometries, has attracted considerable attention. Although SUHPC demonstrates excellent strength and durability, its early-age rheological behavior, early strength development, and shrinkage performance still require significant improvement and further investigation.

The synergistic effects of various binder systems composed of different cementitious materials can effectively improve the early-age rheological performance and strength of SUHPC, while

the addition of alkali-free accelerators at the nozzle can substantially shorten the setting time. However, the influence of these introduced factors on the later-age mechanical performance of SUHPC remains unclear, particularly in terms of compressive strength, flexural strength, flexural fracture energy, and toughness index.

Conventional PC-based SUHPC remains highly vulnerable to explosive spalling under high-temperature conditions such as fires, endangering both structural integrity and occupant safety. Binder optimization through the development of novel binder systems represents a promising research avenue for enhancing the high-temperature spalling resistance of SUHPC. Improving the residual strength of SUHPC following high-temperature exposure is crucial, as it directly affects the structural integrity of fire-damaged concrete elements, which is of great importance in engineering practice.

This research comprises two interconnected parts focusing on UHPC and SUHPC:

**Part I** involves optimizing the binder system of UHPC and investigating its spalling behavior after high-temperature exposure, with the aim of gaining a deeper understanding of its post-heating failure mechanisms.

**Part II** focuses on designing an optimized binder system for SUHPC to enhance early- and later-age performance and enhanced spalling resistance after high-temperature exposure.

The aim of this thesis is to develop a fire-resistant SUHPC tailored for rapid structural repair, based on fundamental insights derived from UHPC research. To fulfill this aim, the following specific research objectives have been formulated:

- To understand the effects of GGBS and LP on the spalling resistance and durability in terms of chloride penetration resistance on UHPC.
- To understand the flexural fracture behavior of UHPC after high temperature exposure.
- To develop a novel sprayed UHPC based on PC-CAC-C$ with superior early-age performance, characterized by high thixotropy, early strength, and micro-expansion properties.
- To clarify the effects of various cementitious materials and alkali-free accelerator on the long-term mechanical properties of sprayed UHPC based on PC-CAC-C$.
- To investigate the spalling resistance of SUHPC based on PC-CAC-C$ reinforced with calcium sulfate whiskers and steel fibers under elevated temperatures.

## 1.3 Outline of the thesis

The research framework of this study is illustrated in Fig. 1.2. The specific contents of each chapter are introduced in the following sections.

**Chapter 1** presents the motivation and background and defines the research scope and objectives.

**Chapter 2** provides a systematic investigation into the mechanisms by which varying dosages of GGBS and LP influence the hydration behavior, pore structure, mechanical properties, and durability of UHPC. This chapter provides a mechanistic understanding of how SCMs influence

the spalling resistance of UHPC via pore structure evolution.

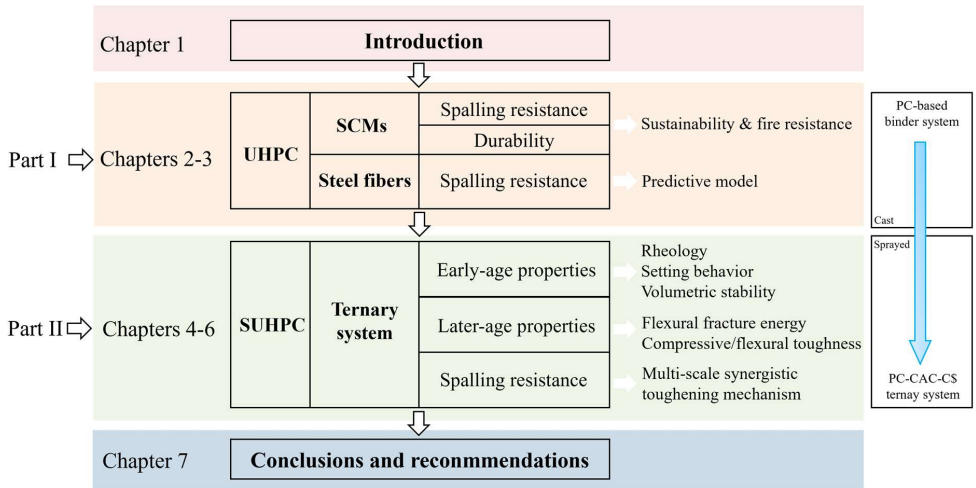


Fig. 1.2. Outline of the thesis.

**Chapter 3** investigates the flexural and fracture performance of UHPC incorporating different steel fiber volume contents under high-temperature exposures of 200 °C, 400 °C, 600 °C, and 800 °C. To clarify the fracture mechanisms of UHPC after high-temperature exposure, several key mechanical parameters, including bending toughness, double-K fracture toughness, and fracture energy, are measured and analyzed. Furthermore, a predictive model for predicting the fracture behavior of UHPC at elevated temperatures is proposed and validated.

**Chapter 4** shifts the focus to sprayed UHPC (SUHPC), aiming to optimize its early-age performance. A novel SUHPC is developed by introducing a ternary binder system (PC–CAC–C$). The effects of the C$/CAC ratio on hydration, rheology, early-age strength, and early expansion behavior of SUHPC are systematically investigated using quantitative X-ray diffraction (QXRD), thermogravimetric analysis (TGA), isothermal calorimetry, rheological measurements, and scanning electron microscopy (SEM). An optimal C$/CAC ratio is identified. In addition, the synergistic effect between the alkali-free accelerator and the ternary binder system on hydration kinetics is further explored.

**Chapter 5** investigates the later-age mechanical properties of SUHPC incorporating an alkali-free accelerator and various binder systems composed of different cementitious materials, including a PC-based system, a binary system (PC–CAC), and a ternary system (PC–CAC–C$). The stress–strain and load–displacement curves are used to characterize the deformation behavior of SUHPC specimens across the elastic, strain-hardening, and failure stages. Furthermore, the observation of failure modes, including crack initiation and propagation, contributes to understanding the correlation between microstructural features and macroscopic mechanical behavior of SUHPC.

**Chapter 6** further investigates the spalling resistance of SUHPC, which incorporates a ternary binder system, reinforced by calcium sulfate whiskers (CSW) and steel fibers. Using PC-based SUHPC as a reference, this chapter systematically investigates the evolution of hydration products, spalling behavior, microstructural changes, residual strength, and pore structure of the

ternary system-based SUHPC across a temperature range of 20 °C to 1000 °C. In addition, the synergistic toughening mechanisms of CSW and steel fibers in the ternary binder matrix and their contribution to improving spalling resistance at elevated temperatures are thoroughly analyzed and summarized.

**Chapter 7** summarises the conclusions of this research and provides recommendations for future study.

# Chapter 2 Effect of SCMs on the explosive spalling resistance of UHPC at elevated temperatures


## *Abstract*

To mitigate cement overuse and associated $CO_2$ emissions, the incorporation of supplementary cementitious materials (SCMs) offers a sustainable strategy for producing eco-friendly ultra-high-performance concrete (UHPC). Moreover, the incorporation of SCMs significantly alter the pore structure characteristics of UHPC, thereby influencing its resistance to explosive spalling at elevated temperatures. This study investigated the effects and underlying mechanisms of varying replacement levels of ground granulated blast furnace slag (GGBS) and limestone powder (LP) on hydration, pore structure, mechanical properties, durability and explosive spalling resistance in designed UHPC. The experimental results showed that GGBS significantly improved durability, with optimal performance at 30 wt%, attributable to enhanced secondary hydration and reduced pore connectivity. In contrast, LP provided strength benefits at 15 wt% but adversely affected chloride resistance due to poor fiber-matrix bonding. Correlation analysis indicated that chloride resistance in UHPC is primarily governed by pore structure and fiber-matrix interfacial transition zone (ITZ) refinement, wherein GGBS enhances both through secondary hydration, while LP replacement tends to impair interfacial bonding at elevated replacement levels. However, both GGBS and LP exhibited detrimental effects on the explosive spalling resistance of UHPC at elevated temperatures.



This chapter is partially published elsewhere:

J. He, T. Liu, W.W. Wu, X. Ling, and Q.L.Yu, Mechanism of SCMs on the hydration, pore structure, and durability of UHPFRC. Journal of Sustainable Cement-Based Materials, 14(9) (2025), 1899–1916.

## 2.1 Introduction

With the rapid development of infrastructure projects such as long-span bridges, harbors, and marine structures, concrete materials increasingly require superior overall performance, particularly regarding strength, durability, and extended service life, due to aggressive corrosion environments. Ultra-high-performance concrete (UHPC) has emerged as a superior construction material due to its exceptional mechanical properties and durability, making it highly suitable for aggressive environments such as marine and coastal regions [51-55]. The incorporation of steel fibers in UHPC significantly enhances its ductility and strength [56, 57]. However, the high cement content and relatively low hydration efficiency in UHPC result in substantial material costs and significant carbon emissions [58, 59].

To address sustainability concerns associated with high cement usage and the resulting carbon footprint, partial replacement of Portland cement with SCMs has attracted increasing attention [60-62]. SCMs such as fly ash (FA) [63, 64], silica fume [65], metakaolin (MK) [66-68], ground granulated blast furnace slag (GGBS) [62, 69], and limestone powder (LP) [60, 61, 70] have been extensively investigated to improve mechanical properties, durability, and the microstructure of cementitious systems. However, the sustainable supply of FA is challenged by the global decline in coal-based power generation. Although silica fume improves strength and durability, excessive replacement levels may lead to increased autogenous shrinkage and microcracking [71]. MK may reduce workability at high replacement levels due to its limited dispersibility. Among these SCMs, GGBS is considered a promising alternative for UHPC due to its high pozzolanic reactivity, low carbon footprint, and potential contributions to pore refinement and durability enhancement. Additionally, LP has attracted growing interest for its filler effect and nucleation effect, which may help refine the pore structure and improve durability in sustainable UHPC systems. However, systematic investigations remain limited, particularly in clarifying the underlying mechanisms and optimizing the incorporation of these SCMs in UHPC.

GGBS is characterized by high contents of $SiO_2$ and $Al_2O_3$, which lead to significant pozzolanic reactivity. This reactivity promotes the secondary hydration and enhances the formation of C-S-H and C-A-S-H gels, thereby improving the physical adsorption of chloride ions in cementitious materials [72]. In addition, the abundant MgO and $Al_2O_3$ in GGBS facilitate the formation of Mg-Al layered double hydroxides (LDHs) and Friedel's salt (Fs), contributing to chemical chloride binding in cement-based systems [73, 74]. However, these chloride-binding mechanisms are generally effective after chloride ingress and are insufficient to fully immobilize continuously penetrating chloride ions from external sources. Given the limited chloride-binding capacity of concrete, the incorporation of GGBS to refine the pore structure and improve the ITZ in UHPC is considered an effective strategy to reduce chloride permeability. The pore refinement induced by GGBS occurs via both macroscopic and microscopic mechanisms. On the macroscopic scale, GGBS optimizes particle packing through filler effects, refining the pore structure [75-77]. At the microscopic level, the pozzolanic reaction of active silica-alumina components within GGBS further contributes to pore refinement in cement paste [69, 70, 78, 79]. Despite the recognized role of GGBS in refining pore structure and improving durability [80], the steel fiber-matrix ITZ, which is considered a

potential pathway for chloride ingress in UHPC, has not been thoroughly investigated. Therefore, systematic studies investigating the effects of GGBS on hydration processes, pore structure evolution, the steel fiber-matrix ITZ, and subsequent chloride permeability in UHPC remain limited.

LP, a by-product from limestone quarries, primarily consists of calcite ($CaCO_3$). As a widely utilized SCM in cement-based materials, LP influences hydration through mechanisms such as nucleation [81], chemical effects [82], and filler effects [83]. Physically, LP fills voids and provides additional nucleation sites for hydration products, thereby reducing the porosity of the cement matrix and consequently decreasing chloride diffusivity [84]. Chemically, the calcite in LP can react with aluminous phases in cement to form monocarboaluminates (Mc) and hemicarboaluminates (Hc) [85]. This reaction reduces monosulfate formation and stabilizes ettringite, increasing the volume of hydration products, refining the microstructure, and ultimately reducing chloride ingress. Due to the relatively low reactivity of LP, the chemical effect is generally limited. In the context of UHPC, research on LP has predominantly focused on its effects on rheology [62], shrinkage [61], strength [86], and pore structure [16], with limited attention to chloride resistance. For example, Li et al. [15] demonstrated that incorporating 50 vol% limestone powder optimizes the strength, shrinkage behavior, and pore structure of UHPC. Luan et al. [85] further reported that the synergistic use of limestone and ultrafine slag significantly enhanced the compressive strength and densified the pore structure of UHPC. Nevertheless, the influence of LP on the steel fiber-matrix ITZ in UHPC, which may serve as a preferential pathway for chloride ingress, remains insufficiently investigated.

Beyond the challenge of high carbon emissions, explosive spalling resistance has also emerged as a critical concern for UHPC. Due to its low porosity and dense microstructure, UHPC hinders vapor dissipation, leading to internal pressure buildup and increasing the risk of explosive spalling under high-temperature exposure [87]. Therefore, improving the pore structure and introducing microscopic voids can provide escape pathways for water vapor, thereby reducing the risk of explosive spalling. At present, polypropylene (PP) fibers are widely used to mitigate explosive spalling in UHPC [88]. However, the incorporation of PP fibers leads to fiber melting at relatively low temperatures (around 200 °C), introducing macropores into the matrix. While this enhances resistance to explosive spalling at high temperatures, the resulting macroporosity significantly compromises the mechanical properties of the material [38]. As previously discussed, SCMs such as GGBS and LP can refine the pore structure and modify the fiber–matrix interface, which may help reduce explosive spalling in UHPC. However, systematic studies on their influence under high-temperature exposure remain scarce.

Considering the dense particle packing of UHPC and the increasing demand for sustainable cementitious systems, this study investigates the effects of different replacement levels of GGBS and LP on hydration behavior, pore structure evolution, mechanical performance, steel fiber–matrix ITZ, durability, and explosive spalling resistance of UHPC. A comprehensive experimental program was conducted to characterize hydration, microstructure, interfacial properties, chloride resistance, and high-temperature spalling behavior. Based on the correlation analysis of the experimental results, this chapter aims to provide a theoretical basis for the design of SCM-incorporated UHPC with improved sustainability, enhanced chloride

resistance, and a mechanistic understanding of spalling resistance related to pore-structure evolution.

## 2.2 Materials and experiments

### 2.2.1 Raw materials

The raw materials used in this study were Portland cement CEM I 52.5 R (PC), GGBS, LP, fine sand, sand, tap water (W), polycarboxylate superplasticizer (PCE) and steel fiber. The chemical properties of the powders were analyzed by X-ray fluorescence (XRF), which are presented in Table 2.1. The particle morphologies of the used GGBS and LP were tested by scanning electron microscopy (SEM, Phenom ProX), shown in Fig. 2.1. The particle size distribution of the raw materials is shown in Fig. 2.2. In this study, 2 vol% short straight steel fibers with the length of 13 mm and diameter of 0.2 mm were adopted, which are provided by Bekaert. Fine sand (0-0.2 mm and 0-2 mm) were added as aggregates. A polycarboxylate-based superplasticizer (PCE) with a solid content of 35% was used at a constant dosage of 2.0 wt% relative to the binder weight in all UHPC mixtures to ensure sufficient and comparable workability across different mixes.

Table 2.1. Chemical compositions of raw materials (wt%).

| | **CaO** | **$SiO_2$** | **$Al_2O_3$** | **$Fe_2O_3$** | **$K_2O$** | **$Na_2O$** | **$SO_3$** | **MgO** | **$TiO_2$** | **$Mn_3O_4$** | **LOI** |
|---|---|---|---|---|---|---|---|---|---|---|---|
| PC | 65.50 | 22.10 | 4.78 | 4.08 | 0.51 | 0.29 | 3.19 | 2.19 | 0.25 | 0.13 | 1.9 |
| GGBS | 37.69 | 33.79 | 13.37 | 0.58 | 0.44 | - | 1.72 | 10.70 | - | - | 1.3 |
| LP | 57.01 | 1.79 | 0.19 | 0.03 | - | 0.13 | 0.07 | 0.18 | - | - | 40.5 |

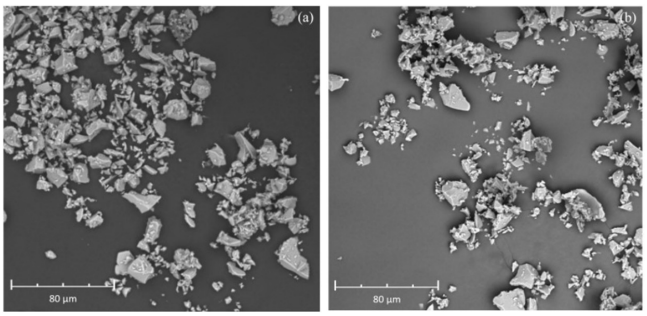


Fig. 2.1. Particle morphologies of (a) GGBS, (b) LP.

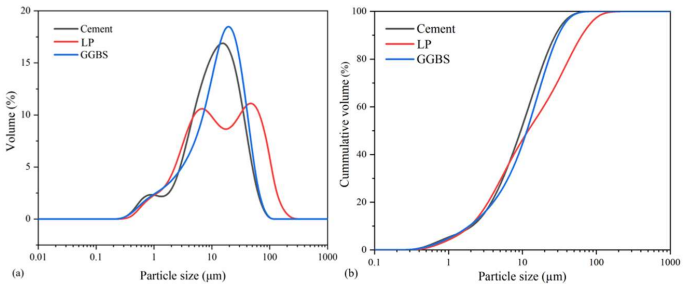


Fig. 2.2. (a) Particle size distribution of raw materials; (b) Cumulative volume of raw materials.

### 2.2.2 Mix proportion and specimen preparation

The mix proportions for UHPC mixtures investigated in this study are summarized in Table 2.2. A water-to-cement ratio (w/c) of 0.20 was adopted, and the HRWR content was fixed at 2 wt.% by mass of binder. The designs of all UHPC mixtures in this study were based on the modified Andreasen and Andersen model [57, 89]. 50×50×50 $mm^3$ cube molds and 40×160×160 $mm^3$ prism moulds were filled to prepare specimens for compressive strength test and three-point bending test, respectively. In this study, all UHPC mixtures were prepared using the same mixing procedure and casting method. The samples for the rapid chloride ion migration (RCM) test were cast into plastic cylinder molds with 100 mm diameter and 50 mm height according to NT Build 492 [90]. Following Standard EN 12390-2 [91], the samples were demolded and cured in water at 20 ℃ until further tests.

In this study, the control group was chosen to be the REF mixture containing 100% PC without any SCMs. In order to facilitate analysis and comparison, the GGBS-cement and LP-cement binder system were classified into two series: Series I concerns only GGBS replacement (REF, G15, G30 and G45 mixes), and Series II concerns only LP replacement (REF, LP15, LP30 and LP45 mixes).

Table 2.2. Mixture proportion of UHPC specimens (kg/$m^3$).

| | Mix ID | PC | GGBS | LP | Fine sand | Sand | W | SP | Steel fiber |
|---|---|---|---|---|---|---|---|---|---|
| Series I | REF | 949 | 0 | 0 | 275 | 1027 | 155 | 54 | 156 |
| | G15 | 807 | 142 | 0 | 275 | 1027 | 155 | 54 | 156 |
| | G30 | 664 | 285 | 0 | 275 | 1027 | 155 | 54 | 156 |
| | G45 | 522 | 427 | 0 | 275 | 1027 | 155 | 54 | 156 |
| Series II | REF | 949 | 0 | 0 | 275 | 1027 | 155 | 54 | 156 |
| | LP15 | 807 | 0 | 142 | 275 | 1027 | 131 | 46 | 156 |
| | LP30 | 664 | 0 | 285 | 275 | 1027 | 108 | 38 | 156 |
| | LP45 | 522 | 0 | 427 | 275 | 1027 | 85 | 30 | 156 |

### 2.2.3 Experimental methods

#### 2.2.3.1 Workability

The flow table tests were conducted in accordance with EN 1015-3 [92] to evaluate the workability of designed UHPC mixtures [93]. The relative slump (Γ) is determined using the following equation:

$$\Gamma = \left( \frac{d_1 + d_2}{2d_0} \right)^2 - 1 \tag{2.1}$$

In this equation, $d_1$ and $d_2$ represent the two perpendicular diameters of the spread sample, and $d_0$ is the base diameter of the cone mold.

#### 2.2.3.2 Isothermal calorimetry

According to the mixture proportion in Table 2.2, the heat evolution of the pastes (without steel fibers and aggregates) was characterized with an isothermal calorimeter (TAM AIR C80). All the pastes were injected into the sample container after a 2-minute mixing period. Heat flow and hydration heat data were continuously recorded for 80 hours and normalized by the total paste weight. Cumulative heat release and hydration exothermal rate were obtained and

analyzed to study the early hydration of UHPC mixtures with different replacement levels of GGBS and LP.

#### 2.2.3.3 Strength

The compressive and flexural strength tests were conducted after curing at the ages of 1, 7, and 28 days according to EN 196-1 [94]. Compression test was carried out on UHPC cubes measuring 50×50×50 $mm^3$ with the loading speed of 2.4 kN/s. Flexural strength tests were performed on a universal testing machine using 40×40×160 $mm^3$ prism samples.

#### 2.2.3.4 Morphology

The morphologies of the ITZs of hardened UHPCs (G30 and LP30 mixes) after 28 days curing were observed by SEM (TESCAN MIRA3). The effects of different SCMs on steel fiber-matrix ITZ and aggregate-matrix ITZ were observed and investigated obviously.

#### 2.2.3.5 XRD

X-ray diffraction (XRD) analysis was performed to evaluate the hydration products of samples incorporating GGBS or LP in Series I and II. The measurements were conducted using a Bruker D2 PHASER diffractometer equipped with an XE-T detector and a cobalt radiation source (Co Kα, $\lambda$ = 1.79 Å), operated at 30 kV and 10 mA. The measurements were conducted over a 2$\theta$ range from 5° to 90°, with a step size of 0.013°.

#### 2.2.3.6 TG

To analyze the thermal decomposition of the designed UHPC mixtures, the thermal gravimetric (TG) and differential thermal gravimetric (DTG) experiments were carried out to evaluate samples after 28 curing days by a Netzsch simultaneous analyzer, model STA 449 C. After the process of grinding, the powder of UHPC mixtures was heated from 20 ℃ to 1000 ℃ with the heating rate of 10 ℃/min.

#### 2.2.3.7 MIP

In this study, a mercury intrusion porosimeter (AutoPore IV 9510, Micromeritics, USA) was utilized to determine the effect of binder replacement with GGBS and LP on the development of pore structure. The MIP tests require blocks with thicknesses ranging from 1 mm to 2 mm, which were obtained by crushing hardened UHPC samples.

#### 2.2.3.8 RCM

In this study, the RCM test was conducted to clarify the effects of different content of GGBS and LP on the resistance to chloride ion penetration of the designed UHPC. The RCM test was set up as shown in Fig. 2.3 according to NT Build 492 [90] . The anode and cathode solutions were 0.3 M NaOH and 10% NaCl, respectively. After switching on the power supply, the initial voltage was set to 30 V. Subsequently, the voltage of the power supply and test duration of the test were carefully adjusted based on the initial electrical current in the first minute. Due to the superior corrosion resistance of UHPC compared to ordinary concrete, the penetration depth is significantly smaller than that of ordinary concrete. To ensure the accuracy of the data and

minimize errors, six parallel specimens were employed for each test group and the collected data were averaged.

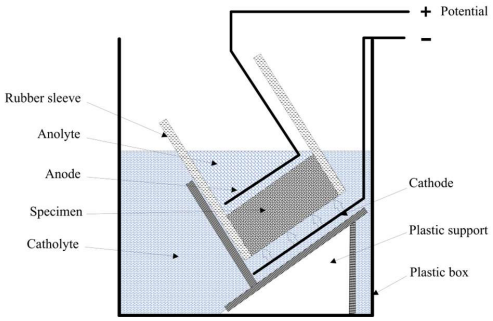


Fig. 2.3. Schematic of the RCM test.

After the test, the disc samples were axially split and sprayed with 0.1 M $AgNO_3$ solution. The applied voltage (U), time duration (t), and the average value of the penetration depths ($X_d$) were recorded. The chloride migration coefficient ($D_{nssm}$) was calculated as follows [90]:

$$D_{nssm} = \frac{0.0239(273+T)L}{(U-2)t}\left(X_d - 0.238\sqrt{\frac{(273+T)LX_d}{U-2}}\right) \quad (2.2)$$

where

$D_{nssm}$: non-steady-state chloride diffusion coefficient, $10^{-12}$ $m^2/s$;

T: average value of the initial and final temperatures in the anolyte solution, °C;

U: absolute value of the applied voltage, V;

L: thickness of the concrete specimen, mm;

$X_d$: average value of the penetration depths, mm;

t: test duration, hour.

**2.2.3.9 Spalling**

After the designated curing period, UHPC specimens were dried in an oven at 80 °C for 24 hours. Subsequently, they were then exposed to elevated temperatures of 250 °C, 500 °C, 750 °C, and 1000 °C using a muffle furnace. To protect the furnace interior from potential damage caused by explosive spalling, the specimens were placed inside steel cages. As shown in Fig. 2.4, the temperature was raised from ambient to the target level at a constant rate of 3 °C/min, followed by natural cooling within the furnace.

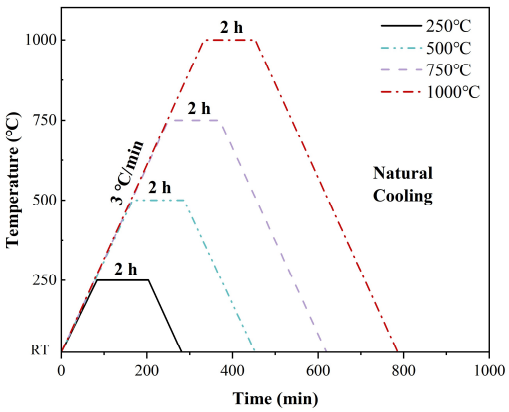


Fig. 2.4. Heating regimes of UHPC specimens.

## 2.3 Results and analysis

### 2.3.1 Workability

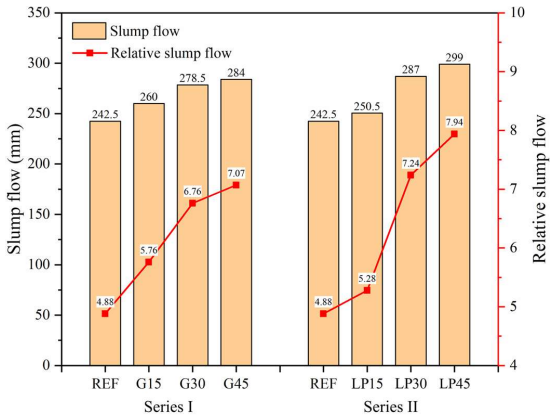


Fig. 2.5. The slump flow and relative slump flow of Series I and Series II.

Fig. 2.5 illustrated that the workability of mixtures in Series I and II was enhanced at all replacement levels within 0-45 wt%. The relative slump flow of UHPC mixes with GGBS-cement and LP-cement binder system ranged from 4.88-7.07 and 4.88-7.94, respectively, and no segregation was observed. In Series I, the relative slump flow of G15, G30, and G45 increased by 18.03%, 38.5% and 44.9% compared to REF, respectively. And the relative slump flow increased linearly when the GGBS replacement level increased in the range of 0-30 wt%. Nevertheless, the improvement rate of relative slump flow slowed down as the level of GGBS replacement exceeded 30 wt%. In Series II, a notable increase from 5.28 to 7.24 in the relative slump flow of LP15 to LP30, represented a 37.12% increment. An excessively high value of the relative slump flow may lead to deteriorative behaviors in the UHPC, such as a significant decrease in compressive strength and the subsidence of steel fibers, which will be further investigated in Section 2.3.3.

### 2.3.2 Hydration reaction at early ages

Based on the calorimetry test results, the effect of different SCMs content on hydration heat was presented in Fig. 2.6. As depicted in Fig. 2.6(a), LP15 and G15 exhibited a faster rate of heat release, reaching their exothermic peak 6.95 h and 5.31 h earlier than REF, respectively. This peak of hydration heat corresponds to $C_3S$ hydration and the growth of C-S-H gel [95]. In addition, LP and GGBS possess larger specific surface areas and smaller particle sizes than cement, which promote the nucleation effect during hydration. Therefore, the nucleation effect induced by superfine LP and GGBS significantly promotes early hydration [96], as evidenced by the accelerated exothermic peaks in LP15 and G15. These findings highlighted that low replacement levels, such as 15 wt%, can effectively enhance early-age hydration kinetics by promoting the nucleation effect of superfine SCMs, while avoiding the negative dilution effects observed at higher replacement levels.

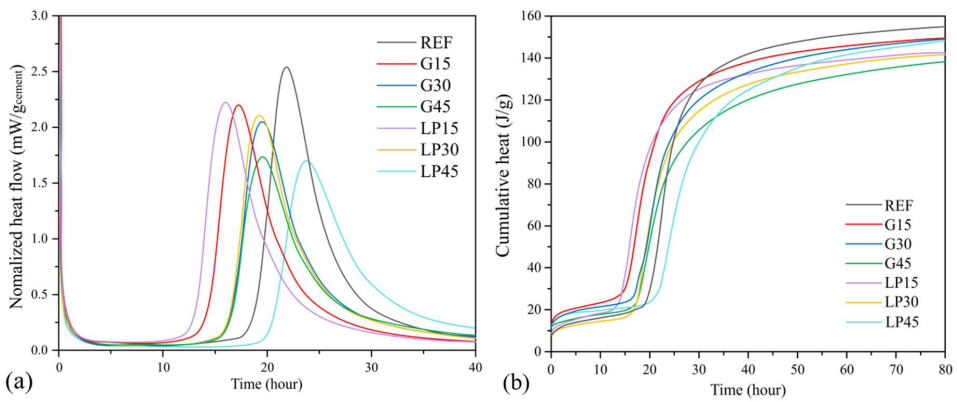


Fig. 2.6. Calorimetry test results of UHPC pastes with different SCMs content: (a) Normalized heat flow; (b) Normalized cumulative heat.

Fig. 2.6(b) illustrated the normalized cumulative heat release of UHPC mixtures at 80 h. The cumulative heat release primarily originates from the hydration reaction of cement, along with the pozzolanic reaction between GGBS and the precipitated $Ca(OH)_2$ [89]. Due to its high $SiO_2$ and $Al_2O_3$ content as shown in Table 2.1, GGBS exhibits significant pozzolanic reactivity. During the hydration process, the $Ca(OH)_2$ produced by cement hydration further reacts with GGBS, wherein the active $SiO_2$ and $Al_2O_3$ in GGBS interact with $Ca^{2+}$ and $OH^-$ to form additional C-S-H and C-A-S-H gels, accompanied by substantial heat release. In contrast, LP is primarily composed of $CaCO_3$ and lacks notable pozzolanic reactivity. According to the normalized cumulative heat release curves in Fig. 2.6(b), compared to the REF mix, the total heat release at 80 h was reduced by 10.74% and 12.86% for the mixtures incorporating 45 wt% GGBS and 45 wt% LP, respectively. Furthermore, the REF mix exhibited the highest cumulative heat release, while an increasing replacement level of GGBS or LP led to a gradual decline in total heat release. This phenomenon could be attributed to the lower pozzolanic reactivity of GGBS and LP, as well as the dilution effect resulting from cement replacement.

### 2.3.3 Mechanical properties of UHPC

#### 2.3.3.1 Effects of SCMs content on compressive strengths of UHPC

The compressive strengths of Series I and Series II specimens after standard curing for 7 and 28 days were presented in Fig. 2.7. It could be observed that Series I and Series II exhibited comparable strengths at 7 days; however, significant differences emerged in the strength development between 7 and 28 days. In Series I, the strength growth rates of REF, G15, G30, and G45 from 7 to 28 days were 5.1%, 10.2%, 29.4%, and 41.2%, respectively. Evidently, GGBS exhibited a notable advantage in promoting later-age strength development compared to the control mix (REF). This observation aligned well with findings reported in a previous study [60]. Despite the considerable strength increment observed in the G45 between 7 and 28 days, its 28-day compressive strength remained substantially lower than that of the G30. This result will be further discussed in Section 2.3.5 through quantitative analysis of hydration products. In Series II, the strength growth rates of REF, LP15, LP30, and LP45 from 7 to 28 days were 5.1%, 21.3%, 3.2% and 6.5%, respectively. Among all samples, G30 in Series I and LP15 in Series II exhibited the highest strength growth rates during the period from 7 to 28 days.

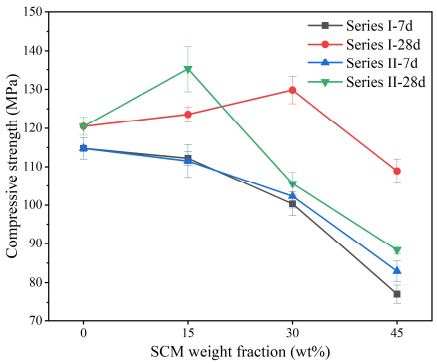


Fig. 2.7. Compressive strength of UHPC.

The compressive strength at 28d of both Series I and Series II initially increased and then decreased as replacement levels rise. In Series I, the compressive strength peaked at 129.8 MPa with a GGBS replacement level of 30 wt%. As the GGBS content further increased from 30 wt% to 45 wt%, the strength decreased significantly by approximately 16.1%. This reduction was attributed to the reduced reactivity of GGBS at higher replacement levels and the dilution of cementitious phases, as further discussed in Section 2.3.5 through the quantitative analysis of hydration products. In Series II, the highest compressive strength of 135.2 MPa was achieved at a LP substitution level of 15 wt%. This enhancement was attributed to the nucleation effect, wherein LP particles serve as nucleation sites for hydration products [97]. With further increases in LP content, the 28-day compressive strengths of LP30 and LP45 decreased by 37.36% and 45.16%, respectively, compared to the REF. This finding indicated that 15 wt% is the optimal replacement level of LP, at which the nucleation and filling effects dominated, promoting the development of strength. Beyond this optimal level, the dilution effect became predominant, diminishing the beneficial influence of nucleation and subsequently impairing strength development.

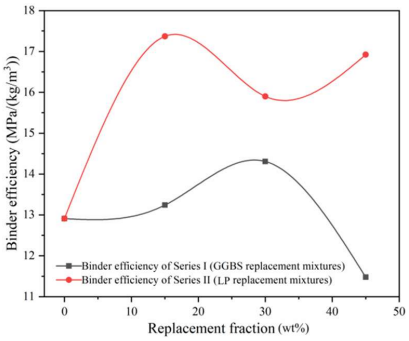


Fig. 2.8. The binder efficiency of Serie I and Serie II.

Binder efficiency, defined as the ratio of normalized compressive strength at 28 days to binder mass [15], was significantly enhanced by partial cement replacement with SCMs, as illustrated in Fig. 2.8. In Series I, the maximum binder efficiency reached 15.90 MPa/(kg/m³), indicating that a 30 wt% GGBS replacement level was optimal for UHPC. In Series II, the maximum binder efficiency reached 17.37 MPa/(kg/m³) with a 15 wt% LP replacement, highlighting 15 wt% LP as the optimal content for UHPC mixtures.

### 2.3.3.2 Effects of SCMs content on flexural load–deflection behaviour of UHPC

The effects of SCMs on flexural load versus mid-span deflection curves of UHPC mixtures under three-point bending at 28d were illustrated in Fig. 2.9(a). From Fig. 2.9(b), the steel fibers being drawn out are clearly visible. The effects of SCMs content on flexural toughness of UHPC mixtures at 28d were shown in Table 2.3. The residual strength factor and toughness index were derived to indicate the ductility and energy absorbed by the beam under flexural load. For example, the toughness index $I_5$ of G15 was defined by this test method as the area OACD ($S_{OACD}$) divided by the area OAB ($S_{OAB}$) up to the first crack as illustrated in Fig. 2.9(a). In brief, the toughness index $I_5$, $I_{10}$ and $I_{20}$ were derived by dividing the area up to a deflection of 3, 5.5, and 10.5 times of the first crack deflection (3$\delta$, 5.5$\delta$ and 10$\delta$) by the area up to first crack, respectively [98].

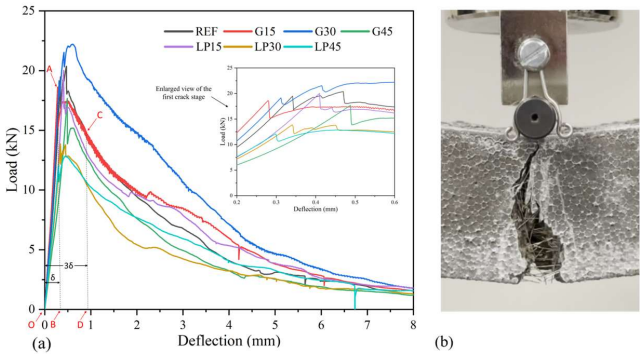


Fig. 2.9. (a) Flexural load-deflection curves at 28 d; (b) The steel fibers being drawn out.

In Series I, the peak strength of REF, G15, G30 and G45 were 20.37, 17.46, 22.22 and 15.20 MPa, respectively. G30 exhibited an increase of 8.82% in peak strength compared to REF

mix. Moreover, G30 exhibited the highest residual strength coefficient among the Series I. It is worth noting that the toughness indices of G30 were significantly elevated by 135.2%, 31.6%, and 45.5% for $I_5$, $I_{10}$, and $I_{20}$, respectively, in comparison to the REF. This phenomenon indicated that the ratio of the energy consumed by G30 in reaching different displacements (such as $3\delta$, $5.5\delta$ and $10\delta$) to the energy consumed before the initial cracking displacement was quite high compared to other mixtures in Series I. Hence, it indicated that the bond between the steel fiber and the matrix was much stronger in G30 than in other mixtures in Series I, which was the major factor for the superior toughness performance of G30. Only fibers sustain the load through mechanical interlock and friction at the fiber-matrix interface after cracking [99]. Therefore, the increase of peak strength in G30 could be attributed to the enriched bond between the matrix and the steel fiber. The morphology of the steel fiber-matrix ITZ of G30 was further observed and investigated in Fig. 2.13(a). Nevertheless, when GGBS replacement further increased from 30 wt% to 45 wt%, the peak strength ($f_r$) and toughness indices ($I_5$, $I_{10}$, and $I_{20}$) demonstrated significantly reductions of 7.81%, 28.74%, 39.70% and 51.67%, respectively. This phenomenon illustrated that it significantly impaired flexural behaviors of UHPC when the replacement level of GGBS for cement exceeded 30 wt%.

In Series II, the toughness index ($I_5$, $I_{10}$, and $I_{20}$) for all LP replacement levels (15 wt%, 30 wt%, 45 wt%) exhibited a significant decrease relative to REF. It indicated that any replacement level of LP within 0-45 wt% had a detrimental effect on the flexural behaviors of UHPC. During the three-point bending test, it was observed that specimens LP15, LP30 and LP45 exhibited fewer but more concentrated micro-cracks than REF, resulting in the extraction of the steel fibers only from the main crack section. Hence, it was assumed that the incorporation of LP resulted in a more concentrated cracks and the degradation of steel fiber-matrix ITZ of UHPC specimens during the bending test. Nevertheless, it is worth noting that pre-cracking strength ($f_{cr}$) of LP15 at 28d was slightly elevated by 2.56% relative to REF. This was primarily attributed to the matrix strength, which governs the initial cracking load [68]. This explanation aligned well with the highest compressive strength observed for LP15 in Series II, as shown in Fig. 2.7.

Table 2.3. Effects of SCMs content on flexural behaviours of UHPC at 28d.

| No. | $f_{cr}$ (MPa) | $f_r$ (MPa) | $\delta_{cr}$ (mm) | $\delta_u$ (mm) | $I_5$ | $I_{10}$ | $I_{20}$ |
|---|---|---|---|---|---|---|---|
| REF | 19.5±0.4 | 20.4±0.6 | 0.34±0.04 | 0.47±0.04 | 2.47±0.43 | 8.23±0.92 | 12.53±1.21 |
| G15 | 18.6±0.2 | 17.5±0.3 | 0.28±0.05 | 0.51±0.08 | 4.84±0.79 | 8.60±0.54 | 14.20±1.08 |
| G30 | 19.2±0.7 | 22.2±1.3 | 0.31±0.02 | 0.61±0.11 | 5.81±0.38 | 10.83±0.84 | 18.23±2.06 |
| G45 | 17.7±0.2 | 15.2±0.6 | 0.49±0.11 | 0.59±0.04 | 4.14±0.21 | 6.53±0.94 | 8.81±1.33 |
| LP15 | 20.0±0.6 | 16.9±0.3 | 0.41±0.06 | 0.49±0.08 | 2.24±0.64 | 6.18±1.01 | 8.26±2.36 |
| LP30 | 13.9±0.7 | 13.8±0.8 | 0.34±0.04 | 0.45±0.02 | 2.19±0.11 | 5.96±1.14 | 7.98±1.14 |
| LP45 | 12.1±1.1 | 12.9±0.4 | 0.30±0.09 | 0.46±0.06 | 1.91±1.04 | 5.37±1.09 | 6.78±2.37 |

### 2.3.4 X-ray diffraction analysis

The XRD patterns of hydrated UHPC pastes in Series I and II for 28 days were presented in Fig. 2.10. In GGBS replacement series (Series I), the main peak of calcium hydroxide (CH) at 21° and 34° could be observed in all blended UHPC pastes. The increase in GGBS replacement level was followed by a progressive weakness of the strength of the CH diffraction peaks. Fig. 2.10(a) demonstrated that the CH peaks of G30 and G45 mixtures were much weaker than those of the other groups in Series I. The gradual weakening of CH peaks with increasing GGBS

content confirmed both the pozzolanic consumption of CH and the dilution effect from reduced cement content. Additionally, the incorporation of GGBS enhances the formation of Al-bearing hydrates such as strätlingite and hydrogarnet, contributing to the overall refinement of the hydration system and potentially improving long-term durability [100]. Furthermore, Al can also be incorporated into the C-S-H structures, forming so-called C-A-S-H (calcium-aluminate-silicate-hydrate) phases with different structures and higher chain lengths than those of C-S-H [101, 102]. Fig. 2.10 demonstrated that the X-ray diffraction peaks of UHPC pastes with different contents of LP. As the LP replacement increases, the peak of calcite became more pronounced [16]. The peaks of $C_3S$ and $C_2S$ were substantially weaker, mostly due to the decreased cement content and the diluting effect of LP as a binder.

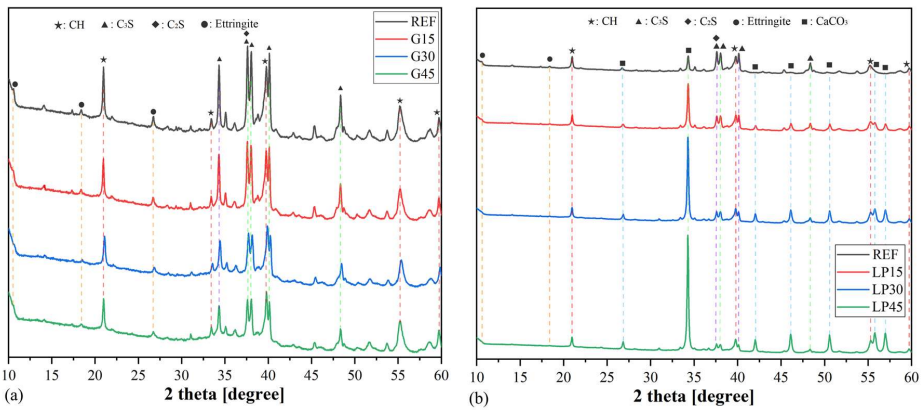


Fig. 2.10. XRD patterns of Series I (a) and Series II (b) at 28d.

### 2.3.5 Thermogravimetric analysis

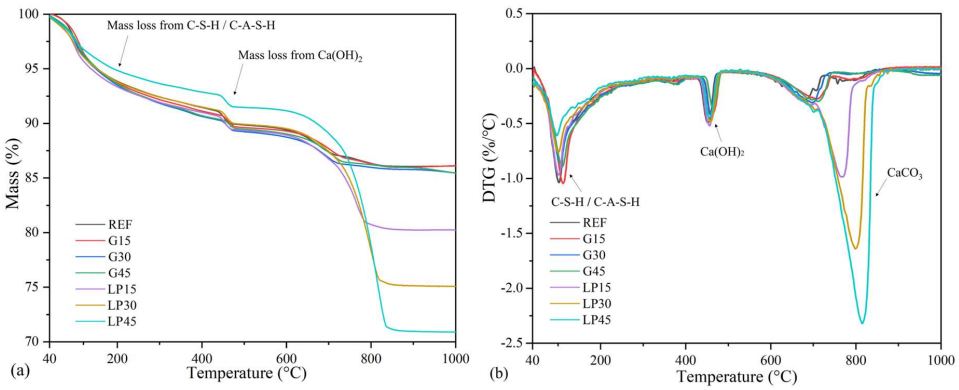


Fig. 2.11. Thermal analysis results of UHPC pastes at 28 days. (a) TG curves; (b) DTG curves.

The thermal characteristics of the developed UHPC pastes in Series I and II were presented in Fig. 2.11. As shown in Fig. 2.11(b), three main endothermic peaks were identified at 100-105 °C, 400-500 °C, and 600-800 °C, corresponding to the evaporation of free or bound water in C-S-H and AFt phases, the decomposition of CH, and the decarbonation of calcium carbonate ($CaCO_3$), respectively [103-105]. To further investigate the hydration products and degree of

hydration at different replacement levels of GGBS and LP, the quantities of C-S-H and CH were calculated and presented in Fig. 2.12.

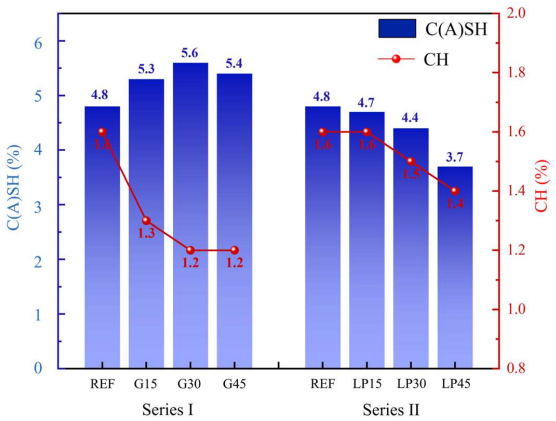


Fig. 2.12. CSH and CH contents by total mass of UHPC in (a) Series I and (b) Series II.

In GGBS replacement series (Series I), when GGBS content increased in the range of 0-30 wt%, CH content decreased from 1.6% to 1.2%, while C-(A)-S-H content increased from 4.8% to 5.6% as shown in Fig. 2.12. Among Series I, the C-(A)-S-H content in G30 reached its peak at 5.6%. It indicated that there was sufficient calcium hydroxide ($Ca(OH)_2$) in cement to activate and facilitate the reaction of GGBS in G30 [61], which resulted in a high reaction degree of GGBS, consequently a high generation of C-(A)-S-H gel. Nevertheless, when GGBS replacement further increased from 30 wt% to 45 wt%, C-(A)-S-H content decreased from 5.6% to 5.4% and CH content maintains at 1.2%. This indicated that when the GGBS replacement exceeded 30 wt%, the limited availability of CH was insufficient to activate the pozzolanic reactivity of GGBS, resulting in a lower content of hydration products such as C-(A)-S-H. This also explained the pronounced reduction in 28-day compressive strength of G45 compared to G30, which could be attributed to the reduced reactivity of GGBS and the dilution effect at higher replacement levels. Therefore, a GGBS replacement level of 30 wt% represented the optimal threshold, beyond which the dilution effect dominated and the pozzolanic reactivity of GGBS significantly declined, leading to reduced C-(A)-S-H formation.

In LP replacement series (Series II), when LP replacement level increases from 0 wt% to 45 wt%, the CH and CSH contents decreased consistently from 4.8% to 3.7%, 1.6% to 1.4% as presented in Fig. 2.12, respectively. It is reported that the reduced hydration products are due to the dilution effect of reactive binders by limestone [15]. Furthermore, the normalized C-S-H contents by mass of reactive binders in Series II (REF, LP15, LP30 and LP45) were 4.8%, 5.5%, 6.3% and 6.7%, respectively. It suggested that the incorporation of LP at any replacement level (0-45 wt%) significantly enhanced the hydration degree of active binder, thereby improving the binder efficiency. It can be noticed that the CH and CSH contents of LP15 exhibited minimal variation compared to REF. This phenomenon suggested that, at the replacement content of 15 wt% for LP, LP primarily exerts its influence on the nucleation effect in designed UHPC, enhancing the hydration degree of binder with a less noticeable dilution effect. Nevertheless, when LP replacement level further increased from 15 wt% to 45 wt%, the C-S-H content

decreased sharply from 4.7% to 3.7% due to the dilution effect of LP, while the hydration degree of cement reached its peak. Thus, a 15 wt% LP replacement represented a critical threshold at which the nucleation effect was maximized and the dilution effect remained negligible, resulting in the most efficient binder hydration.

### 2.3.6 SEM analysis

The morphology of the steel fiber-matrix ITZ and aggregate-matrix ITZ in G30 and LP30 mixes was characterized by SEM and presented in Fig. 2.13. A substantial amount of hydration products, such as C-(A)-S-H gels, was observed on the entire surface of the steel fibers in the G30 mix. This indicated a strong interfacial bond, as shown in Fig. 2.13(a), which was attributed to the high pozzolanic reactivity between GGBS and CH that promoted the formation of additional C-(A)-S-H gels. Interface between the aggregate and the matrix of the G30 was found to be dense in Fig. 2.13(c). It verified the superior flexural behaviour and compressive strength of G30 in Fig. 2.7 and Table 2.3.

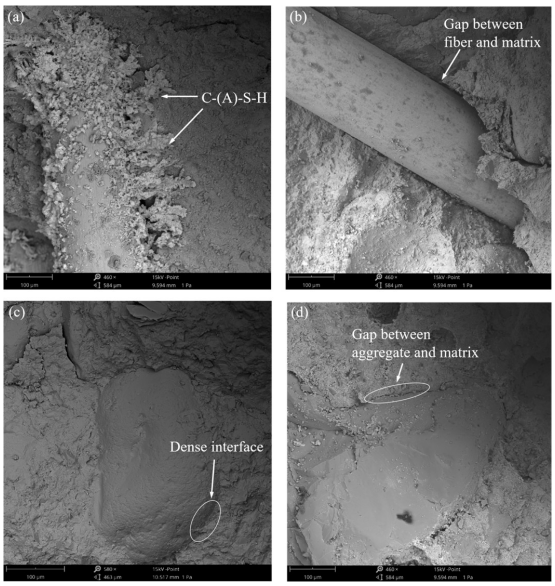


Fig. 2.13. SEM micrographs showing the steel fiber-matrix ITZ for (a) G30 and (b) LP45, and the aggregate-matrix ITZ for (c) G30 and (d) LP45.

In contrast to G30, LP30 showed noticeably fewer hydration products attached to the steel fiber surface, as was observed in Fig. 2.13(b), indicating a weaker fiber-matrix interfacial bond. Moreover, a distinct gap was observed at the aggregate-matrix interface in LP30 (Fig. 2.13(d)), indicating a degraded ITZ. This degradation was primarily attributed to the dilution effect of LP, which reduced the amount of reactive binder available for hydration. As a result, insufficient hydration products were generated, leading to weak bonding at both fiber-matrix and aggregate-matrix interfaces, and ultimately causing significant microstructural defects in both ITZs.

### 2.3.7 Pore structure analysis

To delve deeper into the impact of SCMs on pore structure, the pore size distribution of UHPC mixtures in series I and series II by the MIP test at 28 days was shown in Fig. 2.14. The pores are classified into three ranges as depicted in Table 2.4: (a) gel pores (2-10 nm); (b) capillary pores (10 nm - 10 μm); (c) macropores (>10 μm) [61]. In addition, the critical pore diameter is described as the maximum peak on the pore size distribution curve of UHPC from MIP adsorption in Fig. 2.14(a), as well as the inflection point on the cumulative pore volume curve in Fig. 2.14(b).

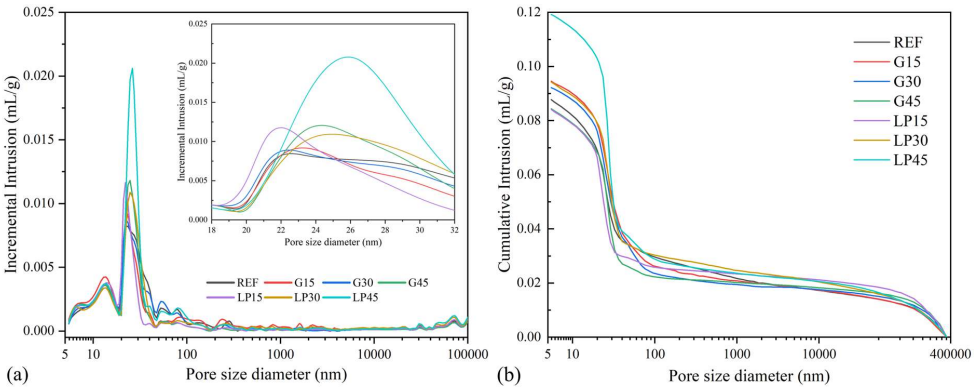


Fig. 2.14. (a) MIP adsorption cumulative pore volume of UHPC at 28 days; (b) Pore size distribution of UHPC from MIP adsorption dV/dlog(w) pore volume at 28 days.

In GGBS replacement series (Series I), as the GGBS content increased from 0 to 30 wt%, the first critical pore diameter decreased from 22.1 nm to 21.5 nm, while the total gel pores increased from 0.8% to 1.0%. An increase in gel pore content from MIP result corresponds to a higher concentration of CSH gel [106]. Therefore, this phenomenon was attributed to the sustained pozzolanic reactivity of GGBS, which continuously generated C-(A)-S-H gels even at a 30 wt% replacement level. Among the mixtures in Series I, G30 exhibited the lowest total porosity, the highest gel pores and the least amount of macro pores. This was in line with the high compressive strength observed in Fig. 2.7. However, as the GGBS content increased further from 30 to 45 wt%, the first critical pore diameter increased significantly from 21.5 nm to 24.2 nm, while the gel pore decreased from 1.0% to 0.7%. This was due to the reduced content of cement, which produced less CH as hydration product. Insufficient CH was not able to activate the excessive GGBS (45 wt%), leading to the low pozzolanic reactivity of GGBS and low amount of hydration product such as C-(A)-S-H gels. It also confirmed the relatively low compressive strength of G45 among Series I shown in Fig. 2.7 and less C-(A)-S-H content in Fig. 2.12.

Within the limestone replacement series (Series II), increasing the LP content from 0 to 15 wt% resulted in a slight reduction in the first critical pore diameter, with the total gel pore volume remaining nearly constant. It is uncommon in previous studies [15, 16]. It indicated that the positive effect of LP on microstructure of UHPC compensated for the negative effect brought by the dilution effect of LP. The positive impact of LP on the microstructure of UHPC arises from three main effects: the promotion effect, which enhances the hydration degree of cement;

the nucleation effect, which stimulates the formation of CSH gel; and the filling effect, which fills the pores and the void. This also corroborated the higher compressive strength of LP15 in Fig. 2.7 and the comparatively greater amount of hydration products in Fig. 2.12. However, as the LP content increased from 15 wt% to 45 wt%, the first critical peak shifted from 21.3 nm to 25.9 nm. It also became broader and more intense. Meanwhile, the gel pore volume markedly decreased from 0.8% to 0.5%. This suggested that LP replacement beyond 15 wt% significantly reduced hydration product formation and deteriorated microstructural refinement due to a pronounced dilution effect.

Table 2.4. Characteristic pore parameters of UHPC mixtures as measured by MIP.

| Mix ID | Porosity | | | | Tortuosity | Threshold diameter (nm) | Median pore diameter (nm) | Average pore diameter (nm) | Total intrusion volume (mL/g) |
|---|---|---|---|---|---|---|---|---|---|
| | Gel pores (2-10 nm) | Capillary pores (10 nm - 10 μm) | Macropores (>10 μm) | Total | | | | | |
| REF | 0.8 | 13.7 | 4.5 | 18.9 | 6.79 | 57.13 | 30.1 | 29.8 | 0.1 |
| G15 | 0.9 | 13.2 | 3.4 | 17.5 | 7.40 | 52.11 | 29.6 | 28.5 | 0.1 |
| G30 | 1.0 | 12.9 | 2.9 | 16.8 | 7.94 | 44.28 | 28.4 | 27.4 | 0.1 |
| G45 | 0.7 | 13.9 | 3.0 | 17.6 | 6.88 | 50.31 | 30.9 | 29.7 | 0.1 |
| LP15 | 0.8 | 13.3 | 2.6 | 16.7 | 6.87 | 56.72 | 26.1 | 26.0 | 0.1 |
| LP30 | 0.7 | 13.6 | 4.7 | 19.0 | 6.26 | 76.28 | 31.9 | 31.1 | 0.1 |
| LP45 | 0.5 | 15.9 | 6.1 | 22.5 | 5.61 | 86.29 | 32.6 | 30.7 | 0.1 |

### 2.3.8 RCM results

The chloride migration coefficient ($D_{nssm}$) and chloride ion penetration depth of designed UHPC were presented in Table 2.5. Cylindrical samples after the RCM tests were shown in Fig. 2.15. Compared with results in previous studies [107], the $D_{nssm}$ values of all designed UHPCs were very low, which indicated the superior durability of UHPC. As for the GGBS replacement series (Series I), $D_{nssm}$ values were 1.13, 0.89, 0.77 and 0.84 $\times 10^{-12}$ $m^2/s$ for REF, G15, G30 and G45 respectively. It was observed that $D_{nssm}$ value firstly decreased and then increased at G45 with the increase of the GGBS replacement levels. However, it was worth noting that the chloride permeation resistance of G45 was comparable to that of G30 and G15, despite the fact that the mechanical properties and pore structure of G45 were significantly inferior to those of G30 according to the results presented in Sections 2.3.3 and 2.3.7. This phenomenon was further investigated and discussed in the subsequent sections.

In the cement replacement series (Series II), as the LP replacement content increased from 0 to 45 wt%, the $D_{nssm}$ value reached the minimum at 15 wt% LP replacement rate, after which it continues to increase significantly at 45 wt% LP replacement rate. This indicated that LP15 mix exhibited the best resistance to the penetration of chloride ions in Series II. It is reported that a small quantity of fine LP as a cement replacement into concrete mainly exhibits the filling effect and the reduction of the chloride permeability of the concrete [82, 108]. As the LP content increased further from 15 wt% to 45 wt%, the chloride ion permeability considerably increased, which was due to the loose microstructure resulting from the lack of sufficient cement and the dilution effect [108]. To maximize the nucleation effect and minimize the dilution effect, the critical replacement value of LP replacing cement in terms of chloride permeability was 142 $kg/m^3$ (at the critical replacement content of 15 wt%).

Fig. 2.15. Cylindrical samples after being tested.

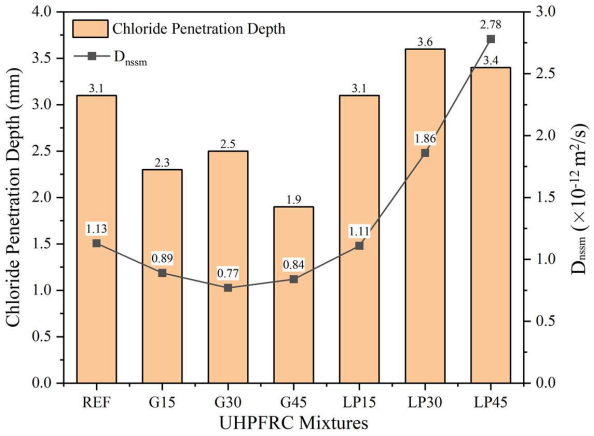


Fig. 2.16. Chloride penetration depth and chloride migration coefficient ($D_{nssm}$) of UHPC mixtures.

To better understand the influence of the type and content of SCMs as variables on chloride penetration resistance, the calculated chloride migration coefficient ($D_{nssm}$) contour plot of UHPC at different SCMs replacement levels in RCM test was illustrated in Fig. 2.17. It displayed the sensitivity of the $D_{nssm}$ of developed UHPC to any variations of the variables (the content of cement, GGBS and LP). It could be noticed that the incorporation of GGBS significantly contributed to the reduction of the $D_{nssm}$ value, and any addition of GGBS within the range of 0-45 wt% was advantageous for enhancing chloride resistance. This phenomenon is attributed to the increasing content of GGBS which can act as a cementitious material, producing hydration products and physically and chemically absorbing chloride ions. Additionally, the unhydrated GGBS can also optimize the pore structure as filler, thereby enhancing the resistance to chloride ions ingress. Whereas, the increased replacement rate of LP for cement had an adverse effect on chloride ion performance. Therefore, based on the concept of optimizing the mix proportion for the best resistance to chloride penetration of UHPC, it is recommended to have a higher amount of GGBS within the range of 0 to 45 wt%, while minimizing the content of LP.

Table 2.5. The calculated chloride migration coefficient ($D_{nssm}$) and penetration depth of designed UHPC.

| | Initial applied voltage U(V) | Applied voltage U (after adjustment) (V) | Chloride penetration depth (mm) | $D_{nssm}$ ($\times 10^{-12}$ $m^2/s$) | Resistance to chloride migration |
|---|---|---|---|---|---|
| REF | 30 | 30 | 3.1 ± 0.4 | 1.13 ± 0.10 | Extremely high |
| G15 | 30 | 25 | 2.3 ± 0.1 | 0.89 ± 0.06 | Extremely high |
| G30 | 30 | 30 | 2.5 ± 0.3 | 0.77 ± 0.11 | Extremely high |
| G45 | 30 | 20 | 1.9 ± 0.1 | 0.84 ± 0.05 | Extremely high |
| LP15 | 30 | 30 | 3.1 ± 0.1 | 1.11 ± 0.03 | Extremely high |
| LP30 | 30 | 20 | 3.6 ± 0.3 | 1.86 ± 0.02 | Very high |
| LP45 | 30 | 10 | 3.4 ± 0.3 | 2.78 ± 0.10 | Very high |

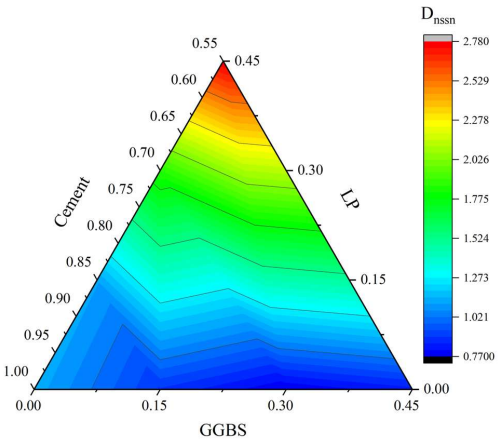


Fig. 2.17. The calculated chloride migration coefficient ($D_{nssm}$) contour plot of UHPC at different SCMs replacement levels.

### 2.3.9 Spalling observation and residual strength

Fig. 2.18 presented the spalling observations of the specimens after exposure to 500 °C. Explosive spalling was evident in G15, G30, G45, and LP15 at this temperature, whereas REF, LP30, and LP45 exhibited spalling after being exposed to 750 °C. These findings suggested that incorporating 15% LP or any level of GGBS ranging from 15 to 45 wt% decreases the onset temperature of explosive spalling in UHPC, demonstrating a clear detrimental impact on its resistance to high-temperature spalling. No significant effect on the onset temperature of explosive spalling in UHPC was observed when LP contents exceeded 15 wt%. Overall, neither GGBS nor LP enhanced the high-temperature spalling resistance of UHPC; on the contrary, a deterioration was observed in certain cases. The influence of SCMs on the spalling resistance of UHPC at elevated temperatures may be related to pore structure, which will be further analyzed and discussed in Section 2.4.3.

Fig. 2.19 illustrated the residual compressive strength of UHPC at elevated temperatures. It was found that all mixtures exhibited a significant increase in residual compressive strength at 250 °C. At 250 °C, the residual compressive strengths of G15, G30, and G45 increased by 10.81%, 11.42%, and 5.63%, respectively, compared to that at room temperature (RT). This improvement was attributed to the continued hydration of cement particles and the secondary pozzolanic reactions of GGBS and silica fume, resulting in a denser matrix microstructure [109].

At 250 °C, the residual compressive strengths of LP15, LP30, and LP45 increased by only 5.25%, 3.83%, and 2.95%, respectively, compared to room temperature. These values were all significantly lower than the 8.81% increase observed in the REF mixture. Accordingly, LP incorporation negatively affected the residual strength at 250 °C, diminishing the post-heating strength gain. This effect was due to the low pozzolanic reactivity of limestone powder, which had limited contribution to secondary hydration and mainly served as a cement diluent.

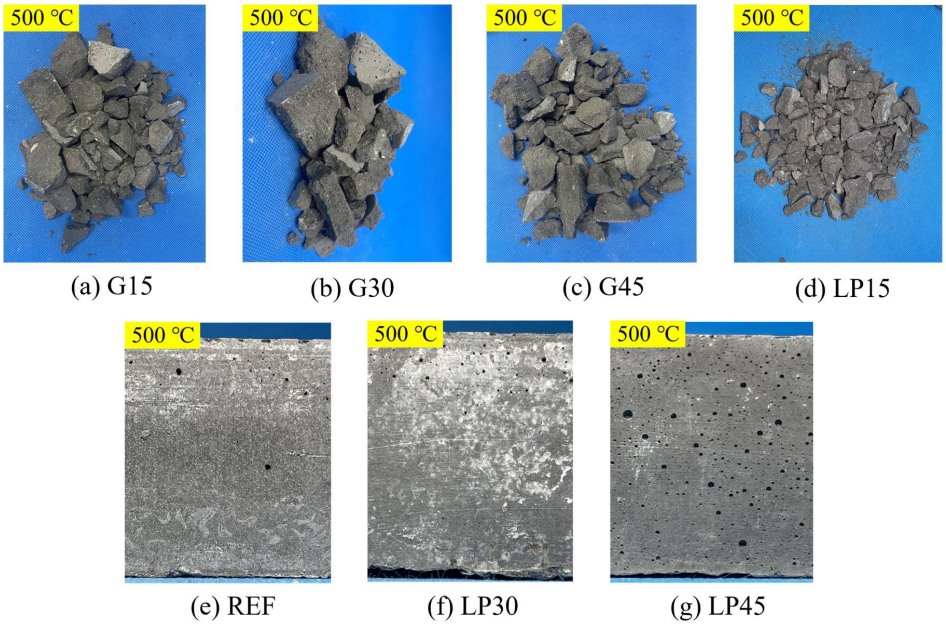


Fig. 2.18. Spalling observation of UHPC samples at 500 °C.

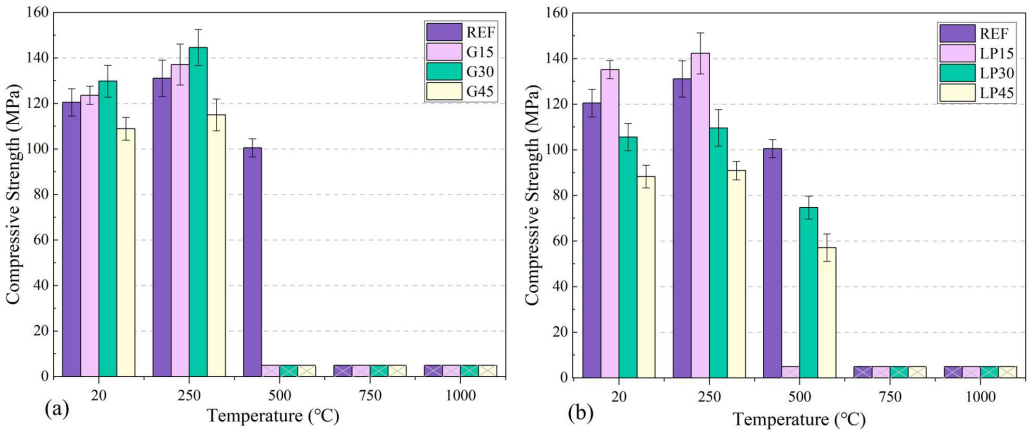


Fig. 2.19. Residual compressive strength of Series I (a) and Series II (b).

## 2.4 Discussion

### 2.4.1 Relationship between the porosity and $D_{nssm}$ of UHPC with SCMs

The chloride diffusivity of UHPC largely depends on its pore structures [110-113]. The incorporation of SCMs affects the hydration products and pore distribution, subsequently influencing the transportation of chloride ions. Therefore, porosity is the critical factor and the correlation analysis between the porosity and $D_{nssm}$ becomes necessary.

A linear correlation existed between different porosity and $D_{nssm}$ in both Series I and II as shown in Fig. 2.20. The linear correlation has been also reported in previous researches [114, 115]. Previous studies indicated that most of the transport mechanisms take place via the capillary pore framework; hence, capillary porosity is presumed to be the paramount parameter linked to the chloride diffusivity [116]. Nevertheless, in Series I, $D_{nssm}$ of UHPC incorporated with GGBS revealed a stronger correlation with the total porosity than with the capillary porosity in Fig. 2.20(a). Mehta et al. [117] suggested that the non-connectivity of small pores could account for a strong correlation between relatively larger pores (diameter > 100 nm) and concrete permeability. Therefore, it indicated that the incorporation of GGBS diminished the connectivity of capillary pore within the range of 10-100nm. Based on the previous results in Table 2.4, the high tortuosity of G45, G30 and G15 further validated the phenomenon that the addition of GGBS led to a tendency of increased independence and non-connectivity among pores, significantly decreasing the permeability of chloride ions of UHPC.

In Series II, there was a strong correlation between $D_{nssm}$ and each of total porosity ($\rho_T$) and capillary porosity ($\rho_{cap}$) as shown in Fig. 2.20(b). This indicated that the addition of LP had a significant impact on various porosity (gel pores, capillary pores and macro pores) which was closely associated with variation in $D_{nssm}$. Based on the MIP results, increasing LP content from 15 wt% to 45 wt% led to deterioration of the pore structure, characterized by increased total porosity and enhanced pore connectivity, thereby reducing chloride resistance in UHPC. Interestingly, in the 0–15 wt% range, both capillary and macro porosity decreased while tortuosity slightly increases, indicating that low LP replacement levels could refine the pore structure. As demonstrated in Section 2.3.3, the enhanced pre-cracking strength ($f_{cr}$) and compressive strength of LP15 were primarily attributed to matrix densification. However, as evidenced by the flexural load-deflection behaviour in Section 2.3.3, all toughness indices for LP mixtures are significantly lower than those of the REF mix, indicating a deterioration in the steel fiber-matrix ITZ. Therefore, although a small amount of LP ($\leqslant$15 wt%) effectively refined the matrix pore structure and enhanced compressive strength, it simultaneously weakened the fiber-matrix bonding. This relatively weak interfacial bond may have served as structural defects that facilitated chloride ingress, resulting in inferior chloride resistance compared to the REF mix. The underlying mechanisms will be further discussed in Section 2.4.2.

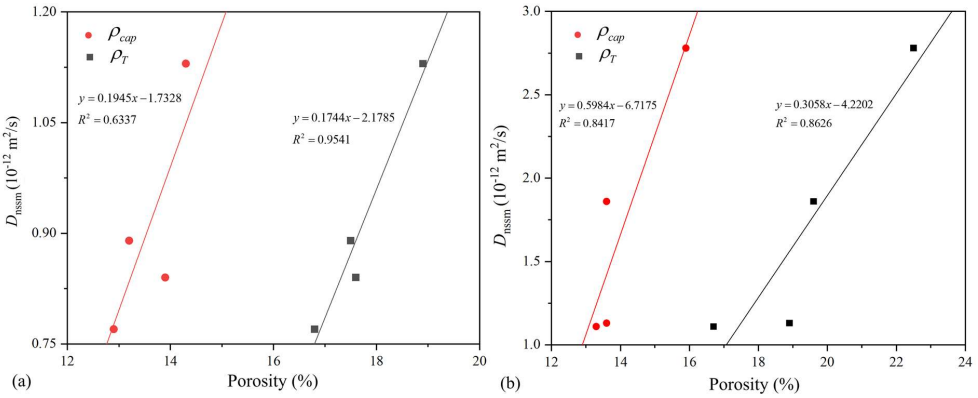


Fig. 2.20. Relationship between pore-type porosity and $D_{nssm}$ for (a) Series I and (b) Series II. (Note: $\rho_{gel}$ and $\rho_{cap}$ denote the porosity of gel pores and capillary pores, respectively.)

### 2.4.2 Understanding the mechanism of SCMs on the chloride ion transportation in UHPC

The incorporation of SCMs primarily influences the hydration products and the distribution of pore structure, consequently affecting the pathways of chloride ion transport. Previous studies have reported that SCMs can optimize the pore structures of UHPC [118, 119]. Moreover, due to the incorporation of the steel fibers, the interfaces between the steel fiber and the matrix may become the potential structural defect for UHPC, thereby reducing its chloride penetration resistance. Fig. 2.21 illustrated schematic diagrams of chloride ion transportation in G30 and LP45.

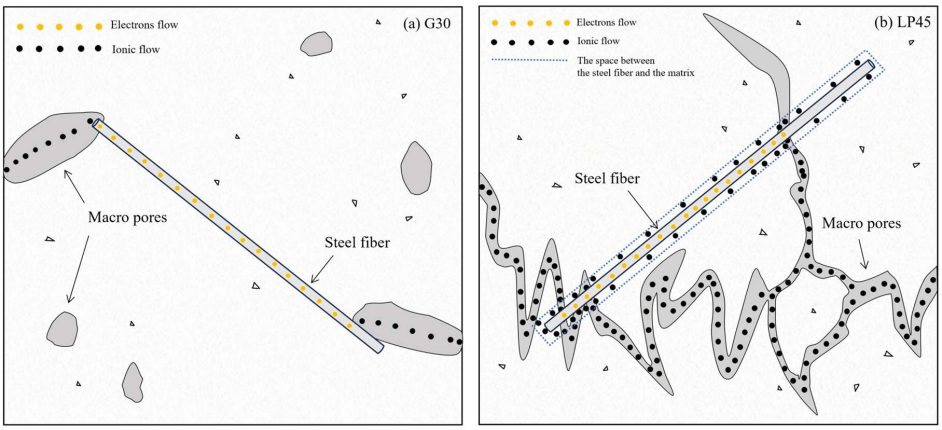


Fig. 2.21. Schematic diagram of chloride ion transportation inside UHPC: (a) G30 mix; (b) LP45 mix.

As for Series I, the mechanism of GGBS was divided into two distinct stages for discussion, specifically addressing the intervals of 0-30 wt% and 30-45 wt%. During the initial stage (0-30 wt%), GGBS effectively decreased the threshold diameter and increased the tortuosity of pore structure, hence reduced the pore connectivity in UHPC matrix. Meanwhile, the correlation analysis showed that the incorporation of GGBS diminished the connectivity of capillary pores with range of the 10-100nm. This is attributed to the high $SiO_2$ and $Al_2O_3$ content in GGBS, which react with calcium hydroxide (CH) released during cement hydration, forming additional C-(A)-S-H gels. This secondary hydration process contributed to an increased matrix density,

reducing pore connectivity and enhancing resistance to external aggressive agents such as chloride ions. Consequently, the effectiveness of GGBS in enhancing chloride penetration resistance depended on its ability to refine the microstructure through secondary hydration, which required a sufficient amount of CH to activate the pozzolanic reaction of GGBS. As the GGBS replacement level ranged from 0% to 30%, a sufficient CH supply promoted the pozzolanic reaction of GGBS, generating an adequate amount of C-(A)-S-H gels. It also explained that the steel fibers are densely wrapped by the C-(A)-S-H gels as shown in the SEM image of Fig. 2.12(a), where there was no gap for ions to pass through. Therefore, the refined pore structure and the bonding behaviors contributed to the superior mechanical properties and the highest chloride penetration resistance of G30 among Series I.

During the second stage in Series I, excessive incorporation of GGBS (> 30 wt%) in UHPC slightly diminished its beneficial impact on pore structure compared to G30, but it remained superior to REF (the control group). TG results showed that excess incorporation of GGBS (over 30 wt%) led to lower generation of C-(A)-S-H gel, which indicated a reduced pozzolanic reactivity of GGBS in G45 compared to G30. Based on the MIP results, excessive content of GGBS increased the threshold diameter and decreased the tortuosity of pore structure, correspondingly decreasing the difficulty of chloride ion transport in the matrix of UHPC. A significant deterioration in the bonding strength at the steel fiber–matrix ITZ was reflected by decreases of 7.81% and 28.74% in the peak strength ($f_r$) and toughness index ($I_5$), respectively. Therefore, in the second stage, the degradation of both pore structure and bonding behaviors explained the decline in the chloride penetration resistance in G45 compared to G30. To conclude, the incorporation of GGBS in the range of 0-45% enhanced resistance to chloride ion penetration in UHPC, reaching optimal performance at 30 wt%, with a decline in advantage beyond this concentration.

In Series II, the $D_{nssm}$ results and the correlation analysis showed that the mechanism of LP on chloride penetration on UHPC could also be categorized into two stages based on different replacement ranges of LP: 0-15 and 15-45 wt%. Within Stage 1 (0-15 wt%), the introduction of LP led to a decrease in macro porosity and total porosity, while the tortuosity increased with the rise in LP content. However, any replacement level of LP within 0-45 wt% adversely affected the flexural behaviors of UHPC as well as the bonding behavior between the steel fiber and the matrix. Therefore, in Stage 1, although LP (0–15 wt%) accelerated hydration and improved matrix densification, it had negligible effect on enhancing chloride penetration resistance.

In Stage 2 of Series II (15-45 wt%), there was a significant decline in both mechanical performance and resistance to chloride ion permeability. As presented in the TG results, the sharp decrease in C-S-H gel and CH content was attributed to the dilution effect of LP on the reactive binder. The limited hydration products could also explain the deterioration of bonding behaviors and the gap in both two ITZs in SEM images as shown in Fig. 2.13. Moreover, MIP results and correlation analysis demonstrated that as the LP content increased within the range of 15-45 wt%, tortuosity decreased significantly with the rise of various porosities, suggesting an increase in pore connectivity in UHPC. Therefore, as depicted in Fig. 2.21(b), gaps between

steel fiber-matrix ITZ could potentially interconnect with pores, forming chloride ion transport pathways, thereby reducing chloride ion penetration resistance.

According to the RCM test results, the effects of varying replacement levels of GGBS and LP on the chloride permeability of UHPC could be quantitatively compared. Specifically, the $D_{nssm}$ clearly illustrated that the optimal incorporation of GGBS (30 wt%) significantly reduced chloride permeability ($D_{nssm} = 0.77 \times 10^{-12}$ m²/s), outperforming the optimal LP incorporation (15 wt%, $D_{nssm} = 1.11 \times 10^{-12}$ m²/s). Furthermore, increasing the LP content beyond the optimal level (to 30 and 45 wt%) resulted in substantially elevated $D_{nssm}$ values (reaching up to $2.78 \times 10^{-12}$ m²/s at 45 wt%), which were attributed to increased pore connectivity and deteriorated fiber-matrix interfaces. In contrast, GGBS continued to exhibit superior chloride resistance even at higher replacement levels (45 wt%, $D_{nssm} = 0.84 \times 10^{-12}$ m²/s), due to the enhanced formation of secondary hydration products (C-(A)-S-H gels), reduced pore connectivity, and improved steel fiber-matrix bonding, as further supported by TG, MIP, and SEM analyses.

To conclude, the mechanisms of different replacement levels of GGBS and LP on hydration, pore structure, mechanical properties and durability in designed UHPC were investigated. The ultimate objective of this study was to provide a theoretical foundation for the mixed and complicated application of GGBS and LP into UHPC. In this study, to achieve high durability of constructions, GGBS is recommended to be SCMs and applied into UHPC instead of LP. Specifically, the optimal incorporation level of 30 wt% GGBS led to the optimization of the pore micro-structure, significantly enhancing the resistance against chloride ion penetration. Moreover, it improved the hydration rate, mechanical strength, bond between steel fibers and the matrix of UHPC. However, if durability enhancement becomes the objective of designed UHPC, LP is not recommended as SCMs to be incorporated into UHPC. Since any replacement level of LP adversely affects the bonding between the steel fiber and matrix, thereby degrading the durability performance of designed UHPC. Whereas, incorporating an appropriate amount (15 wt%) of LP as fine aggregates of filler into UHPC enabled it to demonstrate the great performance observed in this study, with advantages such as high compressive strength and optimized pore structure.

### 2.4.3 Mechanistic understanding of SCMs on high-temperature spalling resistance of UHPC via pore structure evolution

The previous Sections 2.4.1 and 2.4.2 demonstrated that GGBS and LP refine the pore structure and alter chloride transport primarily through changes in capillary connectivity and fiber-matrix bonding. These very microstructural features also govern vapor pressure build-up during heating, which is the direct trigger for explosive spalling in UHPC. Therefore, analysing the evolution of pore size distribution, critical pore diameter and tortuosity enables an indirect yet quantitative assessment of how different SCMs modulate spalling resistance.

For GGBS, a two stage behaviour was observed. Moderate GGBS replacement (0–30 wt%) promoted secondary hydration, forming more C-(A)-S-H gels. This reduces macro-porosity and increased tortuosity. However, the denser matrix inhibited vapor escape, leading to explosive spalling in all GGBS mixtures (G15–G45) at 500 °C. At 250 °C, G30 exhibited the highest residual compressive strength. This was attributed to its high gel pore fraction and low macro-

pore content. However, its highly refined pore structure also trapped vapor, causing pressure to build up more rapidly. As a result, G30 spalled earlier than REF, with a lower spalling threshold of 500 °C. When the GGBS content increased to 45 wt% (G45), the dilution effect became dominant. This reduced tortuosity and increased the critical pore diameter. The more open pore network allowed some vapor release, slightly improving spalling resistance compared to G30. However, this came at the cost of reduced mechanical performance.

In contrast, the behavior of LP was opposite to that of GGBS. At 15 wt% dosage, LP refined the pore structure and densified the matrix, which restricted vapor escape. This caused internal pressure buildup, and triggered explosive spalling at 500 °C. As the LP content increased to 30–45 wt%, macro and total porosity increased significantly, forming more continuous vapor escape channels. The weakened interfacial bond between steel fibers and matrix (ITZ) also contributed to vapor escape channels, helping relieve internal pressure. As a result, explosive spalling of LP30 and LP45 was delayed to 750 °C compared to LP15. This coarser network delayed explosive spalling to 750 °C. However, LP45 consistently exhibited the lowest residual compressive strength across all tested temperatures. This suggested a significant compromise in mechanical performance due to excessive dilution and weakened ITZ bonding.

In summary, neither GGBS nor LP proved effective in enhancing the high-temperature spalling resistance of UHPC. Compared with REF, the pore structures of LP15, G15, G30, and G45 became further densified. Vapor escape was hindered, causing the spalling onset temperature to drop from 750 °C to 500 °C. When LP exceeded 15 wt%, pore connectivity increased significantly and spalling was delayed to 750 °C. The higher LP replacement level, however, significantly reduced residual compressive strength. Therefore, both GGBS and LP exert a negative influence on the high-temperature spalling resistance of UHPC.

## 2.5 Conclusions

This chapter clarified the mechanisms of GGBS and LP on hydration, pore structure, chloride penetration resistance, with special attention to explosive spalling resistance in UHPC. The major conclusions can be drawn as follows:

- The incorporation of 15 wt% GGBS or LP accelerated early hydration, advancing the exothermic peak by 6.95 and 5.31 hours, respectively. However, excessive replacement levels reduced hydration kinetics due to dilution effects.
- The UHPC mixtures with 30 wt% GGBS and 15 wt% LP achieved the highest compressive strength and binder efficiency within their respective binder systems. All GGBS replacement levels (0-45 wt%) promoted strength development from 7 to 28 days, whereas LP enhances early strength but impairs long-term performance beyond 15 wt% replacement.
- A 30 wt% GGBS replacement significantly enhanced flexural toughness, increasing toughness indices by 135.2%, 31.6%, and 45.5% for $I_5$, $I_{10}$, and $I_{20}$. This improvement was attributed to enhanced fiber-matrix bonding, as confirmed by dense ITZ microstructures in

SEM analysis. In contrast, LP weakened fiber-matrix bonding across all replacement levels (0-45 wt%), leading to a reduction in flexural properties.

- Based on qualitative XRD and quantitative TG analyses, optimal replacement levels were identified as 30 wt% for GGBS and 15 wt% for LP. Quantitative TG results confirmed maximum C-(A)-S-H formation and adequate CH availability at 30 wt% GGBS, and enhanced hydration efficiency due to nucleation effects at 15 wt% LP. Additionally, MIP results suggest that mixtures at these thresholds achieve optimal pore structure refinement, as evidenced by reductions in critical pore diameter and total porosity, and increased gel porosity, respectively.
- GGBS replacements ranging from 0 to 45 wt% enhance resistance to chloride penetration, achieving peak performance at 30 wt%. In contrast, LP incorporation reduces chloride resistance, especially above 15 wt%, due to increased pore connectivity and deterioration of fiber-matrix interfacial bonding.
- Correlation analysis revealed that the effects of GGBS and LP on the chloride penetration resistance of UHPC can be divided into two distinct stages: 0-30 wt% and 30-45 wt% for GGBS; 0-15 wt% and 15-45 wt% for LP, respectively. The chloride diffusivity of UHPC is strongly influenced by pore structure characteristics and fiber-matrix interfacial bonding, offering a scientific basis for optimizing SCM incorporation strategies aimed at enhancing both durability and sustainability.
- Both GGBS and LP exert a negative influence on the high-temperature spalling resistance of UHPC. A 15 wt% replacement of cement with LP decreases the spalling onset temperature from 750 °C to 500 °C relative to the reference mix. Similarly, incorporating GGBS within the 0-45 wt% range results in a comparable reduction. High LP replacement levels (15-45 wt%) significantly decrease the residual compressive strength at elevated temperatures. These findings indicate that neither LP nor GGBS contributes to the enhancement of high-temperature spalling resistance in UHPC.

# Chapter 3 Evolution of mechanical properties of UHPC at elevated temperatures


## *Abstract*

To improve the post-fire safety and structural integrity of UHPC, a comprehensive understanding of its fracture behavior under elevated temperature conditions is essential. This study systematically investigated the flexural fracture performance and degradation mechanisms of UHPC incorporating various steel fiber (SF) volume ratios (1.5%, 2.0%, and 2.5%) following exposure to 200, 400, 600, and 800 °C. Key fracture parameters, including flexural strength, fracture toughness, and fracture energy, were evaluated via three-point bending tests on notched specimens. Results revealed a modest increase in compressive and flexural strengths at 200 °C, attributed to internal autoclaving effects. However, as the temperature continued to rise, a sharp decline in strength was observed. At 800 °C, residual strengths decreased to 26.2–30.2% of their ambient values. Elevated temperatures significantly altered the load–deflection response, notably eliminating the sawtooth fluctuations associated with fiber pull-out, indicating severe degradation of the fiber–matrix interface. This transition led to premature brittle failure and substantial reductions in fracture toughness and energy. A predictive model was developed to estimate post-fire compressive strength, flexural strength, and fracture energy of UHPC as functions of temperature and fiber content. Moreover, quantitative relationships among compressive strength, flexural strength, fracture energy, and fracture toughness were established, facilitating practical evaluation of the residual fracture performance of UHPC after fire exposure. These findings provide a theoretical foundation for the structural assessment and design of UHPC components subjected to high-temperature conditions.



This chapter is partially published elsewhere:

J. He, H.Y. Wang, and Q.L. Yu, Flexural fracture behavior of ultra-high performance concrete after high-temperature exposure. Construction and Building Materials, 481 (2025), 141544.

## 3.1 Introduction

UHPC has become the preferred material for key components in major engineering projects such as large-span bridges, high-rise buildings, and nuclear power plants due to its excellent mechanical properties and durability [120, 121]. However, under high-temperature conditions such as fires, the high-density microstructure of UHPC becomes a fatal flaw in its fire resistance performance - the rapidly increasing pore vapor pressure can easily cause severe explosions [122, 123], seriously threatening the structural stability and service life of UHPC components [124]. More seriously, multi-scale damage induced by high temperature (including C-S-H gel dehydration phase transformation, steel fiber matrix interface oxidation, thermal expansion coefficient mismatch, and other synergistic effects) will lead to significant temperature-sensitive properties of materials [125, 126]. The systematic study of the degradation law and damage mechanism of high-temperature mechanical properties of UHPC can not only provide theoretical basis for the post fire safety assessment of existing structures, but also lay a scientific foundation for the material design of the new generation of fire-resistant UHPC. This has significant practical value for promoting the engineering application of UHPC in high-temperature and high-risk environments.

There have been several studies on the mechanical properties of UHPC after exposure to high temperatures [112, 127-129]. These properties are highly sensitive to temperature changes and are influenced by various factors, including curing conditions, the composition of cementitious materials, fiber types, and fiber volume ratios [130-132]. Compared to ordinary and high-strength concrete, UHPC often exhibits distinct degradation patterns under thermal loading, with reduced residual strength and stiffness at elevated temperatures. Early-age steam curing has been shown to promote hydration reactions and reduce the amount of free water within the UHPC matrix. This helps to lower internal vapor pressure during heating and enhances the material's resistance to high-temperature-induced damage. Thermal curing further improves the durability and spalling resistance of UHPC by reducing its permeability [133, 134]. With regard to binder composition, previous studies have shown that different cementitious materials significantly affect the high-temperature performance of UHPC. For example, incorporating appropriate amounts of fly ash can enhance both the flowability and compressive strength of UHPC. Fly ash also contributes to improved thermal stability and recovery capacity of cementitious matrices after exposure to high temperatures [135]. In addition, the use of high-alumina cement as a partial replacement for Portland cement has been reported to enhance the crack resistance of UHPC under thermal conditions [136].

For fiber-reinforced UHPC, existing studies have primarily focused on the high-temperature mechanical properties of UHPC reinforced with steel fibers or hybrid fiber systems in which steel fibers are the dominant component. The incorporation of steel fibers has been shown to significantly inhibit the development of thermal cracks in UHPC under elevated temperatures [137]. Muhammad et al. [138] reported that UHPC containing 2% steel fibers by volume exhibited higher residual tensile strength at 300 °C compared to ambient conditions, particularly in high-strength matrices containing silica fume.

Similarly, the addition of steel or polypropylene fibers can partially mitigate the negative impact of high temperatures on compressive strength and improve the residual compressive performance of UHPC [139]. Sanchavan et al. [140] demonstrated that blending steel fibers with polyvinyl alcohol fibers can effectively enhance the thermal resistance of UHPC. Raza et al. [141] found that UHPC incorporating 1.5% steel fibers and 0.5% carbon fibers achieved residual compressive, tensile, and flexural strengths approximately two, four, and five times higher, respectively, than those of fiber-free UHPC at 800 °C.

Extensive efforts have been devoted to evaluating the mechanical properties of UHPC after high-temperature exposure, with research focusing on the influence of mix design, fiber type, dosage, and curing methods. Among these factors, the type and dosage of fibers are particularly critical in determining thermal performance. However, the fracture behavior of UHPC under elevated temperature conditions remains insufficiently addressed in current literature. Fracture energy, as a key parameter for characterizing crack propagation resistance, plays an essential role in evaluating the load-bearing capacity and failure mode of UHPC subjected to thermal damage. Despite this, most existing studies have been limited to a few discrete temperature levels, and systematic investigations into the temperature dependence of fracture energy are still lacking. Establishing a robust correlation between temperature and fracture performance is therefore essential for ensuring the structural safety of UHPC components exposed to fire or other high-temperature conditions.

This study aims to investigate the flexural fracture mechanism of UHPC after exposure to elevated temperatures. UHPC mixes with varying steel fiber (SF) volume fractions (1.5%, 2.0%, and 2.5%) were evaluated under two conditions: ambient temperature (25 °C) and after exposure to 200, 400, 600, and 800 °C using an induction heating furnace, followed by natural cooling. For each mix design, fifteen prismatic specimens were cast. After heating, the specimens were cooled to room temperature, and notches of specified depth were introduced using a precision cutting saw. Three-point bending tests were then conducted to assess the flexural fracture behavior of UHPC after high-temperature exposure. In addition, uniaxial compression tests were performed on the fractured specimens using a dedicated fixture to evaluate residual compressive performance. Based on the experimental results, a predictive model was established to estimate post-fire compressive strength, flexural strength, and fracture energy as functions of fiber content and temperature. Furthermore, empirical correlations were developed among compressive strength, flexural strength, fracture energy, and fracture toughness, providing a comprehensive understanding of UHPC performance under high-temperature conditions.

## 3.2 Materials and experiments

### 3.2.1 Raw materials

UHPC materials are composed of water, cementitious materials, and steel fibers. Portland cement CEM I 52.5 R (PC), silica fume (microsilica, MS), and fly ash (FA) are cementitious materials. In this study, the modified Andreasen and Andersen model (MAA) [57, 142] for UHPC mix optimization is given by:

$$P(D) = \frac{D^q - D_{min}^q}{D_{max}^q - D_{min}^q} \tag{3.1}$$

$$RSS = \sum_{i=1}^{n} \left[ P_{mix}(D_i^{i+1}) - P_{target}(D_i^{i+1}) \right]^2 \rightarrow min \tag{3.2}$$

In these equations, *P(D)* denotes the cumulative passing fraction by volume of particles with size smaller than *D*. And *D* is the particle size, while $D_{min}$ and $D_{max}$ denote the minimum and maximum particle sizes of the granular constituents, respectively. $P_{mix}$ and $P_{target}$ correspond to the particle size distribution curves of the designed mixture and the target distribution. The parameter *q* is the distribution modulus that controls the shape of the target grading curve. In Eq. (3.2), *RSS* represents the residual sum of squares used to quantify the deviation between the mixture grading curve and the target curve. $D_i^{i+1}$ denotes the discrete particle size intervals used for gradation fitting, and *n* is the total number of particle size classes considered. Minimization of *RSS* ensures optimal packing density of UHPC through improved particle size distribution.

According to the suggestion of existing literature [143], the design *q* value of UHPC is 0.23. Research has shown that adding steel fibers (0-3%) can effectively improve the ductility and toughness of UHPC [144]. Based on this, we designed three SF volume ratios, namely 0.15%, 0.2%, and 0.25%. Calculate the target curve based on the particle size distribution of each aggregate, as shown in Fig. 3.1. Adjusting the proportion of materials in each part matches UHPC, as shown in Table 3.1. This study used steel fibers coated with copper on a straight surface, and the geometric and mechanical properties of the steel fibers are shown in Table 3.2.

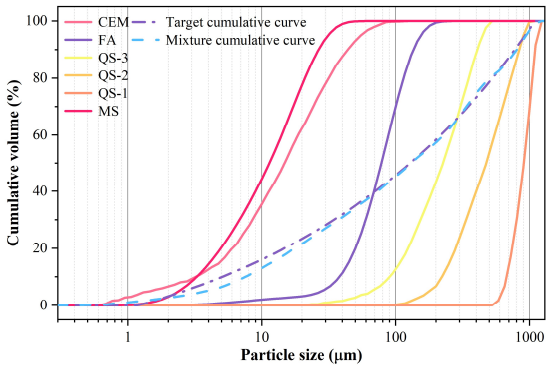


Fig. 3.1. Material particle size distribution curve.

Table 3.1. Mix ratio of UHPC (kg/m$^3$).

| No. | SF % | PC | MS | FA | QS-3 | QS-2 | QS-1 | Steel fiber | SP | Water |
|---|---|---|---|---|---|---|---|---|---|---|
| 1 | 1.5 | 791 | 179 | 144 | 412 | 510 | 192 | 117 | 47 | 198.3 |
| 2 | 2.0 | 791 | 179 | 144 | 412 | 510 | 192 | 156 | 47 | 198.3 |
| 3 | 2.5 | 791 | 179 | 144 | 412 | 510 | 192 | 195 | 47 | 198.3 |

Table 3.2. Geometric and mechanical properties of steel fibers.

| Fiber shape | Density (kg/m$^3$) | Tensile strength (MPa) | Elastic modulus (GPa) | Length (mm) | Diameter (mm) | Aspect ratio |
|---|---|---|---|---|---|---|
| Straight | 7850 | 2500 | 200 | 12 | 0.2 | 65 |

Considering that the UHPC mix proportion adopts a lower water-cement ratio and the volume fraction of steel fibers in this study is variable, up to 2.5%, a unique mixing process is required. In the initial stage, all the cementitious materials and dry mix are added and dry-mixed for two minutes. Subsequently, a portion of steel fibers is added, followed by one minute of dry-mixing. After that, water and a polycarboxylate superplasticizer (PCE, with 40% solid content) were introduced, and the mixture was stirred for 3 min. The water-to-binder ratio (w/b) of the mixtures was 0.19. Finally, the remaining steel fibers are carefully dispersed, and the whole is remixed until UHPC demonstrates good workability. After actual measurement, the density of UHPC was determined to be 2670 kg/m³. After casting, all UHPC test beams were cured in a standard curing environment for 28 days.

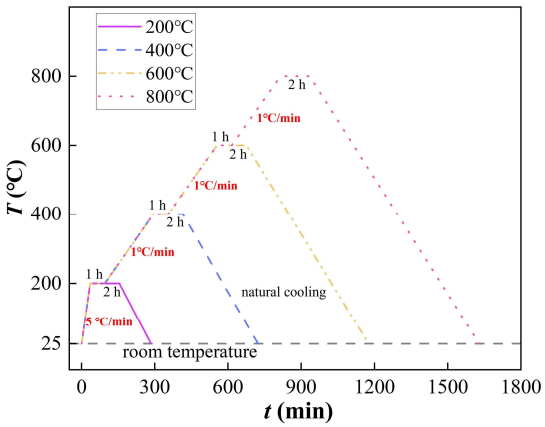


Fig. 3.2. The temperature-rise history curve of UHPC.

An electric furnace with a heating capacity of 1000 °C is used to heat the test beams. To prevent the UHPC from spalling during the heating process, the UHPC specimens are heated in a gradient heating manner proposed by Xue et al. [145]. To ensure that the internal and external temperatures of the test beam are the same after the furnace temperature reaches the target value, the specimen is kept in the constant-temperature furnace for 2 hours. Then, the specimen is clamped out of the furnace and cooled to room temperature for fracture tests. The entire process of UHPC production and high-temperature treatment is shown in Appendix Fig. A1, and the heating process of the induction heating system is illustrated in Fig. 3.2.

### 3.2.2 Experimental methods

This study prepared a total of 45 experimental beams to investigate the fracture behavior of UHPC at temperatures ranging from 25 to 800 ℃. Fig. 3.3 shows the geometric structure diagram of the UHPC fracture performance test. The test beam size is 160 × 40 × 40 mm$^3$, the effective span ($l_0$) is 140 mm, the span-to-height ratio of the test beam is $\beta$ = 3.5, and an initial crack with a length of 10mm and a width of 2 mm is prefabricated using a cutting machine. The load-deflection curve of the fracture test is measured by a weighing sensor and a displacement sensor, respectively. A clamp extensometer measures the crack mouth opening displacement (*CMOD*), and the cracking load of the test beam is measured by a concrete resistance strain gauge. The above equipment is connected to a dynamic acquisition instrument for the same

frequency acquisition, with a sampling frequency set at 20 Hz and a beam loading speed of 0.2 mm/min.

According to the method described in reference [146], the fractured half beam was subjected to a uniaxial compression test after conducting the fracture test. The cross-sectional area of the loading device was 40 mm × 40 mm, and the loading speed was 3 mm/min.

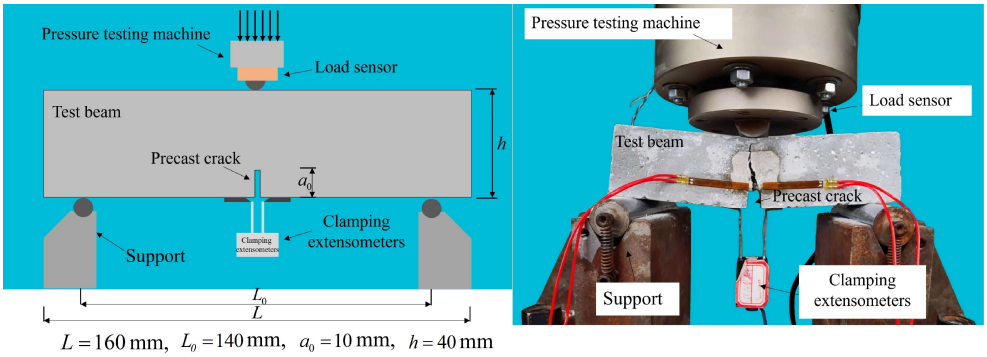


Fig. 3.3. UHPC fracture performance testing and geometric structure diagram.

## 3.3 Results and analysis

### 3.3.1 General mechanical behavior

Crack Width Detector observed the surface cracks of UHPC specimens after high-temperature exposure. Some temperatures were selected for presentation, and the crack distribution can be seen in Table 3.3. Under normal temperature conditions, the surface of UHPC was smooth without any micro-cracks. When exposed to 400 °C, it could be seen that micro-cracks began to appear on the surface of UHPC. Notably, for UHPC with an SF fiber volume ratio of 1.5%, both single and reticular cracks were observed simultaneously. As the fiber volume ratio increased, only single cracks could be observed. When the temperature was raised to 800 °C, it could be observed that the single cracks in UHPC with different SF fiber volume ratios gradually expanded to form reticular cracks.

Fig. 3.4 shows the variation of compressive strength of UHPC with different SF volume ratios after high temperature. The compressive strength of UHPC shows a trend of first increasing and then decreasing, reaching its peak at 200 ℃. At this time, the evaporation of water vapor in the capillary tube causes UHPC to undergo a steam-curing process, effectively promoting the volcanic ash reaction of the active admixture and the hydration of cement particles [134], thereby increasing its compressive strength, with an average increase of 4.3% -5.3%. Moreover, from a microstructural perspective, the temperature increase below 200 ℃ leads to the evaporation of free and bound water in the C-S-H gel [104]. This process reduces porosity and contributes to matrix densification, thereby enhancing the load-bearing capacity of the material. Simultaneously, partially unhydrated particles may become further activated under mild thermal conditions, leading to secondary hydration reactions that strengthen the matrix.

However, after 200 ℃, the compressive strength loss of UHPC increases sharply. When the test temperature increases from 25 ℃ to 400, 600, and 800 ℃, the compressive strength of UHPC is only 89.0-99.0%, 57.4-68.4%, and 26.2-30.2% of the initial strength, respectively, which is worth noting. It should be noted that the compressive performance is best when the SF volume ratio is 2%, and the relative value of compressive strength does not delay the loss of strength with the increase of fiber volume ratio.

Table 3.3. Crack distribution of UHPC after high-temperature exposure.

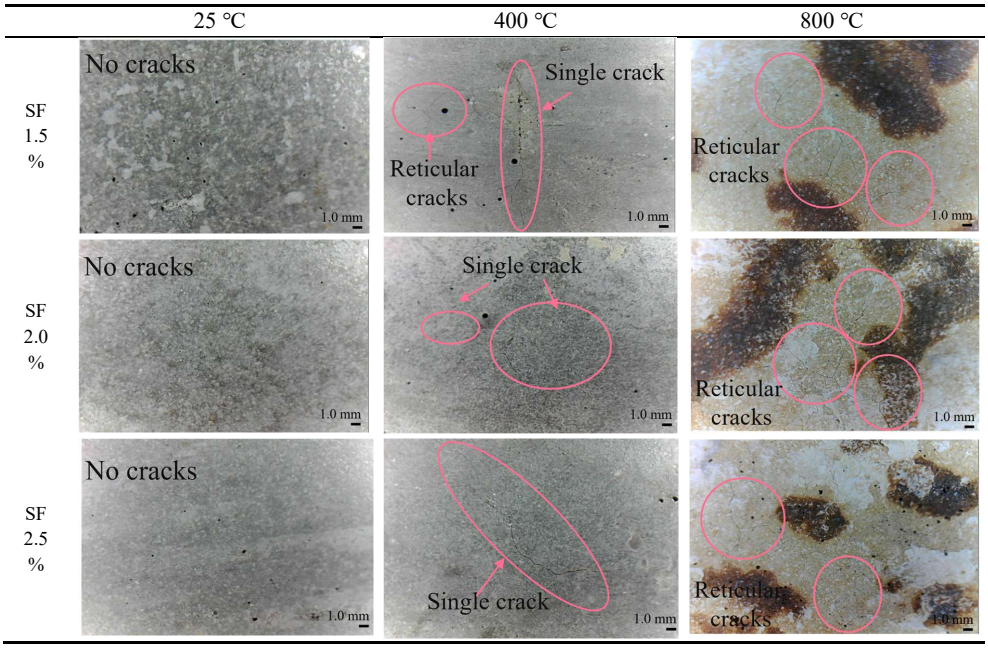


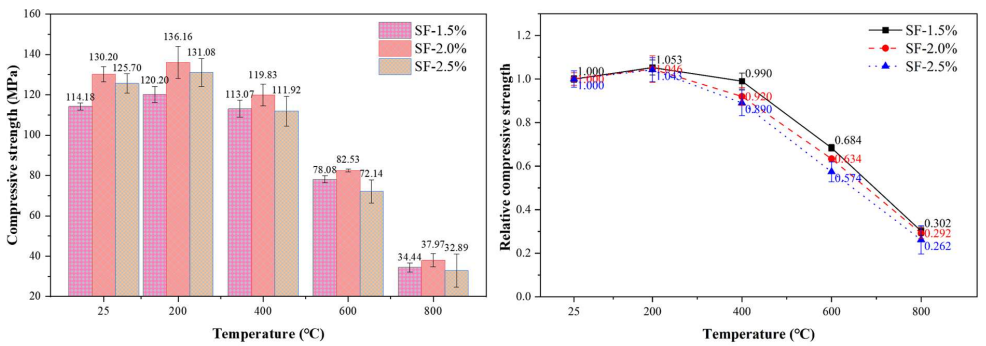


(a) Absolute value of compressive strength (b) Relative value of compressive strength

Fig. 3.4. Compressive strength of UHPC.

Fig. 3.5 shows the fracture patterns of UHPC after high-temperature exposure under different SF volume ratios. It can be seen from the figure that when the SF volume ratio is 1.5%, the crack almost extends straight along the pre-made crack surface to the loading point. The crack propagation path becomes significantly tortuous as the fiber volume ratio increases. High

temperature does not change the fracture morphology of the test beam. However, as shown in Fig. 3.5, by comparing the test beams at different temperatures just before failure, it is found that there is significant SF fiber bridging at the UHPC crack location at room temperature, while at the crack location of the specimen at 800 °C, the SF does not produce obvious bridging, resulting in the brittle fracture characteristics of the specimen directly.

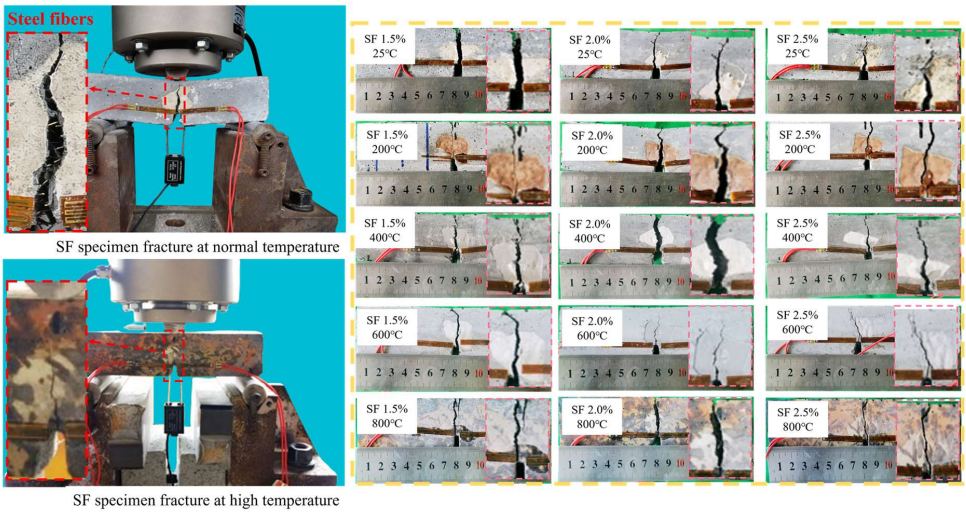


Fig. 3.5. Typical failure modes of fractured specimens.

Fig. 3.6 shows the measured average load-deflection curves of UHPC specimens with different SF volume ratios after bending tests at different temperatures. For UHPC specimens at normal temperature, their load-deflection curve follows a typical three-stage pattern: 1) Linear elastic stage: The load-deflection relationship shows a linear relationship, and UHPC is in an elastic response state; 2) Elastic-plastic stage: The linear relationship between load and deflection disappears, and microcracks appear in UHPC. Although the overall load-bearing capacity still exists, plastic behavior begins to emerge; 3) Strengthening/Destruction Stage: Although the structure may exhibit an increase in strength, it is accompanied by significant plastic deformation until it fails. This paragraph highlights the strength and toughness characteristics of UHPC under extreme load conditions. Comparing UHPC with different SF volume ratios, it is found that the larger the fiber volume ratio, the more significant the efficiency increase at this stage.

At normal temperatures, UHPC exhibits a significant sawtooth effect in the third stage, and the bonding strength of steel fibers in the matrix is generally composed of chemical bonding, mechanical interlocking, and friction. As shown in Fig. 3.7(a), the ITZ around the steel fiber at 25 °C remains dense and intact. When the temperature rises to 200 °C (Fig. 3.7(b)), the ITZ is still relatively compact, and the bond between fiber and matrix remains effective. However, at 600 °C (Fig. 3.7(c)), cracks and microstructural damage become evident near the fiber–matrix interface. At 800 °C (Fig. 3.7(d)), the ITZ is severely damaged, and fiber–matrix debonding is clearly visible. These changes result in reduced fiber anchorage and sawtooth fluctuation suppression on the macroscopic load–deflection curves. With a fixed sampling frequency, the larger the fiber volume ratio, the denser the sawtooth phenomenon.

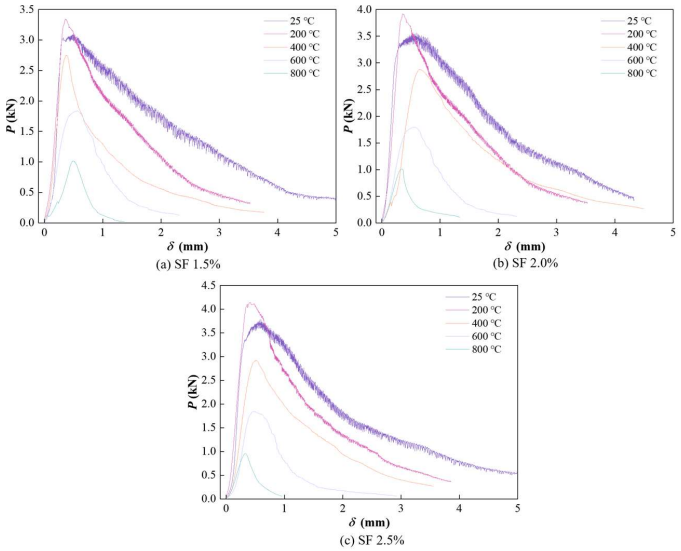


Fig. 3.6. $P-\delta$ curves of beams.

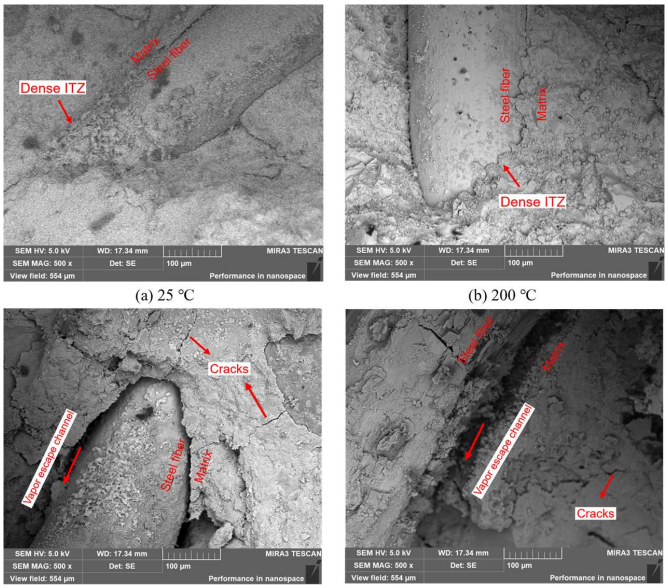


Fig. 3.7. SEM images of the UHPC mixture containing 2.0% steel fiber (SF) after exposure to different temperatures: (a) 25 °C, (b) 200 °C, (c) 600 °C, and (d) 800 °C.

High-temperature conditions significantly modified the development pattern of the load-deflection curve of UHPC. This phenomenon is primarily attributed to the thermal decomposition of hydration products, which subsequently affects the interfacial bond between the steel fibers and the cementitious matrix. Studies have shown that the ultimate load exhibits a trend similar to the increase in compressive strength at 200 °C [147]. This can be explained by accelerating the secondary hydration of unhydrated cement particles and active mineral

admixtures such as silica fume and fly ash cenosphere at elevated temperatures, which promotes additional C-S-H gel formation. This process further densifies the matrix and helps maintain adequate interfacial bonding strength between the steel fibers and the cementitious matrix [147]. Fig. 3.7(a) and (b) present SEM images of the ITZ at 25 °C and 200 °C, respectively, demonstrating that the ITZ retains a compact microstructure at 200 °C with no obvious signs of degradation. In the temperature range of 180-300°C, C-S-H gel dehydrates, weakening the interfacial bond between steel fibers and the matrix [50]. With further temperature increase, the bound water in C-S-H gel is released through dehydration within the 180-300 °C temperature range. Calcium hydroxide and calcium carbonate subsequently decompose at approximately 450 °C and 700 °C, respectively, weakening the interfacial bonding strength between the steel fibers and the cementitious matrix [50]. As shown in Fig. 3.7(c) and (d), SEM images reveal the formation of pronounced gaps at the ITZ between steel fibers and the matrix with increasing temperature. These gaps can serve as escape channels for internal water vapor within the UHPC matrix. This may be due to the successive decomposition of calcium hydroxide (CH) and calcium carbonate at approximately 450 °C and 700 °C, respectively. In addition, the longitudinal expansion of steel fibers at elevated temperatures further promotes widening gaps at the ITZ and the formation of microcracks in the surrounding matrix [148]. Microstructural observations of the ITZ also help explain the disappearance of the sawtooth-shaped fluctuation amplitude in the load-deflection curve, which is caused by stress redistribution during the fiber pull-out process. As a result of the widened gaps and increased microcrack formation at the ITZ under high-temperature exposure, the strengthening phase of the UHPC load-deflection curve suddenly transitions into the failure phase, accompanied by a sharp decline in the third stage of the curve. This behavior reflects a significant increase in the brittleness of UHPC after exposure to elevated temperatures.

Fig. 3.8 shows the variation of flexural strength of UHPC with different SF volume ratios after high temperature, which is consistent with the variation of compressive strength. The flexural strength first increases and then decreases with the temperature increase, reaching its peak at 200 ℃. Under different SF volume ratios, the average increase ranges from 9.5% to 14.4%. When the experimental temperature was increased from 25 ℃ to 400 ℃, 600 ℃, and 800 ℃, the flexural strength of UHPC retained 77.1-88.7%, 48.8-59.3%, and 25.2-32.8% of its initial strength, respectively. The results showed that high temperatures severely damaged the flexural strength of UHPC.

The bending energy absorption of UHPC can be described by its flexural toughness, which can be calculated by the envelope area of the load-deflection ($P-\delta$) curve at characteristic points. According to ASTM C1609 standard [149], it can be expressed by the bending toughness at points $\delta_p$, $l_0/600$ and $l_0/150$, $\delta_p$ represents the deflection corresponding to the maximum load, $l_0$ represents the net span of the test beam, and considers the superior deformation capacity of UHPC. The parameters $l_0/100$ and $l_0/50$ were jointly adopted to characterize the toughness of UHPC after exposure to elevated temperature. The toughness and improvement effect of UHPC characteristic points with different SF volume ratios after high temperature are recorded in Table 3.4, and the trend of bending toughness changes is shown in Fig. 3.9.

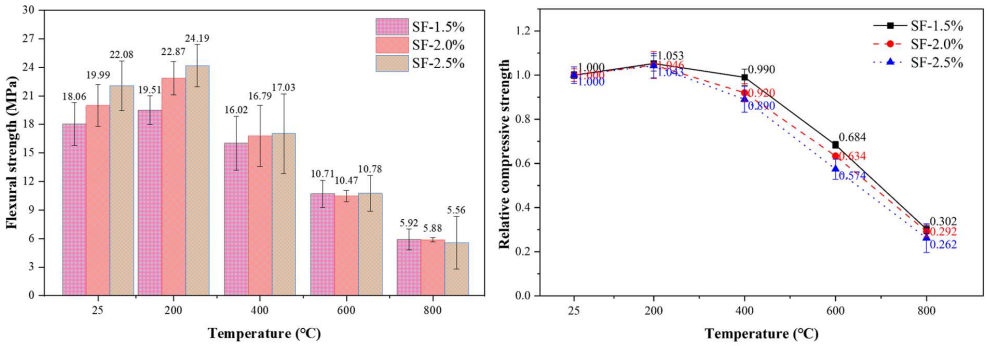


(a) Absolute value of flexural strength (b) Relative value of flexural strength

Fig. 3.8. Flexural tensile strength of UHPC.

Table 3.4. Flexural toughness parameters of UHPC at characteristic deflection points after high-temperature exposure.

| SF volume ratio (%) | Tempera--ture (℃) | $T_p$ | | $T_{l_0/600}$ | | $T_{l_0/150}$ | | $T_{l_0/100}$ | | $T_{l_0/50}$ | |
|---|---|---|---|---|---|---|---|---|---|---|---|
| | | $(N\cdot mm)$ | $T_p/T_{p-25℃}$ | $(N\cdot mm)$ | $T_p/T_{p-25℃}$ | $(N\cdot mm)$ | $T_p/T_{p-25℃}$ | $(N\cdot mm)$ | $T_p/T_{p-25℃}$ | $(N\cdot mm)$ | $T_p/T_{p-25℃}$ |
| 1.5 | 25 | 881.2 | 1.000 | 125.3 | 1.000 | 2123.7 | 1.000 | 3245.3 | 1.000 | 5582.3 | 1.000 |
| | 200 | 602.9 | 0.684 | 205.9 | 1.643 | 2158.1 | 1.016 | 3057.5 | 0.942 | 4486.9 | 0.804 |
| | 400 | 533.1 | 0.605 | 161.3 | 1.287 | 1543.1 | 0.727 | 2061.3 | 0.635 | 2830.1 | 0.507 |
| | 600 | 422.1 | 0.479 | 91.0 | 0.726 | 1177.9 | 0.555 | 1509.8 | 0.465 | 1719.3 | 0.308 |
| | 800 | 217.3 | 0.247 | 40.4 | 0.322 | 455.7 | 0.215 | 492.3 | 0.152 | 492.3 | 0.088 |
| 2.0 | 25 | 1282.0 | 1.000 | 301.5 | 1.000 | 2644.5 | 1.000 | 3976.2 | 1.000 | 6440.9 | 1.000 |
| | 200 | 688.5 | 0.537 | 241.5 | 0.801 | 2529.6 | 0.957 | 3585.2 | 0.902 | 5261.3 | 0.817 |
| | 400 | 665.0 | 0.519 | 59.9 | 0.199 | 1612.6 | 0.610 | 2586.7 | 0.651 | 4159.7 | 0.646 |
| | 600 | 378.1 | 0.295 | 89.4 | 0.297 | 1152.2 | 0.436 | 1476.8 | 0.371 | 1681.9 | 0.261 |
| | 800 | 163.4 | 0.127 | 76.5 | 0.254 | 401.8 | 0.152 | 463.4 | 0.117 | 463.4 | 0.072 |
| 2.5 | 25 | 1366.3 | 1.000 | 190.238 | 1.000 | 2617.488 | 1.000 | 3984.486 | 1.000 | 6467.946 | 1.000 |
| | 200 | 936.7 | 0.686 | 264.99 | 1.393 | 2790.79 | 1.066 | 3902.142 | 0.979 | 5736.34 | 0.887 |
| | 400 | 742.6 | 0.544 | 97.82 | 0.514 | 1795.216 | 0.686 | 2615.736 | 0.656 | 3910.61 | 0.605 |
| | 600 | 267.1 | 0.195 | 79.862 | 0.420 | 1102.592 | 0.421 | 1373.86 | 0.345 | 1611.84 | 0.249 |
| | 800 | 145.0 | 0.106 | 69.204 | 0.364 | 369.088 | 0.141 | 370.402 | 0.093 | 370.402 | 0.057 |

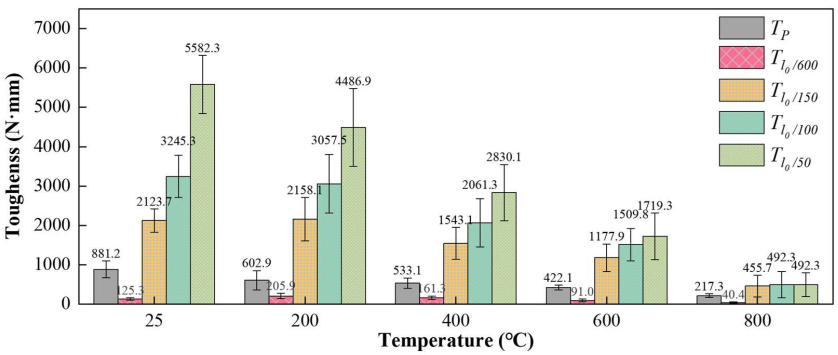


(a) SF 1.5%

Fig. 3.9. Flexural toughness of UHPC at high temperatures: (a) 1.5% SF.

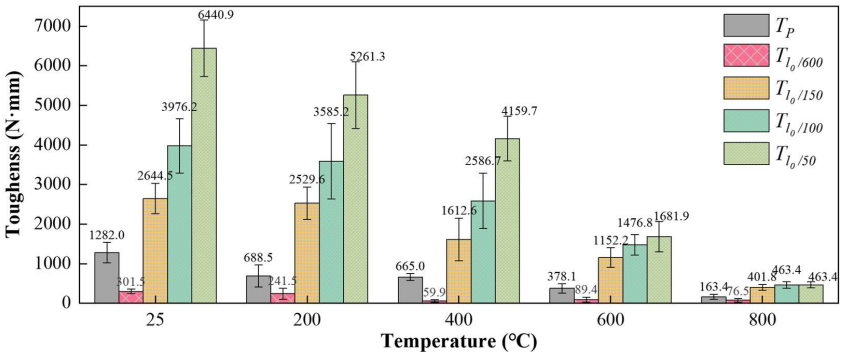


(b) SF 2.0%

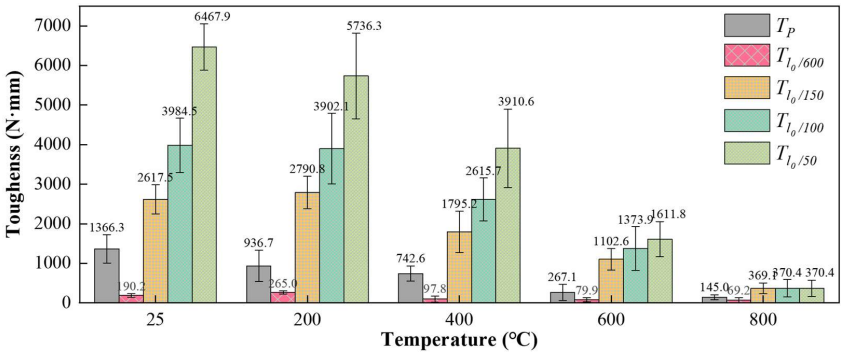


(c) SF 2.5%

Fig. 3.9 (continued). Flexural toughness of UHPC at high temperatures: (b) 2.0% SF and (c) 2.5% SF.

Fig. 3.9 shows that $T_P$ decreases with the increased temperature. When the test temperature rises from ambient temperature to 800 ℃, $T_P$ is only 10.6% -24.7% of the original value. Due to the virtual displacement between the test beam, support, and loading head during the loading process, $T_{l_0/600}$ did not exhibit a direct relationship with temperature and SF volume ratio. Therefore, $T_{l_0/600}$ is not directly applicable for evaluating the bending ductility of high-temperature UHPC. The test temperature was raised from the ambient temperature to 800 ℃, $T_{l_0/600}$ , $T_{l_0/100}$, and $T_{l_0/50}$ are only 14.1% -21.5%, 9.3% -15.2%, and 5.7% -8.8% of of their original values, respectively. Although high temperature severely weakens the bending toughness of UHPC, comparing UHPC with different fiber volume ratios, it is found that the degree of fracture toughness weakening of UHPC before 600 ℃ is inversely proportional to the SF content.

However, after 600 ℃, the larger the fiber volume ratio, the lower the bending toughness. Fig. 3.7 shows that micro-cracks will occur in the interface transition zone between SF fibers and the matrix after 600 ℃. The larger the fiber volume ratio, the more weak bonding surfaces between the matrix and fibers on both sides of the fracture surface. Using the same limit deflection of the test beam as the judgment basis, the less energy consumed during the fiber drawing process, resulting in a lower bending toughness.

### 3.3.2 Fracture behavior

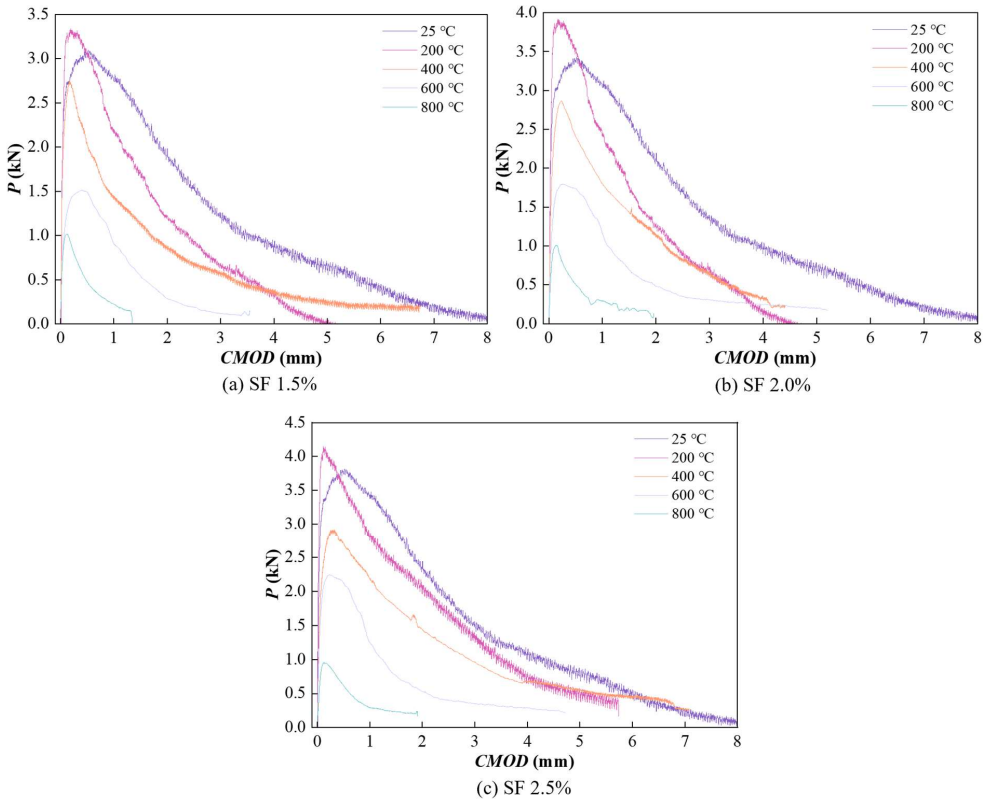


Fig. 3.10. $P-CMOD$ curves of fracture beams: (a) SF 1.5%; (b) SF 2.0%; (c) SF 2.5%.

During the fracture process of UHPC specimens, as the load increases, the main crack appears at the left and right ends of the prefabricated crack and gradually develops to the loading point. The main crack undergoes crack initiation, an increase in crack depth, and a significant increase in crack opening. Steel fibers are gradually pulled out of the matrix, and the test beam makes a sizzling sound before finally being destroyed. Fig. 3.10 shows the load crack mouth opening displacement (*P-CMOD*) curve during the fracture process of the specimen. The development trend of this curve is similar to the load-deflection curve's three-stage characteristics: linear elasticity, elastic-plastic deformation, and strengthening/failure stage. No cracks appeared in the online elastic stage, and the displacement of the crack opening increases linearly with the increase of load. During the elastic-plastic stage, UHPC cracks initiate until the main crack appears, and the curve exhibits nonlinearity. In the strengthening/failure stage, there is an increase in strength accompanied by significant plastic deformation, and steel fibers are gradually pulled out from the UHPC matrix, with the *P-CMOD* curve gradually decreasing. Although the trend of the *P-CMOD* curve is similar to that of the $P-\delta$ curve, it can be observed that the first stage curve area is consistent, which can effectively eliminate the experimental errors caused by random factors such as virtual displacement between the specimen and the support during the test process and roughness of the specimen after high temperature.

The double K fracture model is commonly used to describe the crack development stage of UHPC [150]. In this model, when $K < K_{IC}^{ini}$, the crack does not propagate; When $K_{IC}^{ini} < K < K_{IC}^{um}$, the crack expands steadily; When $K_{IC}^{um} < K$, the crack becomes unstable. The formula for calculating fracture toughness is given as follows [150]:

$$K_{IC} = \frac{3(P + \frac{1}{2}mg)}{2bh^2} l_0 \sqrt{\pi a} \times f(\alpha) \tag{3.3}$$

$$\alpha = \frac{a + h_0}{h + h_0} \tag{3.4}$$

In these equations, $P$ (kN) is the applied load; $mg$ is the weight between the spans of the experimental beam; $l_0$ is the span of the experimental beam; $\alpha$ is the crack length of the test beam; $h_0$ is the blade thickness of the fixed clamp extensometer, which is 1.5 mm in this study; $f(\alpha)$ is a calculated $K_{IC}$ shaped function related to the aspect ratio $\beta$ and $a/h$.

For the experimental beam with a span-to-height ratio of $\beta = 4$, the $f_{\beta=4}(\alpha)$ expression [151] is:

$$f_{\beta=4}(\alpha) = \frac{1}{\sqrt{\pi}} \frac{1.99 - \alpha(1-\alpha)(2.15 - 3.93\alpha + 2.7\alpha^2)}{(1+2\alpha)(1-\alpha)^{3/2}} \tag{3.5}$$

Several studies [152, 153] applied this shape function to beams with span-to-depth ratios other than 4, thereby introducing bias into the calculated fracture toughness and potentially compromising safety assessments.

For the experimental beam with a span-to-height ratio of $\beta = 2.5$, the expression for $f_{\beta=2.5}(\alpha)$ [154] is:

$$f_{\beta=2.5}(\alpha) = \frac{1}{\sqrt{\pi}} \frac{1.83 - 1.65\alpha + 4.76\alpha^2 - 5.3\alpha^3 + 2.51\alpha^4}{(1+2\alpha)(1-\alpha)^{3/2}} \tag{3.6}$$

In this study, if the span-to-height ratio of our experimental beam is $\beta = 3.5$, linear interpolation is applied to the shape functions of span-to-height ratios $\beta = 4$ and $\beta = 2.5$:

$$f_{\beta=3.5}(\alpha) = \frac{3.5-2.5}{4-2.5} f_{\beta=4}(\alpha) - \frac{3.5-4}{4-2.5} f_{\beta=2.5}(\alpha) \tag{3.7}$$

For the initial fracture toughness $K_{IC}^{ini}$, it can be calculated by substituting the precast crack depth $\alpha_0$ and the initial crack load into Eqs. (3.3-3.7), while the fracture toughness $K_{IC}^{um}$ for unstable cracks is determined by $P_{max}$ (kN) and the critical crack length $\alpha_c$, and is given by [150]:

$$a_c = \frac{2}{\pi}(h + h_0) \arctan \sqrt{\frac{bE \times CMOD_P}{32.6 P_{\max}} - 0.1135} - h_0 \tag{3.8}$$

In the formula, $CMOD_P$ is the crack mouth opening displacement to the peak load; The calculated elastic modulus $E$ of the open specimen is [155]:

$$E = \frac{P_i}{b \cdot CMOD_i} \left[ 3.70 + 32.60 \tan^2 (\frac{\pi}{2}\alpha) \right] \tag{3.9}$$

Fig. 3.11 shows the calculated double K fracture toughness of UHPC after high temperature. It can be visually observed from the figure that the double K fracture toughness slightly increases or decreases within 200 ℃. The fluctuation range of $K_{IC}^{ini}$ is between 5.2% increase and 7.5% decrease, and the fluctuation range of $K_{IC}^{um}$ is between 2.3% increase and 4.2% decrease. When the experimental temperature is above 200 ℃, high temperature shows a decreasing trend in fracture toughness. When the temperature is increased from ambient temperature to 400 ℃, 600 ℃, and 800 ℃, $K_{IC}^{ini}$ decreases by 24.4% -26.4%, 42.6% -68.6%, and 70.2% -76.9%, and $K_{IC}^{um}$ decreases by 18.5% -25.0%, 42.7% -52.7%, and 69.2% -75.9%, respectively.

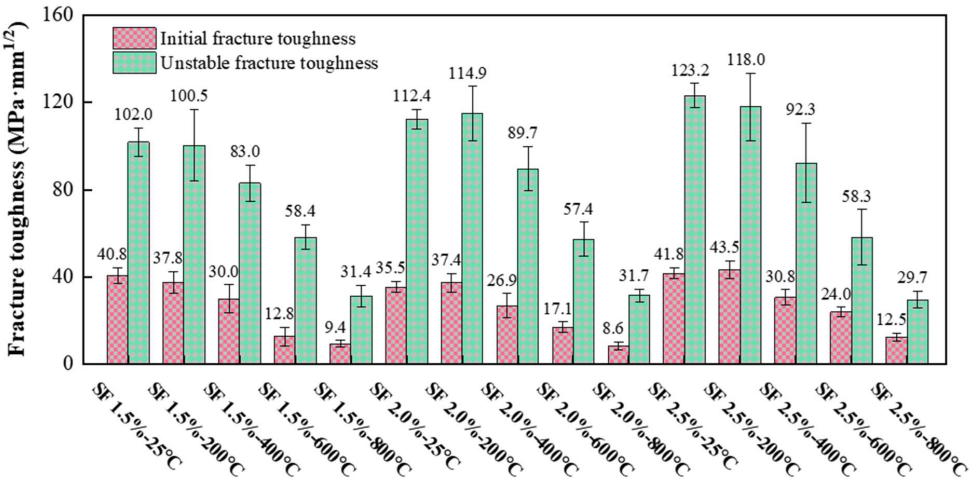


Fig. 3.11. Double K fracture toughness of UHPC after high temperature.

High-temperature exposure can reduce the fracture toughness of UHPC. From the perspective of fiber volume ratio, at all temperatures, the larger the fiber volume ratio, the greater the initial fracture toughness. However, in terms of critical fracture toughness, this law only applies before 400 ℃. After 600 ℃, due to the weakening of the mechanical properties of the matrix and ITZ by high temperature, the critical fracture toughness calculated by the maximum load point did not show a significant change pattern with the change of fiber volume ratio, and the critical fracture toughness was almost unchanged. Overall, from the perspective of improving the fracture toughness of high-temperature UHPC, increasing the fiber volume ratio is advantageous.

For three-point bending experiments with prefabricated notched beams, the Type I fracture energy can be calculated through the load deflection ($P$-$\delta$) curve [156]:

$$G_F = \frac{\int Pd\delta + mg\delta_0}{b(h-a_0)} \tag{3.10}$$

In this formula, $P$ represents the external load; $\delta$ is the mid-span deflection; $\delta_0$ is the maximum deflection during fracture; $b$ is the specimen width; $h$ is the height of the beam; $a_0$ is the notch depth; and $m$ and $g$ are the mass and gravitational acceleration, respectively.

During the experiment, there is a virtual displacement between the specimen and the support, which is affected by random factors such as the surface roughness of the specimen and support,

resulting in a large dispersion of the load-deflection (*P-δ*) curve. Using the load crack opening (*P-CMOD*) curve can effectively avoid this problem. According to the *P-CMOD* curve, the calculation formula for fracture energy is as follows [157]:

$$G_F = \frac{\int Pd(\delta) + mg\delta_0}{b(h-a_0)} \xrightarrow{\delta=\frac{l_0}{4H}CMOD} G_F = \frac{\frac{l_0}{4H}\int Pd(CMOD) + \frac{l_0}{4H}mgCMOD_0}{b(h-a_0)} \tag{3.11}$$

In the formula, $l_0$ is the span length (distance between supports), $H = h+h_0$ is the effective height of the beam including the fixture thickness, $CMOD_0$ is the maximum crack mouth opening displacement, and *CMOD* is the corresponding variable during loading. Other parameters are consistent with Eq.(3.10).

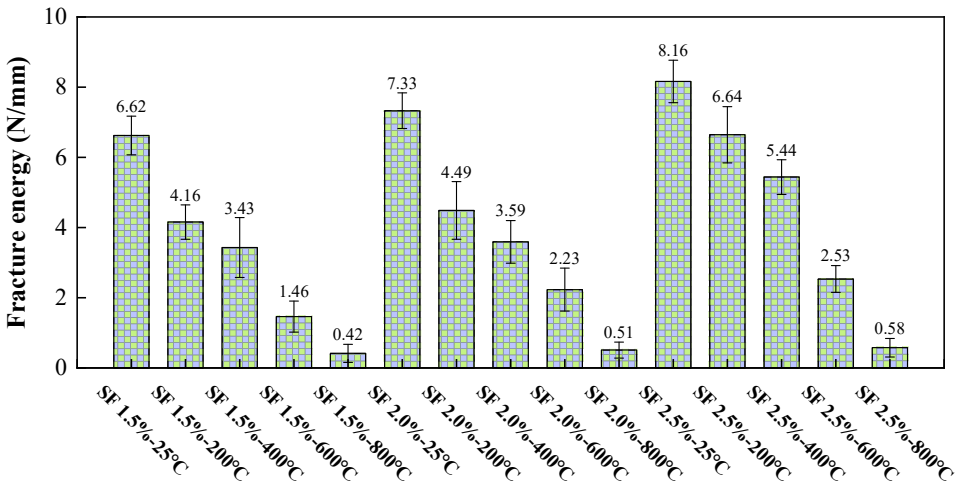


Fig. 3.12. Fracture energy of UHPC after high temperature.

As shown in Fig. 3.12, the fracture energy of UHPC decreases progressively with increasing exposure temperature. When the temperature increases from ambient to 200 °C, 400 °C, 600 °C, and 800 °C, the measured fracture energy drops from 6.62-8.16 (*N/mm*) to 4.16-6.64, 3.43-5.44, 1.46-2.53, and 0.42-0.58 (*N/mm*), corresponding to 61.2-81.4%, 49.0-66.6%, 22.1-31.0%, and 5.1-7.1% of the original values, respectively. These results confirm a clear degradation trend. The fracture energy was calculated based on the area under the complete load–crack mouth opening displacement (P–CMOD) curve. At 600 °C and above, although the mechanical integrity of both the matrix and the ITZ is substantially compromised, resulting in a reduced energy requirement for fiber pull-out, the steel fibers continue to exhibit a degree of residual load-bearing capacity even after slippage. This delayed pull-out behavior helps to maintain energy absorption. Moreover, a higher steel fiber volume ratio results in denser fiber distribution across the crack plane. This increases the crack opening displacement at the stage when the tensile zone no longer contributes to load bearing, thereby expanding the total envelope area and improving the energy absorption capacity. Although elevated temperatures drastically reduce the overall fracture energy of UHPC, the extent of reduction is mitigated by higher fiber volume ratios. This indicates that increasing steel fiber content can partially compensate for thermal damage and improve post-fire fracture resistance.

## 3.4 Prediction of mechanical and fracture properties of UHPC after high-temperature exposure

To describe the relationship between the SF volume fraction and the post-high-temperature compressive strength of UHPC, the compressive-strength influence factor $\beta_{cu}{}^{T}$ is given by:

$$f_{cu}{}^{T} = \beta_{cu}{}^{T} f_{cu} \tag{3.12}$$

$$\beta_{cu}{}^{T} = -0.1779 + 0.02132T_{R25} + 112.79962V_{SF} - 0.0011T_{R25}{}^{2} - 2583.52335V_{SF}{}^{2} - 0.44616T_{R25}V_{SF} \tag{3.13}$$

Eq. (3.13) was obtained by polynomial linear regression through Fig. 3.15(a). Fig. 3.15(a) shows the relationship between high temperature, SF volume ratio, and compressive strength, which was obtained through polynomial fitting of the relationship between temperature, SF fiber volume ratio, and compressive strength. For the convenience of polynomial fitting in the future, the high temperature is normalized. $T_{R25}$ represents the ratio of experimental temperature to ambient temperature of 25 °C, $V_{SF}$ represents the volume content of steel fibers, as shown in Eq. (3.13), and the correlation coefficient $R^2 = 0.988$. Fig. 3.13 compares the experimental and predicted values of the compressive strength of UHPC after high-temperature exposure, which were calculated using Eqs. (3.12-3.13). For further verification, the experimental results of Xue et al. [145], Lin et al. [24], and Khan et al. [158] were also introduced in the figure for comparison. It can be seen from Fig. 3.13 that, except for a few individual data points, the prediction error is controlled within 20%.

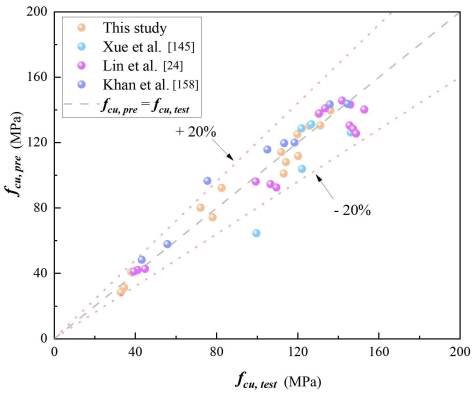


Fig. 3.13. Comparison of UHPC compressive strength test values with predicted values after high-temperature exposure.

Similar to compressive strength, the flexural strength variation process of UHPC specimens is described using the flexural strength influencing factor $\beta_p{}^{T}$, defined as:

$$f_p{}^{T} = \beta_p{}^{T} f_p \tag{3.14}$$

The dependence of $\beta_p{}^{T}$ on normalized temperature and SF volume fraction was obtained by polynomial regression of the data in Fig. 3.15(b) and is given by:

$$\beta_p{}^{T} = 0.38426 + 0.01524T_{R25} + 36.87622V_{SF} - 0.0007T_{R25}{}^{2} - 391.72426V_{SF}{}^{2} - 0.78136T_{R25}V_{SF} \tag{3.15}$$

Fig. 3.15(b) presents the relationship between high temperature, SF volume ratio, and flexural strength. The factors influencing high temperature and SF volume ratio on flexural strength were obtained through normalization and polynomial fitting, as shown in Eq.(3.15), with a correlation coefficient of $R^2 = 0.927$. Fig. 3.14 compares the experimental and predicted values of the flexural strength of UHPC after high-temperature exposure. To further verify the rationality of the proposed formulas, the experimental results of Lin et al. [24] , Huang et al. [45] and Arabani et al. [148] are also introduced in the figure for comparison. It can be seen from the figure that the prediction error is controlled within 20%.

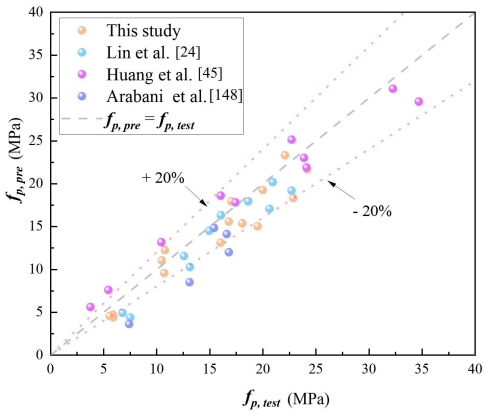


Fig. 3.14. Comparison of UHPC flexural strength test value and predicted value after high-temperature exposure.

To accurately describe the relationship between SF volume ratio and the post-heating fracture energy $G_F{}^T$, the fracture-energy influencing factor $\beta_G$ is used to characterize the change in fracture energy of UHPC specimens after high temperature exposure, as given by:

$$G_F{}^T = \beta_G{}^T G_F \tag{3.16}$$

$$\beta_G{}^T = 1.02831 - 0.01748T_{R25} - 36.73825V_{SF} + 0.0000981T_{R25}{}^2 + 1712.00228V_{SF}{}^2 - 0.74231T_{R25}V_{SF} \tag{3.17}$$

Eq. (3.17) was obtained by polynomial linear regression through Fig. 3.15(c). Fig. 3.15(c) shows the relationship between relative high temperature, fiber volume ratio, and relative fracture energy. The relationship between the high-temperature fracture energy influencing factor $\beta_G$, relative temperature, and fiber content was obtained using polynomial fitting, as shown in Eq. (3.17), with a correlation coefficient of $R^2=0.958$. Fig. 3.16 compares the experimental and predicted values of the fracture energy of UHPC after high-temperature exposure, which are calculated based on Eqs. (3.16-3.17). To further verify the rationality of the proposed formulas, the experimental results of Huang et al. [45], Arabani et al. [148], and Peng et al. [159] are also introduced in the figure for comparison. At present, the directly-referable data regarding the fracture energy of UHPC after high-temperature exposure are somewhat limited. In their study, Huang et al. [45] and Arabani et al. [148] Only the load-displacement curves were provided during the flexural test of UHPC after high-temperature

exposure. The fracture energy mentioned in this study is calculated based on their research by extracting the load-deflection curves of UHPC after high-temperature exposure and combining them with Eq. (3.10). Since the fracture energy is calculated based on the load-deflection curves, it can be seen from the figure that the discreteness of the prediction error is relatively large, but overall, it still conforms to the pattern of the proposed formulas.

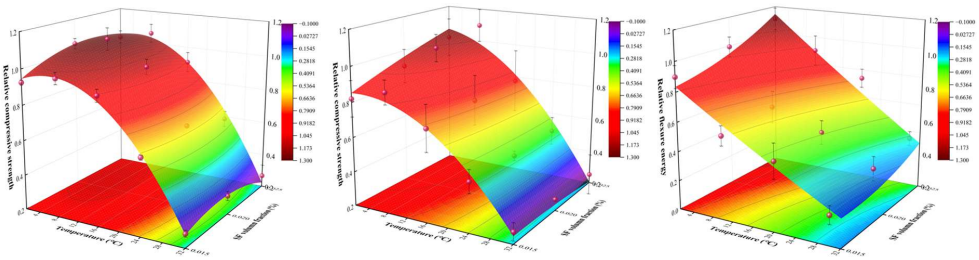

(a) Compressive strength reduction factor (b) Flexural strength reduction factor (c) Reduction coefficient of fracture energy

Fig. 3.15. The relationship between high temperature, strength, and fracture energy.

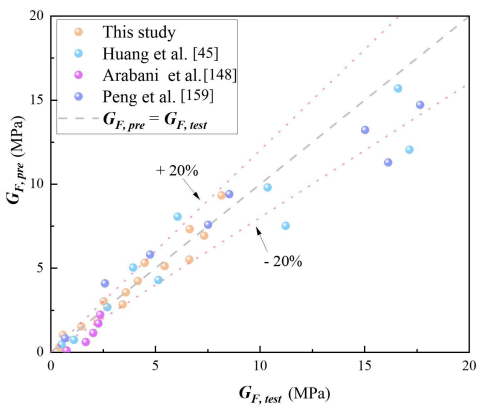


Fig. 3.16. Comparison of the test and predicted values of UHPC fracture energy after high-temperature exposure.

In addition to predicting the effects of high temperature and fiber volume ratio on the mechanical properties of UHPC, experimental results show that as the temperature increases, the compressive strength, flexural strength, fracture energy, and double K fracture toughness of UHPC decrease almost linearly. Based on the experimental results, the relationship between the mechanical properties of UHPC after high-temperature exposure is given by:

$$f_p^{\,T} = k_1^T f_{cu}^{\,T} \tag{3.18}$$

$$G_F^{\,T} = k_2^T f_p^{\,T} \tag{3.19}$$

$$K_{IC}^{ini,T} = k_3^T f_p^{\,T} \tag{3.20}$$

$$K_{IC}^{un,T} = k_4^T K_{IC}^{ini,T} \tag{3.21}$$

In the formula, $f_{cu}{}^{T}$ represents the compressive strength of UHPC after high temperature, $f_{p}{}^{T}$ represents the flexural strength of UHPC after high temperature, $G_{F}{}^{T}$ represents the fracture energy of UHPC after high temperature, $K_{IC}{}^{ini,T}$ represents the initial fracture toughness of UHPC after high temperature, $K_{IC}{}^{un,T}$ represents the fracture toughness of UHPC crack instability after high temperature, and the range of temperature $T$ is (25℃≤T≤800℃), $k^{T}$ is the linear coefficient related to the relative temperature, which varies with the relative temperature, as shown in Fig. 3.17.

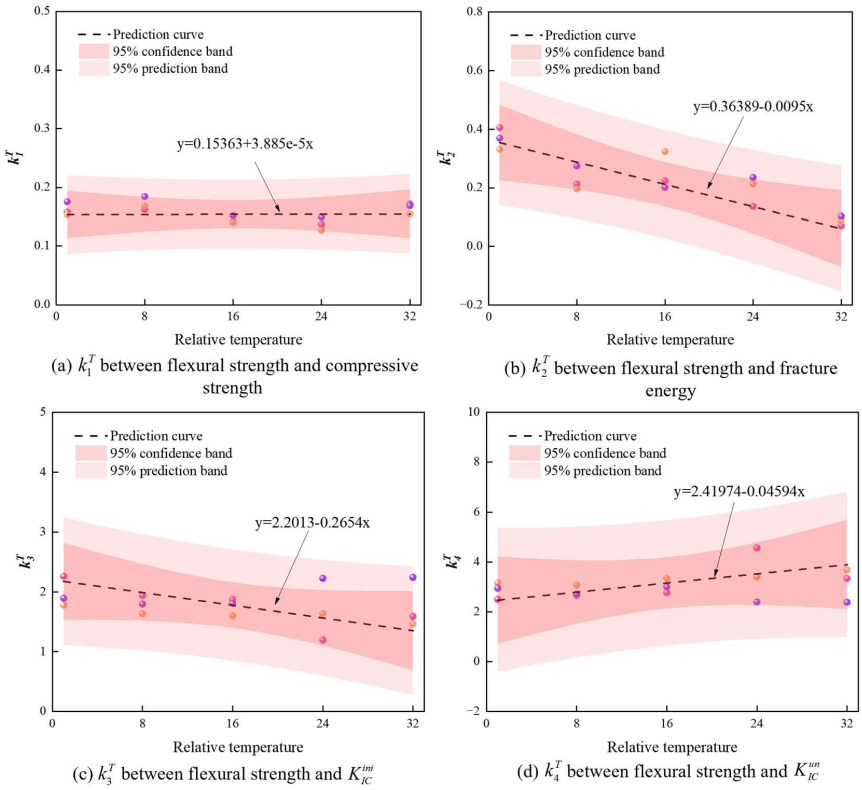


(a) $k_1^T$ between flexural strength and compressive strength

(b) $k_2^T$ between flexural strength and fracture energy

(c) $k_3^T$ between flexural strength and $K_{IC}^{ini}$

(d) $k_4^T$ between flexural strength and $K_{IC}^{un}$

Fig. 3.17. Relationship between mechanical properties of UHPC after high-temperature action.

The fitting effect of the relationship between the mechanical properties of UHPC after high-temperature exposure with the relative temperature change is shown in Fig. 3.17. Judging from the fitting effect, the determined model can accurately reflect the relationship between the mechanical properties of UHPC after high-temperature exposure. After high-temperature exposure, the mechanical properties of UHPC show a linear relationship, according to the flexural strength test and Eqs. (3.19-3.21), the fracture energy and toughness of UHPC can be conveniently estimated. If limited by experimental equipment, according to the cube test results and Eqs. (3.18-3.21), the fracture energy and toughness of UHPC can also be estimated.

It should be noted that the mechanical property prediction model of UHPC after high-temperature exposure proposed in this study is based on limited experimental data. Moreover,

after high-temperature exposure, the fracture experiments were carried out after natural cooling to room temperature in the laboratory, without considering the influence of actual environmental temperature and humidity on the residual stress in UHPC after cooling.

## 3.5 Conclusions

This chapter aims to understand the fracture performance of UHPC under high temperatures. UHPC was designed with different SF volume ratios and tested under temperatures of 200, 400, 600, and 800 ℃, respectively. The degradation behavior of UHPC in terms of flexural strength and fracture energy was investigated. In addition, a prediction formula for the mechanical and fracture properties of UHPC after high-temperature exposure was proposed. The main conclusions are as follows:

- After exposure to high temperatures, the compressive strength and flexural strength of UHPC show a trend of first increasing and then decreasing with the increase in temperature. When the temperature reaches 200 ℃, the residual compressive strength is increased by 4.3-5.3%, and the residual flexural strength is increased by 9.5-14.4%. After 200 ℃, the residual strength of UHPC decreases linearly. When the temperature increases to 800 ℃, the residual compressive strength is only 26.2-30.2% of that at normal temperature, and the residual compressive strength is only 25.2-32.8%.
- Regardless of *P-δ* curve or *P-CMOD* curve, high temperature reshapes the original development trajectory of the curve. In the third stage of curve extension, the sawtooth-shaped fluctuation amplitude caused by stress redistribution due to fiber drawing at 200 ℃ is significantly reduced compared to normal temperature. When the temperature exceeds 600 ℃, the sawtooth-shaped fluctuation amplitude caused by stress redistribution due to fiber drawing disappears directly, seriously affecting the bonding between steel fibers and matrix.
- After exposure to high temperatures, the original strengthening stage of UHPC suddenly transforms into a failure stage, resulting in brittle failure characteristics of UHPC. After high temperature, the bending toughness, fracture toughness, and fracture energy of UHPC were significantly reduced. From the perspective of the SF fiber volume ratio, although the retention of bending toughness and critical fracture toughness after 600 ℃ is not significantly positively correlated with the fiber volume ratio, overall, an increase in SF volume is beneficial for improving the fracture performance of UHPC.
- A new prediction model for the compressive strength, flexural strength, and fracture energy of UHPC after high temperature is established using SF volume ratio and temperature as variables. The model can effectively predict the compressive strength, flexural strength, and fracture energy of UHPC after high temperatures. The conversion relationships among compressive strength, flexural strength, fracture energy, and fracture toughness are established, and the reduction effect takes temperature influence into account.

# Chapter 4 Mix design of SUHPC with superior early-age performance


## *Abstract*

Achieving rapid setting, early-age strength and volumetric stability is critical for shotcrete used in repair applications. In this study, a novel sprayed ultra high performance concrete (SUHPC) incorporating a Portland cement–calcium aluminate cement–gypsum (PC–CAC–C$) ternary binder was developed for the first time to tackle challenges in rheology, shrinkage, and early age strength. A series of SUHPC mixtures with varying C$/CAC ratios (0.25–1.0) and the addition of a 2 wt% alkali-free accelerator were systematically investigated. QXRD, TGA, calorimetry, rheology, and SEM revealed that a C$/CAC ratio of 0.5 maximizes early ettringite formation, resulting in a fourfold increase in thixotropy compared to cast UHPC, and enabling a 3-hour compressive strength of 15.11 MPa. At later stages, the accelerator promotes strätlingite formation, mitigating phase conversion of CAC and preserving strength and durability. Meanwhile, the ternary system induces micro-expansion, effectively offsetting both accelerator-induced shrinkage and autogenous shrinkage of SUHPC, thus ensuring dimensional stability. Overall, this novel SUHPC achieves rapid setting, enhanced thixotropy, early strength, and micro-expansion, making it a promising candidate for large-scale shotcrete applications.



This chapter is partially published elsewhere:

J. He, Y.S. She, X. Ling, H.Y. Wang, H.J.H. Brouwers, and Q.L. Yu, Development of a Novel SUHPC Based on PC-CAC-C$ System: Rheology, Early-Age Strength, and Hydration Kinetics. Construction and Building Materials, 502 (2025), 144420.

## 4.1 Introduction

In large load-bearing structures such as tunnel linings and bridge piers, repair materials must provide high strength and support to the structure within a few hours under emergency scenarios (e.g., localized impacts, fires, collapses, or water infiltration) to ensure the safety of personnel and structures [160, 161]. In recent years, sprayed ultra-high-performance concrete (SUHPC), incorporating fibers and characterized by high strength, excellent durability, and rapid construction for irregular cross-sections, has shown promising potential for widespread application as a rapid repair material [25, 26].

SUHPC integrates the advantages of conventional UHPC and shotcrete, offering a high packing density, lower water-to-binder ratio, and enhanced durability and corrosion resistance [35, 87, 162]. Additionally, SUHPC exhibits superior strength, allowing for the application of thinner sprayed layers while maintaining structural integrity. Despite these benefits, several challenges remain unaddressed, especially regarding rheology, shrinkage, and early-age strength.

A primary challenge lies in enhancing the rheological performance SUHPC to ensure both pumpability and sprayability. Previous studies have shown that incorporating viscosity-enhancing admixtures (VEAs) can increase the yield stress and thixotropy of SUHPC, thereby improving its sprayability [163]. However, the high viscosity induced by VEAs often entraps air bubbles, leading to increased porosity and a reduction in mechanical properties of SUHPC [27, 164]. Therefore, identifying alternative strategies to enhance SUHPC rheology without compromising strength is essential for achieving both efficient spraying and mechanical performance.

A second critical issue is the high autogenous shrinkage inherited from UHPC. Excessive shrinkage increases the risk of cracking and volumetric instability [29]. Moreover, when employed as a repair material, the shrinkage of SUHPC can weaken its bond with the repaired structure, thereby deteriorating the overall repair effectiveness. Various methods, including shrinkage-reducing admixtures (SRA) [165-167], expansive agents (EA) [168-170], and internal curing (IC) agents [171], have been introduced to mitigate shrinkage-induced stresses and enhance the bond strength between the repair material and the substrate. However, these shrinkage-reducing materials can adversely affect the compressive, flexural, and tensile strength of concrete [172]. Consequently, developing new SUHPC formulations with shrinkage compensation is crucial for ensuring volume stability.

A third pressing challenge is achieving high early-age strength and rapid setting in SUHPC to ensure the necessary structural support at early age (e.g., within a few hours), which is essential for emergency repair applications. $Al_2(SO_4)_3$ based alkali-free accelerator are commonly employed in shotcrete to reduce setting time and enhance the early strength [172]. It is typically added at the nozzle of the spraying machine and mixed with the shotcrete. Upon contact with the paste, the accelerator

rapidly dissolves, releasing $Al^{3+}$, which converts to $Al(OH)_4^-$ in the alkaline environment and subsequently interacts with $Ca^{2+}$ and $SO_4^{2-}$, leading to ettringite formation. The formation of ettringite in large quantities within a short time creates a dense spatial network structure, thereby enhancing the early strength of SUHPC. However, the use of accelerators also introduces several drawbacks: 1) Strength instability, as their rapid reaction with the paste traps air bubbles, increasing macro-porosity and reducing strength [27, 164]; 2) Volume instability, as accelerator exacerbate long-term shrinkage [28, 173]; 3) High cost, which hinders the sustained application of the alkali-free accelerator. Therefore, developing alternative methods to accelerate setting and improve early-age strength while reducing reliance on alkali-free accelerators warrants further investigation.

In light of these challenges, this chapter introduces a novel ternary binder system (PC-CAC-C$) into SUHPC, composed of Portland cement (PC), calcium aluminate cement (CAC), and gypsum (C$). This system is designed to systematically improve the rheology, shrinkage, and early-age strength of SUHPC through innovations in the cementitious matrix. The hydration behavior of the ternary binder system is considerably complex [30, 31], being influenced not only by the ratios of PC/CAC and CAC/C$ but also by environmental temperature and curing conditions [174]. During the early hydration stage, CA from CAC cement dissolves and reacts with calcium sulfate to form ettringite [175]. Ettringite is the primary expansive phase formed in PC-CAC-C$ blends, serving as an effective means to mitigate early autogenous shrinkage and accelerate setting [29]. Theoretically, the application of the PC-CAC-C$ system in SUHPC could reduce or even compensate for shrinkage induced by accelerators, thereby potentially partially or completely replacing alkali-free accelerators. Therefore, investigating the individual and synergistic effects of the PC-CAC-C$ system and alkali-free accelerators is a key research focus in optimizing the hydration kinetics of SUHPC.

Currently, the intrinsic hydration mechanisms underlying the optimal gypsum-to-calcium aluminate cement (C$/CAC) ratio, as well as the synergistic interactions between alkali-free accelerators and the PC–CAC–C$ ternary binder system, remain unexplored. Specifically, critical questions include how variations in the C$/CAC ratio influence rheology and phase evolution of SUHPC, and how alkali-free accelerators interact with the ternary binder to modify its hydration kinetics, early-age strength, and shrinkage compensation behavior. To address these gaps, rheological properties and setting time were evaluated to assess the fresh behavior. Calorimetry was employed to measure heat evolution, and SEM was used to analyze morphological changes. The hydration process and phase evolution at early and later stages were analyzed qualitatively and quantitatively evaluated applying Rietveld-refined QXRD and TGA. The effects of different C$/CAC ratios and accelerator on the hydration kinetics, rheological properties, and early-age strength of the PC-CAC-C$ system are systematically investigated. Finally, the optimal C$/CAC ratio and mix proportion for SUHPC were determined, and the synergistic mechanism between the PC-CAC-C$ system and alkali-free accelerators was systematically summarized.

## 4.2 Materials and experiments

### 4.2.1 Raw materials and mix proportions

CEM I 52.5R (PC, supplied by Heidelberg Materials), commercial CAC cement and gypsum ($CaSO_4 \cdot 2H_2O$, abbreviated as C$) were employed as the primary cementitious materials to form ternary binder systems in this study. Silica fume (microsilica, MS) and fly ash cenosphere (FAC) were incorporated into the mixture as supplementary cementitious materials. The chemical compositions of powder materials are illustrated in Table 4.1.

Table 4.1. Chemical composition of the raw materials.

| Oxide (wt%) | PC | CAC | C$ | MS | FAC |
|---|---|---|---|---|---|
| $Al_2O_3$ | 4.98 | 53.31 | 0.20 | 0.23 | 17.89 |
| CaO | 64.61 | 34.28 | 43.3 | 0.41 | 8.20 |
| $SiO_2$ | 20.18 | 6.96 | 0.32 | 94.68 | 55.57 |
| MgO | 2.19 | 0.37 | 1.37 | 0.43 | 1.02 |
| $Fe_2O_3$ | 3.24 | 1.90 | 0.10 | 0.17 | 11.31 |
| $K_2O$ | 0.53 | 0.41 | 0.01 | 0.83 | 2.74 |
| $P_2O_5$ | 0.74 | 0.15 | - | 0.19 | 1.59 |
| $Na_2O$ | 0.27 | 0.12 | - | 0.15 | 0.48 |
| $TiO_2$ | 0.25 | 1.67 | - | - | - |
| $SO_3$ | 3.01 | 0.83 | 53.7 | 0.81 | 1.20 |
| LOI | 1.56 | 1.60 | 1.59 | 2.33 | 1.03 |

Three types of continuously graded quartz sand, designated as 0.38-1.2 mm (QS-1), 0.2-0.47 mm (QS-2), and 0-0.22 mm (QS-3) were used as aggregates. Copper-coated steel fibers with a diameter of 0.22 mm and a length of 6 mm were incorporated. A polycarboxylate superplasticizer (PCE) with a solid content of 40% was applied to ensure the workability of SUHPC, with a dosage of 1.9 wt% relative to the binder weight. To adjust the viscosity of SUHPC, hydroxypropyl methyl cellulose (HPMC) with a viscosity of 200,000 mPa·s (supplied by Shanghai Chenqi Company) was employed. In this study, a liquid alkali-free accelerator (FSA-AF, Shanxi Feike New Material Technology Co., Ltd.) with aluminum sulfate as the main component was utilized, with a dosage of 2% by binder weight.

To achieve the maximum particle packing of the raw materials in the SUHPC mix design, the modified A&A model (MAA) was applied [176, 177]. The particle-size distribution is required to satisfy the MAA gradation function given in Eq. (3.1) of Section 3.2.1, where P(D) denotes the percentage volume fraction of particles with a diameter less than D; $D_{max}$ and $D_{min}$ signifies the largest and smallest particle size, respectively; q refers to the distribution modulus.

Subsequently, the measured cumulative particle-size distribution was fitted to the target curve using the residual sum of squares (RSS), where RSS is the residual sum of squares; $P_{mix}$ refers to the

composite mixture of SUHPC; $P_{tar}$ is the target classification [178, 179]. The fitting criterion is given by Eq. (3.2).

Considering that the SUHPC designed in this study contains a relatively high proportion of fine particles, a low distribution modulus (q = 0.23) was adopted. The optimized SUHPC mixture composition and corresponding fitted cumulative curves are presented in Fig. 4.1 and Table 4.3.

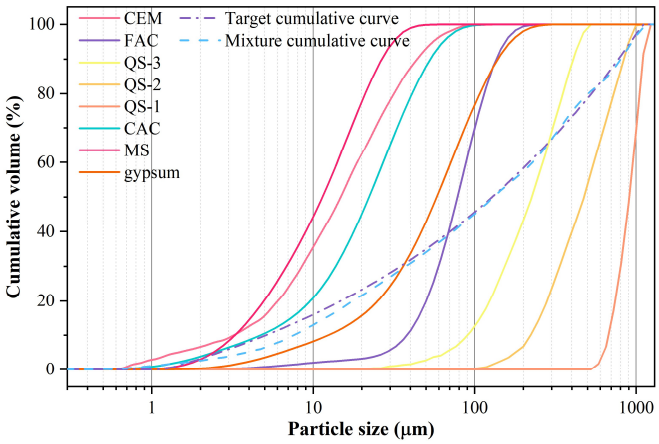


Fig. 4.1. Cumulative curves of raw materials and SUHPC mixtures.

Table 4.2. Composition of the binders in various systems.

| | Mix ID | Composition | C$/CAC |
|---|---|---|---|
| **Neat PC** | U | 100%PC | - |
| **Ternary** | TR1 | 70%PC+24%CAC+6%C$ | 0.25 |
| | TR2 | 70%PC+20%CAC+10%C$ | 0.5 |
| | TR3 | 70%PC+17.14%CAC+12.86%C$ | 0.75 |
| | TR4 | 70%PC+15%CAC+15%C$ | 1 |
| **Accelerator** | U-Afa | U+6%Accelerator | - |
| | TR2-Afa | TR2+6%Accelerator | 0.5 |

Table 4.3. Mix proportion of SUHPC mixtures (kg/m$^3$).

| Materials | U | TR1 | TR2 | TR3 | TR4 | U-Afa | TR2-Afa |
|---|---|---|---|---|---|---|---|
| PC | 791 | 553.7 | 553.7 | 553.7 | 553.7 | 791 | 553.7 |
| CAC | - | 189.8 | 158.2 | 135.6 | 118.7 | - | 158.2 |
| C$ | - | 47.5 | 79.1 | 101.7 | 118.7 | - | 79.1 |
| MS | 179 | 179 | 179 | 179 | 179 | 179 | 179 |
| FAC | 144 | 144 | 144 | 144 | 144 | 144 | 144 |
| QS-1 | 192 | 192 | 192 | 192 | 192 | 192 | 192 |
| QS-2 | 510 | 510 | 510 | 510 | 510 | 510 | 510 |
| QS-3 | 412 | 412 | 412 | 412 | 412 | 412 | 412 |
| Water | 188.3 | 195 | 195 | 195 | 195 | 188.3 | 195 |
| SP | 47 | 49.5 | 49.5 | 49.5 | 49.5 | 47 | 49.5 |
| Accelerator | - | - | - | - | - | 22.3 | 22.3 |
| Steel fiber | 156 | 156 | 156 | 156 | 156 | 156 | 156 |

In this study, U refers to the conventional UHPC mixture with PC as the primary binder, serving as the control group. The water-to-binder ratio (w/b) of U mix was 0.19. TR represents the ternary system (PC-CAC-C$), in which the combined amount of CAC and C$ replaced 30 wt% of the PC. In the ternary system, to ensure that the flowability of the SUHPC meets the required standard [180], the water-to-binder ratio was adjusted to 0.2. Composition of the binders in various systems and mix proportion of SUHPC mixtures are shown in Table 4.2 and Table 4.3.

### 4.2.2 Field spray test and and specimen preparation

Fig. 4.2 illustrates the field spray test, conducted in accordance with EN 934-5:2007 [181]. The field spray test and specimen preparation followed a standardized procedure comprising material weighing, mixing, transportation, spraying equipment setup and loading, mold preparation, and final spraying. The alkali-free accelerator was incorporated at the nozzle of the spraying system during application. In the field spray test, the SUHPC of the ternary system without an accelerator (TR2 mix) achieved a thickness of 41 mm, while the SUHPC of the ternary system with an accelerator (TR2-Afa mix) reached a thickness of 52 mm, confirming the excellent pumpability and sprayability of the ternary binder system [181]. After demolding, the concrete slabs were cut into SUHPC specimens with dimensions of 150 mm×150 mm×150 mm and cured until the specified curing age. U mix was used as conventional poured UHPC and was directly cast into 150 mm×150 mm×150 mm molds.

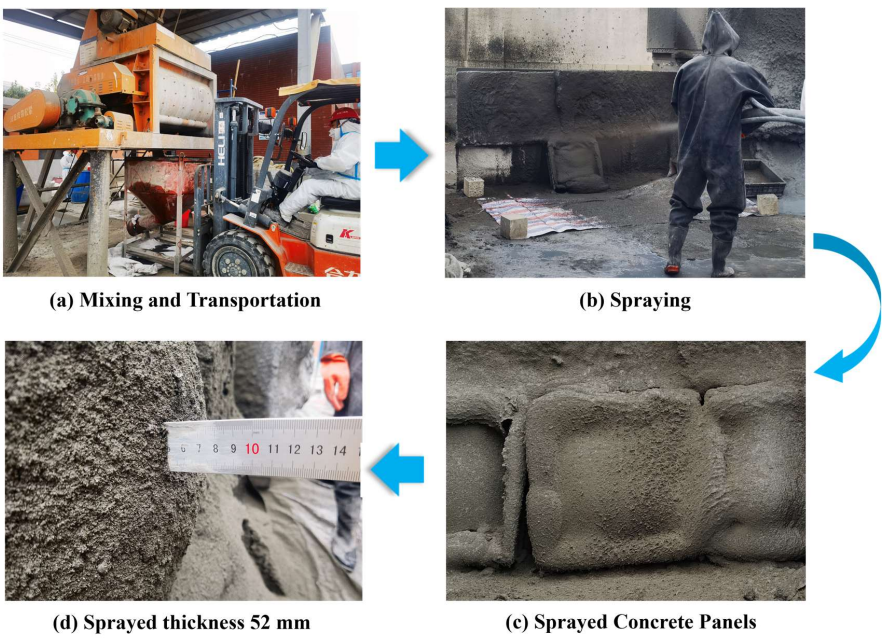


Fig. 4.2. Field spray test.

### 4.2.3 Experimental methods

#### 4.2.3.1 Setting time and flow behavior

The initial and final setting times of SUHPC were determined according to EN 196-3 [182]. Measurements were taken at 20-second intervals because the accelerator reduced the initial setting time to approximately five minutes and the final setting time to less than ten minutes. A flow table test of SUHPC flowability is conducted according to EN 1015-3 [92]. For SUHPC containing alkali-free accelerators, the flowability decreases rapidly within 5 minutes due to flash setting. Therefore, the measurements of U-Afa and TR2-Afa are not conducted.

#### 4.2.3.2 Isothermal calorimetry

The hydration heat evolution of SUHPC in the ternary system was measured and recorded using isothermal calorimetry (TAM Air C80). After external mixing, heat flow was recorded for 48 hours, and cumulative heat was calculated.

#### 4.2.3.3 Rheology

The rotational rheometer (R/S-SST 2000, manufactured by Brookfield, USA) was used to evaluate the SUHPC in the ternary system. The rotor of rheometer with a height of 20 mm and a diameter of 10 mm was used. To avoid potential damage to the rheometer rotor due to the accelerator reducing the initial setting time to less than 5 minutes, U-Afa and TR2-Afa were excluded from the measurements. As shown in Fig. 4.3(a), fresh mixed mortar with different C$/CAC ratios (0, 0.25, 0.5, 0.75 and 1) were continuously sheared at a constant shear rate of 0.1 $S^{-1}$ for 90 seconds at various hydration times. The thixotropy (λ) of the SUHPC mortar, defined from the maximum shear stress ($\tau_i$) and the steady-state equilibrium shear stress ($\tau_e$) as illustrated in Fig. 4.3(b), is given by [183]:

$$\lambda = (\tau_i - \tau_e) / \tau_e \tag{4.1}$$

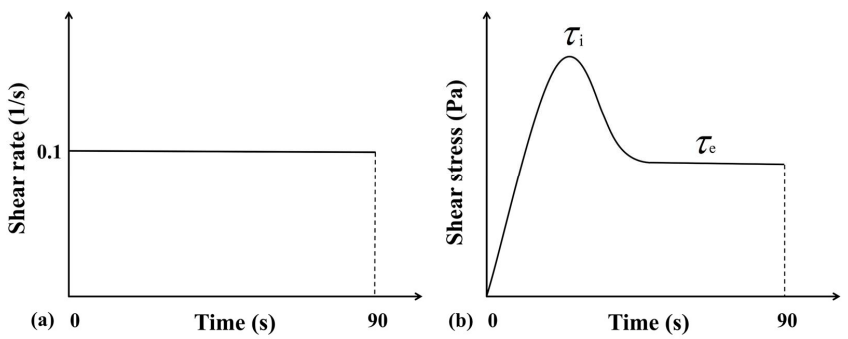


**Fig. 4.3.** (a) Depiction of the shear process and (b) the corresponding shear stress curve from the rheological test of SUHPC.

#### 4.2.3.4 QXRD

Quantitative X-ray diffraction (QXRD) analysis was carried out on a Bruker D2 PHASER with the XE-T detector (Co, λ=1.79 Å). Two-theta values were measured from 5 to 90° with a step size of 0.013°. Crystalline silicon was incorporated at 10 wt% of the total sample weight and used as an internal standard during Rietveld refinement. The Rietveld analysis was performed with Topas software (version 5.0).

#### 4.2.3.5 TG

Thermogravimetric analysis (TGA) was carried out using a TA Instrument (TA 209 F3 Tarsus). Approximately 20 mg of each SUHPC paste sample was tested at a constant rate of 10 ℃/min in a temperature range of 25 to 1000℃.

#### 4.2.3.6 Morphology

The morphology of the SUHPC specimen was observed by scanning electron microscopy (SEM) applying a TESCAN MIRA3 equipment. The block samples were about 0.5 $mm^3$ each and was coated with gold. It features a resolution of 1.2 nm, a magnification range from 2 to 1000,000 times, and an acceleration voltage adjustable between 0.5 kV and 30 kV.

#### 4.2.3.7 Dimensional change

The measurement and evaluation of dimensional change in concrete samples were conducted in accordance with ASTM C490/C490M-21 [184]. The initial measurements were conducted 1 day after demolding. The length change at the specified age is given by:

$$L = \frac{(L_x - L_i)}{G} \times 100 \tag{4.2}$$

Here,

$L_x$= the difference between the comparator reading of the specimen and the comparator reading of the reference bar at the same age x (1, 3, 7, 14, and 28 days).

$L_i$ = the initial difference between the comparator reading of the specimen and that of the reference bar.

$G$ = the nominal gauge length of the measuring apparatus, which was set to 250 mm in this study.

The length change values for each specimen shall be calculated to an accuracy of 0.001%, and the average values shall be reported to the nearest 0.01%.

#### 4.2.3.8 Strength

The compressive strength tests were conducted on cube specimens, which were obtained by cutting SUHPC slabs into 150 mm×150 mm×150 mm sections. The specimens were cured under standard conditions for 3 hours, 1 day, and 28 days, followed by strength testing at a loading rate of 1.0 MPa/s.

## 4.3 Results and analysis

### 4.3.1 Setting time and flow behavior

Fig. 4.4 summarizes the setting time and fresh behavior of SUHPC with different C$/CAC ratios and/or under the influence of alkali-free accelerator. The majority of SUHPC blends show high flowability, with measurements exceeding 230 mm. The various ternary PC-CAC-C$ mixes exhibited superior flowability compared to the poured UHPC mix (U mix) at lower CS/CAC ratios. This improvement in flowability is attributed to the enhancing effect of CAC on the overall flow behavior [185]. With an increase in C$/CAC ratios, the flowability of SUHPC gradually decreased, which could be attributed to the high water absorption capacity of C$ [186].

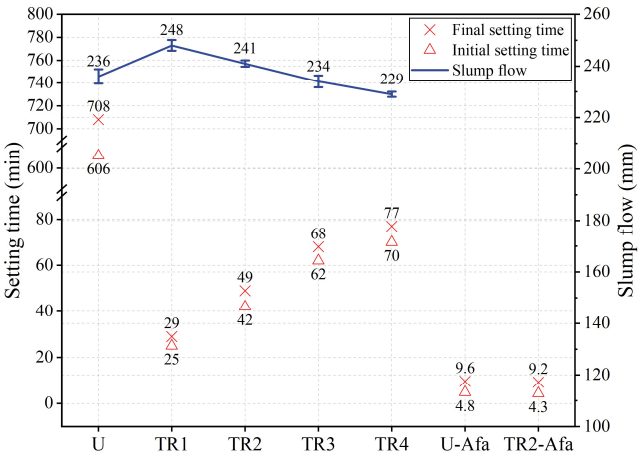


**Fig. 4.4.** Setting time and flow behavior of SUHPC.

Ternary PC-CAC-C$ systems in SUHPC demonstrated significantly shorter initial and final setting times compared to the poured UHPC (U mix). It is noteworthy that an increase in the C$/CAC ratio exhibited a significant positive correlation with both the initial and final setting times in the ternary system. As the CS/CAC ratio increased from 0.25 to 1, the final setting time extended from 29 to 77 min. Moreover, with the incorporation of 2 wt% alkali-free accelerator into both the ordinary UHPC (U mix) and the ternary system (TR2 mix), the initial setting time decreased to less than 5 minutes, and the final setting time was reduced to under 10 minutes in the U-Afa mix and TR2-Afa mix, respectively. This result meets the requirements for accelerator specified in the EN 934-5:2007

standard [187], which mandates that the initial setting time should be less than 10 minutes and the final setting time should be less than 60 minutes.

### 4.3.2 Hydration kinetics

From Fig. 4.5(a), it was observed that the onset of the acceleration period for the TR1 mix with a low C$/CAC ratio occurred at 40 hours, approximately 20 hours later than that of the control group (U mix). In this experiment, it was found that in the ternary system, a CAC content above 24 wt% (or a low C$/CAC ratio of 0.25) leads to a noticeable delay in the silicate hydration peak, as observed in the TR1 mix. This may be attributed to the high $Al^{3+}$ ions concentration and low calcium content in the pore solution of TR1, which hinder the nucleation and precipitation of C-S-H, thereby impeding the dissolution of tricalcium silicate (alite) [188, 189]. The C$/CAC ratio affects not only the heat flow but also the cumulative heat. Within the first hour, the ternary systems with C$/CAC ratios of 0.25, 0.5, 0.75, and 1.0 released cumulative heats of 19.8, 21.3, 31.7, and 36.8 J/g, respectively—significantly higher than the 9.3 J/g of the U mix. Nevertheless, the cumulative heat of the ternary systems at 80 hours was lower than that of the U mix.

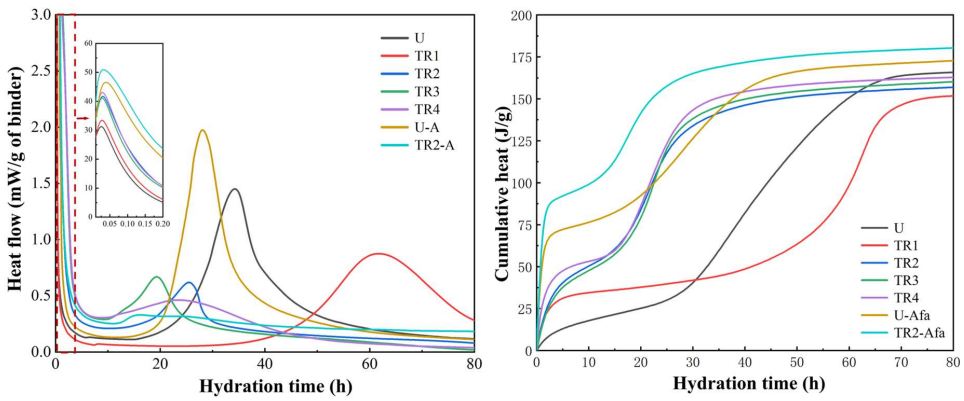


Fig. 4.5. Isothermal calorimetry of SUHPC pastes: (a) Heat-flow curve up to 80 h; (b) Cumulative heat-flow curve up to 80 h.

The incorporation of the accelerator increased the first peak values of U-A and TR2-A to 52.7 and 47.5 mW/g, respectively, as shown in Fig. 4.5(a), significantly higher than those of the other mixtures. The first heat release peak is typically associated with the initial dissolution of cement. However, in this study, a significant amount of heat was released upon the contact of the accelerator with the paste, as $Al(OH)_4^-$ and $SO_4^{2-}$ ions in the accelerator rapidly reacted to form Al-hydrates (ettringite, AFm, or $AH_3$). Therefore, the first heat release peak in this study is not only attributed to the heat of dissolution but also to the rapid formation of hydration products, as shown in the magnified view in Fig. 4.5(a). Additionally, the incorporation of the accelerator significantly advanced the silicate hydration peak.

For instance, the second hydration peak of TR2-Afa mix occurred 4.5 hours earlier than that of TR2 mix, while the second hydration peak of U-Afa mix was 3h ahead of that of the U mix. In addition, the inclusion of the accelerator in U-A mix and TR2-A mix increased the cumulative heat release at 80 hours by 4.4% and 12.7%, respectively, compared to U mix and TR2 mix without the accelerator.

Overall, these results indicate that the hydration kinetics of SUHPC can be effectively controlled by adjusting the C$/CAC ratio and incorporating the accelerator. Particularly, the optimal balance between hydration acceleration and cumulative heat release can be achieved at intermediate C$/CAC ratios (e.g., 0.5), while excessive CAC content (low C$/CAC ratio) delays silicate hydration. Moreover, the incorporation of the accelerator significantly promotes early-age hydration, highlighting its potential in improving early-age performance of SUHPC mixtures.

### 4.3.3 Rheological properties

Fig. 4.6 presents the effects of different C$/CAC ratios on the static yield stress, dynamic yield stress, and thixotropy of SUHPC mortar at various hydration times. With a consistent content of viscosity-enhancing additives, hydration is the main factor influencing changes in yield stress [190]. In this study, the C$/CAC ratio was a critical variable influencing the early-stage hydration kinetics, which further affected the rheological properties of SUHPC.

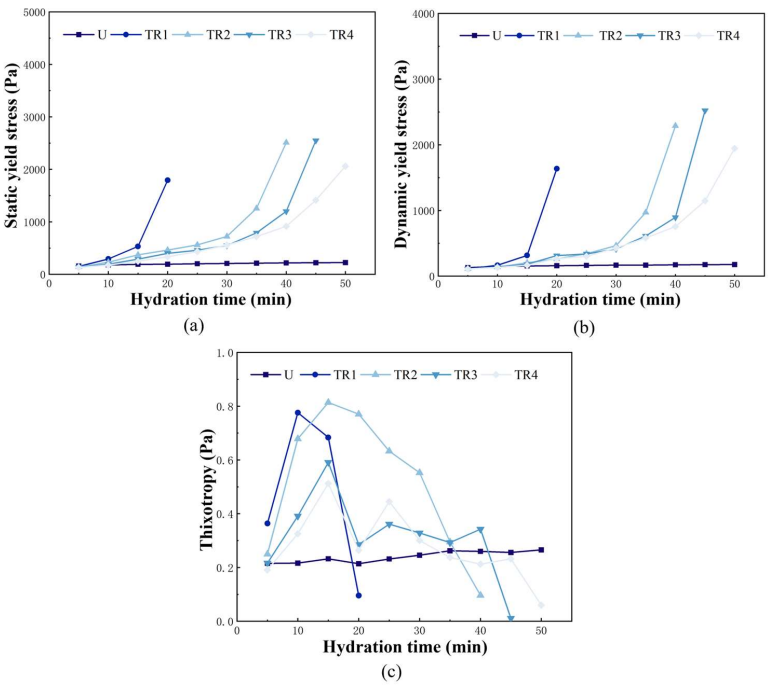


Fig. 4.6. Effect of different C$/CAC ratios and hydration time on: (a) Static yield stress; (b) Dynamic yield stress; (c) Thixotropy.

The static yield stress ($\tau_i$) and dynamic yield stress ($\tau_e$) exhibited a highly similar trend, as shown in Fig. 4.6(a) and (b). At a low C$/CAC ratio (TR1 mix), $\tau_i$ and $\tau_e$ initially increased gradually, followed by a substantial increase after 15 minutes, reaching 1792.3Pa and 1636.8Pa, respectively. And this abrupt increase accounted for 70.32% and 80.69% of the total hydration process, respectively. With the gradual increase of the C$/CAC ratio, the $\tau_i$ and $\tau_e$ of TR2, TR3, and TR4 mix exhibited a significant increase at 35, 40, and 45 minutes, respectively. A previous study [191] demonstrated that an increase in dynamic yield stress within a certain range enhances the pumpability of mortar. Therefore, compared to conventional UHPC (U mix), SUHPC with the ternary system indeed contributes to an early-stage increase in dynamic yield stress, thereby improving pumpability.

The concept of thixotropy entails the recovery capability of the flocculated structure once shear is removed [192]. In this study, the PC-CAC-C$ system accelerated the hydration rate and shortened the setting time of SUHPC. The rapid formation of AFt promoted the development of the flocculated structure in the SUHPC paste. In this study, it was observed that the thixotropy ($\lambda$) of all SUHPC mixtures initially increased and then decreased abruptly. This phenomenon can be attributed to the ternary system significantly accelerating the early hydration rate and shortening the setting time of SUHPC. The rapid formation of AFt facilitated the development of the flocculated structure in the paste, thereby enhancing thixotropy. As SUHPC approached setting, the structural deformation recovery ability irreversibly declined, leading to an abrupt decrease in the thixotropy value. In contrast, with a much lower early hydration rate than the ternary system, conventional UHPC (U mix) exhibited nearly unchanged rheological parameters within the first 0-50 minutes.

The thixotropy ($\lambda$) was observed to decrease rapidly with excessively high static yield stress ($\tau_i$) and dynamic yield stress ($\tau_e$), indicating the failure of thixotropic behavior and the loss of construction feasibility in shotcrete. Open time, which typically refers to the period from the completion of mixing until the loss of construction feasibility, is closely related to thixotropy [193]. The thixotropy ($\lambda$) of TR1 and TR2 mixes reached four times that of poured UHPC (U mix). A low C$/CAC ratio of 0.25 (TR1 mix) led to thixotropy failure at 15 minutes, significantly shortening the open time and making it insufficient for pumping and spraying. In contrast, TR2 mix, with a C$/CAC ratio of 0.5, maintained a higher thixotropy value within 35 minutes. This enhancement increased the cohesion of the SUHPC paste, theoretically providing superior pumpability and sprayability. It indicates that an appropriate C$/CAC ratio of 0.5 increases the cohesion of the SUHPC paste, thereby enhancing pumpability and sprayability. This effect was further validated by the field spray test described in Section 4.2.2, which confirmed that the TR2 mix attained a maximum thickness of 41 mm among the ternary mixtures without an accelerator.

### 4.3.4 Early-stage hydration products

#### 4.3.4.1 QXRD analysis at the early stage

##### 4.3.4.1.1 Intrinsic mechanism of different C$/CAC ratios in early hydration

To investigate the effect of varying C$/CAC ratios (0.25, 0.5, 0.75, and 1.0) in the ternary system on early hydration products, qualitative and quantitative XRD analyses were conducted. The XRD patterns in Fig. 4.7 show the phases detected in the qualitative analysis, including clinker phases from PC ($C_3S$, $C_2S$, $C_3A$, $C_4AF$, and calcite), CAC (CA, $C_{12}A_7$, and $C_2AS$), and gypsum (C$).

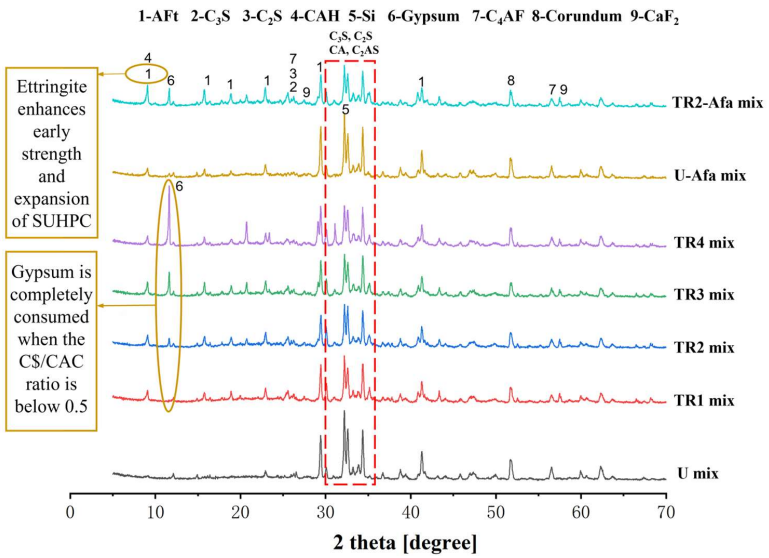


Fig. 4.7. XRD pattern of SUHPC samples at 1h.

Ettringite is the only crystalline hydration product formed in the early-stage hydration of the ternary system. The content is quantified by Rietveld refinement and presented in Table 4.4. As C$/CAC ratio increased from 0.25 to 1.0, the ettringite (AFt) content in TR1, TR2, TR3, and TR4 mixes was 10.2, 12.9, 9.3, and 8.2 wt%, respectively, initially increasing and then decreasing. It was observed that C$ was not detected in TR1 with a low C$/CAC ratio at 1 h. This indicates that the limited C$ had completely reacted with CA to form AFt, as given by:

$$3CA + 3C\overline{S}H_2 + 32H \rightarrow C_6A\overline{S}_3H_{32} + 2AH_3 \tag{4.3}$$

Meanwhile, the excessive CA underwent hydration to form calcium aluminate hydrates (CAH), such as $CAH_{10}$ and $C_2AH_8$, as given by:

$$3CA + 21H \rightarrow CAH_{10} + C_2AH_8 + AH_3 \tag{4.4}$$

At a high C$/CAC ratio of 1.0 (TR4 mix), the paste contained an excess of sulfate ions and a limited aluminum source, delaying the formation of ettringite. As a result, a low amount of ettringite (8.2 wt%) was detected at 1 h. This aligns with the findings in Section 4.3.1, which indicate an extended setting time for TR4 mix.

Table 4.4. Solid phase compositions from Rietveld refinements of UHPC and SUHPC at 1h (<d. l. = below detection limit).

| Phases/Mix | U (wt %) | TR1 (wt %) | TR2 (wt %) | TR3 (wt %) | TR4 (wt %) | U-Afa (wt %) | TR2-Afa (wt %) |
|---|---|---|---|---|---|---|---|
| $C_3S$ | 39.4±0.6 | 25.1±0.4 | 24.9±0.5 | 26.2±0.4 | 26.5±0.6 | 29.6±0.5 | 21.5±0.4 |
| $C_2S$ | 13.7±0.2 | 10.1±0.3 | 9.9±0.1 | 10.0±0.1 | 10.0±0.3 | 13.1±0.1 | 9.8±0.1 |
| CA | <d. l. | 2.1±0.3 | 2.1±0.4 | 2.3±0.3 | 2.0±0.4 | <d. l. | 2.4±0.3 |
| AFt | 1.9±0.5 | 10.2±0.4 | 12.9±0.5 | 9.3±0.5 | 8.2±0.6 | 6.9±0.5 | 16.2±0.4 |
| AFm | <d. l. | <d. l. | <d. l. | <d. l. | <d. l. | <d. l. | <d. l. |
| Gypsum | <d. l. | <d. l. | 1.8±0.2 | 3.2±0.2 | 5.1±0.7 | 2.4±0.2 | 3.7±0.2 |
| Anhydrite | <d. l. | 0.2±0.1 | 0.5±0.2 | 0.2±0.1 | 0.6±0.3 | 0.1±0.1 | 0.7±0.3 |
| Amorphous | 32.9±1.4 | 29.7±1.2 | 40.4±1.6 | 31.6±1.5 | 30.5±1.4 | 42.7±2.1 | 40.4±1.6 |

To investigate the effect of C$/CAC ratio on the hydration degree of primary clinker phases, Table 4.5 presents the hydration degree (α) of $C_3S$ (from PC) and CA (from CAC) in all ternary systems of SUHPC, as given by:

$$\alpha = 100\left(w_{phase-n}^{t_0} - w_{phase-n}^{t}\right) / w_{phase-n}^{t_0} \tag{4.5}$$

Where $w_{phase\text{-}n}^{t0}$ and $w_{phase\text{-}n}^{t}$ represent the phase contents prior to hydration ($t_0$) and at a specific time ($t$), respectively. Here, $t$ denotes 1 hour of hydration.

Table 4.5. Degrees of hydration of $C_3S$ and CA determined by QXRD analysis at 1h (wt%).

| Phases/Mix | U | TR1 | TR2 | TR3 | TR4 | U-Afa | TR2-Afa |
|---|---|---|---|---|---|---|---|
| $C_3S$ | 10.7 | 18.7 | 19.4 | 15.1 | 14.3 | 32.9 | 30.4 |
| CA | - | 42.9 | 46.6 | 40.2 | 39.6 | - | 50.5 |

Compared to the U mix, the early hydration degree of $C_3S$ in ternary systems with different C$/CAC ratios (0.25-1) increased significantly by 74.8%, 81.3%, 41.1%, and 33.6%, as shown in Table 4.5. The early hydration degrees of $C_3S$ and CA exhibited a consistent trend, initially increasing and then decreasing with the increase in CS/CAC ratio. Due to the rapid formation of AFt and heat release in the early hydration stage of the ternary system, the early hydration degrees of $C_3S$ and CA were potentially further enhanced by the elevated temperature [194, 195]. Among the ternary system mixtures, TR2 mix exhibited the highest early hydration product, AFt, reaching 12.9 wt%, while the hydration degree of $C_3S$ also peaked at 18.7 wt%. In summary, the early-stage hydration kinetics and hydration degree in the ternary SUHPC system are significantly influenced by the C$/CAC ratio. The optimal ratio (0.5, TR2 mix) leads to the highest formation of early hydration products (ettringite) and maximizes the early hydration degree of clinker phases, demonstrating the importance of properly balancing sulfate and aluminate sources to enhance early-stage performance.

#### 4.3.4.1.2. Synergistic mechanism of alkali-free accelerator and PC-CAC-C$ system in early hydration

In this chapter, TR2-Afa mix was developed by incorporating the 2 wt% alkali-free accelerator into the TR2 mix to investigate the synergistic mechanism of the alkali-free accelerator and the PC-CAC-C$ system on early-stage hydration kinetics of SUHPC. And U-Afa mix was designed by incorporating the 2 wt% alkali-free accelerator into the U mix to investigate the effect of alkali-free accelerator on Portland cement system of SUHPC. Based on the QXRD results in Table 4.4, the AFt content in U-Afa mix and TR2-Afa mix at 1 hour increased by 263% and 25.6%, respectively, compared to the U mix and TR2 mix. And the early hydration degree of $C_3S$ increased by 207.5% and 56.7%, respectively, indicating that the accelerator can significantly promote silicate hydration at the early stage. This is due to the addition of the alkali-free accelerator, which introduces a large amount of $Al(OH)_4^-$ and $SO_4^{2-}$ ions. These ions rapidly react with $Ca^{2+}$ ions dissolved from gypsum and Portland cement upon initial contact, forming a substantial amount of AFt, as given by:

$$2[Al(OH)_4]^- + 6Ca^{2+} + 4OH^- + 3SO_4^{2-} + 26H \rightarrow C_6A\bar{S}_3H_{32} \quad (4.6)$$

In the U-Afa mix, $Ca^{2+}$ in the paste originates from the dissolution and hydration of $C_3S$. Therefore, the substantial consumption of $Ca^{2+}$ ions further enhances the early hydration degree of $C_3S$ in the cement. In the ternary TR2 mix, $Ca^{2+}$ ions in the paste originates from the dissolution of gypsum, CA, and $C_3S$. Therefore, the alkali-free accelerator enhances the early hydration degree of both $C_3S$ (from PC) and CA (from CAC) in the ternary PC-CAC-C$ system.

In addition, diffraction peaks of $CaF_2$ were observed, as shown in Fig. 4.7. This is attributed to the presence of magnesium fluosilicate ($MgSiF_6$) in the alkali-free accelerator [196]. Magnesium fluosilicate dissolves and releases fluoride ions ($F^-$), which react with $Ca^{2+}$ ions to form $CaF_2$ precipitate, as given by:

$$MgSiF_6 \rightarrow Mg^{2+} + SiF_6^{2-} \quad (4.7)$$

$$SiF_6^{2-} + 4H_2O \rightarrow Si(OH)_4 + 6F^- + 4H^+ \quad (4.8)$$

$$Ca^{2+}(aq) + 2F^-(aq) \rightarrow CaF_2(s) \quad (4.9)$$

However, considering the low dosage (2 wt%) of the accelerator used in SUHPC and the limited content of magnesium fluosilicate contained therein, the presence of $CaF_2$, as observed in XRD pattern, confirms its contribution to the dissolution and hydration of $C_3S$ (from PC), but this effect is not dominant. Instead, the primary synergistic mechanism of the alkali-free accelerator in the PC-CAC-C$ system at early hydration is plausibly associated with accelerating the CA hydration (from CAC) and rapidly consuming gypsum (C$), thereby significantly influencing the hydration kinetics and early-age properties of the SUHPC.

These findings suggest that the alkali-free accelerator significantly enhances the early-stage hydration kinetics of SUHPC primarily by accelerating the hydration of CA (from CAC) and rapidly consuming gypsum (C$), thus facilitating the rapid formation of ettringite. The synergistic effect between the accelerator and the PC-CAC-C$ system substantially improves the early hydration degree of CA, indirectly influencing the hydration of $C_3S$ through enhanced aluminate reactions and rapid sulfate consumption. Although $CaF_2$ precipitates formed due to magnesium fluosilicate theoretically could contribute to $C_3S$ hydration, this mechanism plays only a minor role due to the low dosage and limited fluosilicate content. Hence, the primary synergy arises from accelerated aluminate hydration and gypsum consumption, providing a fundamental basis for optimizing the early strength development of SUHPC.

#### 4.3.4.2 TG analysis at the early stage

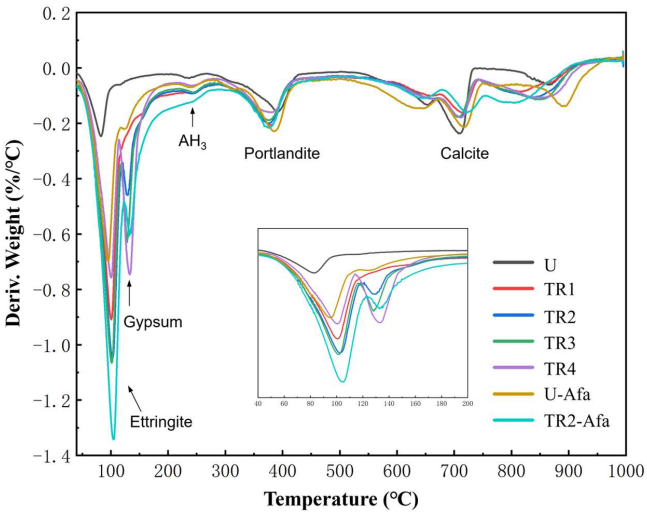


Fig. 4.8. Differential thermogravimetric curves of SUHPC mixes at 1h.

Differential thermogravimetric (DTG) peaks corresponding to C-S-H, portlandite, gypsum, $AH_3$, AFm, and calcite were identified, as presented in Fig. 4.8. The first DTG peak (between 25 and 130 °C) is mainly attributed to dehydration of C-S-H gel and ettringite crystal [197, 198]. Gypsum typically dehydrates between 100 °C and 150 °C, as indicated by the second peak. The gypsum peak in TR4 mix is significantly pronounced, whereas there is almost no detectable gypsum peak in TR1 mix, which aligns with the QXRD results. A small peak around 250 °C was observed in the DTG curves, which is associated with the decomposition of $AH_3$ [199]. However, no corresponding diffraction peak of $AH_3$ was detected in the QXRD analysis. This indicates that $AH_3$ formed within the early hydration stage (1 h) in a limited amount with low crystallinity. In addition, DTG peaks of CH and calcite were observed at 400 °C and 600-750 °C, respectively. Overall, the DTG results are consistent with the QXRD findings, confirming that increasing the C$/CAC ratio ensures a more sufficient

sulfate source, while at lower ratios (e.g., TR1 mix), gypsum is rapidly consumed during early hydration, accompanied by the formation of a small amount of poorly crystalline $AH_3$.

### 4.3.5 Late-stage hydration products

#### 4.3.5.1 QXRD analysis at the late stage

##### 4.3.5.1.1 Intrinsic mechanism of different C$/CAC ratios in late hydration

The XRD patterns for SUHPC at 28d are shown in Fig. 4.9. As for the quantitative QXRD analysis, the solid phase compositions and the hydration degrees from Rietveld refinement are presented in Table 4.6 and Table 4.7, respectively.

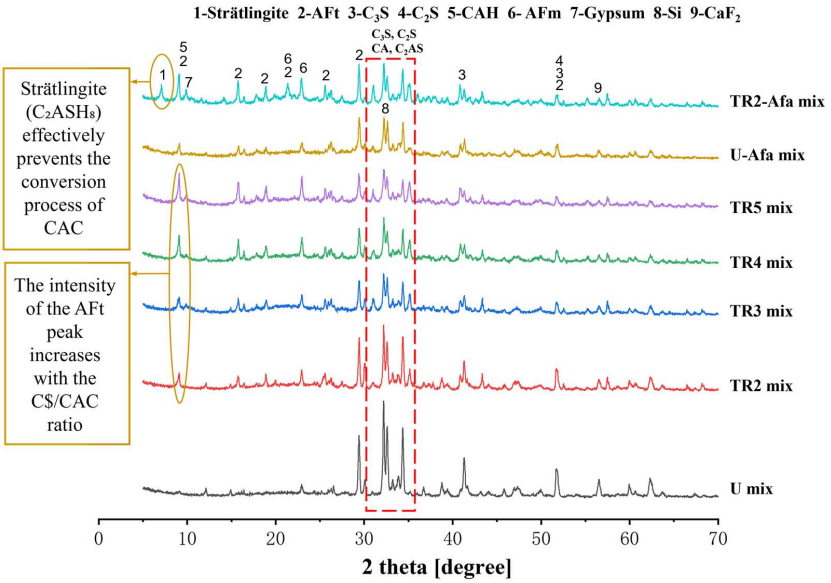


Fig. 4.9. XRD pattern of SUHPC samples at 28d.

Table 4.6. Phase quantification by QXRD of SUHPC at 28d (<d. l. = below detection limit) (wt%).

| Phases/Mix | U | TR1 | TR2 | TR3 | TR4 | U-Afa | TR2-Afa |
|---|---|---|---|---|---|---|---|
| $C_3S$ | 7.3±0.3 | 8.9±0.3 | 5.6±0.3 | 6.7±0.2 | 8.5±0.3 | 6.7±0.2 | 6.3±0.4 |
| $C_2S$ | 3.9±0.2 | 4.0±0.1 | 3.2±0.1 | 3.7±0.1 | 3.8±0.1 | 3.6±0.2 | 3.3±0.1 |
| CA | <d. l. | 0.8±0.1 | 0.9±0.2 | 0.8±0.2 | 0.8±0.2 | <d. l. | 0.9±0.2 |
| AFt | 1.7±0.3 | 4.2±0.3 | 12.8±0.4 | 12.9±0.4 | 14.0±0.4 | 5.7±0.3 | 15.8±0.6 |
| AFm | 0.3±0.1 | 3.3±0.2 | 0.5±0.4 | 0.3±0.2 | 0.3±0.3 | 1.0±0.1 | 2.1±0.1 |
| Gypsum | <d. l. | <d. l. | 0.4±0.2 | 0.6±0.1 | 1.0±0.2 | 0.9±0.1 | 1.1±0.2 |
| Anhydrite | <d. l. | <d. l. | 0.2±0.1 | 0.2±0.1 | 0.3±0.1 | 0.3±0.2 | 0.5±0.4 |
| Strätlingite | <d. l. | <d. l. | <d. l. | <d. l. | <d. l. | <d. l. | 0.5±0.1 |
| Amorphous | 59.2±1.1 | 48.7±0.9 | 56.9±1.2 | 55.1±1.5 | 51.8±1.3 | 59.8±1.0 | 56.3±1.1 |

Table 4.7. Degrees of hydration of $C_3S$ and CA determined by Rietveld XRD analysis at 28d (wt%).

| Phases/Mix | U | TR1 | TR2 | TR3 | TR4 | U-Afa | TR2-Afa |
|---|---|---|---|---|---|---|---|
| $C_3S$ | 81.3 | 71.1 | 80.9 | 78.2 | 72.6 | 82.5 | 79.7 |
| CA | - | 79.9 | 87.2 | 93.1 | 95.0 | - | 82.9 |

As the C$/CAC ratio decreases to 0.25 (TR1 mix), the hydration degree of $C_3S$ remains low even at 28 days, reaching 71.1 wt%. This is attributed to the excessive CAC, which increases the aluminate ion concentration in the pore solution and significantly retards the hydration of $C_3S$ [188, 189]. The underlying reason is that the aluminate ions in the pore solution promote the formation of C-(A)-S-H, which has a lower nucleation efficiency for C-S-H than pure C-S-H, thereby delaying the hydration kinetics of $C_3S$ [199]. As shown in Fig. 4.9, it was also observed that diffraction peaks of calcium aluminate hydrate (CAH), including $CAH_{10}$, $C_2AH_8$, and $C_3AH_6$. This is because CA reacts with the limited amount of C$ in the early stage and fully consumes it, leaving excessive CA in TR1 mix. The remaining CA then hydrates to form $CAH_{10}$ and $C_2AH_8$. In the later stages of hydration, $CAH_{10}$ and $C_2AH_8$ transform into the more stable $C_3AH_6$, as follows:

$$3CAH_{10} \rightarrow C_3AH_6 + 2AH_3 + 18H \tag{4.10}$$

$$3C_2AH_8 \rightarrow 2C_3AH_6 + AH_3 + 9H \tag{4.11}$$

This phenomenon is known as the CAC conversion process, which is accompanied by a loss of pore structure density and an increase in porosity at later stages [200]. Additionally, a high concentration of $Al^{3+}$ ions promotes the gradual transformation of AFt into the more stable AFm or TAH, , as follows:

$$C_6A\bar{S}_3H_{32} + 4[Al(OH)_4]^- + 6Ca^{2+} + 8OH^- \rightarrow 3C_4A\bar{S}H_{12} \tag{4.12}$$

As the C$/CAC ratio increases to 0.75 or 1 (TR3 and TR4 mixes), there are still some gypsum and anhydrite residues at 28 days, indicating the persistent supersaturation of sulfate ions ($SO_4^{2-}$) in the pore solution in the TR3 and TR4 mixes. As shown in Table 4.6, the AFt content in TR3 and TR4 mixes reached 12.9 wt% and 14.0 wt%, respectively, representing a significant increase of 38.7% and 50.5% compared to the early-stage AFt content. This is because the supersaturated sulfate ions ($SO_4^{2-}$) in the solution continuously react with aluminum ($Al^{3+}$) and calcium ($Ca^{2+}$) ions in the mid-to-late stages, leading to the formation of ettringite (AFt). It is also known as Delayed Ettringite Formation (DEF) [201].

At the later stage of hydration, the hydration degree of CA also significantly increases with the formation of DEF. Specifically, in TR4 mix, the late-stage hydration degree of CA reaches 95.0 wt%. This may be attributed to the fact that the formation of DEF requires calcium ($Ca^{2+}$) ions, which in turn promotes the dissolution and further hydration of CA. In addition, the AFm content decreases from an average of 3.3 wt% at the early stage to 0.3 wt% at the later stage of hydration as the C$/CAC

ratio increases. This may be due to the high sulfate ($SO_4^{2-}$) ion concentration, which induces the transformation of AFm and TAH ($C_4AH_{13}$) into AFt [35]. Among all mixtures in the PC-CAC-C$ system, TR2 mix with a C$/CAC ratio of 0.5 shows the highest AFt content and greatest extent of $C_3S$ hydration at later stages, suggesting that this ratio effectively promotes hydration.

These results indicate that varying the C$/CAC ratio significantly influences the hydration kinetics and phase evolution of the PC-CAC-C$ system of SUHPC. An intermediate ratio (0.5, TR2 mix) achieves optimal hydration behavior by maximizing AFt formation and hydration of $C_3S$, while excessively low or high C$/CAC ratios lead to delayed hydration, phase instability, negatively affecting the long-term performance of SUHPC.

Compared with the intrinsic hydration mechanism at the early stage (1 h) discussed in Section 4.3.4.1.1, the ternary system exhibited markedly different intrinsic hydration characteristics at the late stage (28 d). During the early stage, an appropriate C$/CAC ratio (e.g., 0.5 in the TR2 mix) facilitated rapid AFt formation, significantly enhancing the hydration degrees of $C_3S$ and CA. In contrast, an excessively high ratio (e.g., 1.0 in the TR4 mix) delayed AFt formation due to limited aluminum availability. At the later stage, however, a high C$/CAC ratio promoted continuous DEF formation, causing late-age expansion, microcracking, and subsequent strength loss, whereas an excessively low ratio (e.g., 0.25 in the TR1 mix) led to pronounced CAC conversion, further impairing the long-term stability. These distinct intrinsic mechanisms highlight the importance of C$/CAC ratio control throughout the hydration process. A moderate ratio of 0.5 (TR2 mix) is considered optimal, as it promotes rapid AFt formation in the early stage and effectively mitigates DEF formation in the later stage, thereby ensuring superior overall performance of SUHPC.

#### 4.3.5.1.2 Synergistic mechanism of alkali-free accelerator and PC-CAC-C$ system in late hydration

A diffraction peak at 8.15° was identified in TR2-Afa mix at 28 days as shown in Fig. 4.9. It indicates the presence of strätlingite ($C_2ASH_8$), while no such peak was detected in any other mixtures. According to the QXRD results (Table 4.7), strätlingite was detected at 0.5 wt% in the TR2-Afa mix. Previous studies have suggested that the hydration of the silicate phase in PC may facilitate the formation of strätlingite [202]. Strätlingite formation is related to the hydration of gehlenite in CAC cement, as given by:

$$C_2AS + 8H \rightarrow C_2ASH_8 \tag{4.13}$$

However, with the same PC and CAC content in TR2-Afa and TR2 mixes, the diffraction peak of strätlingite appears only in TR2-Afa mix. Therefore, in this study, the silicate phase is not the primary factor for strätlingite formation. Some studies suggested that sulfate ions could accelerate strätlingite formation [203-205]. As a result, this study infers that the incorporation of $Al_2(SO_4)_3$ based alkali-

free accelerator introduced a high concentration of sulfate ions, which promoted the formation and crystallization of strätlingite in the TR2-Afa mix. The stable hydrate strätlingite ($C_2ASH_8$) has been found to inhibit the conversion process of CAC [206], thereby mitigating the degradation of strength and durability in ternary PC-CAC-C$ system of SUHPC.

In addition, the accelerator has a slight enhancing effect on the late-stage hydration degree of $C_3S$ in the Portland cement system (U-Afa mix), increasing it by 1.5% compared to U mix. However, in ternary PC-CAC-C$ system, the incorporation of accelerator decreased the late-stage hydration degrees of $C_3S$ and CA by 1.5% and 4.9%, respectively, compared to TR2 mix without the accelerator. This may be due to the dissolution of CAC in the ternary system, leading to a high concentration of aluminum ions, which is known to delay and inhibit silicate hydration.

Compared to the early-stage synergistic mechanism discussed in Section 4.3.4.1.2, the alkali-free accelerator exhibited notably different effects at the late stage. At the early hydration stage (1 h), the accelerator substantially promoted AFt formation and accelerated hydration of silicate and aluminate phases. However, at the late stage (28 d), although the accelerator continued to facilitate AFt formation, it induced additional effects such as the formation of strätlingite ($C_2ASH_8$), which effectively inhibited CAC conversion and improved the long-term stability of the ternary system. In contrast to the early stage, the presence of a high concentration of aluminum ions due to CAC dissolution in the late stage negatively affected the hydration of silicate phases, slightly reducing the hydration degrees of $C_3S$ and CA. Thus, the influence of the alkali-free accelerator evolves from primarily accelerating early hydration and strength development to playing a more complex role in microstructure refinement and durability enhancement in the later stage.

In conclusion, the results demonstrate a distinct synergistic effect between the alkali-free accelerator and the ternary PC-CAC-C$ system at different hydration stages. While the accelerator primarily enhances early hydration through rapid AFt formation and accelerated silicate hydration, its role at later hydration stages shifts toward promoting stable hydration products such as strätlingite. This, in turn, mitigates CAC conversion and may enhance the long-term durability of SUHPC.

#### 4.3.5.2 TG analysis at the late stage

Based on the DTG curves of SUHPC paste (Fig. 4.10), obvious peaks of ettringite in TR4 and TR2-Afa mixes were observed, which aligns with the QXRD findings (Fig. 4.9). A weak peak was observed in TR2-Afa mix between 160 and 200 °C, attributed to the decomposition of strätlingite and a small amount of AFm [203], which is consistent with the QXRD results. Distinct peaks were found at 160 °C in TR1 and TR2 mixes, corresponding to AFm decomposition. This is due to the lack of sulfate source at late-stage hydration, promoting the transformation of AFt into AFm. A weak peak was observed at 300-330 °C, which is associated with the decomposition of $C_3AH_6$ [207]. Additionally, a distinct decomposition peak of CH at 430 °C was observed exclusively in the U mix,

whereas it was nearly undetectable in all ternary systems and accelerator-containing mixes. This phenomenon can be attributed to the continued consumption of CH by hydration products in the ternary system (e.g., $CAH_{10}$, $C_2AH_8$, and $C_3AH_6$) to form AFt and AFm. And the addition of the accelerator introduces a a substantial amount of $Al(OH)_4^-$, which directly reacts with CH and sulfate ions to form AFt, resulting in substantial consumption of CH. In summary, TG results corroborates the QXRD findings, highlighting the impact of the alkali-free accelerator and C$/CAC ratio on phase evolution in late-stage SUHPC hydration.

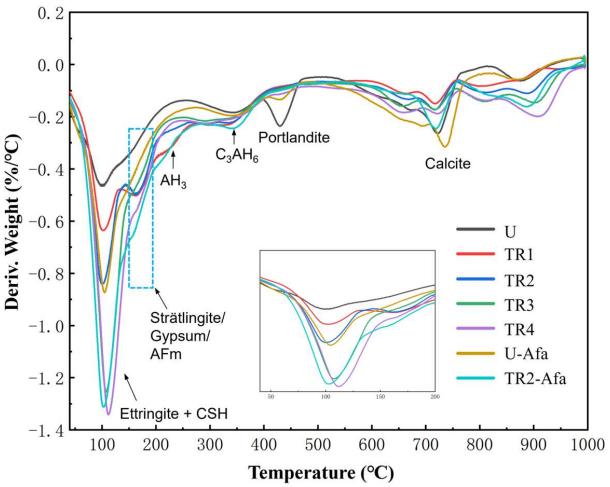


Fig. 4.10. Differential thermogravimetric curves of SUHPC mixes at 28d.

### 4.3.6 Microstructure by SEM analysis

The morphology of SUHPC pastes under the influence of the ternary system and the accelerator at early and later stages is shown in Fig. 4.11. At the early hydration stage (1 h), the TR2 paste of the ternary system had already developed a dense and solid microstructure, with a significant formation of AFt observed in Fig. 4.11(a-b). Unhydrated $C_3S$ particles and spherical FAC particles were also present. Compared to TR2, TR2-Afa with the incorporation of alkaline-free accelerator, showed a higher amount of needle-shaped AFt forming a network structure, as shown in Fig. 4.11(c-d). This may explain the higher early strength of TR2-Afa discussed in Section 4.3.8.

At the later hydration stage (28 d), the coexistence of C-S-H gel and AFt was observed in both the TR2 paste and TR2-Afa paste, along with minor quantities of $AH_3$ gel and CH, as shown in Fig. 4.11 (e-h). AFt acts as nucleation sites, filling the gaps and inducing the formation of C-S-H gel to further fill voids and enhance the hardened structure of SUHPC. Additionally, as shown in Fig. 4.11(i-j), denser AFt was observed in the microstructure of the TR4 paste with a high C$/CAC ratio of 1. This phenomenon is known as delayed ettringite formation (DEF) because it forms continuously during the later stages of hydration, leading to volume expansion and potential development of microcracks.

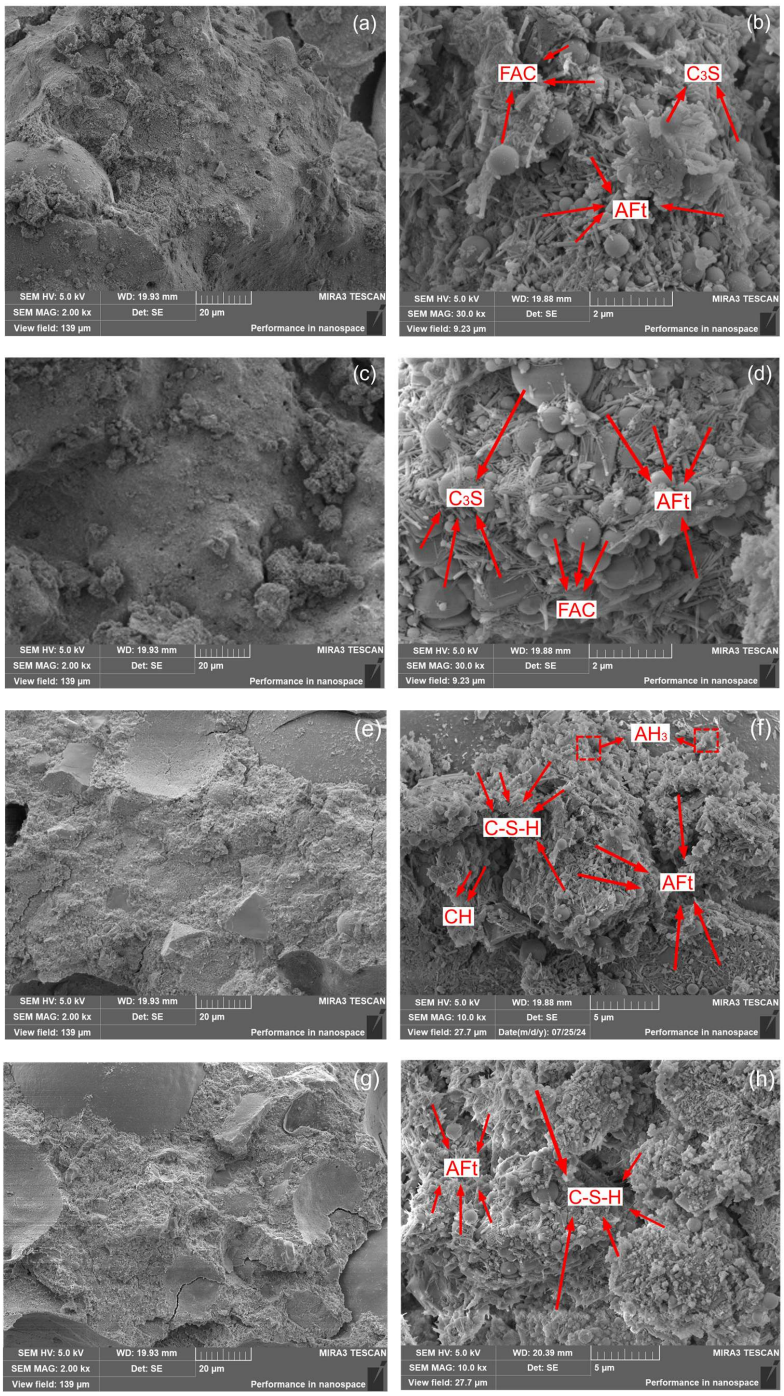


Fig. 4.11. Typical microstructure of SUHPC pastes at various curing ages. (a and b) Micrographs of TR2 at 1d; (c and d) Micrographs of TR2-Afa at 1d; (e and f) Micrographs of TR2 at 28d; (g and h) Micrographs of TR4 at 28d;

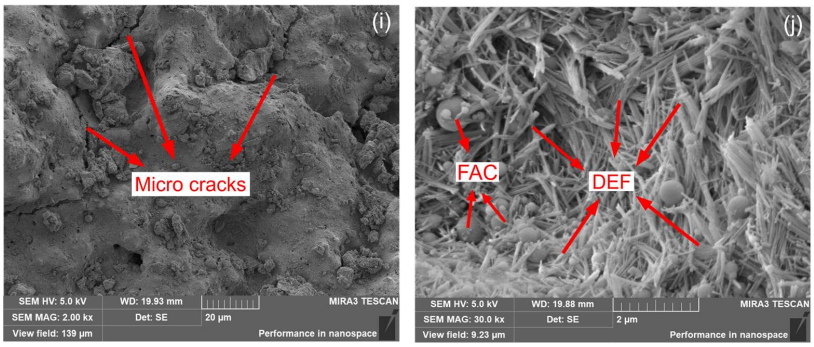


Fig. 4.11 (continued). (i and j) Micrographs of TR4 at 28d.

### 4.3.7 Dimensional change

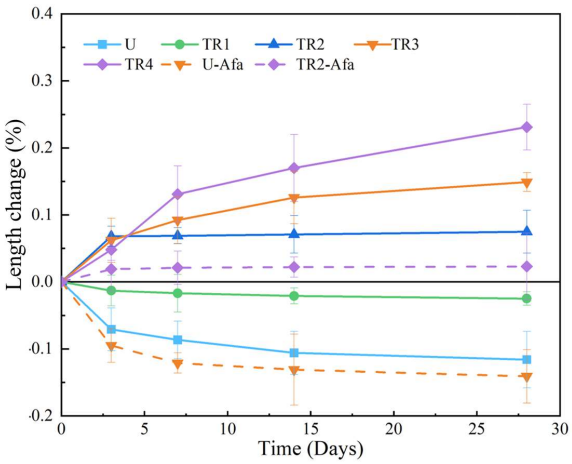


Fig. 4.12. Dimensional change of SUHPC and poured UHPC.

The ordinary UHPC (U mix) exhibited dimensional shrinkage, reaching -0.116% at 28 days as illustrated in Fig. 4.12. The incorporation of C$ and CAC into the ternary system (PC-CAC-C$) can significantly reduce shrinkage and even induce micro expansion, which provided shrinkage compensation for SUHPC. It was observed that the C$/CAC ratio influenced the dimensional change of SUHPC. Compared to U mix, a low C$/CAC ratio of 0.25 reduced the length shrinkage rate from 0.116% to 0.025% in TR1 mix. As the C$/CAC ratio increased from 0.25 to 1, the ternary mixtures in SUHPC gradually shifted from dimensional shrinkage to dimensional expansion. A higher C$/CAC ratio greater than 0.5 (TR3 and TR4 mixes) resulted in more pronounced and sustained expansion at later stages, with the maximum expansions at 28 days reaching 0.149% and 0.231%, respectively, relative to the initial specimen length. This is due to the continuous formation of delayed ettringite formation (DEF), which is consistent with the QXRD results. Notably, TR2 mix

(C$/CAC=0.5) exhibited characteristics of micro expansion, making it a promising candidate for use as a repair material.

Based on the results of Fig. 4.12, it is observed that the effects of alkaline-free accelerator vary significantly across different cement systems. In neat PC system, alkaline-free accelerator intensified the shrinkage of SUHPC. The dimensional shrinkage rate at 28d of U-Afa mix reached 0.141%, a 21.6% increase compared to U mix without accelerator. This may be due to the rapid setting it induced, which increased the porosity and defect in the concrete matrix, making it more susceptible to drying shrinkage [28]. However, in ternary system (PC/CAC/C$), alkaline-free accelerator promoted micro expansion in the ternary system, reaching 0.019% at 3 d in TR2-Afa mix. This is attributed to the rapid and substantial formation of AFt in the early hydration stages in the ternary system, which induces micro expansion. This expansion neutralizes the shrinkage caused by the accelerator, ensuring the volume stability of the TR2-Afa mix as a rapid-setting, micro-expanding SUHPC.

### 4.3.8 Strength development

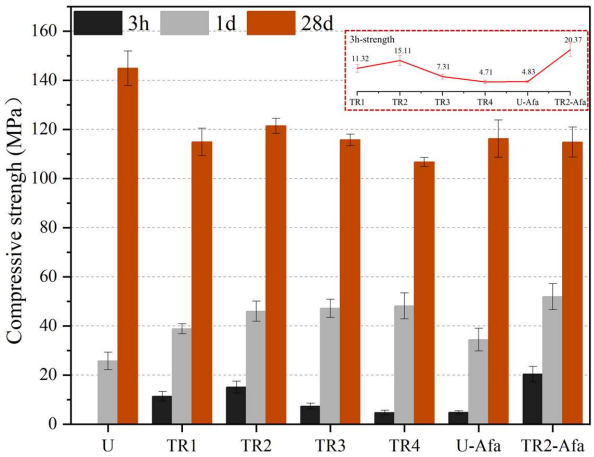


Fig. 4.13. Compressive strengths of SUHPC and poured UHPC.

Fig. 4.13 presents the compressive strength development of the ternary system (PC-CAC-C$) in SUHPC under various C$/CAC ratios and with the addition of alkaline-free accelerator, measured at 3 h, 1 d, and 28 d. At the early hydration stage (3 h), the early strength of the ternary mixtures exhibited a trend of initially increasing and then decreasing with the increase in the C$/CAC ratio. The maximum early strength at 3h was achieved at a C$/CAC ratio of 0.5 in TR2 mix, reaching 15.11 MPa. Some studies [208, 209] have suggested that early strength is highly correlated with the formation of AFt. This further validates the QXRD results, indicating that the ternary system TR2 generated the highest amount of AFt during the early hydration stage.

At 1 d, the strengths of TR3 and TR4 increased significantly, reaching 45.17 MPa and 48.14 MPa, respectively, surpassing that of TR2. This is attributed to the higher C$/CAC ratio, which provided an increased supply of sulfate ions, promoting the continuous formation of AFt. However, at 28 d, the strengths of TR3 and TR4 were both lower than that of TR2, measuring 115.7 MPa and 106.7 MPa, respectively. Based on the result of dimensional change and QXRD, this can be attributed to the excessive C$/CAC ratio, which promoted an increased formation of DEF. Therefore, maintaining the C$/CAC ratio at 0.5 or lower is recommended to mitigate DEF formation, reduce late-age expansion and cracking, and enhance the long-term strength stability of SUHPC.

The incorporation of alkaline-free accelerator significantly improves the early strength development of both the ordinary UHPC (U mix) and the ternary mixtures (PC-CAC-C$) in SUHPC, while causing a decrease in the 28d compressive strength. Specifically, the incorporation of accelerator increased the 3h strength by 21.8% for TR2-Afa compared to the TR2 mix without the accelerator, reaching 20.37 MPa. This can be attributed to the higher availability of $Ca^{2+}$ in the ternary system, which readily react with the $Al^{3+}$ and $SO_4^{2-}$ provided by the accelerator to accelerate the formation of AFt. This observation is consistent with the QXRD results, which show that TR2-Afa mix had a significantly higher AFt content in the early stage of hydration compared to other mixes. However, the accelerator notably reduced the strength at 28d, with U-Afa and TR2-Afa mixes showing reductions of 19.81% and 5.44%, respectively, compared to U and TR2 mixes. This can be explained by the formation of macro pores induced by rapid setting promoted by the accelerator [196]. Additionally, the strength reduction could be attributed to the partial transformation of AFt into AFm phases during the later stages of hydration.

## 4.4 Conclusions

This chapter systematically investigated the effects of a ternary binder system and an alkali-free accelerator on the rheology, shrinkage, early-age strength, hydration kinetics of sprayed UHPC. The main conclusions were summarized as follows:

- The optimized formulation of the PC-CAC-C$ ternary system of SUHPC can significantly reduce the initial setting time to 25 min. And early strength at 3h reached 15.11 MPa at a C$/CAC ratio of 0.5. Incorporating an alkali-free accelerator further shortened the initial setting time to 4.3 min and increased 3 h strength to 20.37 MPa, enabling rapid setting and high early-strength repair.
- Compared to conventional PC system, the PC-CAC-C$ system enhances the rheology of SUHPC rheology by increasing dynamic yield stress and thixotropy, thereby improving pumpability and

sprayability. The C$/CAC ratio governs in the rheological properties of this ternary system. At the optimal ratio of 0.5, a thixotropy reached four times that of poured UHPC.

- The mechanism underlying the influence of different C$/CAC ratios on the hydration kinetics of SUHPC has been elucidated at both early and late stages. At the early stage, the C$/CAC ratio of 0.5 promotes optimal ettringite formation and maximizes the hydration of $C_3S$ and CA. At the late stage, excessive CAC inhibits C-S-H formation, while high sulfate concentrations induce delayed ettringite formation. The C$/CAC ratio of 0.5 achieves a balance between sulfate and aluminate sources, optimizing hydration kinetics in SUHPC.

- The synergistic mechanism of the alkali-free accelerator and the PC-CAC-C$ system on the hydration kinetics of SUHPC has been systematically analyzed. At early ages, the accelerator significantly enhances ettringite formation and accelerates the hydration of $C_3S$ and CA by introducing $Al(OH)_4^-$ and $SO_4^{2-}$ ions. At later ages, the accelerator promotes strätlingite formation, mitigating CAC conversion and enhancing durability of ternary system in SUHPC. However, an excessive concentration of aluminum ions may hinder silicate hydration in the ternary system.

- The incorporation of C$ and CAC effectively mitigates shrinkage and induces micro-expansion in SUHPC. A C$/CAC ratio above 0.5 promotes sustained expansion due to delayed ettringite formation, potentially causing induce microcracks and reduce long-term strength. While the alkali-free accelerator intensifies the shrinkage, the micro-expansion in the ternary system offset this effect. A C$/CAC ratio of 0.5 achieves the optimal balance between shrinkage compensation and volume stability.

This chapter demonstrates that a PC–CAC–C$ ternary binder in SUHPC attains 15 MPa compressive strength at 3 h while providing slight expansion to mitigate autogenous shrinkage.Further incorporation of an alkali-free accelerator can raise the 3-hour strength to approximately 20 MPa, but at the cost of a reduction in 28-day strength due to accelerator-induced pore defects. Therefore, the application of the accelerator should be determined by project requirements. When a set time of under 10 minutes is required for emergency repairs, the “ternary system + accelerator” approach is preferred. For applications prioritizing higher later-age strength and durability, the ternary system alone may be more suitable.

# Chapter 5 Performance of SUHPC with different cementitious materials and accelerators at later age


## *Abstract*

The combination of various cementitious materials can effectively mitigate early-age cracking and flowability issues in concrete that arise from the use of accelerators during the spraying process of sprayed ultra-high-performance concrete (SUHPC). Flexural and compressive strengths serve as critical indicators for evaluating the mechanical performance of SUHPC. This study investigates the effects of various types of cementitious materials, including Portland cement, calcium aluminate cement (CAC), and gypsum ($CaSO_4 \cdot 2H_2O$, abbreviated as C$), as well as alkali-free accelerators, on the flexural and compressive properties of SUHPC. The results show that partial replacement of Portland cement with CAC alone leads to a significant reduction in flexural and compressive strength, with the greatest decrease observed at a CAC dosage of 30%. In contrast, in a ternary binder system incorporating both CAC and C$, increasing the C$ content from 0 to 15 wt% enhances the flexural and compressive strengths, reaching maximum values of 21.5 MPa and 123.7 MPa, respectively. The incorporation of CAC negatively impacts the flexural and compressive properties of SUHPC. However, the incorporation of C$ in the ternary binder system effectively offsets the adverse effects of CAC, leading to improvements in toughness and energy absorption capacity. While alkali-free accelerators enhance early-age strength, such admixtures tend to impair long-term mechanical performance. This degradation can be mitigated through the strategic combination of multiple cementitious components.



This chapter is partially published elsewhere:

J. He, Q.L. Yu, Z.Y. Tang, H.Y. Wang, Z.R. Chen, and B.Y. Wei. Effects of different cementitious materials and accelerators on the flexural and compressive behaviors of SUHPC. Case Studies in Construction Materials, 23 (2025), e04913.

## 5.1 Introduction

With the increasing demands in bridge, tunnel, underground engineering, and water conservancy and hydropower projects, shotcrete has emerged as a crucial concrete material due to its advantages such as rapid setting, fast construction, and excellent adhesion [210, 211]. However, the growing number of engineering projects requiring high strength or adaptability to harsh environments has imposed higher requirements on the mechanical properties and durability of shotcrete. Therefore, exploring the development of shotcrete towards higher strength and durability is of significant importance.

Cui et al. [25] investigated the influence of three different viscosity-enhancing agents on the rheological properties of SUHPC. Al Ameen et al. [212] explored the effects of high glass fiber content on the mechanical, permeability, and durability performance of the developed SUHPC. Additionally, Chen et al. [163] proposed molecular dynamics modeling to analyze the viscosity regulation mechanism of Hydroxypropyl Methylcellulose (HPMC) in SUHPC. In practical shotcrete applications, in addition to mixture design optimization, accelerators are typically added at the nozzle during construction. These accelerators can significantly reduce the setting time of SUHPC and effectively enhance its early-age strength [213]. However, it is important to note that the use of accelerators also introduces certain drawbacks that require improvement: (1) The incorporation of accelerators increases air entrainment in the concrete, leading to a reduction in strength [35, 213]; (2) Accelerators can exacerbate the long-term shrinkage of concrete [213]. These issues highlight the need for further research and optimization to address the limitations associated with the use of accelerators in SUHPC. To address these limitations, researchers have explored the incorporation of alternative cementitious materials, such as calcium aluminate cement (CAC) and calcium sulfate (C$), to improve early hydration and strength development in SUHPC. In addition, the hydration products formed in such systems may increase matrix brittleness [146], highlighting the importance of fiber reinforcement. Among various fiber types, steel fibers are widely used in SUHPC. Among various fiber types, steel fibers are widely used in SUHPC [214-216], as they effectively enhance flexural strength and toughness, thereby supporting the application of SUHPC in complex structural conditions.

In this chapter, combinations of cementitious materials (CEM I 52.5R, CAC, and $CaSO_4$) with different mixing ratios are attempted to achieve SUHPC with more excellent mechanical properties, thereby avoiding the defects introduced by the accelerator. Calcium aluminate cement (CAC) and calcium sulfate source ($CaSO_4$) can be regarded as potential accelerators, which have the functions of increasing early - strength and micro - expansion, and are expected to partially or completely replace the alkali - free accelerator [193, 217]. Currently, some studies have found that an appropriate amount of calcium aluminate cement (CAC) and gypsum ($CaSO_4$) is helpful for shortening the setting time and improving the early - stage mechanical properties of concrete [185]. However, at present, the research on CAC and $CaSO_4$ in the ternary binder system of SUHPC as well as the long - term mechanical properties of the ternary binder system affected by the accelerator is still blank. This chapter addresses various performance evaluation criteria related to flexural and compressive properties, including flexural strength, compressive strength, flexural toughness, compressive toughness, fracture energy, and compressive energy absorption. Moreover, based on the test results of the mechanical properties

of SUHPC, the influence mechanisms of various cementitious materials and their mixing ratios on these mechanical properties are systematically analyzed from both macroscopic and microscopic perspectives. Simultaneously, the influence of accelerators on the performance of SUHPC was explored, providing a theoretical basis and research foundation for further studies on SUHPC.

## 5.2. Materials and experiments

### 5.2.1 Raw materials and mix proportions

CEM I 52.5R (PC), calcium aluminate cement (CAC), and gypsum ($CaSO_4 \cdot 2H_2O$, abbreviated as C$) were utilized as primary binder materials. Three grades of continuously graded sand were selected as fine aggregates. Quartz sand grades 1, 2, and 3 correspond to particle size ranges of 380-1200 μm (QS-1), 100-470 μm (QS-2), and 0-220 μm (QS-3), respectively. The water-reducing agent utilized in this study is the polycarboxylate superplasticizer used at a dosage of 0.19 wt% of the binder weight. Silica fume (microsilica, MS) and fly ash cenosphere (FAC) were added as the supplementary cementitious materials (SCMs).

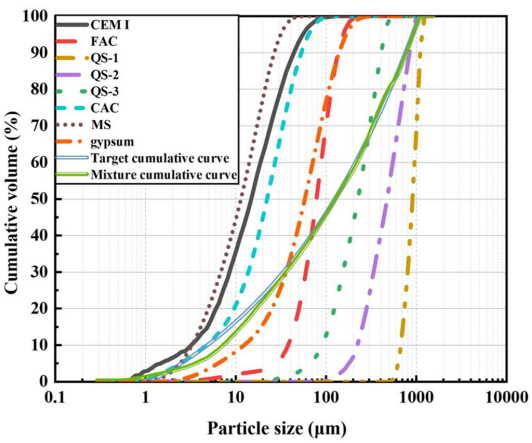


Fig. 5.1. Particle size distribution curves of raw materials.

In this study, modified A&A (MAA) model was utilized to achieve the densest particle packing in SUHPC [176, 177]. Target cumulative curve and mixture cumulative curve of developed SUHPC are illustrated in Fig. 5.1. In addition, copper-plated steel fibers with the diameter of 0.22 mm and length of 6 mm, with the physical performance parameters provided in Table 5.1. Chemical composition of the raw materials is shown in Table 5.2. The relevant performance parameters of alkali free accelerators are shown in Table 5.3.

Table 5.1. Physical performance parameters of steel fibers.

| | Diameter (mm) | Length (mm) | Aspect ratio | Tensile strength (MPa) | Elastic modulus (GPa) |
|---|---|---|---|---|---|
| Steel fiber | 0.2±0.02 | 6±0.2 | 30±6 | 2882 | 210 |

Table 5.2. Chemical composition of the raw materials.

| Oxide (wt%) | PC | CAC | C$ | MS | FAC |
|---|---|---|---|---|---|
| $Al_2O_3$ | 4.98 | 53.31 | 0.20 | 0.23 | 17.89 |
| CaO | 64.61 | 34.28 | 43.3 | 0.41 | 8.20 |
| $SiO_2$ | 20.18 | 6.96 | 0.32 | 94.68 | 55.57 |
| MgO | 2.19 | 0.37 | 1.37 | 0.43 | 1.02 |
| $Fe_2O_3$ | 3.24 | 1.90 | 0.10 | 0.17 | 11.31 |
| $K_2O$ | 0.53 | 0.41 | 0.01 | 0.83 | 2.74 |
| $P_2O_5$ | 0.74 | 0.15 | - | 0.19 | 1.59 |
| $Na_2O$ | 0.27 | 0.12 | - | 0.15 | 0.48 |
| $TiO_2$ | 0.25 | 1.67 | - | - | - |
| $SO_3$ | 3.01 | 0.83 | 53.7 | 0.81 | 1.20 |
| LOI | 1.56 | 1.60 | 1.59 | 2.33 | 1.03 |

Table 5.3. Physical performance parameters of alkali free accelerator.

| Specific gravity (20/20 ℃) | Solid content (%) | pH (25 ℃) | Alkali content (%) | $Cl^-$ (%) | $F^-$ (%) | Stability (mL) |
|---|---|---|---|---|---|---|
| 1.43 | 50.2 | 2.2 | 0.05 | 0.01 | 0.04 | 2 |

Ten mix designs of SUHPC were developed based on the mix proportions listed in Table B1 of Appendix B. To investigate the effect of multi-component cementitious materials on the mechanical performance of SUHPC, a control group (P100) was established, along with a binary system (P70-CAC30) and ternary systems (PC-CAC-C$, e.g., P70-CAC24-C$6). In addition, a 2 wt% dosage of an alkali-free accelerator was incorporated into the mixtures of the control group, binary system, and ternary systems, respectively. This study aims to investigate the effects of the interaction between the binders in the multi-component system and alkali-free accelerator, as well as their combined influence on the mechanical properties of SUHPC.

### 5.2.2 Specimen preparation

(a) Spraying (b) Sprayed thickness 50mm (c) Post-curing cutting

**Fig. 5.2.** Specimen preparation process.

The detailed specimen preparation process of SUHPC is illustrated in Fig. 5.2. The process involves several key steps, including material weighing, mixing, transportation, equipment setup and loading, mold preparation, spraying, and cutting of specimens after curing. The specimen size used in this study is 40 mm × 40 mm × 160 mm, with three parallel specimens designed for each test group.

### 5.2.3 Experimental methods

Conduct flexural and compressive tests on specimens measuring 40 mm×40 mm×160 mm, and obtain load-displacement curves and compressive stress-strain curves [218-220]. The SUHPC specimens were tested using a universal testing machine with a maximum bearing

capacity of 300 kN. The control method employed is displacement loading control, with a loading rate of 0.3 mm/min maintained throughout each loading stage. Throughout the loading process, the generation and propagation of cracks in the specimen were continuously observed. When combined with real-time data displayed on the electro-hydraulic servo machine, the test is terminated when the load-displacement curve approaches the x-axis, indicating that the stiffness of the specimen is approximately zero. Uniaxial compressive testing is then performed on the specimen using the electro-hydraulic servo machine, with a loading rate set at 0.6 mm/min. The flexural and compression test apparatus are illustrated in Fig. 5.3.

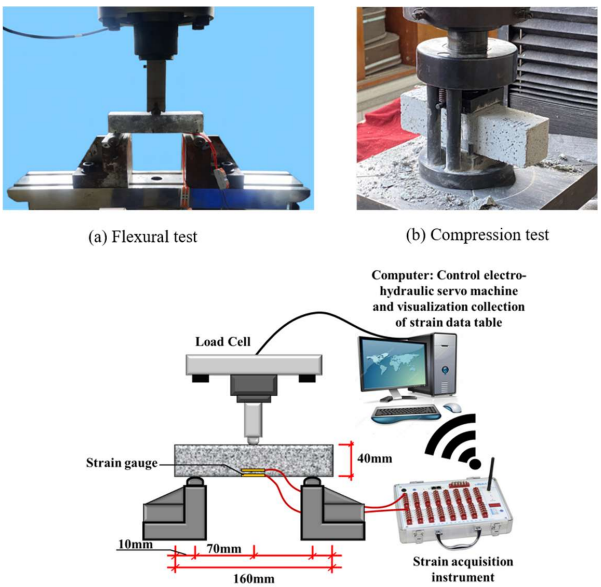


Fig. 5.3. The testing device for test piece.

In the flexural test, the flexural toughness of various cementitious material specimens is evaluated by comparing the fracture energy and flexural toughness index produced by each specimen during the testing process. The calculation of the flexural fracture energy for each specimen involves determining the energy required for fracture during the flexural process. This energy is represented by the area enclosed by the curve and the coordinate axis on the load-displacement curve [221]. When the flexural displacement in the flexural test reaches 4.2 mm, the area enclosed by the load-displacement curve from 0 to 4.2 mm ($G_f$) and the x-axis represents the required fracture energy during the flexural process. The calculation of the flexural toughness index evaluates the flexural toughness of the specimen by determining $I_5$, $I_{10}$, and $I_{20}$ as specified in ASTM C1018 [98]. The calculation diagram for the flexural toughness index in the flexural test is illustrated in Fig. 5.4(a). The corresponding flexural toughness indicators are calculated as follows:

$$I_5 = \frac{A_{3\delta}}{A_{\delta}} \tag{5.1}$$

$$I_{10} = \frac{A_{5.5\delta}}{A_{\delta}} \tag{5.2}$$

$$I_{20} = \frac{A_{10.5\delta}}{A_{\delta}} \tag{5.3}$$

In the formulas, $A_{\delta}$ indicates the area of *OAB* enclosed by the curve and the X-axis in the load displacement curve obtained from the flexural test; $A_{3\delta}$ indicates the area of *OACD*; $A_{5.5\delta}$ indicates the area of *OAEF*; $A_{10.5\delta}$ indicates the area of *OAGH*.

In compressive testing, the compressive toughness of various cementitious material specimens is evaluated by comparing their compressive toughness indicators throughout the compression process. The compression toughness index of each specimen is determined by calculating the area enclosed by the stress-strain curve and the coordinate axes during the compression process. This area represents the compression energy of the specimen. In the context of the compression test, when the compressive strain reaches 0.012, the required compression energy of the specimen during the compression process is represented by the area from 0 to 0.012 ($G_c$). The compression toughness index is defined following the criteria in [221] and is given by:

$$E_2 = \frac{A_{2\varepsilon}}{A_{\varepsilon}} \tag{5.4}$$

$$E_3 = \frac{A_{3\varepsilon}}{A_{\varepsilon}} \tag{5.5}$$

The diagram illustrating the calculation of the compression toughness index for the compression test is presented in Fig. 5.4(b). In the formula, $A_{\varepsilon}$ represents the area of enclosed by the stress-strain curve obtained from the compressive test and the X-axis; $A_{2\varepsilon}$ indicates the area of *OIKL*; $A_{3\varepsilon}$ indicates the area of *OIMN*.

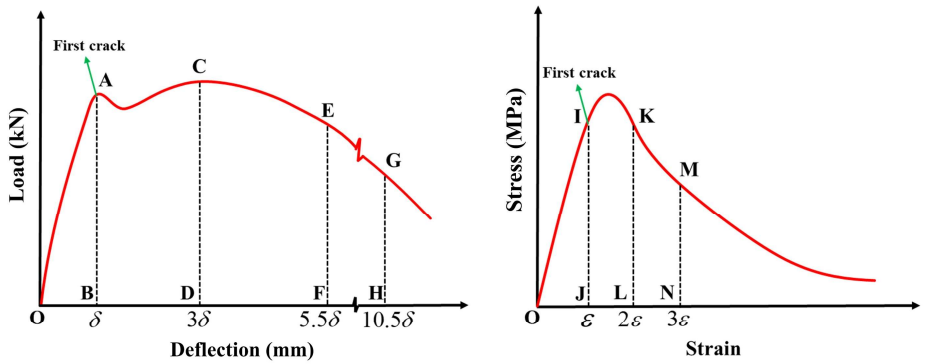


(a) Calculation diagram of flexural toughness index

(b) Schematic diagram for calculating compressive toughness index

Fig. 5.4. Schematic diagram for calculating flexural and compression resistance indicators.

The microstructure of the SUHPC specimen was characterized using a scanning electron microscope (SEM, TESCAN MIRA3) equipped with a backscattered electron (BSE) detector

and an energy-dispersive spectrometer (EDS). The instrument provides a resolution of 1.2 nm, a magnification range from 2× to 1,000,000×, and an acceleration voltage adjustable between 0.5 kV and 30 kV. Prior to observation, the SUHPC samples were crushed into fragments with approximate dimensions of 0.5 $mm^3$, oven-dried, and sputter-coated with a thin layer of gold to improve conductivity.

## 5.3 Results and analysis

### 5.3.1 Flexural resistance of test specimens

The flexural test provides critical insights into the bending performance of SUHPC, which is essential for evaluating its practical engineering applications. Furthermore, the observation of failure modes, including crack initiation and propagation, contributes to understanding the correlation between microstructural features and macroscopic mechanical behavior of SUHPC.

#### 5.3.1.1 Flexural failure mode of the developed SUHPC specimens

Fig. 5.5 illustrates the flexural failure modes of the various specimens. Position the specimen on the flexural test device of the electro-hydraulic servo machine, adjust the loading rate, and commence the test immediately. In the initial stage of the experiment, the load-displacement curve, which is formed by the downward displacement of the loading point of the electro-hydraulic servo machine and the corresponding load value detected by the load sensor, exhibits an approximately linear distribution. This behavior indicates that the specimen possesses good flexural toughness and effectively resists flexural deformation under the initial load. As the load increases, the slope of the load-displacement curve gradually decreases until it reaches the ultimate load. When the load reaches the ultimate load of the specimen, the slope of the curve approaches zero. At this point, the ultimate load corresponds to the cracking load of the specimen, which is accompanied by a distinct sound indicative of the SUHPC cracking. After reaching the ultimate load, as the displacement continues to increase, the cracking zone of the flexural specimen initiates in the tensile region of the specimen. Thus, the phenomenon of steel fibers within the SUHPC being pulled and deboned during flexural testing can be observed in the original cracking zone of the specimen accompanied by a sharp sound, indicating the separation between the steel fibers and the SUHPC. In the later stages of the experiment, the specimen approaches its maximum attainable displacement, and the overall cracking zone reaches its maximum extent. However, the contact area between the top of the specimen and the loading point remains intact and has not completely separated into two parts, with the observed load value at this time being less than 100 N.

The three typical distribution forms of steel fibers in SUHPC are fiber bridging, fiber fracture, and fiber pull-out, as illustrated in Fig. 5.6. Before the specimen reaches the cracking load, the tensile stress experienced by the steel fibers in the tensile zone is less than the sum of the tensile stresses of the steel fiber material and the SUHPC matrix material in that zone. At this stage, the steel fibers primarily exhibit tensile behavior as they bond with the matrix. Upon reaching the cracking load, the mid-span tensile zone develops cracks, while the steel fibers serve a bridging function that suppresses the propagation and extension of these cracks. The steel fibers are embedded at both ends within the SUHPC matrix to enhance adhesive strength against

tensile stress in the tensile zone. As the cracking area evolves, the bonding force between the steel fibers and the matrix becomes insufficient to withstand the tensile stress in the tensile zone; specifically, the tensile stress exceeds the material tensile strength of the steel fibers. At this stage, local steel fibers may fracture or be extracted from the concrete matrix due to excessive tension.

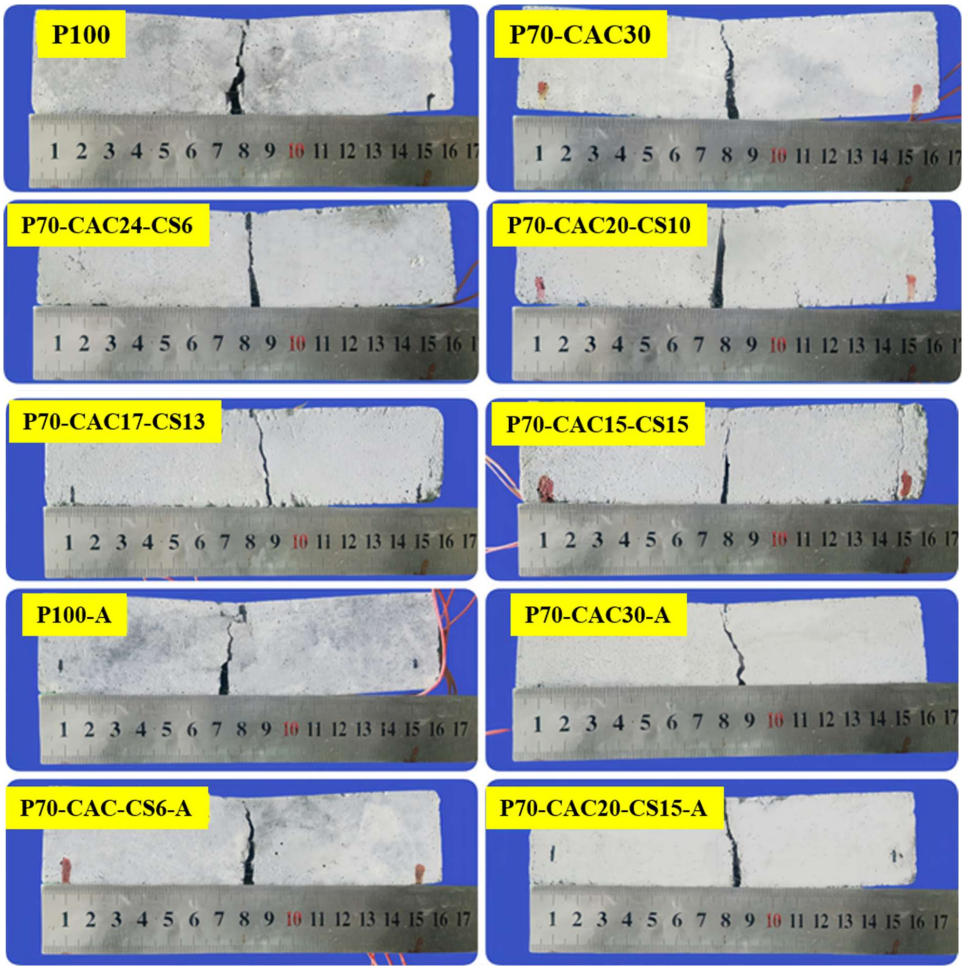


Fig. 5.5. Flexural failure mode of the developed SUHPC specimens.


(a) Fiber bridge (b) Fiber breakage

Fig. 5.6. Three typical distributions of steel fibers in SUHPC specimens.

### 5.3.1.2 Load-displacement curve of the developed SUHPC specimens

The load–displacement curve reflects the deformation and failure characteristics of SUHPC during different loading stages, including the elastic, post-cracking, and failure phases. It provides a basis for evaluating the cracking load, ultimate load, and overall flexural performance of the SUHPC specimens.

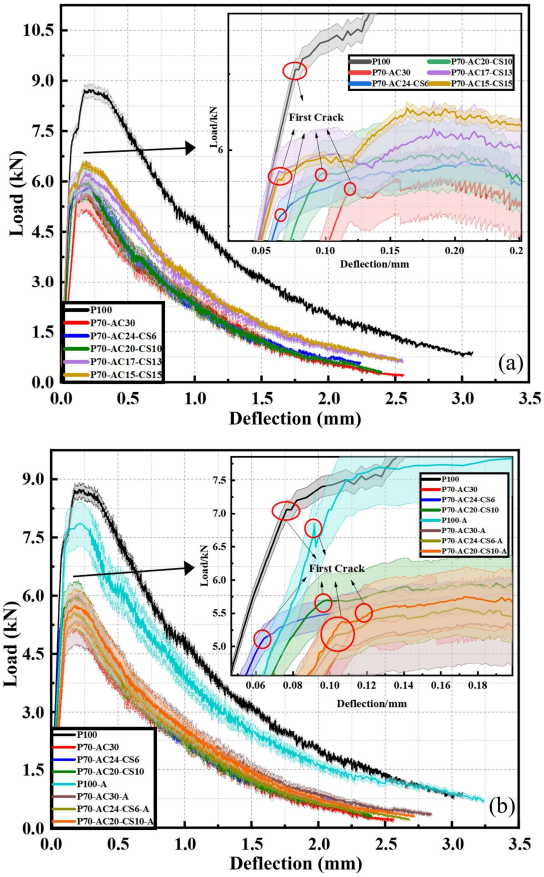


Fig. 5.7. Load-displacement curve of the developed SUHPC specimens: (a) SUHPC with different cementitious materials; (b) SUHPC with and without accelerator.

Fig. 5.7(a) and (b) present the flexural load-displacement curves of SUHPC specimens following the addition of cementitious materials and accelerators, respectively. The load-displacement curve of the SUHPC specimens demonstrates an initial increase followed by a decrease. Prior to reaching the cracking load, the SUHPC specimen exhibits nearly linear stiffness. Upon reaching the cracking load, the curve indicates a sudden change, signaling a modification in the stiffness of the SUHPC specimen. However, the presence of steel fibers introduces local reinforcement after the cracking load is achieved, which contributes to a gradual increase or stabilization of the load-bearing capacity during the post-cracking stage. Beyond the cracking load, the tensile region of the specimen is primarily supported by the internal steel fibers and the SUHPC material above the crack tip, with the steel fibers serving

as the predominant load-bearing component. Owing to the toughening effect of the steel fibers, the bearing capacity of the SUHPC after cracking is slightly enhanced. After reaching the ultimate load, the descending segment of the curve exhibits a fluctuating pattern. Throughout the later stages of the experiment, the bearing capacity of the SUHPC specimens gradually decreases, as the bond between the steel fibers and the cement matrix progressively weakens. As the height of the crack extends further upward, the bond strength between the steel fibers and the cement matrix at the fracture zone becomes inadequate to withstand the tensile stress. Consequently, the steel fibers are pulled out, resulting in a new stress distribution at the fracture zone. Specifically, after reaching the ultimate load, the steel fibers at the fracture section display an approximate periodic cycle of loading, debonding, and pulling out, leading to the observed fluctuations in the load-displacement curve. As the experiment advances, the crack progressively develops into a through-crack, further diminishing the bearing capacity. The descending segment of the load-displacement curve gradually flattens until the conclusion of the experiment. Furthermore, the load-displacement curves of SUHPC with varying cementitious materials exhibit distinct cracking nodes in the rising section of the displacement, specifically between 0.1 and 0.2 mm. For the load-displacement curve of SUHPC containing added accelerators, a significant cracking stage is observed in the rising section of the displacement, specifically between 0.1 and 0.21 mm.

Fig. 5.7(a) displays the load-displacement curves of SUHPC specimens with various added cementitious materials. Among the specimens, P-100 exhibited slightly higher cracking and ultimate loads compared to the other groups, with its primary cementitious material consisting solely of CEM I 52.5R Portland cement. The cracking load and ultimate load of P70-CAC30 are the worst among all specimens, and its internal cementitious material is 70% CEM I 52.5R Portland cement and 30% CAC. It can be attributed to the fact that CAC undergoes flash setting, followed by rapid hydration to form CAH (Calcium Aluminate Hydrates), specifically $CAH_{10}$ and $C_2AH_8$, as illustrated by Eq (4.4).

However, the hydrates $CAH_{10}$ and $C_2AH_8$ are metastable at temperatures below 30℃ and are highly sensitive to hydration duration, temperature, and humidity; they gradually transform into the stable phase $C_3AH_6$, as detailed in Chapter 4 (see Eq.(4.10) and Eq.(4.11)); this process is referred to as the conversion of CAC [222].

The conversion process results in increased porosity within the matrix, ultimately reducing strength and durability over the long term [223]. Consequently, in the binary system (PC-CAC), the incorporation of 30% CAC leads to the most significant reduction in both the load-bearing capacity and ultimate load of the SUHPC specimens.

Compared to the binary binder system (PC-CAC), the reductions in both the cracking load and the ultimate load of SUHPC are less pronounced in ternary binder system (PC-CAC-C$), as shown in Fig. 5.7(a). This improvement is attributed to the reaction between calcium sulfate (C$) and CA (from CAC), forming ettringite (AFt), as illustrated by Eq .(4.3).

This reaction promotes strength development. In addition, the incorporation of C$ mitigates the flash setting of CAC and suppresses the conversion process of CAC [224]. Therefore, the

combination of CAC-C$ can serve as a potential accelerator, not only regulating the setting time but also enhancing strength development of SUHPC.

Fig. 5.7(b) illustrates the load-displacement curve of SUHPC specimens incorporating various cementitious materials and accelerators. The cracking load and ultimate load of the four groups of SUHPC specimens containing accelerators exhibited varying degrees of reduction. Upon contact with the SUHPC paste, $Al^{3+}$ reacts rapidly to form the hydroxy complex $Al(OH)_4^-$, as follows:

$$Al^{3+} + 3OH^- \leftrightarrow Al(OH)_3 + OH^- \leftrightarrow [Al(OH)_4]^- \tag{5.6}$$

As the reaction progresses, $Al(OH)_4^-$ reacts with $SO_4^{2-}$ in the accelerator, as well as compound $Ca^{2+}$ in the cementitious material, to produce a substantial amount of AFt or AFm, as described in Eq. (4.6) in Chapter 4.

The incorporation of the accelerator significantly accelerates the hydration, generating a large amount of hydration products such as AFt/AFm and C-S-H, which ensure the spray thickness and early strength of SUHPC [35, 225, 226]. However, according to Fig. 5.7(b), the addition of the accelerator significantly reduces the strength of both binary and ternary system SUHPC. This reduction is primarily attributed to the rapid setting induced by the accelerator, which causes SUHPC to solidify within 5-10 minutes. Such an instantaneous reaction introduces some air bubbles into the structure of SUHPC, leading to an increase in macro pores and, in turn, a decrease in the mechanical properties of SUHPC [35, 227]. Therefore, alkali-free accelerators can accelerate the early hydration process and increase the spraying thickness, but they have a negative effect on the long-term strength.

#### 5.3.1.3 Flexural strength of the developed SUHPC specimens

Fig. 5.8(a) and (b) illustrate the flexural strength of SUHPC specimens incorporating various cementitious materials and accelerators. The P100 specimen exhibits the highest flexural bearing capacity, whereas the P70-CAC30 specimen, which includes a 30% substitution of Portland cement with CAC, demonstrates the lowest flexural bearing capacity. The differing hydration products of CAC and Portland cement result in changes to the pore structure within the cement matrix. The hydration products of Portland cement primarily consist of C-S-H and $Ca(OH)_2$. Additionally, the incorporation of silica fume and fly ash promotes further reactions with ettringite, leading to the formation of more C-S-H. However, when CAC partially replaces Portland cement at a 30% substitution rate in binary binder system (PC-CAC), the hydration reaction of the cementitious materials alters, resulting in hydration products that primarily consist of metastable phase hydration ($CAH_{10}$ and $C_2AH_8$). The stability of the products is influenced by the internal temperature, humidity, and hydration duration of the concrete, which can lead to negatively impact long-term performance [228].

In the ternary binder system (PC-CAC-C$). As the C$ content increases from 0 wt% to 15 wt%. The flexural strength of SUHPC specimens increases from 18.5 MPa to 21.5 MPa, which represents an increase of 16.22%. The addition of C$ functions as a retarder of the ternary binder system in SUHPC, effectively inhibiting the phase transitions of hydration products in

CAC. Therefore, it improves the stability of the internal pore structure and enhances the strength development.

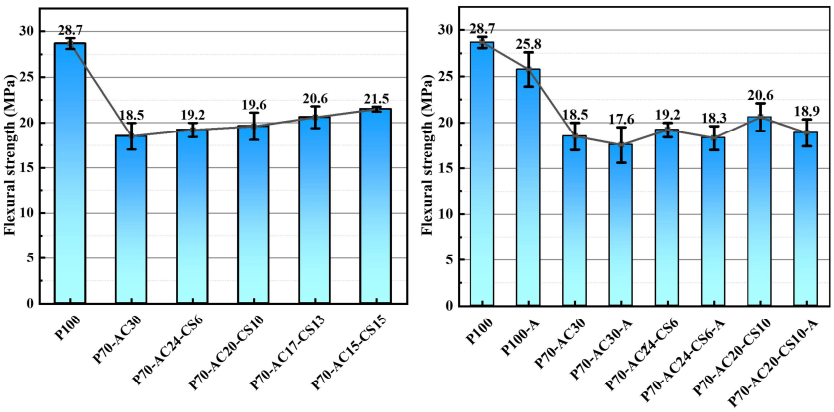


(a) SUHPC with different cementitious materials (b) SUHPC with alkali-free accelerator

Fig. 5.8. Flexural strength of the developed SUHPC specimens.

Following the addition of alkali-free accelerator, the flexural strength of each group of specimens exhibited varying degrees of decrease. As is known, the flexural strength is closely related to the content of C-S-H gel. Therefore, it is also possible that the alkali - free accelerator introduces a large amount of $Al^{3+}$. Aluminum ions delay and inhibit the hydration of $C_3S$ in Portland cement, thereby reducing the content of C-S-H gel and flexural strength. In addition, it has also been observed that the deteriorating effect of the accelerator on ordinary SUHPC is greater than that on other systems. For example, the flexural strength of ordinary SUHPC is reduced by 10.1% by the accelerator, while that of binary - system SUHPC is reduced by 4.9%.

#### 5.3.1.4 Flexural fracture energy and toughness index of the developed SUHPC specimens

Fig. 5.9 and Fig. 5.10 illustrate the flexural fracture energy ($G_f$) and the flexural toughness index ($I_5$, $I_{10}$, and $I_{20}$) of SUHPC specimens. The P100 mixture, which contains only Portland cement, shows the highest fracture energy and toughness. In binary binder system (PC-CAC), the introduction of 30 wt% CAC significantly reduced performance. Compared with P100, the flexural fracture energy and toughness indices of P70-CAC30 decreased by 53.8%, 21.91%, 26.98%, and 35.03%, respectively. In contrast, the ternary PC–CAC–C$ system exhibited clear improvements. As C$ content increased and CAC content decreased, both fracture energy and toughness were gradually restored. Relative to P70-CAC30, the fracture energy of P70-CAC24-C$6, P70-CAC20-C$10, P70-CAC17-C$13, and P70-CAC15-C$15 increased by 3.74%, 4.21%, 30.67%, and 35.63%, respectively. A similar trend was observed for flexural toughness. The flexural toughness indicators ($I_5$, $I_{10}$, and $I_{20}$) of ternary binder system have increased by the following percentages: $I_5$ by 1.85%, 10.23%, 20.67%, and 22.38%; $I_{10}$ by 9.58%, 21.93%, 29.57%, and 33.45%; and $I_{20}$ by 17.23%, 33.90%, 38.55%, and 40.19%, respectively. These results demonstrate that the ternary PC–CAC–C$ system effectively compensates for the strength and toughness reductions caused by the sole use of CAC, and that an appropriate balance between CAC and C$ is critical for optimizing the flexural performance of SUHPC.

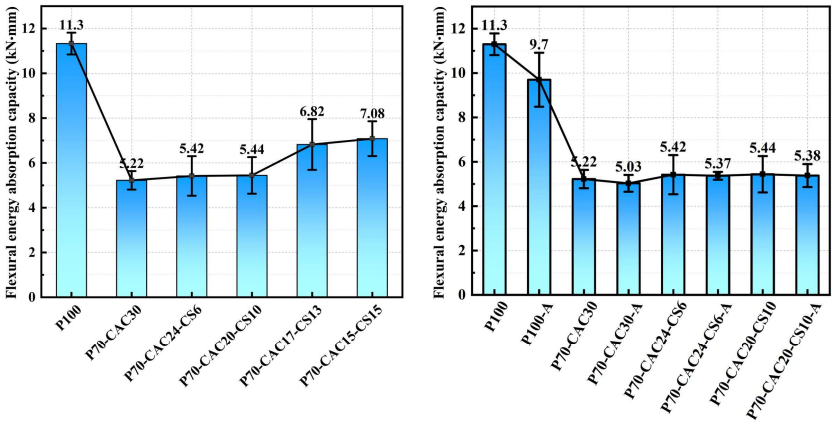


(a) SUHPC with different cementitious materials (b) SUHPC with alkali-free accelerator

Fig. 5.9. The flexural fracture energy $G_f$ of the SUHPC specimen.

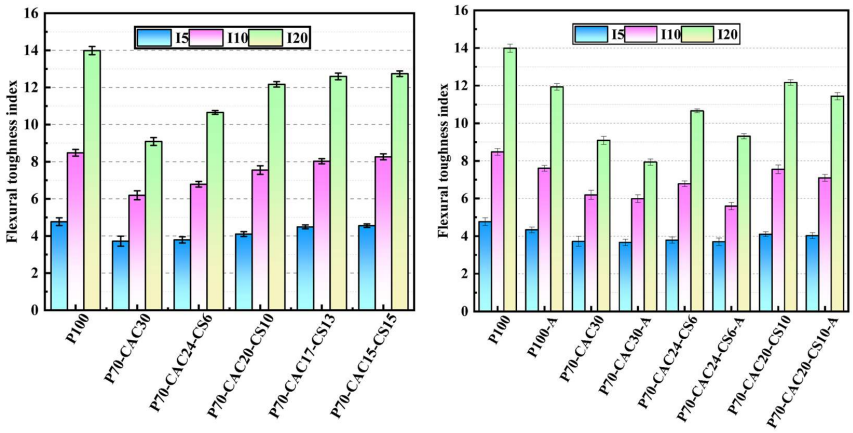


(a) SUHPC with different cementitious materials (b) SUHPC with alkali-free accelerator

Fig. 5.10. Flexural toughness index of the developed SUHPC specimens.

Following the addition of accelerators, the flexural fracture energy absorption capacity and the flexural toughness index ($I_5$, $I_{10}$, and $I_{20}$) of each SUHPC specimen exhibited varying degrees of reduction. Compared to SUHPC specimens without accelerators, the flexural fracture energy absorption capacities of P100-A, P70-CAC30-A, P70-CAC24-C$6-A, and P70-CAC20-C$10-A decreased by 14.12%, 3.61%, 0.78%, and 1.09%, respectively. In the specimens without accelerators exhibited the following decreases in the flexural toughness indices: for P100-A, the $I_5$, $I_{10}$, and $I_{20}$ decreased by 9.12%, 10.28%, and 14.72%, respectively; for P70-CAC30-A, the decreases were 1.45%, 3.26%, and 12.68%; for P70-CAC24-C$6-A, they decreased by 2.33%, 17.55%, and 12.61%; and for P70-CAC20-C$10-A, the reductions were 1.74%, 6.02%, and 6%, respectively. This result indicates that the addition of the accelerator has a negative impact on the flexural fracture energy absorption capacity of SUHPC in the ternary binder system (PC-CAC-C$). However, it has been observed that when the C$ content is higher than 6 wt%, the negative impact of the accelerator on the fracture energy absorption capacity of the ternary system is significantly reduced.

### 5.3.2 Compressive performance of developed SUHPC specimens

Compressive strength is a critical performance indicator for SUHPC. Compressive testing enables the accurate assessment of the capacity of SUHPC to withstand damage under axial loading, thereby providing essential data for evaluating material performance. The compressive test generates the stress-strain curve of SUHPC specimens throughout the loading process, illustrating the deformation characteristics of the materials during the elastic, elastoplastic, and failure stages.

#### 5.3.2.1 Compressive stress-strain characteristics

Fig. 5.11(a) and (b) present the stress-strain curves of SUHPC specimens subjected to compressive tests, incorporating various cementitious materials and the accelerator. For SUHPC specimens that incorporated additional cementitious materials and accelerators, the stress-strain curves exhibited a consistent trend of initially increasing and then subsequently decreasing during compression. The variations in the types and dosages of cementitious materials used in the specimens result in changes to the hydration products of SUHPC, which ultimately compromise its performance. In line with the differential analysis of the flexural performance of SUHPC specimens across various groups in the flexural performance test, the addition of CAC reduces the strength of SUHPC, while C$ effectively mitigates the degree of strength degradation. In contrast to the flexural test, the stress-strain curve of SUHPC exhibits a stable slope in the descending section, showing no significant fluctuations in stress. The stress fluctuations observed in the specimen are attributed to the relative slip between the steel fibers and the cement matrix during compression, resulting in their pull-out. In the compressed state, the steel fibers also share the compressive stress with the matrix; however, the bonding slip between the steel fibers and the cement matrix is minimal. Consequently, the stress fluctuations observed in the descending section of the stress-strain curve are minimal.

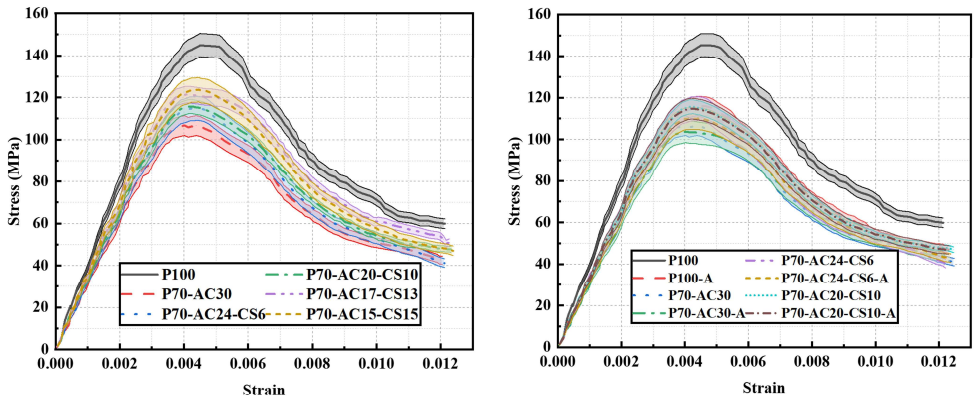


(a) SUHPC with different cementitious materials (b) SUHPC with alkali-free accelerator

Fig. 5.11. Stress-strain curve of compressive SUHPC specimens.

### 5.3.2.2 Compressive strength

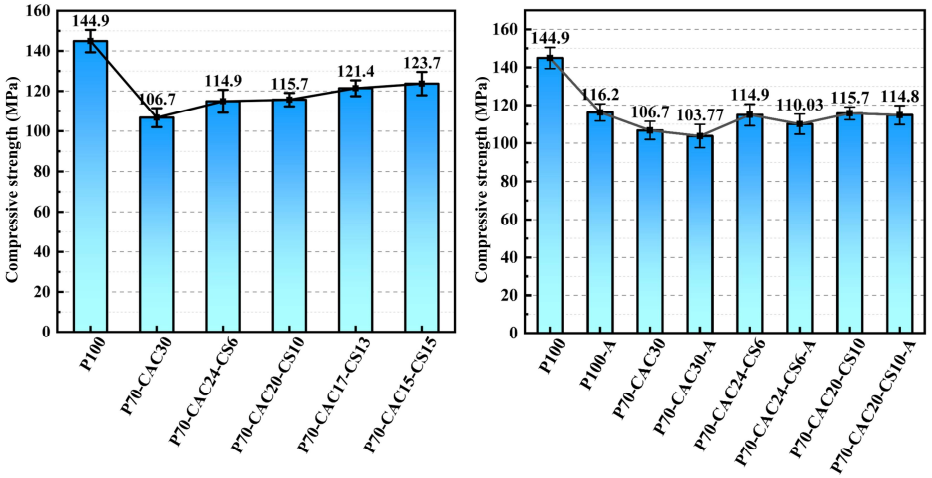


(a) SUHPC with different cementitious materials (b) SUHPC with alkali-free accelerator

Fig. 5.12. Compressive strength of the developed SUHPC specimens.

Fig. 5.12(a) and (b) present the compressive strength of SUHPC specimens incorporating different cementitious materials and the accelerator. Among the specimens, the P100 exhibits the highest compressive strength, reaching 144.9 MPa. The compressive strength of two mixtures in ternary systems exceeds 120 MPa at 28d, with P70-CAC17-C$13 reaching 121.4 MPa and P70-CAC15-C$15 achieving 123.7 MPa. In the binary binder system, replacing 30% of PC with component CAC results in a 26.36% reduction in compressive strength of the P70-CAC30 compared to P100. And in ternary binder system, the increase in C$ (and/or the decrease in CAC) results in a consistent trend between the changes in compressive strength and flexural strength. This may be due to the influence of the CAC to C$ ratio on the balance between the aluminum source (from CAC) and $SO_4^{2-}$ (from C$) in the ternary system, which further affects the hydration process. When the ratio of CAC/C$ is very high, such as in P70-CAC24-C$6, the limited C$ is completely consumed by CAC in the early stage of the reaction and a limited amount of AFt is generated as shown in Eq. (5.4). Meanwhile, most of the remaining CAC will be hydrated to generate a large amount of metastable CAH ($CAH_{10}$ and $C_2AH_8$), which will be converted into the stable hydrate $C_3AH_6$ in the later stage, that is, the conversion process. Both the limited AFt and the conversion process will affect the development of strength [229, 230].

The addition of the accelerator will have an obvious deteriorating effect on the compressive strength of all SUHPC. However, the degree of strength deterioration of SUHPCs with different cementitious systems caused by the accelerator is different. For example, the accelerator reduces the compressive strength of ordinary SUHPC (P100) by 19.8%, while it reduces that of binary-system SUHPC by 2.7%. Therefore, the combined use of multi-component cementitious materials can effectively reduce the deteriorating effect of the accelerator on the strength of SUHPC.

### 5.3.2.3 Compressive energy absorption and toughness index

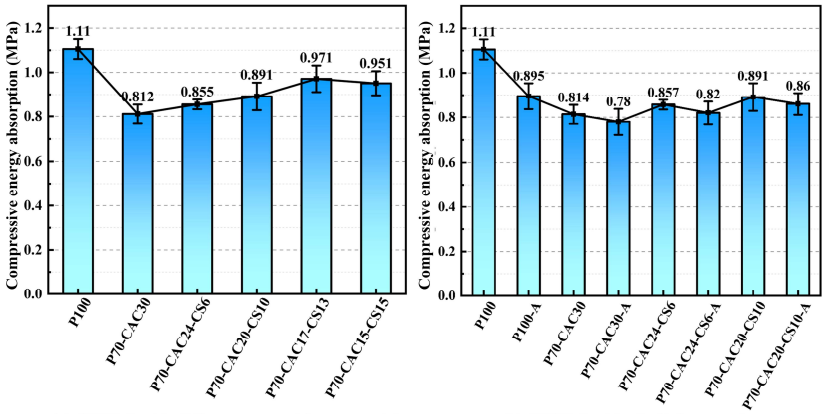


(a) SUHPC with different cementitious materials (b) SUHPC with alkali-free accelerator

Fig. 5.13. The compressive energy absorption $G_c$ of the developed SUHPC.

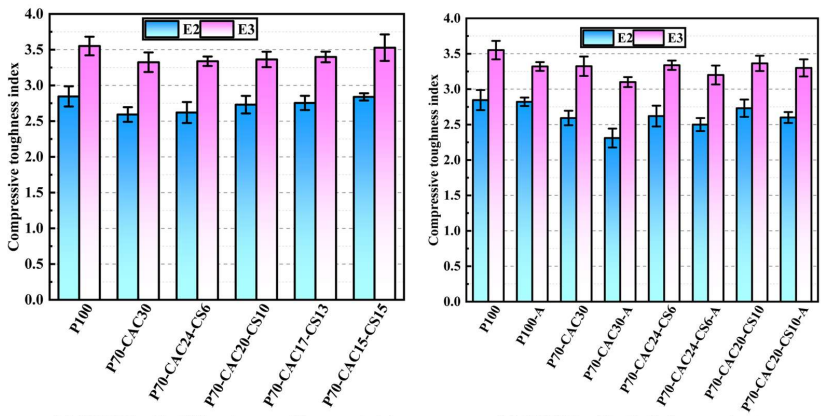


(a) SUHPC with different cementitious materials (b) SUHPC with alkali-free accelerator

Fig. 5.14. The toughness index of the developed SUHPC specimens.

Fig. 5.13 and Fig. 5.14 show the compressive energy absorption and compressive toughness indices ($E_2$, $E_3$) of the SUHPC specimens, respectively. The results indicate that the P100 exhibits the highest compressive energy absorption capacity and the compressive toughness. In binary binder system (PC-CAC), the compressive energy absorption capacity and the compressive toughness of the P70-CAC30 decreased by 26.59%, 8.89% and 6.41%, respectively, compared to that of the P100 specimen. In ternary binder system (PC-CAC-C$), it is observed that the compressive energy absorption and the compressive toughness of SUHPC increases with C$ content. In comparison to binary binder system (P70-CAC30), the compressive energy absorption capacity of the P70-CAC24-C$6, P70-CAC20-C$10, P70-CAC17-C$13, and P70-CAC15-C$15 in ternary binder system increased by 5.33%, 9.82%, 19.64%, and 17.15%, respectively. The indices $E_2$ and $E_3$ significantly increased with the increase in C$ content. In comparison to P70-CAC30, the toughness index $E_2$ of ternary binder system (PC-CAC-C$) increased by 1.06%, 5.33%, 6.24%, and 9.51%, while the toughness index $E_3$ of those increased by 0.43%, 1.21%, 2.22%, and 6.14%, respectively. Compared to

the conventional system with 100% Portland cement (P100), the incorporation of CAC significantly reduced the compressive energy absorption capacity and the compression toughness index in the binary system. However, the further addition of C$ in the ternary system mitigated the detrimental effects caused by the sole introduction of CAC.

The addition of accelerator led to a reduction in the compressive energy absorption capacity and the compressive toughness of each SUHPC to varying extents. Compared to the SUHPC specimens without accelerators, the compressive energy absorption capacities of the P100-A, P70-CAC30-A, P70-CAC24-C$6-A, and P70-CAC20-C$10-A decreased by 19.03%, 4.14%, 4.32%, and 3.51%, respectively. And the toughness indices $E_2$ and $E_3$ of the P100-A decreased by 0.87% and 6.51%, respectively. The $E_2$ and $E_3$ values of the P70-CAC30-A decreased by 10.9% and 6.73%, respectively, compared to P70-CAC30. Similarly, the $E_2$ and $E_3$ values of the P70-CAC24-C$6-A decreased by 4.58% and 4.13%, respectively, while those for the P70-CAC20-C$10-A specimen decreased by 4.78% and 1.9%, respectively.

### 5.3.3 Morphology

The hydration products of SUHPC were identified using SEM. Different hydration products exert distinct influences on the performance of SUHPC. Analyzing these hydration products facilitates a deeper understanding of the hydration process and the mechanisms underlying the formation of SUHPC's performance characteristics.

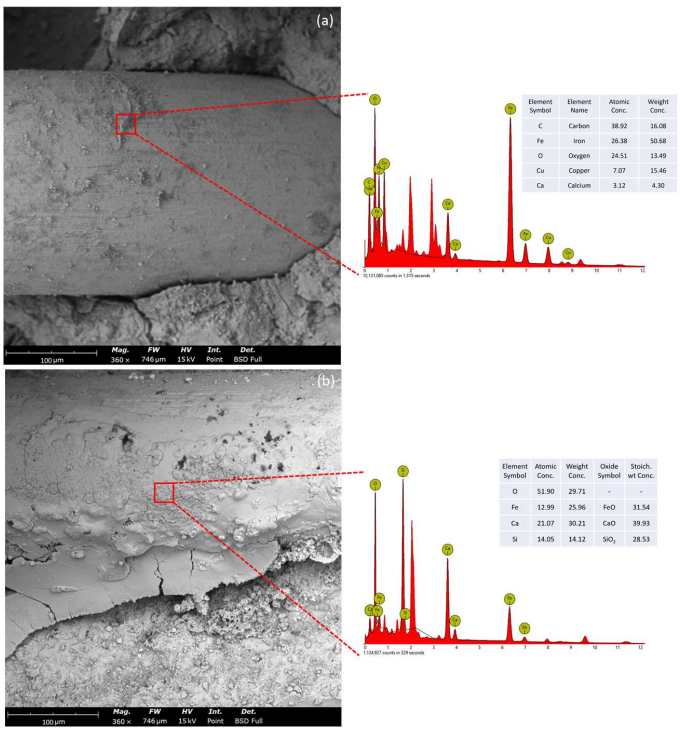


Fig. 5.15. SEM images of SUHPC samples at 28 days: surface morphology and EDS analysis of steel fibers in P70-CAC30 (a); surface morphology and EDS analysis of steel fibers in P70-CAC15-C$15 (b).

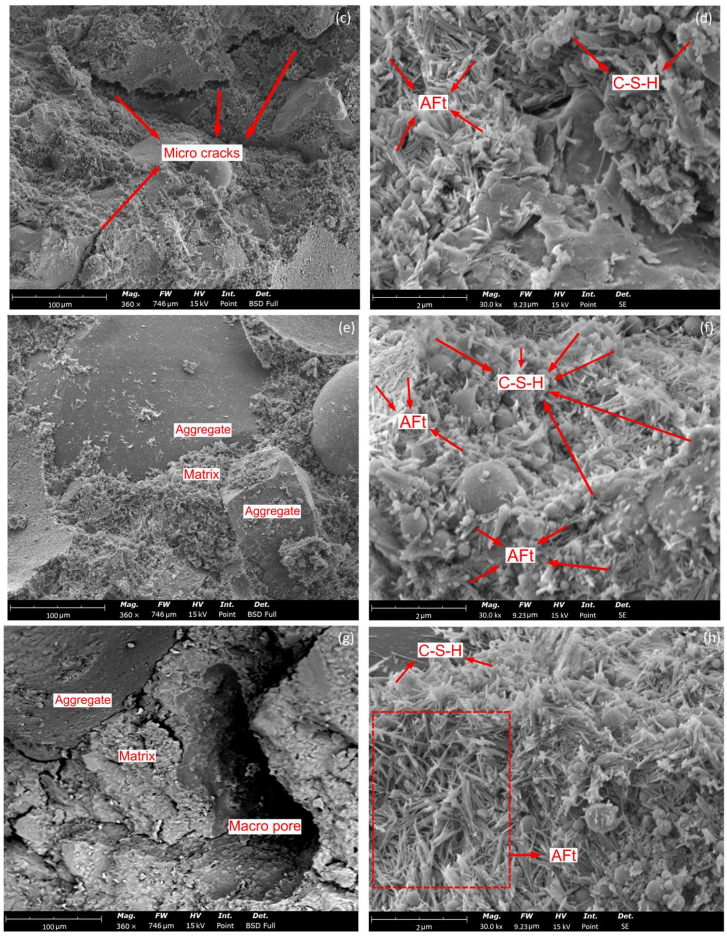


Fig. 5.15 (continued). Microstructure of P70-CAC30 (c, d), P70-CAC15-C$15 (e, f) and P70-CAC20-C$10-A (g, h).

Fig. 5.15 presents SEM images illustrating the effects of the binary and ternary binder systems, as well as the incorporation of an alkali-free accelerator, on the microstructure of SUHPC. Fig. 5.15(a) and (b) show the surface morphology of steel fibers in the binary system (P70-CAC30) and ternary system (P70-CAC15-C$15), respectively. In comparison with the binary system, more hydration products are observed on the steel fiber surface in the ternary system. Further EDS point analysis of the deposits on the steel fiber surface indicated that Cu and Fe were the dominant elements, originating from the copper coating on the fibers. However, the steel fiber surface in the ternary system exhibited higher contents of Ca and Si, with a Ca/Si atomic ratio of approximately 1.5. A relatively high Ca/Si value may indicate the formation of calcium-rich C-S-H gel and is associated with a finer pore structure [231]. These results suggest that, compared to the binary system, the steel fiber surface in the ternary system is covered with more abundant hydration products, indicating a stronger fiber-matrix interfacial bond. It also helps explain the higher flexural strength, cracking load, and ultimate load observed in the ternary system.

Fig. 5.15 (c) and (d) reveal microstructural deterioration in the matrix of binary system, such as microcracks and voids. Such defects may be related to the conversion process of CAC, during which the early-formed hydrates (e.g., $CAH_{10}$ and $C_2AH_8$) transform into the more stable but less dense $C_3AH_6$ phase. This process increases porosity and leads to microstructural degradation, which also explains the low compressive strength observed in the binary system. In comparison with the binary system, Fig. 5.15(e) and (f) demonstrate the formation of abundant AFt and C-S-H gel within the ternary system, accompanied by a notably denser matrix structure. These observations suggest that the synergistic effect of the multi-component hydration reactions in the ternary system enhances the microstructural compactness, thereby accounting for its superior compressive strength. Furthermore, Fig. 5.15(g) and (h) depict the microstructure of the P70-CAC20-C$10-A sample incorporating an accelerator. A denser formation of needle-like AFt crystals is evident; however, the rapid setting induced by the accelerator may entrap air, resulting in the development of macro pores [196]. The formation of macro pores is considered one of the major factors responsible for the deterioration of the mechanical properties of SUHPC upon the addition of an accelerator.

## 5.4. Conclusions

This chapter investigates the effects of various binder systems (with CEM I 52.5R, CAC and C$) and alkaline-free accelerator on the mechanical properties of SUHPC. The main findings are as follows:

- The regulatory effect of cementitious material composition on strength. When partially replacing PC with CAC alone, the flexural and compressive strengths of SUHPC are significantly reduced. Notably, when CAC is incorporated at a rate of 30%, the reductions in both flexural and compressive strengths are most pronounced compared to all other binder systems. However, the ternary binder systems composed of CAC and C$ exhibit a significant synergistic enhancement effect. As the C$ content increases from 0 to 15 wt%, the flexural strength of SUHPC rises from 18.5 MPa to 21.5 MPa (representing an increase of 16.21%), while the compressive strength increases from 106.7 MPa to 123.7 MPa (an increase of 15.93%). This observation underscores the crucial role of the multiple cementitious system in optimizing strength development.
- Mechanism of toughness improvement through multiple cementitious system. The introduction of CAC into the binary binder system significantly reduces the flexural and compressive energy absorption capacities and overall toughness of SUHPC. However, the ternary system effectively mitigates this degradation through the addition of C$. As the C$ content increases, the compressive toughness index ($E_2$) of the ternary system improves by 1.06%, 5.33%, 6.24%, and 9.51%, while the flexural toughness index ($E_3$) increases by 0.43%, 1.21%, 2.22%, and 6.14%, respectively. This phenomenon suggests that the interaction between C$ and the hydration products of CAC enhances the internal microstructure of SUHPC, thereby improving the material's ductility and deformation capacity.

- Interaction between accelerators and multiple cementitious systems. Although alkali-free accelerators can significantly enhance the early strength of SUHPC, they adversely affect its long-term mechanical properties. Notably, the response of various binder systems to accelerators varies significantly. The accelerators reduced the compressive strength of ordinary SUHPC by 19.8%, while the binary system exhibited only a 2.7% decrease. This observation confirms that multiple cementitious materials can effectively mitigate the strength degradation associated with the use of accelerators.

# Chapter 6 Spalling resistance of SUHPC under elevated temperatures


## *Abstract:*

Conventional sprayed ultra-high-performance concrete (SUHPC) based on Portland cement is prone to explosive spalling at elevated temperatures, posing a serious threat to structural integrity and safety. To address this issue, the present study develops a novel spalling-resistant SUHPC incorporating a Portland cement–calcium aluminate cement–gypsum (PC–CAC–C$) ternary system and reinforced with calcium sulfate whiskers (CSW) and steel fibers. The results reveal that the ternary system still retains thermally stable crystalline phases, such as $Al_2O_3$, $C_{12}A_7$, and wollastonite, even after exposure to 1000 °C. The ternary system increases the capillary porosity of SUHPC within the 20 nm to 10 μm range, accompanied by an increase in total porosity from 9.70% to 12.18% compared to PC-based system. The incorporation of CSW into the ternary system enhances the formation of hydration products and pore filling, which strengthens the CSW–matrix bond and increases flexural strength by 27.81%. In the PC–CAC–C$ system, the synergistic effect of CSW and steel fibers establishes a homogeneous network for vapor pressure relief, which significantly enhances the spalling resistance and residual mechanical performance of SUHPC at elevated temperatures. Conventional PC-based SUHPC undergoes severe explosive spalling under high-temperature exposure. In contrast, the PC–CAC–C$-based SUHPC maintains its structural integrity even after exposure to 1000 °C, retaining a high residual compressive strength of 45.78 MPa and a flexural strength of 7.35 MPa.



This chapter is partially published elsewhere:

J. He, Y.S. Liu, X. Ling, H.Y. Wang, Z.Y. Tang, Z.R. Chen, and Q.L. Yu, Spalling resistance of SUHPC based on PC-CAC-C$ at elevated temperature: Role of whiskers and steel fibers. Construction and Building Materials, 507 (2026), 145100.

## 6.1 Introduction

Sprayed ultra-high-performance concrete (SUHPC), with its excellent durability and adaptability to rapid construction of geometrically complex sections, demonstrates strong potential for application in the field of rapid repair materials [25, 232]. Due to its low porosity and dense microstructure comparable to UHPC, SUHPC tends to retain vapor under elevated temperatures [35, 87]. This results in high internal pressure buildup and makes it more susceptible to explosive spalling compared to ordinary shotcrete. Accordingly, exploring mitigation strategies and mechanisms for high-temperature spalling is crucial for extending the applicability of SUHPC in fire-related conditions.

Recent studies have explored multiple approaches to enhance the high-temperature resistance of UHPC. Among existing mitigation strategies, incorporating polypropylene (PP) fibers has proven effective in alleviating explosive spalling by creating vapor escape channels upon melting of PP fibers at 150–200 °C [88]. Nevertheless, the associated formation of macro-voids can adversely affect the residual strength and long-term durability of UHPC [38, 233, 234]. The high thermal conductivity of steel fibers may intensify internal temperature gradients within concrete, thereby increasing localized thermal stresses [22]. However, steel fibers can retain their crack-bridging capability at elevated temperatures [40], contributing to improved residual strength and toughness of UHPC [235]. The hybrid incorporation of steel fibers and PP fibers can partially mitigate strength reduction, particularly when using optimized dosages such as 2% steel and 0.15% PP fibers [236]. However, the adverse structural effects caused by PP fiber melting remain unresolved. Accordingly, tailoring the binder composition to develop a refined matrix with uniformly distributed fine pores emerges as a promising alternative for improving the high-temperature spalling resistance of SUHPC.

Calcium aluminate cement (CAC) is widely used in high-temperature-resistant concrete structures due to its excellent thermal stability, as it can withstand temperatures exceeding 1580 °C [237]. The high-temperature spalling resistance of CAC-based concrete is primarily associated with the presence of alumina phases, which generate additional porosity upon heating, thereby facilitating the release of internal vapor pressure during exposure to elevated temperatures [136]. Specifically, the hydration products of CAC, such as $CAH_{10}$ and $C_2AH_8$, are metastable and tend to convert into the stable phase $C_3AH_6$ at elevated temperatures. This transformation is commonly referred to as the conversion process of CAC [200]. Nevertheless, an excessive dosage of CAC can intensify the detrimental effects of the conversion process, such as strength loss and elevated cost. To minimize these drawbacks, previous studies have recommended limiting the CAC content to no more than 400 kg/m³ and maintaining a water-to-binder ratio below 0.40 [238]. Previous studies have demonstrated that a critical dosage of CAC can delay not only the silicate reaction but also the renewed dissolution of $C_3A$ in PC [217]. However, it has also been reported that the addition of calcium sulfate (C$) to a PC–CAC mixture can effectively counteract the CAC-induced delay in the silicate reaction [239]. In PC-CAC-C$ ternary system, the dissolution of C$ provides $SO_4^{2-}$ ions, which, at a very early stage, rapidly react with $Ca^{2+}$ and $AlO_2^-$ released from CAC to form a substantial amount of ettringite (AFt). This process not only enhances early-age strength but also rapidly consumes aluminate ions in the pore solution, thereby mitigating their inhibitory effect on $C_3S$ dissolution,

ultimately restoring or even accelerating the main hydration process of the silicate phase [240]. In this context, a ternary binder system comprising Portland cement (PC), calcium aluminate cement (CAC), and gypsum (C$), with a limited CAC content, may offer a promising pathway for improving SUHPC performance under low water-to-binder conditions and elevated temperatures. Our previous research has demonstrated that the ternary binder system (PC-CAC-C$) exhibits excellent mechanical performance when the C$/CAC ratio is 0.5 [44]. However, investigations into the effect of such a system on the high-temperature spalling resistance of concrete remain limited, particularly in the case of SUHPC.

To enhance the residual strength of concrete after high-temperature exposure, reinforcing materials such as steel fibers, carbon fibers, calcium carbonate whiskers, and calcium sulfate whiskers are commonly used. However, calcium carbonate whiskers decompose at approximately 750 °C, releasing $CO_2$, which increases internal pore pressure and consequently elevates the risk of explosive spalling in concrete at elevated temperatures [241]. Carbon fibers, although effective, are prohibitively expensive, limiting their large-scale application in engineering practice [242]. In contrast, calcium sulfate whiskers (CSW), produced from recycled gypsum waste, are abundant, cost-effective, and exhibit excellent high-temperature resistance [243, 244]. CSW begin to dehydrate at approximately 100–200 °C, eventually transforming into anhydrous gypsum crystals that remain thermally stable until decomposition occurs at 1300–1450 °C [245]. Furthermore, the surface of CSW can react with CAC to form ettringite (AFt), which is expected to enhance CSW–matrix interfacial bonding and thereby improve residual strength after high-temperature exposure. Steel fibers effectively bridge cracks and improve toughness at temperatures up to their critical threshold of approximately 600 °C. Beyond this threshold, however, their yield strength decreases rapidly and their toughening capacity is markedly reduced [246]. Therefore, steel fibers play a dominant role at low to moderate temperatures, whereas CSW can compensate for their performance loss at higher temperatures. The multi-scale synergistic toughening mechanism of CSW and steel fibers holds significant research value for enhancing the residual strength of SUHPC under high-temperature conditions. However, relevant studies remain scarce.

This chapter introduces a PC–CAC–C$ ternary system into SUHPC with the aim of modifying its pore structure under high-temperature conditions to promote vapor pressure release and enhance resistance to explosive spalling. To enhance the residual mechanical performance of SUHPC at elevated temperatures, this study further examines the effect of CSW and steel fibers on the spalling behavior of SUHPC incorporating the PC–CAC–C$ ternary system, in comparison with conventional PC-based SUHPC. QXRD, SEM, TGA, mechanical tests, MIP, and micro-XCT are employed for characterization. The underlying mechanisms by which the ternary binder system, CSW, and steel fibers enhance the spalling resistance and residual strength of SUHPC after high-temperature exposure are systematically investigated and clarified in this study.

## 6.2. Materials and experiments

### 6.2.1 Raw materials and mix proportions

In this chapter, P-SUHPC refers to conventional SUHPC mixture with portland cement as the primary binder. According to our previous study [44], the optimal mix proportion of the ternary binder system (PC–CAC–C$) resulted in the highest measured early-age (3 h) and later-age strengths, reaching 15.11 MPa and 121.4 MPa, respectively. Therefore, this optimal proportion was adopted for the preparation of T-SUHPC in the present study. T-SUHPC refers to the ternary system (PC-CAC-C$), in which 20 % of the portland cement (PC) was replaced by calcium aluminate cement (CAC), and 10 wt% of the PC was substituted with gypsum (C$). CEM I 52.5R (PC, supplied by Heidelberg Materials), commercial calcium aluminate cement (CAC), and gypsum ($CaSO_4 \cdot 2H_2O$, abbreviated as C$) as the primary cementitious components to prepare the ternary binder system. Silica fume (microsilica, MS) and fly ash cenosphere (FAC) were added as supplementary cementitious materials to enhance the composite performance.

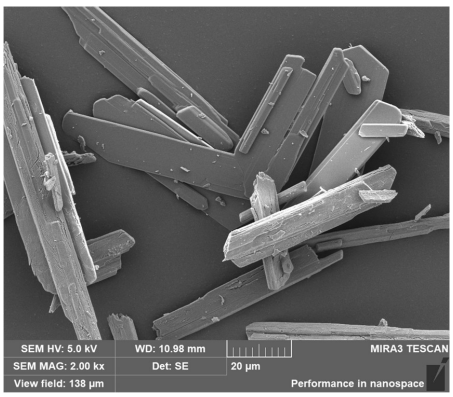


Fig. 6.1. The morphology of the CSW.

Table 6.1. Chemical composition of raw materials.

| Oxide (wt%) | PC | CAC | C$ | MS | FAC | CSW |
|---|---|---|---|---|---|---|
| $Al_2O_3$ | 4.98 | 53.31 | 0.20 | 0.23 | 17.89 | 1.68 |
| CaO | 64.61 | 34.28 | 43.3 | 0.41 | 8.20 | 38.34 |
| $SiO_2$ | 20.18 | 6.96 | 0.32 | 94.68 | 55.57 | 4.23 |
| MgO | 2.19 | 0.37 | 1.37 | 0.43 | 1.02 | 2.10 |
| $Fe_2O_3$ | 3.24 | 1.90 | 0.10 | 0.17 | 11.31 | 0.40 |
| $K_2O$ | 0.53 | 0.41 | 0.01 | 0.83 | 2.74 | 0.27 |
| $P_2O_5$ | 0.74 | 0.15 | - | 0.19 | 1.59 | - |
| $Na_2O$ | 0.27 | 0.12 | - | 0.15 | 0.48 | 0.12 |
| $TiO_2$ | 0.25 | 1.67 | - | - | - | - |
| $SO_3$ | 3.01 | 0.83 | 53.7 | 0.81 | 1.20 | 52.85 |
| LOI | 1.56 | 1.60 | 1.59 | 2.33 | 1.03 | 3.10 |

Table 6.2. Physical properties of CSW.

| Parameters | Specific density | Moisture content | Dry bulk density | Length (mean) |
|---|---|---|---|---|
| CSW | 2710 kg/m$^3$ | 4.86% | 1090 kg/m$^3$ | 80 µm |

Commercial calcium sulfate dihydrate whiskers ($CaSO_4 \cdot 2H_2O$ whisker, abbreviated as CSW) with lengths ranging from 60 to 120 μm were incorporated at a dosage of 4 wt% relative to the total binder mass. The microstructural features of the plate-shaped CSW are presented in Fig. 6.1. Copper-coated steel fibers with a diameter of 0.22 mm and a length of 6 mm were incorporated. The chemical compositions and physical properties of powder materials are illustrated in Table 6.1 and Table 6.2.

Table 6.3. Mix proportion of SUHPC mixtures ($kg/m^3$).

| | P-SUHPC | | | | T-SUHPC | | | |
|---|---|---|---|---|---|---|---|---|
| **Materials** | **P0** | **P-CSW** | **P-SF** | **P-CSWSF** | **T0** | **T-CSW** | **T-SF** | **T-CSWSF** |
| PC | 791 | 791 | 791 | 791 | 553.7 | 553.7 | 553.7 | 553.7 |
| CAC | - | - | - | - | 158.2 | 158.2 | 158.2 | 158.2 |
| C$ | - | - | - | - | 79.1 | 79.1 | 79.1 | 79.1 |
| MS | 179 | 179 | 179 | 179 | 179 | 179 | 179 | 179 |
| FAC | 144 | 144 | 144 | 144 | 144 | 144 | 144 | 144 |
| QS-1 | 192 | 192 | 192 | 192 | 192 | 192 | 192 | 192 |
| QS-2 | 510 | 510 | 510 | 510 | 510 | 510 | 510 | 510 |
| QS-3 | 412 | 412 | 412 | 412 | 412 | 412 | 412 | 412 |
| Water | 188.3 | 188.3 | 188.3 | 188.3 | 195 | 195 | 195 | 195 |
| SP | 47 | 47 | 47 | 47 | 49.5 | 49.5 | 49.5 | 49.5 |
| CSW | - | 44.6 | - | 44.6 | - | 44.6 | - | 44.6 |
| Steel fiber | - | - | 156 | 156 | - | - | 156 | 156 |

Three types of quartz sand with continuous gradation were employed as fine aggregates, categorized by particle size ranges: 0.38-1.2 mm (QS-1), 0.2-0.47 mm (QS-2), and 0-0.22 mm (QS-3). To achieve workability of the SUHPC mixture, a polycarboxylate superplasticizer (PCE) with a solid content of 40% was incorporated at 1.9 wt% of the total binder.

To achieve the maximum particle packing of the raw materials in the SUHPC mix design [176, 177], SUHPC reference was formulated based on the target curve illustrated in Fig. 4.1 of Section 4. The corresponding mix proportions are detailed in Table 6.3. Specifically, T0 refers to the control group of T-SUHPC without CSW or steel fibers. T-CSW denotes T-SUHPC incorporating 4 wt% CSW. T-SF represents T-SUHPC with 2 vol% steel fibers. T-CSWSF-1000 corresponds to T-SUHPC containing both 4 wt% CSW and 2 vol% steel fibers, after exposure to 1000 °C. And T-CSWSF-20 refers to the T-CSWSF mixture tested at room temperature (RT, approximately 20 ℃), without thermal exposure.

### 6.2.2 Field spray test and heating regimes

Considering that the spraying process can influence both the porosity and mechanical strength of SUHPC, all specimens in this study were fabricated via field spraying to ensure experimental reliability. The field spraying procedure (see Fig. 4.2) was conducted in accordance with EN 934-5:2007 [181]. At the nozzle, a liquid alkali-free accelerator primarily composed of aluminum sulfate was added at a dosage of 2 wt% relative to the binder content. The full procedure included material weighing, mixing, transport, equipment assembly and loading, mold setup, and final spraying. After demolding, the concrete slabs were cut into SUHPC specimens with dimensions of 150 mm × 150 mm × 150 mm and cured to the designated age.

After reaching the specified curing age, the SUHPC specimens were oven-dried at 80 °C for 24 hours. Subsequently, they were subjected to heat treatment in a muffle furnace at four target temperatures: 250 °C, 500 °C, 750 °C, and 1000 °C. According to the heating regimes illustrated in Fig. 6.2(a), the specimens were continuously heated from room temperature to the target temperature at a rate of 3 °C/min [136, 232], and then allowed to cool naturally to room temperature inside the furnace. As shown in Fig. 6.2(b), steel cages were employed to prevent explosive spalling of SUHPC from damaging the internal components of the muffle furnace.

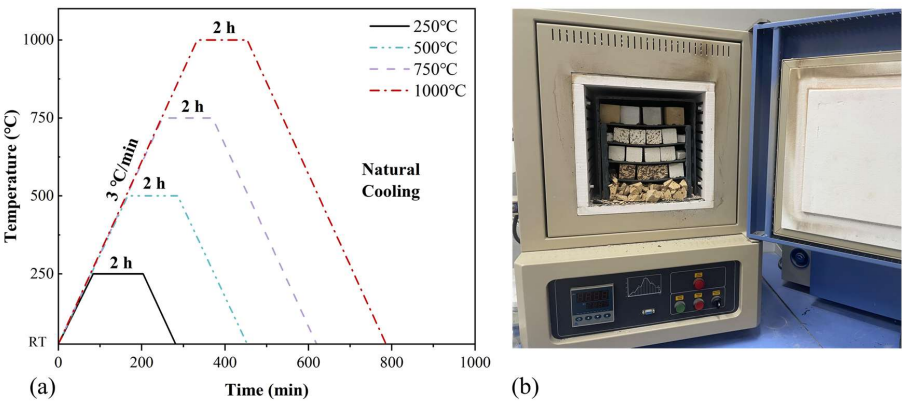


**Fig. 6.2.** (a) Heating profile for SUHPC specimens; (b) Muffle furnace setup.

### 6.2.3 Experimental methods

#### 6.2.3.1 QXRD

Quantitative X-ray diffraction (QXRD) analysis was performed using a Bruker D2 PHASER equipped with the XE-T detector and a cobalt radiation source (λ=1.79 Å). The diffraction patterns were collected over a 2θ range of 5–90°, with an increment of 0.013°. To enable accurate phase quantification, 10 wt% of crystalline silicon was added to each sample as an internal reference material. Rietveld refinement was conducted using the Topas software (version 5.0).

#### 6.2.3.2 TG

Thermogravimetric analysis (TGA) was conducted using a TA Instrument (TA 209 F3 Tarsus). The slurry samples were prepared based on the specified mix proportions and cured for 28 days under standard conditions. Hydration was terminated using isopropanol, followed by drying to obtain powdered samples. Approximately 20 mg of each SUHPC paste sample was subjected to thermogravimetric analysis over a temperature range of 25 to 1000 °C, using a constant heating rate of 10 °C/min.

#### 6.2.3.3 Morphology

The morphologies of bulk SUHPC concrete specimens after high-temperature exposure after high-temperature exposure was observed by a TESCAN MIRA3 equipment. Cubic samples with approximate dimensions of 0.5 $mm^3$ were coated with a thin layer of gold to enhance

conductivity. The instrument offers a resolution of 1.2 nm, a magnification range of 2 to 1,000,000 times, and an adjustable accelerating voltage from 0.5 to 30 kV.

#### 6.2.3.4 Spalling and crack observation

After the heat treatment, the spalling phenomenon of SUHPC was observed. A crack observation instrument was utilized to investigate the distribution of surface cracks on SUHPC specimens following high-temperature exposure.

#### 6.2.3.5 Strength

Mechanical testing of the residual flexural and compressive strengths of P-SUHPC and T-SUHPC specimens was carried out according to EN 196-1 [50]. Following each high-temperature exposure, six replicate prism specimens (40 × 40 × 160 $mm^3$) were prepared for each mix design. Flexural strength was first measured using a three-point bending test, and the the fractured halves (40 × 40 × 40 $mm^3$) were collected and utilized for compressive strength testing.

#### 6.2.3.6 MIP

Mercury intrusion porosimeter (MIP) was conducted to examine the pore characteristics of P-SUHPC and T-SUHPC specimens under ambient conditions. This analysis aimed to further investigate the effects of CSW whiskers and the ternary system on the pore structure of T-SUHPC. The pore structure of the hardened SUHPC specimens was characterized by mercury intrusion porosimetry (MIP) using an AutoPore IV 9510 (Micromeritics, USA). The measurable pore diameter ranged from 3 nm to 400 μm.

#### 6.2.3.7 Micro-XCT

Micro X-ray Computed Tomography (Micro-XCT) analysis was performed using a system provided by SCANCO Medical AG (Switzerland) to investigate the internal structure of SUHPC specimens after high-temperature exposure. SUHPC specimens (25 × 25 × 25 $mm^3$) were scanned using micro-computed tomography, yielding 1800 sequential 2D slices. The images were reconstructed into a 3D model, and pore characteristics were analyzed with IPL software for visualization and quantitative assessment.

## 6.3 Results and analysis

### 6.3.1 Effect of CSW in hydration products of P-SUHPC under elevated temperatures

Fig. 6.3(a) and (b) present the XRD patterns of pure PC pastes (P-SUHPC) specimens without and with CSW, respectively, after exposure to elevated temperatures. At room temperature (RT, approximately 20 °C), unhydrated clinker phases ($C_3S$, $C_2S$, $C_4AF$) and hydration products such as CH and ettringite were identified, as shown in Fig. 6.3(a). Gypsum crystals were detected in the P-SUHPC sample incorporating CSW. Compared to P0-20, P-CSW-20 exhibited a more pronounced AFt peak, indicating that CSW incorporation enhanced ettringite formation. This is attributed to the surface dissolution of the CSW whiskers, which locally increased the concentration of sulfate ions in the surrounding pore solution. These sulfate ions rapidly reacted

with the aluminum source from the $Al_2(SO_4)_3$ based alkali-free accelerator, resulting in localized and accelerated formation of AFt at the whisker surfaces.

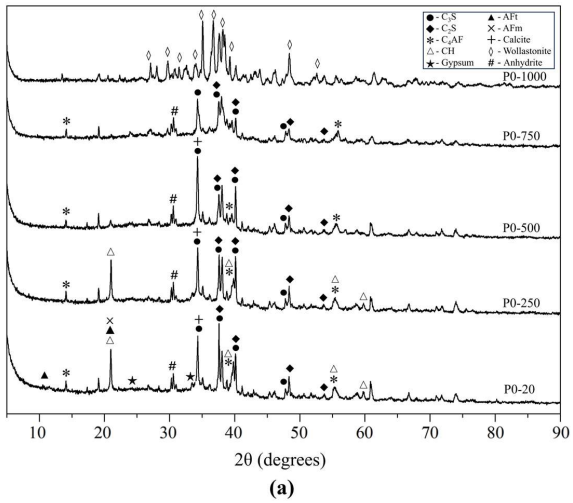


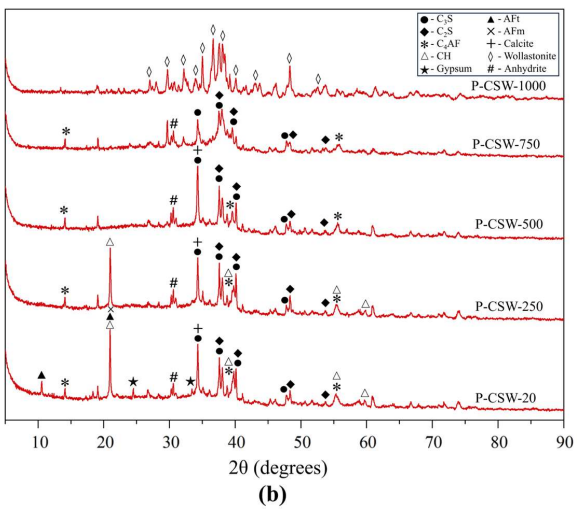


Fig. 6.3. XRD patterns after exposure to elevated temperatures: (a) P0 paste; (b) P-CSW paste.

At 250 °C, the AFt phase was no longer detected, which can be attributed to its decomposition occurring between 80 °C and 170 °C [247]. Additionally, the disappearance of the dihydrate gypsum peak accompanied by an increase in the anhydrite peak was observed. As reported in [248], CSW undergoes a phase transition to hemihydrate ($CaSO_4 \cdot 0.5H_2O$) at approximately 120–130 ℃. Further heating leads to complete dehydration and the formation of anhydrite at around 190 °C, as given by:

$$C\bar{S}H_2 \xrightarrow{120\sim130℃} C\bar{S}H_{0.5} + 1.5H \tag{6.1}$$

$$C\bar{S}H_{0.5} \xrightarrow{190℃} C\bar{S} + 0.5H \tag{6.2}$$

At 500 ℃, the CH phase was no longer detected due to its decomposition within the range of 400–500 °C. At 750 °C, calcite disappeared, which can be attributed to its thermal decomposition occurring between 600 °C and 750 °C. At 1000 °C, the C–S–H gel decomposed and crystallized into wollastonite [134]. Although gypsum crystals possess a relatively high melting point (approximately 1460 °C) [249], no crystalline peaks corresponding to anhydrite were detected at this temperature. This lack of anhydrite peaks may be associated with a phase transformation or the formation of an amorphous phase.

Table 6.4. Phase quantification by QXRD of P-SUHPC at 20 ℃ (wt%).

| Mix/Phases | AFt | AFm | Gypsum | Anhydrite | Amorphous |
|---|---|---|---|---|---|
| P0-20 | 5.7±0.3 | 1.0±0.1 | 0.9±0.1 | 0.3±0.2 | 59.8±1.0 |
| P-CSW-20 | 6.5±0.1 | 0.7±0.3 | 4.2±0.2 | 0.7±0.1 | 55.3±1.6 |

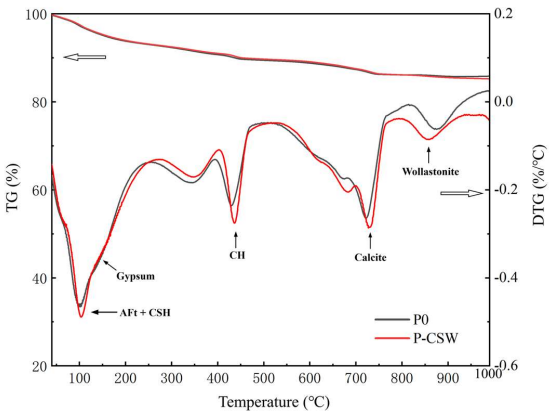


Fig. 6.4. TG/DTG curves of P-SUHPC.

Quantitative XRD analyses further provided the phase contents of AFt, AFm, gypsum, and anhydrite in P0 and P-CSW at elevated temperatures, as summarized in Table 6.4. By comparing the specific phase contents of P-CSW-20 and P0-20, the effect of CSW on the hydration products of PC-SUHPC under elevated temperatures can be analyzed. The contents of gypsum and anhydrite in P-CSW-20 were significantly higher than those in P0-20, indicating that most of the CSW remained intact, with minor surface dissolution and partial consumption through reaction. Compared to P0-20, the AFt content in P-CSW-20 increased from 5.7 wt% to 6.5 wt%. These differences may be linked to the partial surface dissolution of CSW, which released sulfate and calcium ions. These ions rapidly reacted with the abundant $Al(OH)_4^-$ provided by the alkali-free accelerator, leading to the localized formation of a large amount of AFt at the whisker surfaces, as described in Eq. (4.6) in Chapter 4.

Fig. 6.4 presents the TG/DTG curves of P-SUHPC samples without CSW (P0) and with CSW (P-CSW). The DTG curve can be divided into four stages, with four characteristic peaks corresponding to the thermal decomposition processes in each stage. The first stage (ranging from RT to 350 °C) is primarily attributed to the loss of physically bound water, along with the dehydration of ettringite (AFt) and C–S–H gel [250]. In addition, a minor peak observed between 100 °C and 150 °C may be related to the dehydration of calcium sulfate whiskers [199]. The second stage (ranging from 350 °C to 450 °C) corresponds to the decomposition of calcium

hydroxide (CH) [103, 104]. The third stage (from 450 °C to 700 °C) is associated with the decarbonation of calcite ($CaCO_3$) [251]. The fourth stage (ranging from 800 °C to 1000 °C) corresponds to the formation of wollastonite. Overall, the TG/DTG curves of both samples were largely consistent, supporting the XRD findings that CSW underwent only limited surface dissolution and partial consumption during hydration, with minimal impact on the overall content of hydration products in the matrix.

### 6.3.2 Effect of CSW in the hydration products of ternary system-based SUHPC under elevated temperatures

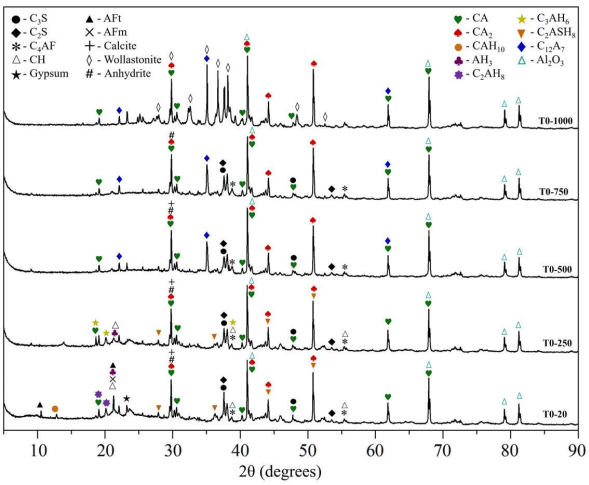


Fig. 6.5. XRD patterns after exposure to elevated temperatures of T0 paste.

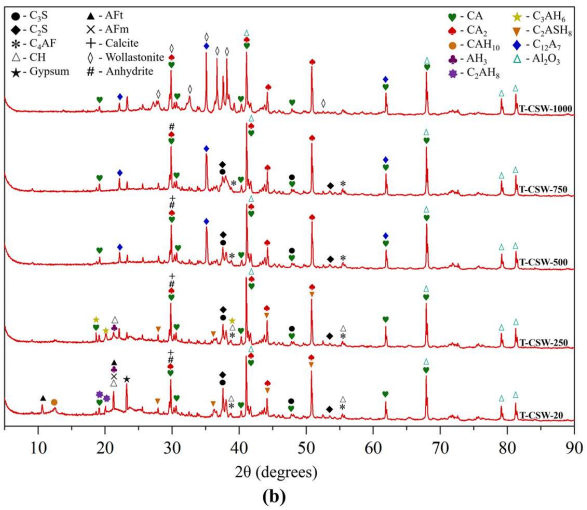


Fig. 6.6. XRD patterns after exposure to elevated temperatures of T-CSW paste.

Fig. 6.5 and Fig. 6.6 display the XRD patterns of PC-CAC-C$ ternary pastes (T-SUHPC) without CSW (T0) and with CSW incorporation (T-CSW), respectively, after exposure to

elevated temperatures. The phase evolution at different temperatures is discussed as follows: (i) 20 °C, (ii) 250 °C, (iii) 500 °C, (iv) 750 °C, and (v) 1000 °C.

(i) At 20 °C, unhydrated clinkers from both CAC (CA, $CA_2$) and PC ($C_3S$, $C_2S$, $C_4AF$) were identified. The main hydration products included $CAH_{10}$, $C_2AH_8$, $C_2ASH_8$, $AH_3$, CH, and ettringite. In addition, the presence of gypsum was detected due to the incorporation of CSW. Strätlingite ($C_2ASH_8$) was also identified, which is considered to form through further reactions among CAC, silica fume, and FAC [252].

(ii) At 250 °C, the disappearance of $CAH_{10}$ and $C_2AH_8$ phases was observed, accompanied by the emergence of diffraction peaks corresponding to $C_3AH_6$. This transformation is attributed to the dehydration of $CAH_{10}$ and $C_2AH_8$ within the temperature range of 120–200 °C, resulting in the formation of $C_3AH_6$, as described in Eq. (4.10) and Eq. (4.11) in Chapter 4 [253]. The AFt phase was no longer detected, which can be attributed to its decomposition within the temperature range of 80–170 °C [247].

(iii) At 500 °C, the formation of $C_{12}A_7$ was identified, along with the disappearance of $C_3AH_6$ and $AH_3$ phases. This transformation is attributed to the dehydration of $C_3AH_6$ and $AH_3$ at approximately 450 °C, resulting in the generation of $C_{12}A_7$, as given by [254]:

$$4C_3AH_6 + 3AH_3 \rightarrow C_{12}A_7 + 33H \tag{6.3}$$

A noticeable increase in the intensity of anhydrite peaks was also observed, which is associated with the complete dehydration of CSW (gypsum crystals) into anhydrite crystals. Additionally, $C_2ASH_8$ was converted to $C_2AS$ through dehydration [255]. The CH phase was no longer detected, as it decomposes between 400 °C and 500 °C.

(iv) At 750 °C, the disappearance of calcite was observed, which is attributed to its decomposition within the temperature range of 600–750 °C.

(v) At 1000 °C, an increase in the peak intensities of CA and $CA_2$ was detected, suggesting that part of the $C_{12}A_7$ phase reconverted to CA and $CA_2$ at elevated temperatures. The C–S–H gel decomposed and subsequently crystallized into wollastonite [134]. High-temperature-resistant $Al_2O_3$ was also identified. However, no crystalline peaks corresponding to anhydrite were observed at 1000 °C, possibly due to phase transformation into an amorphous phase. $Al_2O_3$ crystals remained stable across all temperature conditions. Even at 1000 °C, thermally stable hydration products such as $C_{12}A_7$ and wollastonite, along with cement clinkers like CA and $CA_2$, were still present in the ternary system.

To further investigate the effect of CSW on the hydration products of PC-CAC-C$ ternary pastes (T-SUHPC) under elevated temperatures, a quantitative XRD analysis was performed to determine the contents of AFt, AFm, gypsum, and anhydrite, as summarized in Table 6.5. The contents of gypsum and anhydrite in T-CSW-20 were significantly higher than those in T0-20, indicating that most of the CSW remained intact, with only limited surface dissolution. Therefore, the accumulation of hydration products at the CSW surfaces may enhance the interfacial bonding between the whiskers and the matrix at various temperatures. This aspect will be further discussed in Section 6.3.5. Compared to T0-20, the AFt content in T-CSW-20

increased from 15.8 wt% to 17.5 wt%, which can be attributed to the surface reaction between CA (from CAC) and CSW, leading to the formation of AFt and $AH_3$, as described in Eq. (4.3) in Chapter 4.

Table 6.5. Phase quantification by QXRD of T-SUHPC at 20℃ (wt%).

| Mix/Phases | AFt | AFm | Gypsum | Anhydrite | Amorphous |
|---|---|---|---|---|---|
| T0-20 | 15.8±0.6 | 2.1±0.1 | 1.1±0.2 | 0.5±0.4 | 56.3±1.1 |
| T-CSW-20 | 17.5±0.1 | 1.9±0.4 | 4.1±0.1 | 0.6±0.1 | 54.7±0.4 |

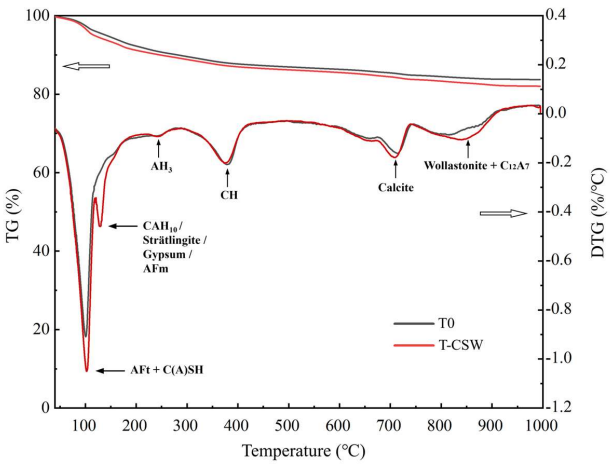


Fig. 6.7. TG/DTG curves of PC-CAC-C$ based SUHPC.

As shown in Fig. 6.7, the DTG curves of the ternary pastes exhibit a pronounced peak around 100 °C, within the range of 25–130 °C. This peak is attributed to the release of free water and physically adsorbed water from Aft and C(A)SH. The second peak appeared between 100 °C and 150 °C, which is typically associated with the dehydration of gypsum [33, 199]. Previous study has indicated that the peak at 125 °C may be related to the dehydration of $CAH_{10}$ [254]. A broad peak observed within the range of 160–200 °C indicates the presence of strätlingite ($C_2ASH_8$) and a small amount of AFm [203], which is consistent with the XRD results. A small peak appeared around 250 °C on the DTG curve, corresponding to the decomposition of aluminum hydroxide ($AH_3$) [40].

In addition, DTG analysis revealed a peak near 400 °C attributed to calcium hydroxide (CH), and another in the range of 600–750 °C associated with the decomposition of calcite. Peaks were also detected between 800 and 1000 °C, corresponding to the thermal decomposition of wollastonite and $C_{12}A_7$, which is consistent with the XRD results.

### 6.3.3 Spalling

Fig. 6.8 presents the spalling behavior of P-SUHPC and T-SUHPC following exposure to elevated temperatures. Supplementary images showing specimens after exposure to other temperatures are presented in Fig. A2 and A3 of Appendix A. In the P-SUHPC, the reference specimen (P0) underwent severe explosive spalling at 500 °C, producing small debris fragments all less than 3 cm in length. P-CSW exhibited no spalling until 1000 °C, indicating that the incorporation of CSW raised the spalling onset temperature compared to P0. Compared with

P0, the incorporation of steel fibers increased the spalling onset temperature of P-SF from 500 °C to 750 °C. In contrast, the P-CSWSF specimen, incorporating both whiskers and steel fibers, remained intact even after exposure to 1000 °C. Numerous brownish marks were observed on the surface, attributed to chemical reactions between the steel fibers and oxidizing gases at 1000 °C. These reactions led to the formation of oxide layers, including wüstite (FeO), hematite ($Fe_2O_3$), and magnetite ($Fe_3O_4$), resulting in the appearance of visible oxide scales [40]. As the temperature approaches 1000 °C, internal oxidation of the steel fibers may also occur, forming complex oxides such as $Fe_2SiO_4$ [256]. The rapid growth of these oxide layers can induce volumetric expansion, which may further promote intrusion into the surrounding cementitious matrix [40]. In the T-SUHPC, the spalling onset temperature of the ternary mix (T0) increased from 500 °C to 750 °C compared with the P0. The T-CSWSF specimen, which incorporated both CSW and steel fibers, also remained visually intact after exposure to 1000 °C. These results demonstrate that both the individual and combined effects of the ternary binder system, CSW, and steel fibers contributed to enhanced spalling resistance in SUHPC.

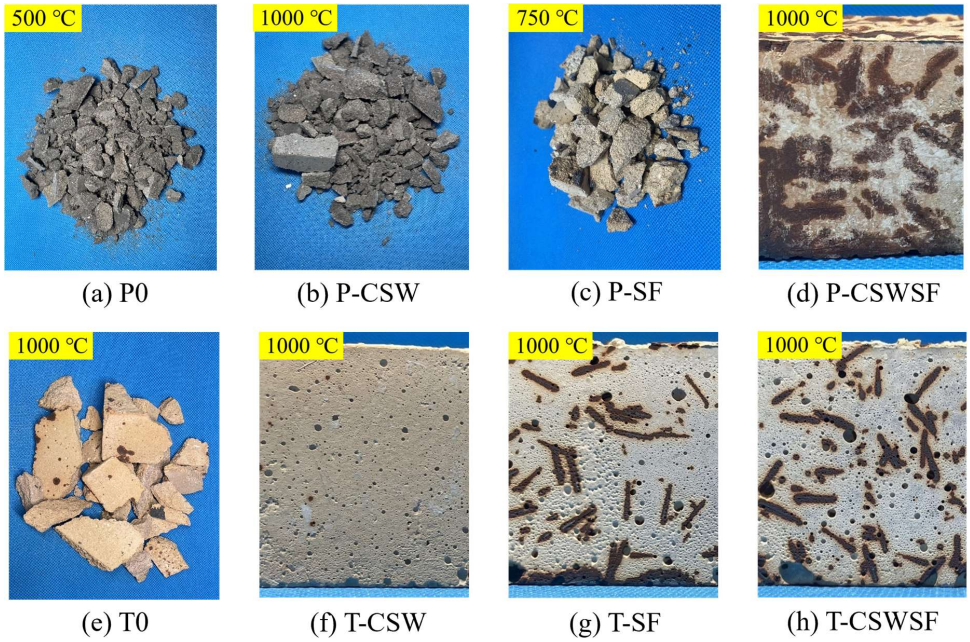


Fig. 6.8. Spalling observation of SUHPC samples at elevated temperatures.

Surface cracking patterns of P-SUHPC and T-SUHPC specimens after exposure to elevated temperatures are shown in Fig. 6.9. P0 exhibited microcracks at 250 °C, while visible surface cracks in T0 appeared only at 500 °C, indicating that the ternary binder system raised the cracking threshold temperature. In the specimens incorporating CSW, P-CSW and T-CSW exhibited no significant surface cracking at 250 °C and 500 °C, respectively. Pronounced radial cracks were first observed at 500 °C for P-CSW and 750 °C for T-CSW. This indicates that the use of CSW can further elevate the surface cracking initiation temperature in both PC-based and ternary systems. Network-like cracks were observed in T-SF at 500 °C, but the crack width was reduced compared to that of T0 at the same temperature. This suggests that the

incorporation of steel fibers contributed to mitigating surface cracking. Both P-CSWSF and T-CSWSF exhibited dense networks of fine surface cracks at 1000 °C, as shown in the Fig. 6.9 (g) and (h). This indicates that the synergistic effect of CSW and steel fibers provided effective crack control in both PC-based and ternary binder systems under high-temperature exposure.

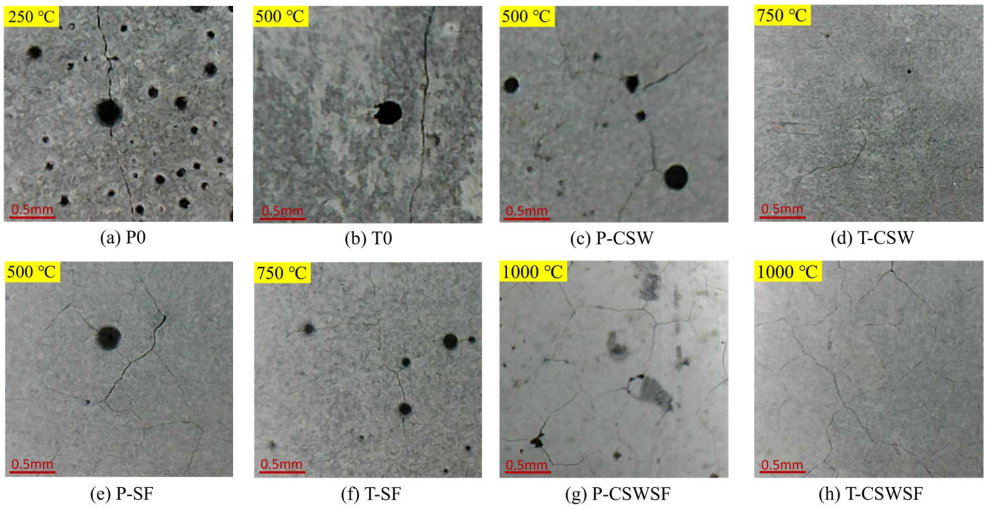


(a) P0 (b) T0 (c) P-CSW (d) T-CSW

(e) P-SF (f) T-SF (g) P-CSWSF (h) T-CSWSF

Fig. 6.9. Representative magnified images of surface cracks in SUHPC.

### 6.3.4 Morphology

The micro-morphologies of the SUHPC samples after high-temperature exposure are presented in Fig. 6.10. After exposure to 500 °C, interfacial gaps were observed between the steel fibers and the matrix in P-CSWSF, along with microcracks in the surrounding matrix (Fig. 6.10(a)). In contrast, a dense ITZ between the fiber and the matrix was observed in T-CSWSF (Fig. 6.10(b)). The influence of fiber-matrix bond on flexural performance will be further discussed in Section 6.3.5.

After exposure to 1000 °C, SEM observations revealed that the CSW in T-CSWSF remained and appeared to deflect the propagation path of microcracks (Fig. 6.10(d)). This suggests that CSW played a bridging role in crack development even at 1000 °C. Previous studies have shown that deflected cracks require more energy to propagate than straight ones [255]. CSW enhances the toughness of SUHPC through mechanisms such as whisker pull-out, crack deflection, and bridging, which dissipates fracture energy and slows down crack growth. Compared with T-CSWSF, CSW in P-CSWSF did not exhibit a pronounced effect on altering the propagation path of microcracks, and the bonding with the surrounding matrix appeared to be weaker (Fig. 6.10(c)). Therefore, the crack deflection mechanism and the bridging action of CSW across cracks at 1000 °C in the ternary system remains effective, providing notable toughening and crack resistance compared with the PC-based system (P-CSWSF). This also explains the relatively high residual strength observed in T-CSW and T-CSWSF, as discussed in Section 6.3.5.

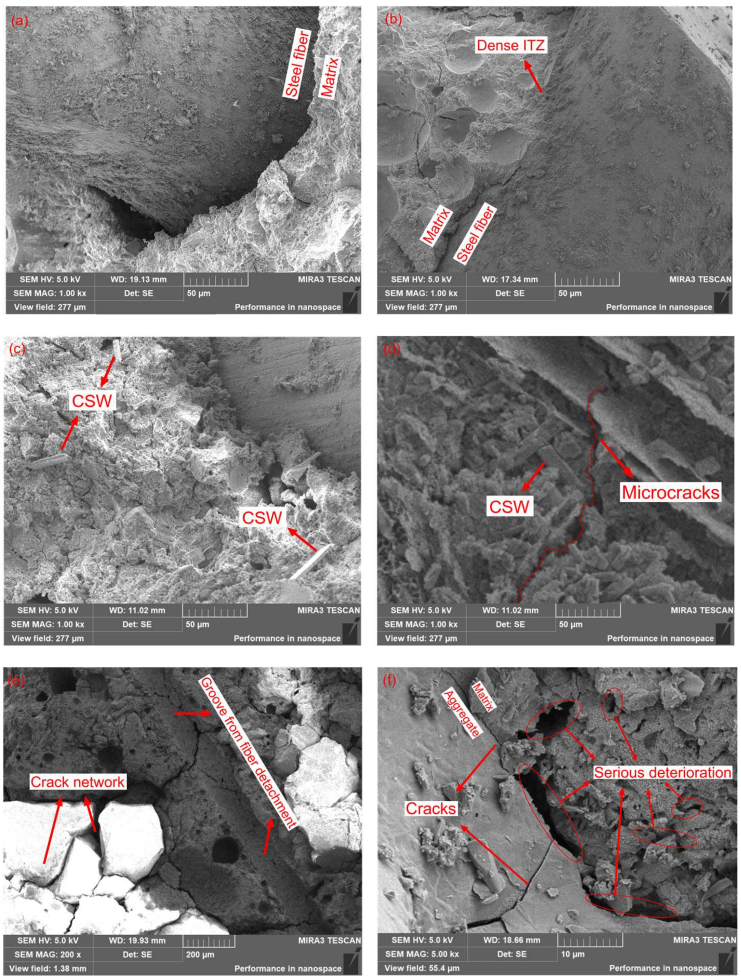


Fig. 6.10. Morphology of SUHPC samples at elevated temperatures.

At 1000 °C, numerous cracks were observed in the matrix surrounding the steel fibers in T-CSWSF (Fig. 6.10(e)). This phenomenon is attributed to the thermal expansion mismatch between the steel fibers and the matrix at elevated temperatures [257]. In addition, noticeable darkening of the matrix surrounding the steel fibers was observed. This discoloration is attributed to excessive oxidation of the steel fibers at elevated temperatures (600–1000 °C). The resulting oxidation products may infiltrate nearby pores in the cementitious matrix, leading to localized color changes [40], which were also evident at the macroscopic level (Fig. 6.8).

Fig. 6.10(f) further illustrates that a distinct network of microcracks formed in the matrix of T-CSWSF at 1000 °C. These interconnected microcracks, along with the steel fiber–matrix interface and surrounding tangential cracks, created a continuous pathway for vapor release. In addition to cracking, numerous pores were observed in the microstructure, particularly at the aggregate–matrix interface. Cracking at the aggregate–matrix interface is attributed to the thermal deformation mismatch between the aggregates and the matrix, as well as to the decomposition of phases at elevated temperatures, as discussed in Section 6.3.2. The combined

effect of extensive cracking and pore formation significantly contributed to the reduction in residual strength at elevated temperatures.

### 6.3.5 Residual strength

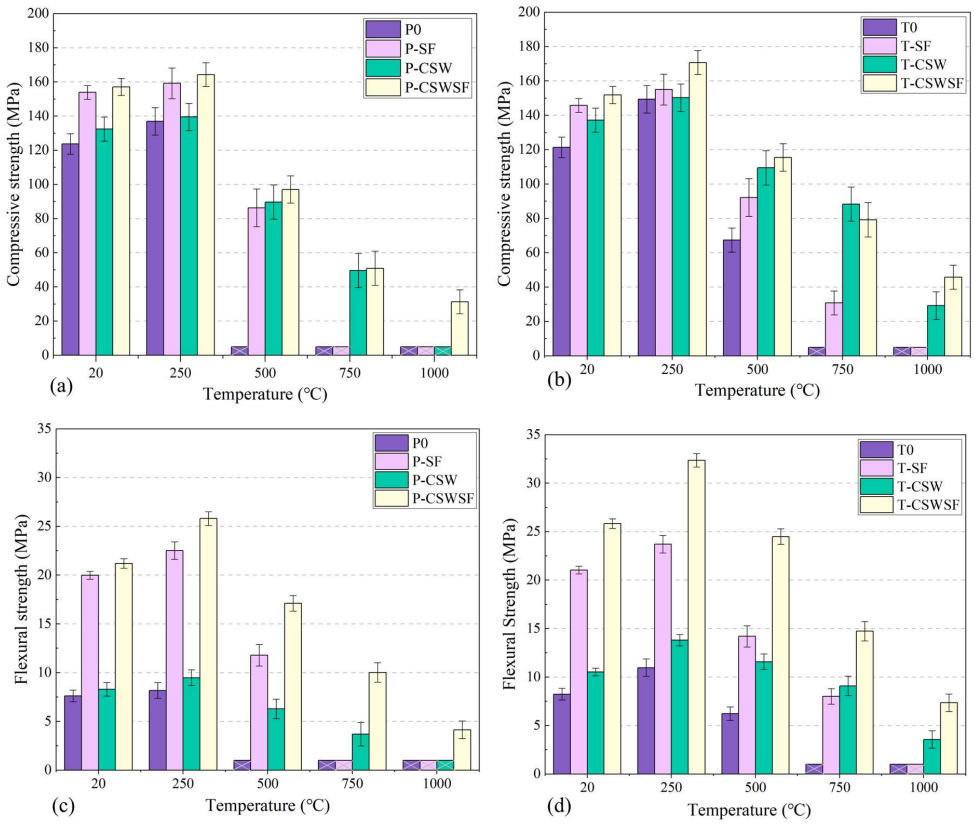


Fig. 6.11. Residual compressive strength (a, b) and residual flexural strength (c, d) of P-SUHPC and T-SUHPC specimens after exposure to high temperatures.

Fig. 6.11 presents the residual compressive and flexural strengths of T-SUHPC and P-SUHPC after exposure to elevated temperatures. At RT, P0-20 and T0-20 exhibited comparable compressive strengths of 123.7 MPa and 121.3 MPa, respectively. At 250 °C, the compressive strength of P0-250 increased by 10.71% compared to P0-20. This improvement is primarily attributed to the continued hydration of cement particles and secondary pozzolanic reactions of fly ash and silica fume, which contributed to a denser matrix microstructure [109]. For T0-250, a more pronounced strength gain of 23.13% was observed relative to T0-20. The observed strength gain is mainly driven by the high reactivity of CAC clinker, which actively reacts with silica fume and fly ash to form additional C–A–S–H gel, thereby enhancing the microstructural densification at elevated temperatures [109]. Explosive spalling occurred in P0 at 500 °C, whereas T0 exhibited comparable spalling behavior at an elevated temperature of 750 °C. As a result, strength data at and beyond these temperatures are partially unavailable.

The incorporation of CSW led to flexural strength increases of 8.78% and 27.81% in P-CSW-20 and T-CSW-20, respectively, compared to P0-20 and T0-20. And the flexural strength enhancement provided by CSW was more pronounced in the ternary T-SUHPC. At 1000 °C, P-CSW experienced explosive spalling, whereas T-CSW maintained a flexural strength of 3.56 MPa. This suggests that CSW formed a stronger and more stable bond with the ternary matrix at high temperatures, thereby enhancing spalling resistance and residual strength compared to the P-SUHPC.

The incorporation of steel fibers significantly enhanced the flexural strength of P-SF and T-SF at room temperature (RT) by 162.20% and 155.33%, respectively, compared with P0 and T0. Increasing the temperature from RT to 250 °C resulted in a 12.71% and 12.64% increase in the flexural strength of P-SF and T-SF, respectively. This indicates that moderate heating can effectively enhance the steel fiber–matrix interfacial bond strength [258]. This improvement is primarily attributed to the continued hydration of partially hydrated cement clinker, which generates additional hydration products that fill the ITZ and pores [259]. However, the steel fiber–reinforced specimens (P-SF, P-CSWSF, T-SF, and T-CSWSF) exhibited significantly reductions in flexural strength at 500 °C compared to 250 °C, by 47.64%, 33.67%, 40.06%, and 24.42%, respectively. This phenomenon is attributed to the thermal incompatibility between steel fibers and the SUHPC matrix, which weakens the bonding at the steel fiber–matrix interface zone (ITZ) [260]. Moreover, steel fibers begin to lose their mechanical performance as the temperature approaches the critical threshold (approximately 600 °C) [40]. This degradation is often accompanied by oxidation, softening, and structural changes [258]. P-CSWSF and T-CSWSF showed markedly less reduction in flexural strength at 500 °C than P-SF and T-SF, respectively, suggesting a synergistic effect between CSW and steel fibers. At 1000 °C, T-CSWSF-1000 retained a high residual compressive strength of 45.78 MPa and a flexural strength of 7.35 MPa, both substantially exceeding those of P-CSWSF-1000. This suggests that the ternary system forms stronger interfacial bonds with both CSW and steel fibers at elevated temperatures, compared to PC-based system.

In summary, the residual mechanical performance of SUHPC was significantly improved by three factors: the ternary binder system, CSW, and steel fibers. Specifically, (i) each factor individually contributed to raising the spalling onset under elevated temperatures; (ii) compared to the PC-based system, the ternary system exhibited stronger interfacial bonding with CSW, which continued to enhance the residual strength even after exposure to 1000 °C; and (iii) the synergistic interaction between CSW and steel fibers within the ternary matrix further mitigated the degradation of residual strength following high-temperature exposure.

### 6.3.6 Pore structure

High-temperature exposure can induce spatially heterogeneous alterations in the pore structure of concrete, leading to deviations between MIP measurements and the actual pore network of heated specimens [254]. Consequently, in this study, MIP was restricted to characterizing the pore structure of SUHPC at room temperature (RT). Micro-XCT analysis was further used to quantify porosity and pore size characteristics of P-SUHPC and T-SUHPC after 1000 °C exposure.

### 6.3.6.1. Pore structure at room temperature

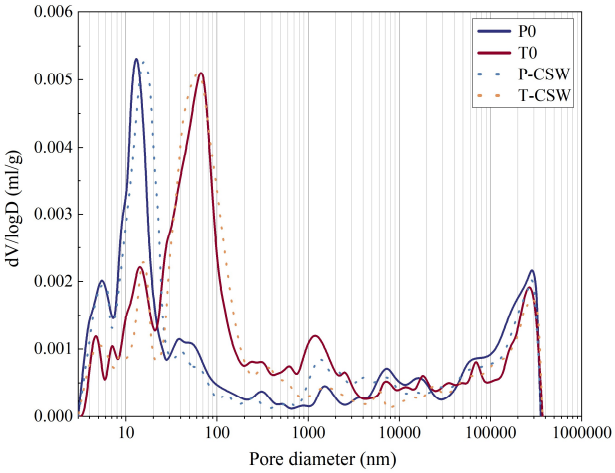


Fig. 6.12. Pore size distribution of SUHPC pastes.

Table 6.6. Pore characteristics of SUHPC as measured by MIP.

| Sample | Median pore diameter (nm) | Porosity (%) | Total intrusion volume (ml/g) |
|---|---|---|---|
| P0-20 | 56 | 9.70 | 0.0412 |
| P-CSW-20 | 77 | 10.37 | 0.0229 |
| T0-20 | 106 | 12.18 | 0.0274 |
| T-CSW-20 | 94 | 11.83 | 0.0391 |

Fig. 6.12 illustrates the effect of CSW on the pore structure of T-SUHPC and P-SUHPC, with the corresponding pore structure parameters summarized in Table 6.6. Compared to P0, the ternary system significantly increased the capillary porosity of T0 in the range of 20 nm to 10 μm, with the total porosity rising from 9.70% to 12.18%. This is attributed to CAC phase conversion, where $CAH_{10}$ and $C_2AH_8$ transform into the stable $C_3AH_6$, leading to an increase in porosity. It has been suggested that an increase in capillary porosity facilitates the release of internal water vapor, thereby enhancing the resistance of concrete to explosive spalling under high temperature exposure [50]. Therefore, the improved spalling resistance of SUHPC in the ternary system can be attributed to the optimization of its pore structure, which helps to reduce the vapor pressure within the concrete matrix.

In P-SUHPC, the incorporation of CSW increased the total porosity from 9.70% to 10.37%, accompanied by a notable rise in pore volume within the 1–10 μm range. Previous research [260] has indicated that pores within this size range are largely associated with residual voids left by the localized dissolution of CSW. The formation of hydration products around the CSW was insufficient to fully fill these voids, leading to an increase in the porosity. This indicates that the interfacial bonding between CSW and the matrix in P-SUHPC remained weak. This is confirmed by the results in Section 6.3.5, where the flexural strength of P-CSW increased by only 14.35% compared to P0, which is significantly lower than the 27.79% improvement observed for T-CSW relative to T0.

In T-SUHPC, the incorporation of CSW reduced the total porosity of T-CSW from 12.18% (T0) to 11.83% and slightly decreased the pore volume in the 400 nm to 4 μm range. This indicates that the surface of CSW reacted with the ternary matrix to form abundant hydration products, which effectively filled the interface between the whiskers and the matrix as well as the adjacent capillary pores. This process led to a reduction in porosity and a marked improvement in interfacial bonding. This is confirmed by the results in Section 6.3.5, where the flexural strength of T-CSW-20 significantly increased by 27.79% compared to T0-20.

### 6.3.6.2. Pore structure after high-temperature exposure

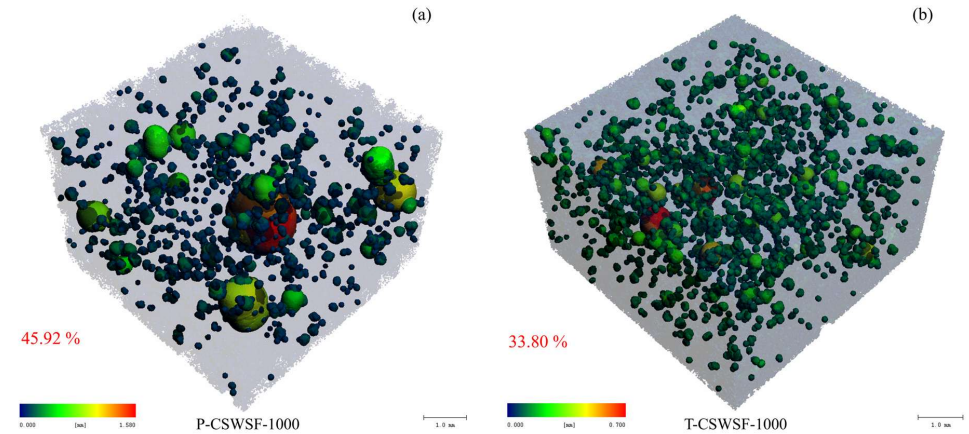


Fig. 6.13. Micro-XCT image of SUHPC after exposure to 1000 °C.

Micro-XCT analysis was further conducted to quantitatively evaluate the pore structures of P-SUHPC and T-SUHPC containing CSW and steel fibers after exposure to 1000 °C, as shown in Fig. 6.13. The results show that the total porosity of T-CSWSF-1000 was 33.80%, significantly lower than that of P-CSWSF-1000 at 45.92%. The maximum and average pore diameters of T-CSWSF-1000 were 0.70 mm and 0.32 mm, respectively, whereas those of P-CSWSF-1000 reached as high as 1.58 mm and 0.88 mm. These findings indicate that the ternary system demonstrates a more refined and uniform pore structure compared to the PC-based system after high-temperature exposure.

As shown in Fig. 6.13(a), the Micro-XCT image of P-CSWSF-1000 revealed the presence of large pores with diameters up to 1.58 mm, along with several dispersed and isolated pores of relatively large size. Given that their sizes are much larger than the original pore size range at room temperature, these large pores are presumed to result from explosive spalling induced by high-temperature exposure. This suggests that no systematic vapor escape channels were established within the P-CSWSF matrix, making it difficult for steam to be released in a timely manner. As a result, localized vapor pressure buildup may have triggered explosive spalling.

The formation of these large pores also explains the relatively low residual mechanical performance of P-CSWSF-1000 observed in Section 6.3.5, with residual compressive and flexural strengths of 31.30 MPa and 4.14 MPa, respectively.

As shown in Fig. 6.13(b), T-CSWSF-1000 exhibited lower porosity, smaller maximum and average pore sizes, and a more uniform pore distribution compared to P-CSWSF-1000. According to the results in Section 6.3.6, T-SUHPC exhibited a high capillary porosity and a fine, uniform microstructure at 20 °C. With increasing temperature, these fine pores gradually coarsened and, together with the ITZ, formed continuous and uniformly distributed pathways for steam release, effectively reducing the risk of explosive spalling at high temperatures. This also accounts for the highest residual mechanical performance observed in T-CSWSF-1000, with residual compressive and flexural strengths reaching 45.78 MPa and 7.35 MPa, respectively.

Compared to PC-based system, a PC–CAC–C$ ternary binder system with CSW and steel fibers effectively suppresses the formation of large pores under extreme high temperatures. It also reduces overall porosity and promotes the development of a continuous and uniform vapor release network. These effects collectively contribute to the superior spalling resistance and higher residual mechanical strength of SUHPC.

## 6.4 Discussion

Fig. 6.14 compares the evolution of hydration products, spalling behavior, crack propagation, and residual strength in T-SUHPC and P-SUHPC reinforced with whiskers and steel fibers under elevated temperatures.

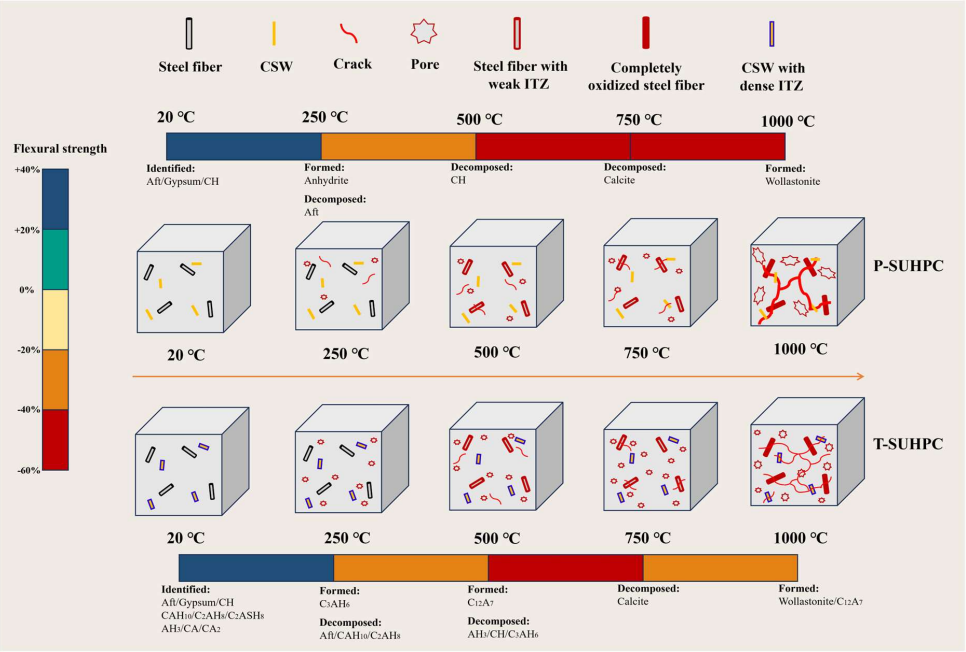


Fig. 6.14. Mechanism of SUHPC at elevated temperatures.

- **The high-temperature resistance mechanisms of the ternary binder system in SUHPC**

These mechanisms can be categorized into three main aspects: (i) compositional changes, (ii) evolution of the pore structure, and (iii) residual strength and the onset temperature of spalling.

**(i) Compositional changes:** The PC–CAC–C$ ternary binder system retains a diverse assemblage of high-temperature-resistant crystalline phases after exposure to 1000 °C, in contrast to the PC-based system in which wollastonite is the predominant phase. This complex phase assemblage indicates a superior recrystallization capacity of the ternary system at elevated temperatures, leading to the formation of a denser and more thermally stable matrix. Therefore, the superior recrystallization capability of the ternary system at elevated temperatures leads to the formation of denser and more stable mineral phases that markedly enhance the residual strength of the matrix. Moreover, these high-temperature phases are also present within the ITZs, thereby strengthening the CSW-matrix or steel fiber-matrix bonding in ternary system. This is evidenced by the fact that the residual flexural strength of T-CSWSF-1000 increased by 77.53% compared to P-CSWSF-1000, reaching 7.35 MPa. As shown in Fig. 6.14, between 750 °C and 1000 °C, the percentage reduction in residual flexural strength of T-SUHPC (28.61%) was lower than that of P-SUHPC (41.07%).

**(ii) Pore structure evolution:** The ternary binder system exhibited an almost opposite response in pore structure at ambient and elevated temperatures. At room temperature, the ternary system developed a uniform pore structure with a relatively high capillary pore content. The increase in capillary pores provided continuous pathways for vapor release, thereby mitigating vapor pressure buildup and minimizing the potential for explosive spalling under high-temperature exposure. MIP results revealed that, compared with the PC-based matrix, the ternary system (T0) showed a marked increase in capillary pore volume within the range of 20 nm to 10 μm. Micro-CT analysis further demonstrated that, after exposure to 1000 °C, the maximum pore size, average pore size, and total porosity of the ternary system were all substantially smaller than those of the PC-based system. During heating, the initially fine capillary pore network in the ternary system gradually coarsened but maintained a uniform distribution and relatively small mean pore diameter. This evolution facilitated the formation of continuous and evenly distributed vapor escape channels throughout the matrix, thereby enhancing its resistance to explosive spalling at elevated temperatures.

**(iii) Residual strength and the onset temperature of spalling:** The high-temperature-resistant crystalline phases generated through recrystallization in the ternary system significantly enhanced the matrix strength. T0-250 exhibited a residual compressive strength of 149.36 MPa, representing a 9.1% increase over P0-250. It was primarily attributed to the high reactivity of CAC clinker, which reacted with silica fume and fly ash to generate additional C–A–S–H gel, thereby further improving the microstructural densification under elevated temperatures. Moreover, explosive spalling occurred in the PC-based system (P0) at 500 °C. In contrast, the ternary mix (T0) experienced explosive spalling at 750 °C, effectively increasing the spalling onset temperature. This improvement can be ascribed to the enhanced thermal stability and microstructural robustness provided by the ternary binder composition, which collectively mitigated vapor pressure buildup and delayed the onset of explosive spalling.

- **Strengthening mechanism of CSW in the ternary system**

The strengthening role of CSW differs between the ternary and PC-based systems and can be analyzed through: **(i)** its surface chemistry, **(ii)** its influence on pore structure, and **(iii)** its effect on spalling resistance and residual strength.

**(i) Surface chemistry:** In both the ternary and PC-based matrices, CSW underwent limited surface dissolution while largely retaining its structural integrity. In the ternary system, however, the CSW surface actively reacted with CAC constituents, leading to the precipitation of abundant AFt and $AH_3$ at the whisker–matrix interfaces, thereby markedly enhancing the ITZ bonding. QXRD results confirmed that the AFt content in T-CSW-20 was 1.7 wt% higher than that in T0-20, whereas the corresponding increase in P-CSW-20 over P0-20 was only 0.3 wt%.

**(ii) Pore structure:** CSW exerts opposite effects on pore structure in the PC-based and the ternary matrices. In the PC-based system, the incorporation of CSW increased total porosity from 9.70% to 10.37% and enlarged the 1–10 μm pore fraction. These changes are consistent with residual voids from localized CSW dissolution and inadequate interfacial infilling, indicating a weaker ITZ. In contrast, in the ternary matrix, the addition of CSW slightly reduced the total porosity from 12.18% to 11.83% and the pore volume in the 400 nm–4 μm range. This response is consistent with the precipitation of AFt and $AH_3$ at the CSW–matrix interface, which filled interfacial gaps and adjacent capillaries and densified the ITZ.

**(iii) Spalling behavior and residual strength:** The incorporation of CSW effectively improved the high-temperature performance of both PC-based and ternary SUHPC, with the enhancement being substantially more pronounced in the ternary system. In the PC-based matrix, the incorporation of CSW delayed the onset temperature of explosive spalling from 500 °C to 1000 °C. In contrast, in the ternary system, spalling was completely suppressed, with specimens retaining their structural integrity even after exposure to 1000 °C. The incorporation of CSW resulted in residual flexural strengths of T-CSW that were 22.01% and 50.71% higher than those of P-CSW after exposure to 500 °C and 750 °C, respectively. This superior performance is closely associated with the presence of multiple high-temperature-resistant crystalline phases in the ternary system, which enhance not only the matrix strength but also the bonding between the matrix and CSW.

The synergistic effect between CSW and steel fibers in the ternary system manifests in CSW dominating above 500 °C and steel fibers below 500 °C, thereby effectively mitigating the degradation of residual strength across the temperature range. Below the critical temperature of steel fibers (approximately 500 °C), their contribution to enhancing the residual flexural strength is more pronounced. Above 500 °C, the reinforcing effect of steel fibers exhibits a marked decline relative to that observed at lower temperatures, primarily due to thermal incompatibility with the surrounding matrix, although a residual contribution remains. The bridging action of CSW remains effective even at 1000 °C, compensating for the reduced reinforcement from steel fibers and highlighting their synergistic contribution to residual mechanical performance in ternary system.

In summary, the ternary system exhibits superior resistance to high-temperature-induced spalling compared to conventional PC-based systems. The underlying mechanisms can be

summarized in two aspects: (1) On one hand, the ternary system demonstrates excellent recrystallization capacity under elevated temperatures, resulting in the formation of multiple high-temperature-resistant crystalline phases. These phases significantly enhance the strength of the matrix itself as well as the interfacial bonding with both CSW and steel fibers. (2) On the other hand, the ternary system initially presents a fine and uniform capillary pore structure at room temperature. As the temperature increases, these pores gradually coarsen, while remaining uniformly distributed. Together with the interconnected microcracks in the matrix and the ITZ, they form continuous and well-connected pathways for vapor release. Moreover, the ternary binder system with CSW and steel fibers effectively suppresses the formation of large pores and reduces overall porosity under extreme temperatures compared to the PC-based system. This optimized pore network alleviates internal vapor pressure buildup, thereby significantly lowering the risk of explosive spalling during high-temperature exposure. It is noteworthy that the reinforcing effect of CSW in the ternary system originates not only from its physical bridging ability but also from its chemical interaction with CAC. This interaction promotes the formation of abundant AFt and $AH_3$ on the CSW surface, significantly enhancing the interfacial bonding compared to that in PC-based matrix. Benefiting from the dual optimization of microstructure and phase assemblage, the CSW and steel fiber–reinforced ternary SUHPC (T-SUHPC) retains high residual mechanical performance and structural integrity even after exposure to extreme temperatures up to 1000 °C. Particularly, the synergistic action between CSW and steel fibers leads to simultaneous improvements in both compressive and flexural strengths. This integrated high-temperature resistance mechanism provides a robust performance foundation and theoretical basis for the application of steel fiber and CSW-reinforced ternary SUHPC in fire-prone or high-temperature engineering environments.

## 6.5 Conclusions

In this chapter, the role of CSW and steel fibers on the explosive spalling resistance of ternary system-based SUHPC (T-SUHPC) at elevated temperatures were investigated, with the PC-based SUHPC (P-SUHPC) used as a reference. The key findings are summarized as follows:

- **High-temperature phase assemblage and thermal stability**

The ternary binder system (PC–CAC–C$) retained multiple high-temperature-stable crystalline phases at 1000 °C ($Al_2O_3$, $C_{12}A_7$, wollastonite, CA, $CA_2$), whereas the PC-based system preserved only wollastonite. This phase stability confers superior recrystallization capacity and thermal stability to the ternary matrix under extreme temperatures.

- **Evolution of pore structure at elevated temperatures**

At room temperature, the ternary matrix featured a higher fraction of fine capillary pores that facilitated vapor release; with CSW, total porosity slightly decreased and ITZ bonding was strengthened by hydration product accumulation at the CSW–matrix interface. After exposure to 1000 °C, Micro-XCT showed markedly smaller and more uniformly distributed pores in the ternary system reinforced with CSW and steel fibers (porosity 33.8 %, average pore size 0.32 mm) than in the PC-based system (45.92 %, 0.88 mm), suppressing large-pore formation and establishing a continuous vapor-escape network.

- **Spalling resistance and residual mechanical performance**

Incorporating the ternary binder system raised the spalling onset temperature of SUHPC from 500 °C to 750 °C, while the subsequent addition of steel fibers further increased it to 1000 °C. SEM analysis revealed that CSW continued to deflect microcrack propagation and bridge cracks effectively, even at 1000 °C. The synergistic effect of CSW and steel fibers within the ternary matrix mitigated residual strength loss at elevated temperatures. Consequently, T-CSWSF retained high residual mechanical performance after exposure to 1000 °C, with compressive and flexural strengths reaching 45.78 MPa and 7.35 MPa, respectively.

# Chapter 7 Conclusions and recommendations

## 7.1 Conclusions

In this PhD thesis, novel SUHPCs have been developed through binder optimization, demonstrating significantly improved spalling resistance at elevated temperatures. As a two-part investigation, this study builds upon UHPC research to develop a novel SUHPC. In the first part, binder optimization of UHPC is investigated by examining the effects of SCM incorporation on its spalling behavior after high-temperature exposure, with the aim of gaining a deeper understanding of post-heating failure mechanisms. In the second part, a ternary binder system is introduced as a strategy for binder optimization to improve the early- and later-age strength of SUHPC, with the ultimate objective of enhancing its explosive spalling resistance at elevated temperatures.

The research encompasses the following five interrelated topics:

- Understanding the effects of SCMs on the explosive spalling resistance and durability on UHPC.
- Understanding the flexural fracture behavior of UHPC after high-temperature exposure.
- Developing a novel SUHPC based on PC-CAC-C$ with excellent early-age performance.
- Understanding the effects of various cementitious materials and alkali-free accelerator on the later-age performance of SUHPC based on PC-CAC-C$.
- Enhancing the spalling resistance of SUHPC based on PC-CAC-C$ reinforced with calcium sulfate whiskers and steel fibers under elevated temperatures.

### 7.1.1 Understanding the effects of SCMs on the explosive spalling resistance of SUHPC

- The incorporation of SCMs modifies the hydration products and pore structure of SUHPC, thereby influencing its resistance to both chloride penetration and explosive spalling at elevated temperatures.
- Chloride ion transport primarily occurs through the capillary pore network, and capillary porosity is widely regarded as the parameter most closely associated with chloride diffusivity. In UHPC incorporating GGBS, the correlation between $D_{nssm}$ and total porosity is stronger than that with capillary porosity.
- The incorporation of GGBS reduces the connectivity of capillary pores in the 10-100 nm range and leads to higher tortuosity in the pore structure. The increased tortuosity reflects a more discontinuous and less connected pore network, which effectively lowers chloride ion permeability.
- For UHPC containing LP, although a low replacement level of LP ($\leqslant$15 wt%) improves the matrix pore structure and enhances compressive strength in UHPC, the fiber–matrix interfacial bonding is adversely affected across all replacement levels. The weakened

interface may act as a potential structural defect, providing pathways for chloride ingress and thereby reducing chloride resistance compared to the control specimen.

- Both GGBS and LP exhibit a detrimental effect on the spalling resistance of UHPC at elevated temperatures. Replacing 15 wt% of cement with LP reduces the spalling onset temperature from 750 °C to 500 °C compared to the reference mix. And incorporating GGBS in the range of 0–45 wt% results in a comparable reduction.
- Higher LP replacement levels (15–45 wt%) also lead to a pronounced decrease in residual compressive strength at elevated temperatures. These results demonstrate that neither LP nor GGBS is effective in improving the spalling resistance of UHPC under high-temperature conditions.

### 7.1.2 Understanding the flexural fracture behavior of SUHPC after high temperature exposure

- After high-temperature exposure, both the compressive strength and flexural strength of UHPC exhibit a trend of first increasing and then decreasing with increasing temperature. The load–displacement and stress–strain responses indicate that elevated temperatures significantly alter the typical mechanical evolution behavior of UHPC.
- At 200 °C, the saw-tooth fluctuations in the load–displacement curves, which are associated with stress redistribution during steel fiber pull-out, are significantly reduced compared to those observed at room temperature.
- When the temperature exceeds 600 °C, the sawtooth-shaped fluctuation amplitude caused by stress redistribution due to fiber drawing disappears completely, indicating severe deterioration of the steel fiber-matrix interfacial bond.
- As a result of interfacial degradation, the strengthening stage is significantly shortened, and the material transitions prematurely into the failure stage, exhibiting a more brittle fracture behavior.
- Correspondingly, bending toughness, fracture toughness, and fracture energy decrease markedly after high-temperature exposure. Nevertheless, a higher steel fiber volume ratio helps to retain greater residual fracture capacity.
- A predictive model for post-fire compressive strength, flexural strength, and fracture energy of UHPC is developed based on steel fiber volume ratio and exposure temperature.
- In addition, conversion relationships among compressive strength, flexural strength, fracture energy, and fracture toughness are established and validated, with temperature-induced degradation effects taken into consideration. This model provides a practical reference for the structural assessment and design of UHPC elements subjected to high-temperature service conditions.

### 7.1.3 Developing a novel SUHPC based on PC-CAC-C$ with superior early-age performance

- To enhance the early-age performance of SUHPC, including early strength, rheology, and early-age shrinkage, a PC-CAC-C$ ternary binder system is incorporated into SUHPC.
- The optimized PC–CAC–C$ ternary binder formulation significantly improves the early-age strength of SUHPC, reaching 15.11 MPa at 3 hours with a C$/CAC ratio of 0.5.
- Compared to the conventional PC-based system, the PC-CAC-C$ ternary system improves the rheological performance of SUHPC by increasing dynamic yield stress and thixotropy, thereby enhancing its pumpability and sprayability.
- The C$/CAC ratio plays a critical role in regulating rheological behavior. An optimal C$/CAC ratio of 0.5 results in a thixotropy value approximately four times higher than that of cast UHPC.
- The effects of varying C$/CAC ratios on the hydration kinetics of SUHPC are clarified for both early and later stages. At early ages, a C$/CAC ratio of 0.5 promotes sufficient ettringite formation and accelerates the hydration of both $C_3S$ and CA.
- At later stages, excessive CAC suppresses C–S–H development, while elevated sulfate content increases the potential risk of delayed ettringite formation (DEF).
- In addition, the synergistic mechanism of the alkali-free accelerator and the PC-CAC-C$ system on the hydration kinetics of SUHPC has been systematically analyzed at both early and late stages.

### 7.1.4 Understanding the effects of various cementitious materials and alkali-free accelerator on the later-age performance of SUHPC based on PC-CAC-C$

- For engineering applications, the later-age mechanical performance of SUHPC depends not only on early-age strength development but also on the combined design of binder systems and alkali-free accelerators.
- The binary binder system, in which CAC partially replaces PC, leads to a significant reduction in both flexural and compressive strengths. The most pronounced strength loss occurs when the CAC content reaches 30%.
- In contrast, the ternary binder system (PC-CAC-C$) improves mechanical performance. As the C$ content increases from 0 to 15 wt%, the flexural strength of SUHPC increases from 18.5 MPa to 21.5 MPa. The compressive strength increases from 106.7 MPa to 123.7 MPa.
- Although the alkali-free accelerator enhances early-age strength, it has a negative impact on later-age mechanical performance. This reduction is partially mitigated by an appropriate combination of different cementitious components.
- In terms of toughness improvement, the ternary binder system exhibits enhanced toughness and energy absorption capacity compared to the binary system. As the C$ content increased from 6% to 15%, the compressive toughness index ($E_2$) of the ternary system increased by

1.06% and 9.51%, respectively, while the flexural toughness index ($E_3$) increased by 0.43% and 6.14%.

- The incorporation of the ternary binder system results in enhanced ductility and toughness of SUHPC, accompanied by observable improvements in microstructural characteristics.
- The synergistic effects between the alkali-free accelerator and multi-component binder systems are further clarified. While the accelerator causes a 19.8% reduction in compressive strength in conventional PC-based SUHPC, the corresponding reduction is limited to only 2.7% in the binary system, demonstrating that multi-component binder systems can effectively mitigate accelerator-induced strength degradation.

### 7.1.5 Enhancing the spalling resistance of SUHPC based on PC-CAC-C$ reinforced with calcium sulfate whiskers and steel fibers under elevated temperatures

- The spalling resistance of SUHPC incorporating a PC–CAC–C$ ternary binder system is significantly influenced by the combined effects of calcium sulfate whiskers (CSW) and steel fibers under elevated temperatures.
- A systematic evaluation was conducted on the evolution of hydration products, spalling behavior, microstructural characteristics, residual mechanical strength, and pore structure of SUHPC after exposure to temperatures ranging from 20 °C to 1000 °C.
- Three primary factors govern the residual mechanical performance and spalling resistance of SUHPC after high-temperature exposure, namely the PC–CAC–C$ binder system, CSW, and steel fibers, whose respective roles are summarized as follows:

  (1) Each factor, when acting individually, increased the spalling-onset temperature of SUHPC.

  (2) Compared with the PC-based system, the strength-enhancing effect of CSW was more pronounced in the ternary system. Specifically, CSW incorporation improved the flexural strength of PC-based SUHPC and ternary-based SUHPC by 8.78% and 27.81%, respectively.

  (3) The synergistic effect of CSW and steel fibers within the ternary matrix further mitigated residual strength loss at elevated temperatures.
- Relative to PC-based SUHPC, the incorporation of the ternary binder system significantly increases the capillary pore volume in the size range of 20 nm to 10 μm. Consequently, the total porosity increases from 9.70% to 12.18%, which facilitates water vapor release at elevated temperatures and enhances spalling resistance.
- In contrast, the addition of CSW effectively reduces the overall porosity of SUHPC. Micro-XCT analysis confirms that the porosity of T-CSWSF after exposure to 1000 °C reaches 33.8%, which is markedly lower than the 45.92% observed in the PC-based system.
- Moreover, the maximum pore diameter in the CSW- and steel fiber-reinforced ternary system is reduced to approximately 0.32 mm.

- These results collectively indicate that the synergistic effect of CSW and steel fibers within the PC–CAC–C$ ternary matrix promotes the formation of more uniform and continuous vapor-release channels, thereby effectively enhancing the spalling resistance of SUHPC under elevated temperature conditions.

## 7.2 Recommendations

Recommendations for further investigation based on the current findings are proposed:

- Future studies on ternary or quaternary SCM combinations are recommended to further clarify their synergistic effects on hydration behavior, pore structure, fiber matrix bonding, chloride resistance and fire resistance. Given that both GGBS and LP reduce the spalling resistance of UHPC at elevated temperatures, alternative binder systems could be explored in future studies to optimize pore structure and enhance fire resistance.
- A prediction model is established and validated in this study to estimate the residual compressive strength, flexural strength, and fracture energy of UHPC after thermal exposure, using steel fibre volume fraction and temperature as the primary governing variables. Future research may build upon this model by incorporating hybrid and alternative fibres in combination with steel fibres. Developing such extended models would facilitate more accurate predictions of the post-fire mechanical and fracture performance of UHPC across a broader range of fibre reinforcement configurations.
- A novel SUHPC incorporating a PC-CAC-C$ system has been proposed to enhance early-age properties, including rheology, shrinkage control, and early strength development. The synergistic effects between the alkali-free accelerator and the PC-CAC-C$ system on the hydration kinetics of SUHPC at both early and later stages have been systematically investigated. Although this ternary binder system demonstrates significant potential in improving the early-age performance of SUHPC, its adaptability under complex environmental conditions (such as high humidity, saline exposure, or sub-zero temperatures) still requires further consideration. Future research is recommended to focus on the durability performance of this system, particularly regarding resistance to chloride ingress, carbonation, freeze–thaw cycles, and self-healing capacity.
- The effects of various binder systems and alkali-free accelerator on the later-age mechanical properties of SUHPC are investigated in this study. Future research could explore alternative binder formulations, including slag, fly ash and metakaolin in different proportions to assess their influence on SUHPC performance. In addition, the interactions between different accelerator chemistries (such as alkali activated accelerators) and cementitious blends could also be examined. Future studies are encouraged to incorporate durability evaluation protocols, including impermeability, carbonation resistance, sulfate attack resistance, and freeze–thaw durability, in addition to mechanical properties.

- This thesis systematically investigates the spalling behaviour of SUHPC based on PC-CAC-C$ system over the temperature range of 20 ℃ to 1000 ℃. The evolution of hydration products, spalling behaviour, microstructural characteristics, residual mechanical properties, and pore structure is comprehensively analysed. In addition, the post-fire performance enhancement mechanisms associated with calcium sulfate whiskers and steel fibres are elucidated. Future research may extend this approach by exploring multiscale fibre hybridization within the ternary binder matrix. Combinations of calcium sulfate whiskers with other thermally resistant fibres, such as polypropylene, carbon, basalt, or additional steel fibres, merit further investigation due to their potential to improve the mechanical performance of SUHPC after high-temperature exposure. Moreover, the influence of such hybrid reinforcement systems on pumpability and sprayability is an important aspect for further investigation, considering the practical demands of field application.
- Future research could incorporate AI-assisted methods for mix design and fire performance evaluation of SUHPC. By integrating surrogate or machine learning models, mix proportions of SUHPC (PC–CAC–C$ system, various SCMs, and different fibre types and volume fractions) could be intelligently optimized under multiple constraints, including pumpability/sprayability, early-age rheology and shrinkage, pore structure, cost, and sustainability. Moreover, AI approaches could be applied to predict and optimize the performance evolution of SUHPC under fire exposure, such as moisture and vapor pressure build-up, explosive spalling risk, residual mechanical properties, and microstructural changes, thereby accelerating materials development and improving the reliability and safety of SUHPC in practical applications.

# Bibliography

[1] M.S. Tomar, S. Khurana, Impact of passive fire protection on heat release rates in road tunnel fire: A review, Tunnelling and Underground Space Technology 85 (2019) 149-159.
[2] P. Wasantha, M. Guerrieri, T. Xu, Effects of tunnel fires on the mechanical behaviour of rocks in the vicinity–A review, Tunnelling and Underground Space Technology 108 (2021) 103667.
[3] Porousmedia.nl, n.d. Moisture transport and clogging of concrete under fire conditions. Available at: http://porousmedia.nl/nfcmr/Restop30.html (Accessed: 30 September 2025).
[4] Sika, Manual de Concreto Reforzado SikaFiber. Available at: https://ury.sika.com/dam/dms/co01/5/SikaFiber_handbook_ESP.pdf (Accessed: 30 September 2025).
[5] Y. Dong, Performance assessment and design of ultra-high performance concrete (UHPC) structures incorporating life-cycle cost and environmental impacts, Construction and Building Materials 167 (2018) 414-425.
[6] P. Zhan, J. Xu, J. Wang, C. Jiang, Multi-scale study on synergistic effect of cement replacement by metakaolin and typical supplementary cementitious materials on properties of ultra-high performance concrete, Construction and Building Materials 307 (2021) 125082.
[7] I.Y. Hakeem, F. Althoey, A. Hosen, Mechanical and durability performance of ultra-high-performance concrete incorporating SCMs, Construction and Building Materials 359 (2022) 129430.
[8] H. Hamada, F. Abed, Optimization and Modeling of 7-Day Ultra-High-Performance Concrete Comprising Desert Sand and Supplementary Cementitious Materials Using Response Surface Methodology, Buildings (2075-5309). 14(7) (2024).
[9] Y. Huang, Q. Chen, H. Shang, J. Wang, N. Song, Development of sustainable ultra-high-performance concrete (UHPC) by synergistic utilization of red mud and limestone powder, Journal of Building Engineering 90 (2024) 109372.
[10] G. Cai, Y. Zhou, J. Li, L. Han, C.S. Poon, Deep insight into mechanical behavior and microstructure mechanism of quicklime-activated ground granulated blast-furnace slag pastes, Cement and Concrete Composites 134 (2022) 104767.
[11] D. Ndahirwa, H. Zmamou, H. Lenormand, N. Leblanc, The role of supplementary cementitious materials in hydration, durability and shrinkage of cement-based materials, their environmental and economic benefits: A review, Cleaner Materials. 5 (2022) 100123.
[12] R.K. Majhi, A.N. Nayak, B.B. Mukharjee, Characterization of lime activated recycled aggregate concrete with high-volume ground granulated blast furnace slag, Construction and Building Materials 259 (2020) 119882.
[13] M.N.A. Metla, M.N. Amin, S.A. Rizwan, K. Khan, Self-consolidating paste systems using ground granulated blast furnace slag and limestone powder mineral admixtures, Case Studies in Construction Materials 20 (2024) e03316.
[14] S. Yoon, W. Choi, C. Jeon, Hydration properties of mixed cement containing ground-granulated blast-furnace slag and expansive admixture, Journal of Material Cycles and Waste Management 24(5) (2022) 1878-1892.
[15] P.P. Li, H.J.H. Brouwers, W. Chen, Q.L. Yu, Optimization and characterization of high-volume limestone powder in sustainable ultra-high performance concrete, Construction and Building Materials 242 (2020) 118112.
[16] W. Huang, H. Kazemi-Kamyab, W. Sun, K. Scrivener, Effect of cement substitution by limestone on the hydration and microstructural development of ultra-high performance concrete (UHPC), Cement and Concrete Composites 77 (2017) 86-101.

[17] P.P. Li, Y.Y.Y. Cao, H.J.H. Brouwers, W. Chen, Q.L. Yu, Development and properties evaluation of sustainable ultra-high performance pastes with quaternary blends, Journal of Cleaner Production 240 (2019) 118124.
[18] W. Zhuang, S. Li, Q. Yu, The effect of supplementary cementitious material systems on dynamic compressive properties of ultra-high performance concrete paste, Construction and Building Materials 321 (2022) 126361.
[19] Y. Li, P. Du, K.H. Tan, Fire resistance of ultra-high performance concrete columns subjected to axial and eccentric loading, Engineering Structures 248 (2021) 113158.
[20] K. Chi, J. Li, C. Wu, Behavior of reinforced ultra-high performance concrete slabs under impact loading after exposure to elevated temperatures, International Journal of Computational Methods. 21(08) (2024) 2241001.
[21] G. Ren, X. Gao, H. Zhang, Utilization of hybrid sisal and steel fibers to improve elevated temperature resistance of ultra-high performance concrete, Cement and Concrete Composites 130 (2022) 104555.
[22] M.M. Ridha, Combined effect of natural fibre and steel fibre on the thermal-mechanical properties of UHPC subjected to high temperature, Cement and Concrete Research 180 (2024) 107510.
[23] J. Lin, Y. Zhang, Z. Guo, H. Du, Impact of synthetic fibers on spalling and intrinsic pore structure of ultra-high performance concrete (UHPC) under elevated temperatures, Construction and Building Materials 439 (2024) 137325.
[24] J. Lin, Y. Zhang, S. Huang, H. Du, K. Jiang, Influence of synthetic fibers on the performance of ultra-high performance concrete (UHPC) at elevated temperatures, Journal of Building Engineering 97 (2024) 110735.
[25] J. Cui, Z. He, G. Zhang, X. Cai, Rheological properties of sprayable ultra-high performance concrete with different viscosity-enhancing agents, Construction and Building Materials 321 (2022) 126154.
[26] J. Cui, Z. He, G. Zhang, X. Cai, L. Hu, Rheology, mechanical properties and pore structure of sprayed ultra-high performance concrete (SUHPC) with viscosity-enhancing agent, Construction and Building Materials 350 (2022) 128840.
[27] A.L. Van Overmeir, S.C. Figueiredo, B. Šavija, F.P. Bos, E. Schlangen, Design and analyses of printable strain hardening cementitious composites with optimized particle size distribution, Construction and Building Materials 324 (2022) 126411.
[28] Y. Sheng, B. Xue, H. Li, Y. Qiao, H. Chen, J. Fang, A. Xu, Preparation and Performance of a New‐Type Alkali‐Free Liquid Accelerator for Shotcrete, Advances in Materials Science and Engineering 2017(1) (2017) 1264590.
[29] L. Yang, C. Shi, Z. Wu, Mitigation techniques for autogenous shrinkage of ultra-high-performance concrete–A review, Composites Part B: Engineering 178 (2019) 107456.
[30] K. Onishi, T.A. Bier, Investigation into relations among technological properties, hydration kinetics and early age hydration of self-leveling underlayments, Cement and Concrete Research 40(7) (2010) 1034-1040.
[31] E. Qoku, T.A. Bier, T. Westphal, Phase assemblage in ettringite-forming cement pastes: A X-ray diffraction and thermal analysis characterization, Journal of Building Engineering 12 (2017) 37-50.
[32] L. Noor, A. Tuinukuafe, J.H. Ideker, A critical review of the role of ettringite in binders composed of CAC–PC–C andCSA–PC–C, Journal of the American Ceramic Society 106(6) (2023) 3303-3328.
[33] L. Noor, P. Rost, I. Kirchberger, F. Goetz-Neunhoeffer, J.H. Ideker, Hygrothermal stability of ettringite in blended systems with CAC-OPC-CŠ, Cement and Concrete Research 184 (2024) 107590.

[34] A. Qorllari, E. Qoku, T.A. Bier, T. Dilo, Investigation of ternary binder based systems in terms of Calorimetry, Shrinkage and In-Situ XRD, (2017).
[35] J. Cui, Z. He, X. Cai, Mechanical properties and key intrinsic factors of sprayed ultra-high performance concrete (SUHPC) with alkali-free accelerator, Construction and Building Materials 349 (2022) 128788.
[36] H. Chen, Y. Yu, C. Tang, Mechanical properties of ultra-high performance concrete before and after exposure to high temperatures, Materials. 13(3) (2020) 770.
[37] L. Dong, Y. Yang, Z. Liu, Y. Zhang, C. Wu, Interface bonding characteristics of 3D printed ultra-high performance concrete after elevated temperatures, Journal of Building Engineering 93 (2024) 109801.
[38] F. Sciarretta, S. Fava, M. Francini, L. Ponticelli, M. Caciolai, B. Briseghella, C. Nuti, Ultra-High performance concrete (UHPC) with polypropylene (Pp) and steel Fibres: Investigation on the high temperature behaviour, Construction and Building Materials 304 (2021) 124608.
[39] R. Ma, J. Yang, G. Peng, Influence of steel fiber types on residual mechanical properties and explosive spalling of hybrid fiber reinforced ultra-high performance concrete: Optimization and evaluations, Case Studies in Construction Materials 19 (2023) e02538.
[40] D. Gao, W. Zhang, J. Tang, Z. Zhu, Effect of steel fiber on the compressive performance and microstructure of ultra-high performance concrete at elevated temperatures, Construction and Building Materials 435 (2024) 136830.
[41] E. Vejmelková, D. Koňáková, L. Scheinherrová, M. Doleželová, M. Keppert, R. Černý, High temperature durability of fiber reinforced high alumina cement composites, Construction and Building Materials 162 (2018) 881-891.
[42] W. Khaliq, H.A. Khan, High temperature material properties of calcium aluminate cement concrete, Construction and Building Materials 94 (2015) 475-487.
[43] J. Zhang, G. Li, X. Yang, S. Ren, Z. Song, Study on a high strength ternary blend containing calcium sulfoaluminate cement/calcium aluminate cement/ordinary Portland cement, Construction and Building Materials 191 (2018) 544-553.
[44] J. He, Q. Yu, Z. Tang, H. Wang, Z. Chen, B. Wei, Effects of Different Cementitious Materials and Accelerators on the Flexural and Compressive Behaviors of SUHPC, Case Studies in Construction Materials (2025) e04913.
[45] H. Huang, R. Wang, X. Gao, Improvement effect of fiber alignment on resistance to elevated temperature of ultra-high performance concrete, Composites Part B: Engineering 177 (2019) 107454.
[46] B. He, X. Zhu, Q. Ren, Z. Jiang, Effects of fibers on flexural strength of ultra-high-performance concrete subjected to cryogenic attack, Construction and Building Materials 265 (2020) 120323.
[47] M. Rasul, S. Ahmad, S.K. Adekunle, S.U. Al-Dulaijan, M. Maslehuddin, S.I. Ali, Evaluation of the effect of exposure duration and fiber content on the mechanical properties of polypropylene fiber-reinforced UHPC exposed to sustained elevated temperature, Journal of Testing and Evaluation 48(6) (2020) 4355-4369.
[48] J. Park, D. Yoo, S. Kim, S. Kim, Benefits of synthetic fibers on the residual mechanical performance of UHPFRC after exposure to ISO standard fire, Cement and Concrete Composites 104 (2019) 103401.
[49] Z. Yu, X. Zhan, M. Jiao, J. Zhang, X. Yan, T. Zhang, X. Du, Study on the fracture mechanical properties of high performance concrete (HPC) with rapid cooling after high temperature, Construction and Building Materials 422 (2024) 135718.
[50] O. Zaid, F. Althoey, M.A. Abuhussain, Y. Alashker, Spalling behavior and performance of ultra-high-performance concrete subjected to elevated temperature: A review, Construction and Building Materials 411 (2024) 134489.

[51] L. Li, B. Wang, M.H. Hubler, Carbon nanofibers (CNFs) dispersed in ultra-high performance concrete (UHPC): Mechanical property, workability and permeability investigation, Cement and Concrete Composites 131 (2022) 104592.
[52] Y. Liu, Y. Wei, L. Ma, L. Wang, Restrained shrinkage behavior of internally-cured UHPC using calcined bauxite aggregate in the ring test and UHPC-concrete composite slab, Cement and Concrete Composites 134 (2022) 104805.
[53] K. Lu, Z. Pang, Q. Xu, Y. Yao, J. Wang, C. Miao, Bond strength between substrate and post-cast UHPC with innovative interface treatment, Cement and Concrete Composites 133 (2022) 104691.
[54] K. Wei, G. Xu, J. Yang, Y. Zhao, Y. Sun, Study on mechanical and shrinkage properties of ES-UHPC, Construction and Building Materials 377 (2023) 131137.
[55] D.Y. Yoo, T. Oh, N. Banthia, Nanomaterials in ultra-high-performance concrete (UHPC)–A review, Cement and Concrete Composites 134 (2022) 104730.
[56] Z. Li, W. Zhou, Tensile behavior of UHPFRC made by a fiber orientation device with adjustable vibrational frequency, Construction and Building Materials 401 (2023) 132914.
[57] R. Yu, P. Spiesz, H.J.H. Brouwers, Mix design and properties assessment of ultra-high performance fibre reinforced concrete (UHPFRC), Cement and Concrete Research 56 (2014) 29-39.
[58] O. Kayali, M.S. Ahmed, Assessment of high volume replacement fly ash concrete–Concept of performance index, Construction and Building Materials 39 (2013) 71-76.
[59] A. Korpa, T. Kowald, R. Trettin, Phase development in normal and ultra high performance cementitious systems by quantitative X-ray analysis and thermoanalytical methods, Cement and Concrete Research 39(2) (2009) 69-76.
[60] H. Zhu, W. Chen, S. Cheng, L. Yang, S. Wang, J. Xiong, Low carbon and high efficiency limestone-calcined clay as supplementary cementitious materials (SCMs): Multi-indicator comparison with conventional SCMs, Construction and Building Materials 341 (2022) 127748.
[61] S. Park, S. Wu, Z. Liu, S. Pyo, The role of supplementary cementitious materials (SCMs) in ultra high performance concrete (UHPC): A review, Materials. 14(6) (2021) 1472.
[62] V. Tanwar, K. Bisht, K.S.A. Kabeer, P. Ramana, Experimental investigation of mechanical properties and resistance to acid and sulphate attack of GGBS based concrete mixes with beverage glass waste as fine aggregate, Journal of Building Engineering 41 (2021) 102372.
[63] W. Chenjie, M. Zhipeng, W. Dezhi, Z. Haiwei, K. Long, L. Yu, Influence in the mechanical properties and salt erosion resistance of recycled sand UHPC made from fly ash content, Journal of Building Engineering 96 (2024) 110337.
[64] A. Abushanab, W. Alnahhal, Combined effects of treated domestic wastewater, fly ash, and calcium nitrite toward concrete sustainability, Journal of Building Engineering 44 (2021) 103240.
[65] C. Luan, J. Wang, J. Gao, J. Wang, P. Du, Z. Zhou, Y. Huang, S. Du, Changes in fractal dimension and durability of ultra-high performance concrete (UHPC) with silica fume content, Archives of Civil and Mechanical Engineering 22(3) (2022) 123.
[66] F. Hong, S. Yu, W. Sun, W. Xia, D. Hou, M. Wang, Mix proportion design based on particle compact packing theory and research on the resistance of metakaolin to chloride salt erosion in UHPC cementitious system, Construction and Building Materials 447 (2024) 137982.
[67] W. Zhang, D. Ding, M. Li, T. Wang, H. Ma, B. Chen, H. Hu, J. Chen, X. Liu, D. Hou, Chloride binding mechanism in seawater-mixed UHPC, Construction and Building Materials 427 (2024) 136191.
[68] Q. Song, R. Yu, Z. Shui, Y. Wang, S. Rao, S. Wu, Y. He, Physical and chemical coupling effect of metakaolin induced chloride trapping capacity variation for Ultra High Performance Fibre Reinforced Concrete (UHPFRC), Construction and Building Materials 223 (2019) 765-774.

[69] A. Rafeet, R. Vinai, M. Soutsos, W. Sha, Guidelines for mix proportioning of fly ash/GGBS based alkali activated concretes, Construction and Building Materials 147 (2017) 130-142.
[70] G. Ye, X. Liu, G. De Schutter, A.-M. Poppe, L. Taerwe, Influence of limestone powder used as filler in SCC on hydration and microstructure of cement pastes, Cement and Concrete Composites 29(2) (2007) 94-102.
[71] E. Tazawa, S. Miyazawa, Influence of cement and admixture on autogenous shrinkage of cement paste, Cement and Concrete Research 25(2) (1995) 281-287.
[72] T. Zhang, W. Tian, Y. Guo, A. Bogush, E. Khayrulina, J. Wei, Q. Yu, The volumetric stability, chloride binding capacity and stability of the Portland cement-GBFS pastes: An approach from the viewpoint of hydration products, Construction and Building Materials 205 (2019) 357-367.
[73] O. Kayali, M. Khan, M.S. Ahmed, The role of hydrotalcite in chloride binding and corrosion protection in concretes with ground granulated blast furnace slag, Cement and Concrete Composites 34(8) (2012) 936-945.
[74] H. He, H. Qiao, T. Sun, H. Yang, C. He, Research progress in mechanisms, influence factors and improvement routes of chloride binding for cement composites, Journal of Building Engineering 86 (2024) 108978.
[75] B. Song, X. Hu, S. Liu, C. Shi, Chloride binding of early CO2-cured Portland cement-fly ash-GGBS ternary pastes, Cement and Concrete Composites 134 (2022) 104793.
[76] K.D. Weerdt, E. Sellevold, K.O. Kjellsen, H. Justnes, Fly ash–limestone ternary cements: effect of component fineness, Advances in Cement Research 23(4) (2011) 203-214.
[77] D. Wang, C. Shi, N. Farzadnia, Z. Shi, H. Jia, Z. Ou, A review on use of limestone powder in cement-based materials: Mechanism, hydration and microstructures, Construction and Building Materials 181 (2018) 659-672.
[78] N. Hammad, A. El-Nemr, H.E.-D. Hasan, The performance of fiber GGBS based alkali-activated concrete, Journal of Building Engineering 42 (2021) 102464.
[79] M.K. Kamyab, Autogenous shrinkage and hydration kinetics of SH-UHPFRC under moderate to low temperature curing conditions, Verlag nicht ermittelbar, 2013.
[80] P. Ganesh, A.R. Murthy, Tensile behaviour and durability aspects of sustainable ultra-high performance concrete incorporated with GGBS as cementitious material, Construction and Building Materials 197 (2019) 667-680.
[81] B. Lothenbach, G. Le Saout, E. Gallucci, K. Scrivener, Influence of limestone on the hydration of Portland cements, Cement and Concrete Research 38(6) (2008) 848-860.
[82] L.G. Li, A.K. Kwan, Adding limestone fines as cementitious paste replacement to improve tensile strength, stiffness and durability of concrete, Cement and Concrete Composites 60 (2015) 17-24.
[83] S. Kang, Y. Jeong, K.H. Tan, J. Moon, The use of limestone to replace physical filler of quartz powder in UHPFRC, Cement and Concrete Composites 94 (2018) 238-247.
[84] S. Gao, X. Guo, S. Ban, Y. Ma, Q. Yu, S. Sui, Influence of supplementary cementitious materials on ITZ characteristics of recycled concrete, Construction and Building Materials 363 (2023) 129736.
[85] C. Luan, Q. Yang, X. Lin, X. Gao, H. Cheng, Y. Huang, P. Du, Z. Zhou, J. Wang, The synergistic effects of ultrafine slag powder and limestone on the rheology behavior, microstructure, and fractal features of ultra-high performance concrete (UHPC), Materials. 16(6) (2023) 2281.
[86] C. Li, L. Jiang, S. Li, Effect of limestone powder addition on threshold chloride concentration for steel corrosion in reinforced concrete, Cement and Concrete Research 131 (2020) 106018.

[87] X. Wang, R. Yu, Q. Song, Z. Shui, Z. Liu, S. Wu, D. Hou, Optimized design of ultra-high performance concrete (UHPC) with a high wet packing density, Cement and Concrete Research 126 (2019) 105921.
[88] D. Zhang, Y. Zhang, A. Dasari, K.H. Tan, Y. Weng, Effect of spatial distribution of polymer fibers on preventing spalling of UHPC at high temperatures, Cement and Concrete Research 140 (2021) 106281.
[89] R. Yu, P. Spiesz, H.J.H. Brouwers, Development of an eco-friendly Ultra-High Performance Concrete (UHPC) with efficient cement and mineral admixtures uses, Cement and Concrete Composites 55 (2015) 383-394.
[90] C. Nordtest, mortar and cement-based repair materials: Chloride migration coefficient from non-steady-state migration experiments, NT Build 492, Nordtest, Espoo, Finland, 1999.
[91] European Committee for Standardization (CEN), Testing hardened concrete – Part 2: Making and curing specimens for strength tests, EN 12390-2, CEN, Brussels, Belgium, 2019.
[92] European Committee for Standardization (CEN), EN 1015-3, CEN, Brussels, Belgium, 2019.
[93] A. Arora, M. Aguayo, H. Hansen, C. Castro, E. Federspiel, B. Mobasher, N. Neithalath, Microstructural packing-and rheology-based binder selection and characterization for Ultra-high Performance Concrete (UHPC), Cement and Concrete Research 103 (2018) 179-190.
[94] European Committee for Standardization (CEN), Methods of testing cement – Part 1: Determination of strength, EN 196-1:2016, CEN, Brussels, Belgium, 2016.
[95] J. Zhang, F. Bian, Y. Zhang, Z. Fang, C. Fu, J. Guo, Effect of pore structures on gas permeability and chloride diffusivity of concrete, Construction and Building Materials 163 (2018) 402-413.
[96] Z. Xu, J. Gao, Y. Zhao, S. Li, Z. Guo, X. Luo, G. Chen, Promoting utilization rate of ground granulated blast furnace slag (GGBS): Incorporation of nanosilica to improve the properties of blended cement containing high volume GGBS, Journal of Cleaner Production 332 (2022) 130096.
[97] S.A. X. Dai, M.Y. Yardimci, R.E.N. Qiang, K. Lesage, G. De Schutter, Rheology, early-age hydration and microstructure of alkali-activated GGBFS-Fly ash-limestone mixtures, Cement and Concrete Composites 124(0958-9465) (2021).
[98] ASTM, 1997. ASTM C1018-97: Standard test method for flexural toughness and first-crack strength of fiber-reinforced concrete (using beam with third-point loading). ASTM International, West Conshohocken, PA, USA.
[99] Z. Wu, C. Shi, W. He, L. Wu, Effects of steel fiber content and shape on mechanical properties of ultra high performance concrete, Construction and Building Materials 103 (2016) 8-14.
[100] O. Burciaga Díaz, I.E. Betancourt Castillo, M.E. Montes Escobedo, J.I. Escalante García, One-part pastes and mortars of CaO-Na2CO3 activated blast furnace slag: Microstructural evolution, cost and CO2 emissions, Construction and Building Materials 368 (2023) 130431.
[101] I. García Lodeiro, A. Fernández-Jimenez, A. Palomo, D.E. Macphee, Effect on fresh C-S-H gels of the simultaneous addition of alkali and aluminium, Cement and Concrete Research 40(1) (2010) 27-32.
[102] E. L'Hôpital, B. Lothenbach, G. Le Saout, D. Kulik, K. Scrivener, Incorporation of aluminium in calcium-silicate-hydrates, Cement and Concrete Research 75 (2015) 91-103.
[103] B. Ma, X. Liu, H. Tan, T. Zhang, J. Mei, H. Qi, W. Jiang, F. Zou, Utilization of pretreated fly ash to enhance the chloride binding capacity of cement-based material, Construction and Building Materials 175 (2018) 726-734.
[104] P. Hou, K. Wang, J. Qian, S. Kawashima, D. Kong, S.P. Shah, Effects of colloidal nanoSiO2 on fly ash hydration, Cement and Concrete Composites 34(10) (2012) 1095-1103.

[105] S. Mohammed, G. Elhem, B. Mekki, Valorization of pozzolanicity of Algerian clay: Optimization of the heat treatment and mechanical characteristics of the involved cement mortars, Applied Clay Science 132 (2016) 711-721.
[106] J. Yang, Y. Su, X. He, H. Tan, Y. Jiang, L. Zeng, B. Strnadel, Pore structure evaluation of cementing composites blended with coal by-products: Calcined coal gangue and coal fly ash, Fuel Processing Technology 181 (2018) 75-90.
[107] J. Liu, C. Liao, H. Jin, Z. Jiang, R. Xie, L. Tang, Electrically driven ionic transport in the RCM and RIM: Investigations based on experiments and numerical simulations, Construction and Building Materials 331 (2022) 127331.
[108] D. Wang, C. Shi, N. Farzadnia, Z. Shi, H. Jia, A review on effects of limestone powder on the properties of concrete, Construction and Building Materials 192 (2018) 153-166.
[109] Y. Zhu, H. Hussein, A. Kumar, G. Chen, A review: Material and structural properties of UHPC at elevated temperatures or fire conditions, Cement and Concrete Composites 123 (2021) 104212.
[110] S. Zhutovsky, K. Kovler, Effect of internal curing on durability-related properties of high performance concrete, Cement and Concrete Research 42(1) (2012) 20-26.
[111] E. Serelis, V. Vaitkevicius, H. Hilbig, L. Irbe, Z. Rudzionis, Effect of ultra-sonic dispersion time on hydration process and microstructure development of ultra-high performance glass powder concrete, Construction and Building Materials 298 (2021) 123856.
[112] J. Li, Z. Wu, C. Shi, Q. Yuan, Z. Zhang, Durability of ultra-high performance concrete–A review, Construction and Building Materials 255 (2020) 119296.
[113] A.M. Matos, S. Nunes, C. Costa, J.L.B. Aguiar, Durability of an UHPC containing spent equilibrium catalyst, Construction and Building Materials 305 (2021) 124681.
[114] S. Lian, S. Ruan, S. Zhan, C. Unluer, T. Meng, K. Qian, Unlocking the role of pores in chloride permeability of recycled concrete: A multiscale and a statistical investigation, Cement and Concrete Composites 125 (2022) 104320.
[115] B.H. Oh, S.Y. Jang, Prediction of diffusivity of concrete based on simple analytic equations, Cement and Concrete Research 34(3) (2004) 463-480.
[116] M. Abd Elrahman, B. Hillemeier, Combined effect of fine fly ash and packing density on the properties of high performance concrete: An experimental approach, Construction and Building Materials 58 (2014) 225-233.
[117] P.K. Mehta, and Paulo JM Monteiro, Concrete: microstructure, properties, and materials, McGraw-Hill Education2014.
[118] N. Van Tuan, G. Ye, K. van Breugel, A.L.A. Fraaij, D.D. Bui, The study of using rice husk ash to produce ultra high performance concrete, Construction and Building Materials 25(4) (2011) 2030-2035.
[119] S. Ahmad, I. Hakeem, M. Maslehuddin, Development of an optimum mixture of ultra-high performance concrete, European Journal of Environmental and Civil Engineering 20(9) (2016) 1106-1126.
[120] M. Bajaber, I. Hakeem, UHPC evolution, development, and utilization in construction: A review, J. Mater. Res. Technol. 10 (2021) 1058-1074.
[121] J. Xue, B. Briseghella, F. Huang, C. Nuti, H. Tabatabai, B. Chen, Review of ultra-high performance concrete and its application in bridge engineering, Construction and Building Materials 260 (2020) 119844.
[122] Y. Qian, D. Yang, Y. Xia, H. Gao, Z. Ma, Properties and improvement of ultra-high performance concrete with coarse aggregates and polypropylene fibers after high-temperature damage, Construction and Building Materials 364 (2023) 129925.
[123] L. Missemer, E. Ouedraogo, Y. Malecot, C. Clergue, D. Rogat, Fire spalling of ultra-high performance concrete: From a global analysis to microstructure investigations, Cement and Concrete Research 115 (2019) 207-219.

[124] Q. Ma, R. Guo, Z. Zhao, Z. Lin, K. He, Mechanical properties of concrete at high temperature—A review, Construction and Building Materials 93 (2015) 371-383.
[125] I.M. Nasser, M.H.W. Ibrahim, S.S.M. Zuki, H.A. Algaifi, A.F. Alshalif, The effect of nanosilica incorporation on the mechanical properties of concrete exposed to elevated temperature: a review, Environmental Science and Pollution Research 29(11) (2022) 15318-15336.
[126] P. Zhang, L. Kang, J. Wang, J. Guo, S. Hu, Y. Ling, Mechanical properties and explosive spalling behavior of steel-fiber-reinforced concrete exposed to high temperature—a review, Applied Sciences 10(7) (2020) 2324.
[127] J. Holan, J. Novak, P. Müller, R. Štefan, Experimental investigation of the compressive strength of normal-strength air-entrained concrete at high temperatures, Construction and Building Materials 248 (2020) 118662.
[128] G.F. Peng, W.W. Yang, J. Zhao, Y.F. Liu, S.H. Bian, L.H. Zhao, Explosive spalling and residual mechanical properties of fiber-toughened high-performance concrete subjected to high temperatures, Cement and Concrete Research 36(4) (2006) 723-727.
[129] Y. Ju, L. Wang, H. Liu, K. Tian, An experimental investigation of the thermal spalling of polypropylene-fibered reactive powder concrete exposed to elevated temperatures, Science bulletin 60(23) (2015) 2022-2040.
[130] M. Zhou, X. He, H. Wang, C. Wu, B. Wei, Y. Li, 3D mesoscale discrete element modeling of hybrid fiber-reinforced concrete, Construction and Building Materials 447 (2024) 138006.
[131] H. Wang, X. He, M. Zhou, B. Wei, W. Wu, G. Zhou, J. He, A study on the tensile fracture behavior of polypropylene fiber reinforced concrete based on a microscale model, Construction and Building Materials 417 (2024) 135291.
[132] M. Zhou, X. He, H. Wang, C. Wu, J. He, Mesoscale modeling of polypropylene fiber reinforced concrete under split tension using discrete element method, Construction and Building Materials 404 (2023) 133274.
[133] A. Pourjahanshahi, H. Madani, Chloride diffusivity and mechanical performance of UHPC with hybrid fibers under heat treatment regime, Materials Today Communications 26 (2021) 102146.
[134] G.F. Peng, X.J. Niu, Y.J. Shang, D.P. Zhang, X.W. Chen, H. Ding, Combined curing as a novel approach to improve resistance of ultra-high performance concrete to explosive spalling under high temperature and its mechanical properties, Cement and Concrete Research 109 (2018) 147-158.
[135] S. Donatello, C. Kuenzel, A. Palomo, A. Fernández-Jiménez, High temperature resistance of a very high volume fly ash cement paste, Cement and Concrete Composites 45 (2014) 234-242.
[136] M. Khan, J. Lao, M.R. Ahmad, M.F. Kai, J.G. Dai, The role of calcium aluminate cement in developing an efficient ultra-high performance concrete resistant to explosive spalling under high temperatures, Construction and Building Materials 384 (2023) 131469.
[137] A. Lau, M. Anson, Effect of high temperatures on high performance steel fibre reinforced concrete, Cement and Concrete Research 36(9) (2006) 1698-1707.
[138] M.D. Bhat, M.U. Rehman, I. Shafi, A. Parveen, A. Fayaz, B.A. Malik, F. Bashir, The effect of polypropylene and steel fibers on the properties of concrete at normal and elevated temperatures—a review, Iranian Journal of Science and Technology, Transactions of Civil Engineering 46(3) (2022) 1805-1823.
[139] O. Babalola, P.O. Awoyera, D.H. Le, L.B. Romero, A review of residual strength properties of normal and high strength concrete exposed to elevated temperatures: Impact of materials modification on behaviour of concrete composite, Construction and Building Materials 296 (2021) 123448.

[140] S. Sanchayan, S.J. Foster, High temperature behaviour of hybrid steel–PVA fibre reinforced reactive powder concrete, Materials and Structures 49(3) (2016) 769-782.
[141] S.S. Raza, L.A. Qureshi, Effect of carbon fiber on mechanical properties of reactive powder concrete exposed to elevated temperatures, Journal of Building Engineering 42 (2021) 102503.
[142] R. Yu, P. Spiesz, H.J.H. Brouwers, Static properties and impact resistance of a green Ultra-High Performance Hybrid Fibre Reinforced Concrete (UHPHFRC): Experiments and modeling, Construction and Building Materials 68 (2014) 158-171.
[143] P.P. Li, Q.L. Yu, H.J.H. Brouwers, W. Chen, Conceptual design and performance evaluation of two-stage ultra-low binder ultra-high performance concrete, Cement and Concrete Research 125 (2019) 105858.
[144] J. Xiao, Q. Xie, W. Xie, Study on high-performance concrete at high temperatures in China (2004–2016)-An updated overview, Fire safety journal 95 (2018) 11-24.
[145] C. Xue, M. Yu, H. Xu, L. Xu, M. Saafi, J. Ye, Compressive performance and deterioration mechanism of ultra-high performance concrete with coarse aggregates under and after heating, Journal of Building Engineering 64 (2023) 105502.
[146] K. Yang, G. Long, Z. Tang, H. Wu, G. Ma, Z. Cheng, Y. Xiang, Y. Xie, Enhancement in strength and toughness of ultra-high performance concrete (UHPC) from micron-and nano-scale, Journal of Building Engineering 69 (2023) 106308.
[147] S. Agrawal, E. Yulianti, M. Amran, C.C. Hung, Behavior of unconfined steel-fiber reinforced UHPC post high-temperature exposure, Case Studies in Construction Materials 22 (2025) e04173.
[148] A.S. Arabani, H.D. Naserabadi, S. Aminyavari, Experimental investigation of energy absorption in fiber-reinforced ultra high-performance concrete after exposure to elevated temperatures, Case Studies in Construction Materials 22 (2025) e04451.
[149] ASTM C1609/C1609M, Standard Test Method for Flexural Performance of Fiber Reinforced Concrete (Using Beam with Third-point Loading), ASTM International, West Conshohocken, PA, 2012, pp. 1–9.
[150] S. Xu, H.W. Reinhardt, Determination of double-Determination of double-K criterion for crack propagation in quasi-brittle fracture Part I: experimental investigation of crack propagation, International Journal of Fracture. 98(2) (1999) 111-149.
[151] European Committee for Standardization (CEN), Eurocode 4: Design of composite steel and concrete structures – Part 1-1: General rules and rules for buildings, EN 1994-1-1, CEN, Brussels, Belgium, 2004.
[152] A.S. Dastgerdi, R.J. Peterman, K. Riding, B.T. Beck, Effect of concrete mixture components, proportioning, and compressive strength on fracture parameters, Construction and Building Materials 206 (2019) 179-192.
[153] X. Sun, Z. Gao, P. Cao, C. Zhou, Y. Ling, X. Wang, Y. Zhao, M. Diao, Fracture performance and numerical simulation of basalt fiber concrete using three-point bending test on notched beam, Construction and Building Materials 225 (2019) 788-800.
[154] M. D'ESSAI, T. MÉ, P. De La Rilem, Size-effect method for determining fracture energy and process zone size of concrete, Materials and Structures. 1(1) (1990) 7.
[155] J. Ye, J. Yu, C. Cui, Y. Wang, Flexural size effect of ultra-high ductile concrete under different damage and ductility levels, Cement and Concrete Composites 115 (2021) 103852.
[156] Y. Liu, J. Xie, J.-B. Yan, Flexural and fracture performance of UHPC exposed to low-temperature environment, Construction and Building Materials 373 (2023) 130865.
[157] B. Barr, M. Lee, E.J. de Place Hansen, D. Dupont, E. Erdem, S. Schaerlaekens, B. Schnütgen, H. Stang, L. Vandewalle, Round-robin analysis of the RILEM TC 162-TDF beam-bending test: Part 2—Approximation of δ from the CMOD response, Materials and Structures. 36(9) (2003) 621-630.

[158] M. Khan, J. Lao, M.R. Ahmad, J.G. Dai, Influence of high temperatures on the mechanical and microstructural properties of hybrid steel-basalt fibers based ultra-high-performance concrete (UHPC), Construction and Building Materials 411 (2024) 134387.
[159] G. Peng, J. Yang, Y. Shi, Experimental study on residual mechanical properties of ultra-high performance concrete exposed to high temperature, China Civ. Eng. J 50 (2017) 73-79.
[160] J.M. Yang, J.K. Kim, D.Y. Yoo, Performance of shotcrete containing amorphous fibers for tunnel applications, Tunnelling and Underground Space Technology 64 (2017) 85-94.
[161] C.K. Leung, R. Lai, A.Y. Lee, Properties of wet-mixed fiber reinforced shotcrete and fiber reinforced concrete with similar composition, Cement and Concrete Research 35(4) (2005) 788-795.
[162] K. Shirai, H. Yin, W. Teo, Flexural capacity prediction of composite RC members strengthened with UHPC based on existing design models, Structures, Elsevier, 2020, pp. 44-55.
[163] F. Chen, R. Yang, Z. Wang, G. Zhang, R. Yu, Rheological analysis and molecular dynamics modeling of Ultra-High Performance Concrete for wet-mix spraying, Journal of Building Engineering 68 (2023) 106167.
[164] H. Zhu, K. Yu, V.C. Li, Sprayable engineered cementitious composites (ECC) using calcined clay limestone cement (LC3) and PP fiber, Cement and Concrete Composites 115 (2021) 103868.
[165] J. Wei, N. Farzadnia, K.H. Khayat, Flexural post-cracking performance of macro synthetic fiber reinforced super workable concrete influenced by shrinkage-reducing admixture, Cement and Concrete Composites 155 (2025) 105847.
[166] G. Moelich, P. Kruger, R. Combrinck, Mitigating early age cracking in 3D printed concrete using fibres, superabsorbent polymers, shrinkage reducing admixtures, B-CSA cement and curing measures, Cement and Concrete Research 159 (2022) 106862.
[167] P.m. Zhan, Z.h. He, Application of shrinkage reducing admixture in concrete: A review, Construction and Building Materials 201 (2019) 676-690.
[168] Y. Zhang, L. Duan, H. Xin, C. Wang, Shrinkage behavior of ultra-high-performance concrete (UHPC) in cold winter conditions with shrinkage reducing agent (SRA) and expansive agent (EA), Construction and Building Materials 436 (2024) 136645.
[169] L. Fang, D. Fu, Q. Yuan, S. Xu, D. Zhang, H. Cai, X. Zeng, Y. Wang, J. Zhou, Combined effects of low-heat cement, expansive agent and shrinkage-reducing admixture on drying shrinkage and cracking of concrete, Case Studies in Construction Materials (2025) e04344.
[170] X. Ji, B. Wang, M. Liu, W. Zhang, Y. Ming, H. Ma, Expansion and creep of concrete with expansive agents at variable temperature, Journal of Building Engineering 87 (2024) 108982.
[171] P. Chen, T. Zhou, C. Pei, W. Tan, Y. Fang, Q. Liu, J. Wang, High-efficiency internal curing for ultra-high performance concrete using perforated cenospheres via an equivalent substitution approach, Construction and Building Materials 466 (2025) 140259.
[172] J. Wei, N. Farzadnia, K.H. Khayat, Synergistic effect of macro synthetic fiber and shrinkage-reducing admixture on engineering properties of fiber-reinforced super-workable concrete, Construction and Building Materials 414 (2024) 134566.
[173] M.D. Andersen, H.J. Jakobsen, J. Skibsted, Characterization of white Portland cement hydration and the CSH structure in the presence of sodium aluminate by 27Al and 29Si MAS NMR spectroscopy, Cement and Concrete Research 34(5) (2004) 857-868.
[174] G. Li, A. Zhang, G. Zhang, T. Tian, Study on a high strength ternary binder cured under different conditions, Construction and Building Materials 107 (2016) 385-393.
[175] P. Gu, Y. Fu, J. Beaudoin, A study of the hydration and setting behaviour of OPC-HAC pastes, Cement and Concrete Research 24(4) (1994) 682-694.

[176] R. Karim, M. Najimi, B. Shafei, Assessment of transport properties, volume stability, and frost resistance of non-proprietary ultra-high performance concrete, Construction and Building Materials 227 (2019) 117031.
[177] Z. Yang, S. Dong, Y. Zhang, Particle packing optimization and pore structure assessment of ternary cementitious system based on X-ray computed tomography and mercury intrusion porosimetry, Construction and Building Materials 413 (2024) 134913.
[178] L. Keke, L. Yong, X. Liuliu, Z. Junjie, L. Kangning, F. Dingqiang, Y. Rui, Rheological characteristics of Ultra-High performance concrete (UHPC) incorporating bentonite, Construction and Building Materials 349 (2022) 128793.
[179] H.J.H. Brouwers, Particle-size distribution and packing fraction of geometric random packings, Physical Review E 74, 031309-1-031309-14, Erratum, ibid. 069901(E) (2006), Erratum, Physical Review E 84, 059905 (E) (2011).
[180] Stradard for test method of performance on ordinary fresh concrete, in: S.A.O.T. China (Ed.)(GB50086-2016), China Quality and Standard Publishing & Media Co., Ltd., 2016.
[181] CEN (European Committee for Standardization), 2007. Sprayed concrete-Part 5: Admixtures for sprayed Concrete-Definitions, requirements, conformity, marking and labelling. EN 934-5:2007, CEN, Brussels.
[182] European Committee for Standardization (CEN), Methods of testing cement – Part 3: Determination of setting times and soundness, EN 196-3, CEN, Brussels, Belgium, 2016.
[183] J. Ouyang, Y. Tan, D.J. Corr, S.P. Shah, The thixotropic behavior of fresh cement asphalt emulsion paste, Construction and Building Materials 114 (2016) 906-912.
[184] ASTM International, Standard practice for use of apparatus for the determination of length change of hardened cement paste, mortar, and concrete, ASTM C490/C490M-21, ASTM International, West Conshohocken, PA, USA, 2021.
[185] F. Chen, R. Yang, S. Cheng, G. Zhang, S. Chen, A novel development of ultra-high performance concrete (UHPC) incorporating ordinary portland cement/calcium aluminate cement: Mechanical properties and microstucture, Journal of Building Engineering 99 (2025) 111672.
[186] A. Çolak, Physical, mechanical, and durability properties of gypsum Portland cement natural pozzolan blends, Canadian Journal of Civil Engineering 28(3) (2001) 375-382.
[187] European Committee for Standardization (CEN), Sprayed concrete – Part 5: Admixtures for sprayed concrete – Definitions, requirements, conformity, marking and labelling, EN 934-5:2007, CEN, Brussels, Belgium, 2007.
[188] D. Damidot, A. Rettel, Study of the interaction between the hydration of CA and of C3S at room temperature, Proceedings of the 11th International Congress on the Chemistry of Cement (ICCC), Durban, South Africa, 2003, p. 1854.
[189] F. Begarin, S. Garrault, A. Nonat, L. Nicoleau, Hydration of alite containing aluminium, Advances in Applied Ceramics 110(3) (2011) 127-130.
[190] Z.H. Ou, B.G. Ma, S.W. Jian, Influence of cellulose ethers molecular parameters on hydration kinetics of Portland cement at early ages, Construction and Building Materials 33 (2012) 78-83.
[191] Y. Yin, J. Huang, T. Wang, R. Yang, H. Hu, M. Manuka, F. Zhou, J. Min, H. Wan, D. Yuan, Effect of Hydroxypropyl methyl cellulose (HPMC) on rheology and printability of the first printed layer of cement activated slag-based 3D printing concrete, Construction and Building Materials 405 (2023) 133347.
[192] L. Ma, D. Yin, J. Ren, M. Tian, X. Chen, L. Li, An effective thixotropic structural dynamics rheological model for 3D printed concrete materials in the flow state, Construction and Building Materials 447 (2024) 138215.
[193] A. Das, L. Reiter, S. Mantellato, R.J. Flatt, Early-age rheology and hydration control of ternary binders for 3D printing applications, Cement and Concrete Research 162 (2022) 107004.

[194] X. Hu, L. Xu, M. Li, J. Wang, B. Ran, R. Huang, X. Zhou, Y. Xiong, Effect of temperature and superplasticizer on hydration of C3S and carbonation products of CSH, Construction and Building Materials 444 (2024) 137864.
[195] P. Rost, F. Goetz-Neunhoeffer, Increased monocarbonate formation during long-term hydration of CAC-limestone binder by calcium sulfate addition – A temperature-dependent XRD study, Cement and Concrete Research 176 (2024) 107395.
[196] Y. Cui, Z. Tan, Z. Zhou, J. Wu, J. Wang, Preparation and application of low rebound liquid alkali-free accelerator for shotcrete, Construction and Building Materials 367 (2023) 130220.
[197] E. Berodier, K. Scrivener, Understanding the Filler Effect on the Nucleation and Growth of C‐S‐H, Journal of the American Ceramic Society 97(12) (2014) 3764-3773.
[198] V. ŠATAVA, O. VEPŘEK, Thermal decomposition of ettringite under hydrothermal conditions, Journal of the American Ceramic Society 58(7‐8) (1975) 357-359.
[199] K. Scrivener, R. Snellings, B. Lothenbach, C. Press, A practical guide to microstructural analysis of cementitious materials, CRC press Boca Raton, FL, USA:2016.
[200] R. Yu, X. Zhang, Y. Hu, J. Li, F. Zhou, K. Liu, J. Zhang, J. Wang, Z. Shui, Development of a rapid hardening ultra-high performance concrete (R-UHPC): From macro properties to micro structure, Construction and Building Materials 329 (2022) 127188.
[201] H.F.W. Taylor, C. Famy, K. Scrivener, Delayed ettringite formation, Cement and Concrete Research 31(5) (2001) 683-693.
[202] E. Qoku, T.A. Bier, G. Schmidt, J. Skibsted, Impact of sulphate source on the hydration of ternary pastes of Portland cement, calcium aluminate cement and calcium sulphate, Cement and Concrete Composites 131 (2022) 104502.
[203] J. Seo, D. Jang, J.-H. Bae, N. Kim, J. Park, A. Cho, H.-K. Lee, Transformations in the reaction products and properties of carbonation-cured CSA cements exposed to a sulfate attack, Journal of CO2 Utilization 89 (2024) 102964.
[204] F. Winnefeld, B. Lothenbach, Phase equilibria in the system Ca4Al6O12SO4–Ca2SiO4–CaSO4–H2O referring to the hydration of calcium sulfoaluminate cements, RILEM Technical Letters 1 (2016) 10-16.
[205] W. Kunther, Z. Dai, J. Skibsted, Thermodynamic modeling of hydrated white Portland cement–metakaolin–limestone blends utilizing hydration kinetics from 29Si MAS NMR spectroscopy, Cement and Concrete Research 86 (2016) 29-41.
[206] K. Şengül, S.T. Erdoğan, Influence of ground perlite on the hydration and strength development of calcium aluminate cement mortars, Construction and Building Materials 266 (2021) 120943.
[207] E. Litwinek, D. Madej, Structure, microstructure and thermal stability characterizations of C3AH6 synthesized from different precursors through hydration, Journal of Thermal Analysis and Calorimetry 139(3) (2020) 1693-1706.
[208] J. Yu, J. Qian, J. Tang, Z. Ji, Y. Fan, Effect of ettringite seed crystals on the properties of calcium sulphoaluminate cement, Construction and Building Materials 207 (2019) 249-257.
[209] S.H. Kosmatka, W.C. Panarese, B. Kerkhoff, Design and control of concrete mixtures, Portland cement association Skokie, IL2002.
[210] J. Wang, Y. Tan, H. Li, J. Wang, Y. Gao, Comparative study on the moisture transfer properties of shotcrete and casting concrete, Construction and Building Materials 448 (2024) 138133.
[211] Z. Yao, J. Wang, L. Bi, H. Liao, T. Yu, R. Zhang, Y. Fang, Experimental study on dynamic tensile behavior of modified shotcrete-rock composite with different interface inclinations, Construction and Building Materials 458 (2025) 139606.

[212] E. Al Ameen, A. Blanco, S. Cavalaro, Comparative life cycle assessment of sprayed-UHPC sandwich panels over brick & block cavity construction, Engineering Structures 303 (2024) 117492.
[213] Y. Wang, C. Shi, Y. Ma, Y. Xiao, Y. Liu, Accelerators for shotcrete–Chemical composition and their effects on hydration, microstructure and properties of cement-based materials, Construction and Building Materials 281 (2021) 122557.
[214] J. Liu, S. Zang, F. Yang, Synergism of steel fibres and PVA fibres on the fracture and mechanical properties of ultra-high-performance concrete, Magazine of Concrete Research 76(14) (2024) 755-768.
[215] D.Y. Yoo, N. Banthia, Y.S. Yoon, Recent development of innovative steel fibers for ultra-high-performance concrete (UHPC): a critical review, Cement and Concrete Composites 145 (2024) 105359.
[216] Y. Deng, Z. Zhang, C. Shi, Z. Wu, C. Zhang, Steel fiber–matrix interfacial bond in ultra-high performance concrete: A review, Engineering 22 (2023) 215-232.
[217] J. Nehring, J. Neubauer, S. Berger, F. Goetz-Neunhoeffer, Acceleration of OPC by CAC in binary and ternary systems: The role of pore solution chemistry, Cement and Concrete Research 107 (2018) 264-274.
[218] Z. Wu, C. Shi, K.H. Khayat, Investigation of mechanical properties and shrinkage of ultra-high performance concrete: Influence of steel fiber content and shape, Composites Part B: Engineering 174 (2019) 107021.
[219] T. Liu, H. Wei, A. Zhou, D. Zou, H. Jian, Multiscale investigation on tensile properties of ultra-high performance concrete with silane coupling agent modified steel fibers, Cement and Concrete Composites 111 (2020) 103638.
[220] K. Cui, K. Liang, J. Chang, D. Lau, Investigation of the macro performance, mechanism, and durability of multiscale steel fiber reinforced low-carbon ecological UHPC, Construction and Building Materials 327 (2022) 126921.
[221] S. Ahmad, M. Rasul, S.K. Adekunle, S.U. Al-Dulaijan, M. Maslehuddin, S.I. Ali, Mechanical properties of steel fiber-reinforced UHPC mixtures exposed to elevated temperature: Effects of exposure duration and fiber content, Composites Part B: Engineering 168 (2019) 291-301.
[222] Z. Cheng, K. Yang, Z. Tang, F. Ge, X. Zhou, X. Zeng, K. Ma, G. Long, Experimental investigation on flexural and compressive toughness of mortar and concrete with hybrid toughening materials, Structures, Elsevier, 2022, pp. 1592-1599.
[223] N.Y. Mostafa, Z. Zaki, O.H. Abd Elkader, Chemical activation of calcium aluminate cement composites cured at elevated temperature, Cement and Concrete Composites 34(10) (2012) 1187-1193.
[224] H. Son, S. Park, H. Kim, J. Seo, H.K. Lee, Effect of CaSO4 on hydration and phase conversion of calcium aluminate cement, Construction and Building Materials 224 (2019) 40-47.
[225] S. Zhang, X. Xu, S.A. Memon, Z. Dong, D. Li, H. Cui, Effect of calcium sulfate type and dosage on properties of calcium aluminate cement-based self-leveling mortar, Construction and Building Materials 167 (2018) 253-262.
[226] J. Wang, Y. Xie, X. Zhong, L. Li, Test and simulation of cement hydration degree for shotcrete with alkaline and alkali-free accelerators, Cement and Concrete Composites 112 (2020) 103684.
[227] C. Paglia, F. Wombacher, H. Böhni, The influence of alkali-free and alkaline shotcrete accelerators within cement systems: I. Characterization of the setting behavior, Cement and Concrete Research 31(6) (2001) 913-918.
[228] B. Lothenbach, D. Rentsch, E. Wieland, Hydration of a silica fume blended low-alkali shotcrete cement, Physics and Chemistry of the Earth, Parts A/B/C 70 (2014) 3-16.

[229] H. Son, S. Park, J. Jang, H.K. Lee, Effect of nano-silica on hydration and conversion of calcium aluminate cement, Construction and Building Materials 169 (2018) 819-825.
[230] H. Kim, H. Son, H.K. Lee, Review on recent advances in securing the long-term durability of calcium aluminate cement (CAC)-based systems, Functional composites and structures 3(3) (2021) 035002.
[231] H.A. Ali, K. Sun, J.X. Lu, C.S. Poon, R. Shilton, N. Banthia, Functionalizing heavy metal contained incinerated sewage sludge ash in recycled glass-based alkali-activated materials for sewer environment, Construction and Building Materials 450 (2024) 138724.
[232] B. Luo, C. Deng, Y. Luo, Mechanical properties and microstructure of UHPC with recycled glasses after exposure to elevated temperatures, Journal of Building Engineering 62 (2022) 105369.
[233] J. Yang, G.F. Peng, J. Zhao, G.S. Shui, On the explosive spalling behavior of ultra-high performance concrete with and without coarse aggregate exposed to high temperature, Construction and Building Materials 226 (2019) 932-944.
[234] D. Zhang, K.H. Tan, Fire performance of ultra-high performance concrete: effect of fine aggregate size and fibers, Archives of Civil and Mechanical Engineering 22(3) (2022) 116.
[235] S. Banerji, V. Kodur, Effect of temperature on mechanical properties of ultra‐high performance concrete, Fire and Materials. 46(1) (2022) 287-301.
[236] Z. Mao, J. Zhang, Z. Luo, Q. Ma, Y. Duan, S. Li, Y. Miao, Behavior evaluation of hybrid fibre-reinforced reactive powder concrete after elevated temperatures, Construction and Building Materials 306 (2021) 124917.
[237] J. Tang, W. Ma, Y. Pang, J. Fan, D. Liu, L. Zhao, S.A. Sheikh, Uniaxial compression performance and stress–strain constitutive model of the aluminate cement-based UHPC after high temperature, Construction and Building Materials 309 (2021) 125173.
[238] L. Bodnarova, J. Valek, L. Sitek, J. Foldyna, Effect of high temperatures on cement composite materials in concrete structures, Acta geodynamica et geomaterialia 10(2) (2013) 173-180.
[239] L. Amathieu, T.A. Bier, K. Scrivener, Mechanisms of set acceleration of Portland cement through CAC addition, CAC: calcium aluminate cements 2001 (Edinburgh, 16-19 July 2001), 2001, pp. 303-317.
[240] G. Le Saoût, B. Lothenbach, A. Hori, T. Higuchi, F. Winnefeld, Hydration mechanism of quick hardening cement based on OPC blended with an amorphous calcium aluminate, 18th Internationale Baustofftagung (IBAUSIL) Weimar (2012) 474-481.
[241] K.S. Karunadasa, C. Manoratne, H. Pitawala, R. Rajapakse, Thermal decomposition of calcium carbonate (calcite polymorph) as examined by in-situ high-temperature X-ray powder diffraction, Journal of Physics and Chemistry of solids 134 (2019) 21-28.
[242] T. Peijs, R. Kirschbaum, P.J. Lemstra, A critical review of carbon fiber and related products from an industrial perspective, Advanced Industrial and Engineering Polymer Research 5(2) (2022) 90-106.
[243] S. Maiti, N. Jain, P. Prajapati, Synthesis of calcium sulfate whiskers via acidification exploiting FGD gypsum for improved binder properties, Sustainable Chemistry and Pharmacy 42 (2024) 101745.
[244] G. Liu, Y. Liao, X. Sha, G. Liu, Y. Zhang, R. Guo, Y. Yue, Application of calcium sulfate whiskers to cement-based materials: A review, Materials. 17(5) (2024) 1138.
[245] A. Bhardwaj, S. Maiti, N. Jain, A. Pathak, R.R. Gupta, Calcium Sulphate whiskers (CSW) an innovative material for civil engineering applications: A critical review of its preparation, characterization, current trends, and prospects, Construction and Building Materials 420 (2024) 135624.
[246] Y. Chen, Y. Zhang, S. Zhang, Q. Guo, Y. Gao, T. Zhang, W. Zhao, Q. Chen, H. Zhu, Experimental study on the thermal properties of a novel ultra-high performance concrete

reinforced with multi-scale fibers at elevated temperatures, Construction and Building Materials 366 (2023) 130229.
[247] Y. Li, E.H. Yang, K.H. Tan, Effects of heating followed by water quenching on strength and microstructure of ultra-high performance concrete, Construction and Building Materials 207 (2019) 403-411.
[248] K. Ishikawa, 1.17 bioactive ceramics: cements,, Comprehensive Biomaterials II, (2017) 368-391.
[249] H.C. Yang, T.P. Tsai, C.T. Hsieh, Enhancement on fireproof performance of construction coatings using calcium sulfate whiskers prepared from wastewater, Chemical Papers 71(7) (2017) 1343-1350.
[250] D. Suescum-Morales, J.D. Ríos, A. Martínez-De La Concha, H. Cifuentes, J.R. Jiménez, J.M. Fernández, Effect of moderate temperatures on compressive strength of ultra-high-performance concrete: A microstructural analysis, Cement and Concrete Research 140 (2021) 106303.
[251] S. Mohammed, G. Elhem, B. Mekki, Valorization of pozzolanicity of Algerian clay: Optimization of the heat treatment and mechanical characteristics of the involved cement mortars, Applied Clay Science. 132-133 (2016) 711-721.
[252] A. Hidalgo, J. García, M. Alonso, L. Fernández, C. Andrade, Microstructure development in mixes of calcium aluminate cement with silica fume or fly ash, Journal of thermal analysis and calorimetry 96(2) (2009) 335-345.
[253] N. Ukrainczyk, T. Matusinovic, S. Kurajica, B. Zimmermann, J. Sipusic, Dehydration of a layered double hydroxide—C2AH8, Thermochimica Acta 464(1-2) (2007) 7-15.
[254] N. Lee, K. Koh, S. Park, G. Ryu, Microstructural investigation of calcium aluminate cement-based ultra-high performance concrete (UHPC) exposed to high temperatures, Cement and Concrete Research 102 (2017) 109-118.
[255] X. Cheng, Q. Dong, Z. Li, X. Guo, High-temperature mechanical properties of calcium sulfate whisker-reinforced high-alumina cement, Magazine of Concrete Research 72(2) (2020) 55-67.
[256] L. Xing, C. Gu, Z. Lv, Y. Bao, High-temperature internal oxidation behavior of surface cracks in low alloy steel bloom, Corrosion Science 197 (2022) 110076.
[257] F.L. Yaggee, E. Gilbert, J. Styles, Thermal expansivities, thermal conductivities, and densities of vanadium, titanium, chromium and some vanadium-base alloys: A comparison with austenitic stainless steel, Journal of the Less Common Metals 19(1) (1969) 39-51.
[258] R. Serafini, R.R. Agra, L.A. Bitencourt Jr, A. de la Fuente, A.D. de Figueiredo, Bond-slip response of steel fibers after exposure to elevated temperatures: Experimental program and design-oriented constitutive equation, Composite Structures 255 (2021) 112916.
[259] B. Chen, J. Liu, Residual strength of hybrid-fiber-reinforced high-strength concrete after exposure to high temperatures, Cement and Concrete Research 34(6) (2004) 1065-1069.
[260] Y. Li, K.H. Tan, E.H. Yang, Synergistic effects of hybrid polypropylene and steel fibers on explosive spalling prevention of ultra-high performance concrete at elevated temperature, Cement and Concrete Composites 96 (2019) 174-181.

# Appendix A. Images of UHPC/SUHPC after high-temperature exposure.

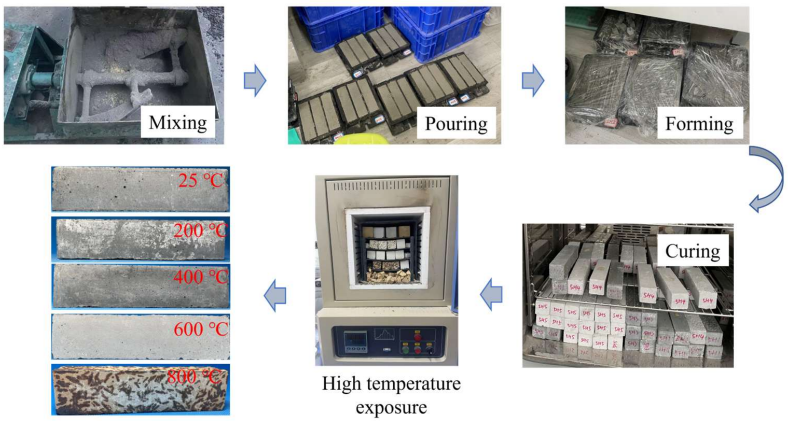


Fig. A1. UHPC production and high-temperature treatment.

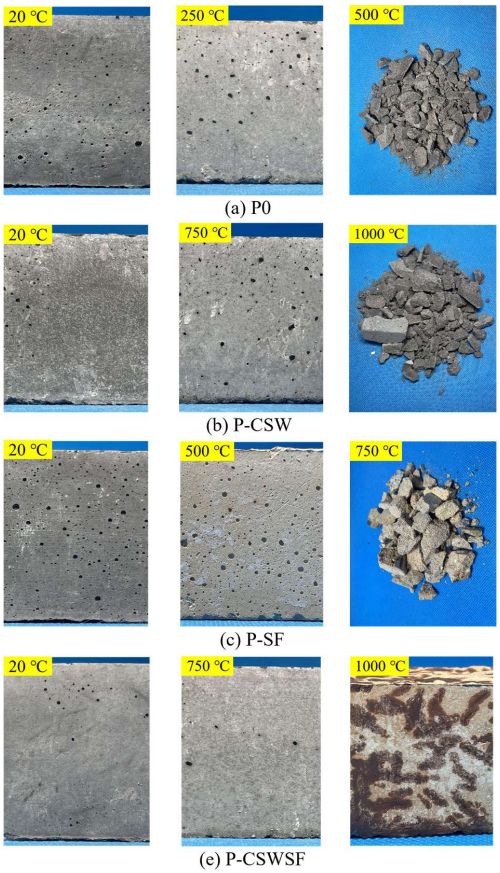


Fig. A2. Images of P-SUHPC specimens after exposure to elevated temperatures.

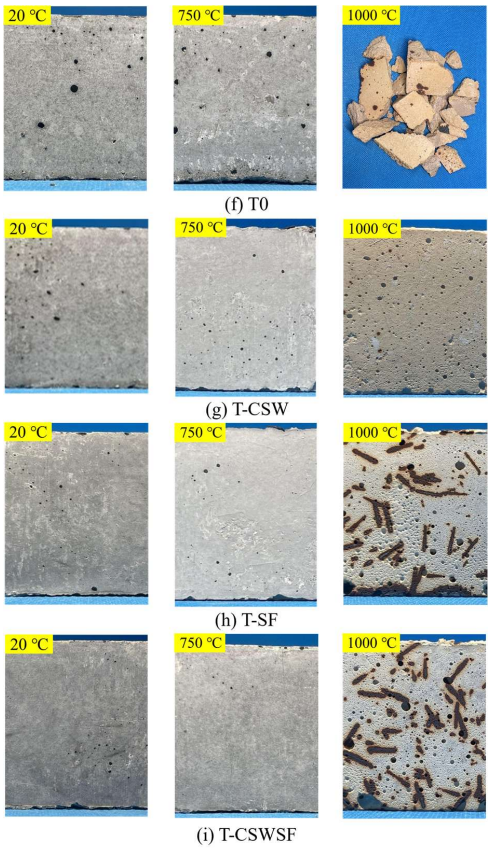


Fig. A3. Images of T-SUHPC specimens after exposure to elevated temperatures.

# Appendix B. Mix proportions of SUHPC.

Table B1. Mix proportions of SUHPC (kg/m$^3$).

| Mixture | PC | CAC | C$ | MS | FAC | QS-3 | QS-2 | QS-1 | Steel fiber | SP | Water | Accelerator |
|---|---|---|---|---|---|---|---|---|---|---|---|---|
| P100 | 791 | - | - | 179 | 144 | 412 | 510 | 192 | 156 | 47 | 188.3 | - |
| P70-CAC30 | 553.7 | 237.3（30%） | - | 179 | 144 | 412 | 510 | 192 | 156 | 49.5 | 195 | - |
| P70-CAC24-C$6 | 553.7 | 189.8（24%） | 47.5(6%) | 179 | 144 | 412 | 510 | 192 | 156 | 49.5 | 195 | - |
| P70-CAC20-C$10 | 553.7 | 158.2（20%） | 79.1(10%) | 179 | 144 | 412 | 510 | 192 | 156 | 49.5 | 195 | - |
| P70-CAC17-C$13 | 553.7 | 135.6（17%） | 101.7(13%） | 179 | 144 | 412 | 510 | 192 | 156 | 49.5 | 195 | - |
| P70-CAC15-C$15 | 553.7 | 118.7（15%） | 118.7(15%) | 179 | 144 | 412 | 510 | 192 | 156 | 49.5 | 195 | - |
| P100-A | 791 | - | - | 179 | 144 | 412 | 510 | 192 | 156 | 47 | 188.3 | 22.28 |
| P70-CAC30-A | 553.7 | 237.3（30%） | - | 179 | 144 | 412 | 510 | 192 | 156 | 49.5 | 195 | 22.28 |
| P70-CAC24-C$6-A | 553.7 | 189.8（24%） | 47.5(6%) | 179 | 144 | 412 | 510 | 192 | 156 | 49.5 | 195 | 22.28 |
| P70-CAC20-C$10-A | 553.7 | 158.2（20%） | 79.1(10%) | 179 | 144 | 412 | 510 | 192 | 156 | 49.5 | 195 | 22.28 |

**Note:** P indicates the Portland cement CEM I 52.5 R (PC); CAC indicates the calcium aluminate cement; C$ indicates the gypsum; A indicates the accelerator; P100 indicates the cementitious material consists of 100 wt.% PC; P70-CAC30 indicates that 70 wt.% of the cementitious material is PC and 30 wt.% is CAC; P70-CAC24-C$6 indicates that 70 wt.% of the cementitious material is PC, with 24 wt.% CAC and 6 wt.% C$.

# List of notations

*Abbreviations*

| | |
|---|---|
| AFm | Alumina-ferric oxide-mono Phase |
| AFt | Alumina-ferric oxide-tri Phase |
| C-(A)-S-H | Calcium (aluminum) silicate hydrate |
| $C_3S$ | Tricalcium silicate |
| $C_2S$ | Dicalcium silicate |
| CAC | Calcium aluminate cement |
| C$, $C\overline{S}$ | Gypsum |
| CH | Calcium hydroxide |
| CSW | Calcium sulfate whiskers |
| CMOD | Crack mouth opening displacement |
| CAH | Calcium Aluminate Hydrates |
| DTG | Differential thermogravimetry |
| DEF | Delayed ettringite formation |
| EDS | Energy-dispersive spectrometer |
| FA | Fly ash |
| FAC | Fly ash cenosphere |
| FT-IR | Fourier transform infrared spectroscopy |
| GGBS | Ground granulated blast furnace slag |
| Hc | Hemicarboaluminates |
| HPMC | Hydroxypropyl Methylcellulose |
| ITZ | Interfacial transition zone |
| LOI | Loss on ignition |
| LP | Limestone powder |
| LDHs | Layered double hydroxides |
| MIP | Mercury intrusion porosimetry |
| MK | Metakaolin |
| MAA | Modified Andreasen and Andersen model |
| MS | Microsilica (Silica fume) |
| Micro-XCT | Micro X-ray Computed Tomography |
| Mc | Monocarboaluminates |
| NSC | Normal Strength Concrete |
| OPC | Ordinary Portland cement |
| PC | Portland cement |
| PCE | Polycarboxylate superplasticizer |
| PC–CAC–C$ | Portland cement–calcium aluminate cement–gypsum |
| PP | Polypropylene |
| PVA | Polyvinyl alcohol |
| PET | Polyethylene terephthalate |
| Q-XRD | Quantitative X-ray diffraction |
| RT | Room temperature |

| | |
|---|---|
| SEM | Scanning Electron Microscope |
| SF | Steel fiber |
| SUHPC | Sprayed ultra-high-performance concrete |
| SRA | Shrinkage-reducing admixtures |
| SCMs | Supplementary cementitious materials |
| TG | Thermogravimetry |
| UHPC | Ultra-High-Performance Concrete |
| UHPFRC | Ultra-high-performance fiber-reinforced concrete |
| VEAs | Viscosity-enhancing admixtures |
| w/b | Water to binder ratio |
| XRD | X-ray diffraction |
| XRF | X-ray fluorescence |

| *Nomenclature* | | SI unit |
|---|---|---|
| $\Gamma$ | Relative slump | - |
| U | Applied voltage | v |
| $X_d$ | Penetration depths | mm |
| $D_{nssm}$ | Chloride migration coefficient | - |
| T | Average value of the initial and final temperatures | °C |
| L | Thickness of the concrete specimen | mm |
| $f_{cr}$ | Pre-cracking strength | MPa |
| $f_r$ | Peak strength | MPa |
| d | Day | d |
| E | Immobilization efficiency of the element in each mix | % |
| $D_{min}$ | Minimum particle size of aggregate | mm |
| $D_{max}$ | Maximum particle size of aggregate | mm |
| $P_{mix}$ | Gradation of the mixture | - |
| h | Hour | h |
| $P_{target}$ | Target mixture gradation | - |
| q | Distribution modulus | - |
| P-CMOD | Load crack mouth opening displacement curve | - |
| min | Minute | min |
| $V_{SF}$ | Volume content of steel fibers | % |
| $L_i$ | Initial comparator reading of the specimen minus | mm |
| G | Nominal gauge length of the apparatus | mm |

| *Greek letters* | | SI unit |
|---|---|---|
| $\delta_{cr}$ | Deflection corresponding to the first crack load | mm |
| $\delta_p$ | Deflection corresponding to the maximum load | mm |
| $a$ | Crack length of the test beam | mm |
| $\beta_{cu}{}^{T}$ | Compressive strength influence factor | - |
| $\beta_G$ | Fracture energy influencing factor | - |

# Acknowledgements

This dissertation presents the research work I have conducted at Eindhoven University of Technology during my doctoral study since October 2021. I am deeply grateful for the valuable opportunity provided by Eindhoven University of Technology and the support of the China Scholarship Council. Over the past four years, I have made meaningful progress in my research and, more importantly, learned to cultivate an effective mindset and methodology for problem-solving, which has contributed to my growth and development.

I would like to express my sincere gratitude to my supervisors, Prof. dr. ir. H.J.H. (Jos) Brouwers and Dr. Qingliang Yu. I am truly thankful to Jos for granting me the opportunity to join the Building Materials group. Throughout my PhD study, his inspiring guidance during countless meetings and his continuous concern about whether I needed further support made my academic journey smoother and more fulfilling. I am deeply indebted to Qingliang for his patient supervision and insightful guidance at every stage of my research. His professional guidance has been of great importance for both my experimental work and manuscript writing, significantly improving the quality of this thesis. It has been my great honor to work under the supervision of Jos and Qingliang, from whom I have learned not only essential research skills but also the passion and perseverance required for academic inquiry.

I also wish to extend my sincere appreciation to the members of my committee: Prof. dr. Caijun Shi (Hunan University), Prof. dr. Maria Chiara Bignozzi (University of Bologna), Prof. dr. Päivö Kinnunen (University of Oulu), Prof. dr. David M.J. Smeulders, Dr. E. Bosco, and Dr. Rob Wolfs from TU/e, for their interest in my research and their constructive suggestions for improving this thesis.

An essential part of this research was the field spraying tests, which required access to facilities, spraying equipment, and technical support. I am grateful to the technicians in both the Netherlands and China for making these experiments possible, especially ing. G.A.H. (Geert-Jan) Maas and Dr. Rob Wolfs for their friendly help and insightful discussions during the spraying experiments. My sincere thanks go to all my co-authors, whose cooperation has significantly supported the progress of this work.

I am also delighted to have met so many friendly colleagues in the Netherlands. To my wonderful colleagues—Alex, Anna, Beatrice, Ceren, Charles, Daoru, Fan, Felix, Helong, Hossein, Iris, Jawad, Jiale, Jinyang, Jonathan, Kinga, Leila, Marc, Marina, Marvin, Naomi, Quan, Ricardo, Samantha, Samuel, Shaohua, Shashank, Tao, Winnie, Xuan, Yan, Yanjie, Yanshuo, Yilu, Yuxuan, Zhihan, and Zixing—I am sincerely thankful for the enjoyable time we shared together. I would like to thank my friends ZY, LM, GG, HX, Fang, SQ and Pei, whose presence made my life in the Netherlands relaxed and joyful.

I would like to express my deepest gratitude to my parents. I am truly grateful that we have always communicated like friends, offering mutual support and encouragement.

# Summary

Fire exposure remains a critical challenge in civil engineering disaster prevention, posing a significant and unavoidable threat to modern structural systems. Repair materials should be capable of delivering high-strength structural support within hours following fire exposure, while exhibiting adequate thermal resistance to ensure the safety of both occupants and the structural system. Sprayed ultra-high-performance concrete (SUHPC) exhibits high strength and excellent durability, along with the advantage of rapid placement on complex geometries. These characteristics make it a promising candidate for use in rapid repair applications. However, the development of SUHPC still faces several critical challenges that require urgent improvement, including early-age performance (such as rheological behavior and early strength), later-age mechanical properties, and spalling resistance after high-temperature exposure.

Building upon previous investigations into binder optimization and high-temperature performance of UHPC, this thesis develops a novel SUHPC incorporating a PC–CAC–C$ ternary binder system. The proposed SUHPC simultaneously achieves excellent early-age properties, improved later-age mechanical performance, and enhanced resistance to explosive spalling under elevated temperatures. The research framework of this thesis consists of two main parts: Part I focuses on binder optimization and high-temperature performance of UHPC, while Part II extends these findings to the design and development of a spalling-resistant SUHPC.

**Part I (Chapters 2 and 3) addresses binder optimization and durability of UHPC, with a particular emphasis on its spalling resistance under elevated temperatures.**

**Chapter 2** systematically investigates the effects of SCMs, GGBS and LP, on the hydration process, pore structure, chloride penetration resistance, and spalling resistance of UHPC under elevated temperatures. Pore structure analysis identifies 30 wt% and 15 wt% as the optimal replacement levels for GGBS and LP, respectively. At these replacement levels, the pore structure of UHPC is significantly refined, as evidenced by a reduction in critical pore diameter and total porosity, an increase in gel porosity, and improved mechanical performance. Within the range of 0–45 wt%, GGBS effectively enhances the chloride penetration resistance of UHPC, with the optimal performance observed at 30 wt%. In contrast, the incorporation of LP tends to weaken chloride resistance, particularly at replacement levels exceeding 15 wt%, primarily due to increased pore connectivity and reduced fiber–matrix interfacial bonding. Despite the improvements in durability, the high-temperature spalling behavior of UHPC incorporating GGBS or LP remains a concern. Both GGBS and LP exhibit detrimental effects on the explosive spalling resistance of UHPC at elevated temperatures. At a replacement level of 15 wt%, LP significantly lowers the spalling onset temperature from 750 °C to 500 °C relative to the reference specimen. A comparable trend is noted with the inclusion of GGBS at 0–45 wt%.

**Chapter 3** investigates the fracture mechanisms of UHPC incorporating different steel fiber volume contents after exposure to elevated temperatures of 200 °C, 400 °C, 600 °C, and 800 °C. Elevated temperatures lead to a pronounced degradation in the bending toughness, double-K

fracture toughness, and fracture energy of UHPC. This deterioration eliminates the characteristic strengthening stage, inducing a direct transition to failure and resulting in a more brittle fracture response. A predictive model is developed using steel fiber volume fraction and exposure temperature as variables, enabling the estimation of residual compressive strength, flexural strength, and fracture energy. The model shows strong predictive capability, as confirmed by experimental validation.

**Part II (Chapters 4 to 6) extends these investigations to SUHPC, addressing its binder design and explosive spalling resistance under elevated temperatures.**

**Chapter 4** builds upon the findings from Part I on UHPC and extends the research toward the development of a sprayed UHPC. Rapid setting and early load-bearing capacity are essential requirements, making early-age performance a critical design focus. Chapter 4 presents the development of a novel SUHPC incorporating a PC–CAC–C$ ternary binder system, which improves early-age strength, rheological behavior, and shrinkage resistance. An optimal C$/CAC ratio of 0.5 results in SUHPC with elevated thixotropy and dynamic yield stress, thereby improving its rheological performance and facilitating better pumpability and sprayability. The optimized PC–CAC–C$ ternary system significantly improves the early-age strength of SUHPC, achieving a 3-hour compressive strength of 15.11 MPa. With the further incorporation of an alkali-free accelerator, the initial setting time is reduced to 4.3 minutes, and the 3-hour strength increases to 20.37 MPa. The results meet the performance requirements for rapid setting and high early strength in structural repair applications.

**Chapter 5** builds upon the early-age performance improvements presented in Chapter 4 by focusing on the later-age mechanical properties of SUHPC, thereby ensuring its structural applicability in engineering practice. Chapter 5 investigates the effects of various binder systems (with PC, CAC and C$) and alkali-free accelerator on the later-age mechanical properties of SUHPC. Compared to PC-based system, the binary system (PC–CAC) leads to a significant reduction in both the flexural and compressive strengths. The ternary binder system (PC–CAC–C$) enhances both flexural and compressive strength at later ages, with progressive improvements observed as the C$ content increases up to 15 wt%. Although the alkali-free accelerator enhances early-age strength, it adversely affects later-age mechanical performance. This adverse effect can be partially mitigated by incorporating the PC–CAC–C$ ternary binder system.

**Chapter 6** further develops a spalling-resistant SUHPC incorporating a PC–CAC–C$ binder system, reinforced with CSW and steel fibers, and evaluates its performance at elevated temperatures. The role of CSW and steel fibers in enhancing the explosive spalling resistance of SUHPC based on a ternary binder system is systematically examined at elevated temperatures. Even after exposure to 1000 °C, the ternary binder system exhibits the presence of thermally stable crystalline phases, including $Al_2O_3$, $C_{12}A_7$, and wollastonite. The ternary binder system significantly increases the capillary pore volume of SUHPC within the 20 nm to 10 μm range, while the total porosity rises from 9.70% to 12.18%. This promotes vapor release at elevated temperatures and thereby enhances resistance to explosive spalling. Even after exposure to 1000 °C, the SUHPC maintains high residual mechanical strength, with compressive and flexural strengths reaching 45.78 MPa and 7.35 MPa, respectively. The

incorporation of CSW and steel fibers into the ternary binder system effectively enhances the spalling resistance of SUHPC at elevated temperatures.

## List of publications

[1] **J. He**, H.Y. Wang, and Q.L. Yu, Flexural fracture behavior of ultra-high performance concrete after high-temperature exposure. ***Construction and Building Materials***, 481 (2025), 141544.

[2] **J. He**, Q.L. Yu, Z.Y. Tang, H.Y. Wang, Z.R. Chen, and B.Y. Wei, Effects of different cementitious materials and accelerators on the flexural and compressive behaviors of SUHPC. ***Case Studies in Construction Materials***, 23 (2025), e04913.

[3] **J. He**, T. Liu, W.W. Wu, X. Ling, and Q.L. Yu, Mechanism of SCMs on the hydration, pore structure, and durability of UHPFRC. ***Journal of Sustainable Cement-Based Materials*** 14(9) (2025) 1899–1916.

[4] **J. He**, Y.S. She, X. Ling, H.Y. Wang, H.J.H. Brouwers, and Q.L. Yu, Development of a Novel SUHPC Based on PC-CAC-C$ System: Rheology, Early-Age Strength, and Hydration Kinetics. ***Construction and Building Materials***, 502 (2025),144420.

[5] **J. He**, Y.S. Liu, X. Ling, H.Y. Wang, Z.Y. Tang, Z.R. Chen, and Q.L. Yu, Spalling resistance of SUHPC based on PC-CAC-C$ at elevated temperature: Role of whiskers and steel fibers. ***Construction and Building Materials***, 507 (2026),145100.

## Curriculum vitae

Jia He was born on 24 July 1995 in Hubei, China. She obtained her Bachelor's degree in Civil Engineering from China Three Gorges University in July 2018. In July 2021, she obtained her Master's degree in Bridge and Tunnel Engineering from Wuhan University of Technology. The research topic of her master study was Experimental and Numerical Analysis of Polypropylene Fiber-Reinforced Concrete Beams. In October 2021, she commenced her PhD study at Eindhoven University of Technology, the Netherlands, under the supervision of Prof. dr. ir. H.J.H. Brouwers and Dr. Qingliang Yu. Her doctoral research focused on the spalling resistance of UHPC and SUHPC after high-temperature exposure, the outcomes of which are presented in this dissertation.

**Bouwstenen** is een publicatiereeks
van de Faculteit Bouwkunde,
Technische Universiteit Eindhoven.
Zij presenteert resultaten van
onderzoek en andere activiteiten op
het vakgebied der Bouwkunde,
uitgevoerd in het kader van deze
Faculteit.

**Bouwstenen** en andere proefschriften van de
TU/e zijn online beschikbaar via:
https://research.tue.nl/

Reeds verschenen in de serie
**Bouwstenen**

nr 1
**Elan: A Computer Model for Building Energy Design: Theory and Validation**
Martin H. de Wit
H.H. Driessen
R.M.M. van der Velden

nr 2
**Kwaliteit, Keuzevrijheid en Kosten: Evaluatie van Experiment Klarendal, Arnhem**
J. Smeets
C. le Nobel
M. Broos
J. Frenken
A. v.d. Sanden

nr 3
**Crooswijk: Van 'Bijzonder' naar 'Gewoon'**
Vincent Smit
Kees Noort

nr 4
**Staal in de Woningbouw**
Edwin J.F. Delsing

nr 5
**Mathematical Theory of Stressed Skin Action in Profiled Sheeting with Various Edge Conditions**
Andre W.A.M.J. van den Bogaard

nr 6
**Hoe Berekenbaar en Betrouwbaar is de Coëfficiënt k in x-ksigma en x-ks?**
K.B. Lub
A.J. Bosch

nr 7
**Het Typologisch Gereedschap: Een Verkennende Studie Omtrent Typologie en Omtrent de Aanpak van Typologisch Onderzoek**
J.H. Luiten

nr 8
**Informatievoorziening en Beheerprocessen**
A. Nauta
Jos Smeets (red.)
Helga Fassbinder (projectleider)
Adrie Proveniers
J. v.d. Moosdijk

nr 9
**Strukturering en Verwerking van Tijdgegevens voor de Uitvoering van Bouwwerken**
ir. W.F. Schaefer
P.A. Erkelens

nr 10
**Stedebouw en de Vorming van een Speciale Wetenschap**
K. Doevendans

nr 11
**Informatica en Ondersteuning van Ruimtelijke Besluitvorming**
G.G. van der Meulen

nr 12
**Staal in de Woningbouw, Korrosie-Bescherming van de Begane Grondvloer**
Edwin J.F. Delsing

nr 13
**Een Thermisch Model voor de Berekening van Staalplaatbetonvloeren onder Brandomstandigheden**
A.F. Hamerlinck

nr 14
**De Wijkgedachte in Nederland: Gemeenschapsstreven in een Stedebouwkundige Context**
K. Doevendans
R. Stolzenburg

nr 15
**Diaphragm Effect of Trapezoidally Profiled Steel Sheets: Experimental Research into the Influence of Force Application**
Andre W.A.M.J. van den Bogaard

nr 16
**Versterken met Spuit-Ferrocement: Het Mechanische Gedrag van met Spuit-Ferrocement Versterkte Gewapend Betonbalken**
K.B. Lubir
M.C.G. van Wanroy

nr 17
**De Tractaten van Jean Nicolas Louis Durand**
G. van Zeyl

nr 18
**Wonen onder een Plat Dak: Drie Opstellen over Enkele Vooronderstellingen van de Stedebouw**
K. Doevendans

nr 19
**Supporting Decision Making Processes: A Graphical and Interactive Analysis of Multivariate Data**
W. Adams

nr 20
**Self-Help Building Productivity: A Method for Improving House Building by Low-Income Groups Applied to Kenya 1990-2000**
P. A. Erkelens

nr 21
**De Verdeling van Woningen: Een Kwestie van Onderhandelen**
Vincent Smit

nr 22
**Flexibiliteit en Kosten in het Ontwerpproces: Een Besluitvormingondersteunend Model**
M. Prins

nr 23
**Spontane Nederzettingen Begeleid: Voorwaarden en Criteria in Sri Lanka**
Po Hin Thung

nr 24
**Fundamentals of the Design of Bamboo Structures**
Oscar Arce-Villalobos

nr 25
**Concepten van de Bouwkunde**
M.F.Th. Bax (red.)
H.M.G.J. Trum (red.)

nr 26
**Meaning of the Site**
Xiaodong Li

nr 27
**Het Woonmilieu op Begrip Gebracht: Een Speurtocht naar de Betekenis van het Begrip 'Woonmilieu'**
Jaap Ketelaar

nr 28
**Urban Environment in Developing Countries**
editors: Peter A. Erkelens
George G. van der Meulen (red.)

nr 29
**Stategische Plannen voor de Stad: Onderzoek en Planning in Drie Steden**
prof.dr. H. Fassbinder (red.)
H. Rikhof (red.)

nr 30
**Stedebouwkunde en Stadsbestuur**
Piet Beekman

nr 31
**De Architectuur van Djenné: Een Onderzoek naar de Historische Stad**
P.C.M. Maas

nr 32
**Conjoint Experiments and Retail Planning**
Harmen Oppewal

nr 33
**Strukturformen Indonesischer Bautechnik: Entwicklung Methodischer Grundlagen für eine 'Konstruktive Pattern Language' in Indonesien**
Heinz Frick arch. SIA

nr 34
**Styles of Architectural Designing: Empirical Research on Working Styles and Personality Dispositions**
Anton P.M. van Bakel

nr 35
**Conjoint Choice Models for Urban Tourism Planning and Marketing**
Benedict Dellaert

nr 36
**Stedelijke Planvorming als Co-Produktie**
Helga Fassbinder (red.)

nr 37
**Design Research in the Netherlands**
editors: R.M. Oxman
M.F.Th. Bax
H.H. Achten

nr 38
**Communication in the Building Industry**
Bauke de Vries

nr 39
**Optimaal Dimensioneren van Gelaste Plaatliggers**
J.B.W. Stark
F. van Pelt
L.F.M. van Gorp
B.W.E.M. van Hove

nr 40
**Huisvesting en Overwinning van Armoede**
P.H. Thung
P. Beekman (red.)

nr 41
**Urban Habitat: The Environment of Tomorrow**
George G. van der Meulen
Peter A. Erkelens

nr 42
**A Typology of Joints**
John C.M. Olie

nr 43
**Modeling Constraints-Based Choices for Leisure Mobility Planning**
Marcus P. Stemerding

nr 44
**Activity-Based Travel Demand Modeling**
Dick Ettema

nr 45
**Wind-Induced Pressure Fluctuations on Building Facades**
Chris Geurts

nr 46
**Generic Representations**
Henri Achten

nr 47
**Johann Santini Aichel: Architectuur en Ambiguiteit**
Dirk De Meyer

nr 48
**Concrete Behaviour in Multiaxial Compression**
Erik van Geel

nr 49
**Modelling Site Selection**
Frank Witlox

nr 50
**Ecolemma Model**
Ferdinand Beetstra

nr 51
**Conjoint Approaches to Developing Activity-Based Models**
Donggen Wang

nr 52
**On the Effectiveness of Ventilation**
Ad Roos

nr 53
**Conjoint Modeling Approaches for Residential Group preferences**
Eric Molin

nr 54
**Modelling Architectural Design Information by Features**
Jos van Leeuwen

nr 55
**A Spatial Decision Support System for the Planning of Retail and Service Facilities**
Theo Arentze

nr 56
**Integrated Lighting System Assistant**
Ellie de Groot

nr 57
**Ontwerpend Leren, Leren Ontwerpen**
J.T. Boekholt

nr 58
**Temporal Aspects of Theme Park Choice Behavior**
Astrid Kemperman

nr 59
**Ontwerp van een Geïndustrialiseerde Funderingswijze**
Faas Moonen

nr 60
**Merlin: A Decision Support System for Outdoor Leisure Planning**
Manon van Middelkoop

nr 61
**The Aura of Modernity**
Jos Bosman

nr 62
**Urban Form and Activity-Travel Patterns**
Daniëlle Snellen

nr 63
**Design Research in the Netherlands 2000**
Henri Achten

nr 64
**Computer Aided Dimensional Control in Building Construction**
Rui Wu

nr 65
**Beyond Sustainable Building**
editors: Peter A. Erkelens
Sander de Jonge
August A.M. van Vliet
co-editor: Ruth J.G. Verhagen

nr 66
**Das Globalrecyclingfähige Haus**
Hans Löfflad

nr 67
**Cool Schools for Hot Suburbs**
René J. Dierkx

nr 68
**A Bamboo Building Design Decision Support Tool**
Fitri Mardjono

nr 69
**Driving Rain on Building Envelopes**
Fabien van Mook

nr 70
**Heating Monumental Churches**
Henk Schellen

nr 71
**Van Woningverhuurder naar Aanbieder van Woongenot**
Patrick Dogge

nr 72
**Moisture Transfer Properties of Coated Gypsum**
Emile Goossens

nr 73
**Plybamboo Wall-Panels for Housing**
Guillermo E. González-Beltrán

nr 74
**The Future Site-Proceedings**
Ger Maas
Frans van Gassel

nr 75
**Radon transport in Autoclaved Aerated Concrete**
Michel van der Pal

nr 76
**The Reliability and Validity of Interactive Virtual Reality Computer Experiments**
Amy Tan

nr 77
**Measuring Housing Preferences Using Virtual Reality and Belief Networks**
Maciej A. Orzechowski

nr 78
**Computational Representations of Words and Associations in Architectural Design**
Nicole Segers

nr 79
**Measuring and Predicting Adaptation in Multidimensional Activity-Travel Patterns**
Chang-Hyeon Joh

nr 80
**Strategic Briefing**
Fayez Al Hassan

nr 81
**Well Being in Hospitals**
Simona Di Cicco

nr 82
**Solares Bauen: Implementierungs- und Umsetzungs-Aspekte in der Hochschulausbildung in Österreich**
Gerhard Schuster

nr 83
**Supporting Strategic Design of Workplace Environments with Case-Based Reasoning**
Shauna Mallory-Hill

nr 84
**ACCEL: A Tool for Supporting Concept Generation in the Early Design Phase**
Maxim Ivashkov

nr 85
**Brick-Mortar Interaction in Masonry under Compression**
Ad Vermeltfoort

nr 86
**Zelfredzaam Wonen**
Guus van Vliet

nr 87
**Een Ensemble met Grootstedelijke Allure**
Jos Bosman
Hans Schippers

nr 88
**On the Computation of Well-Structured Graphic Representations in Architectural Design**
Henri Achten

nr 89
**De Evolutie van een West-Afrikaanse Vernaculaire Architectuur**
Wolf Schijns

nr 90
**ROMBO Tactiek**
Christoph Maria Ravesloot

nr 91
**External Coupling between Building Energy Simulation and Computational Fluid Dynamics**
Ery Djunaedy

nr 92
**Design Research in the Netherlands 2005**
editors: Henri Achten
Kees Dorst
Pieter Jan Stappers
Bauke de Vries

nr 93
**Ein Modell zur Baulichen Transformation**
Jalil H. Saber Zaimian

nr 94
**Human Lighting Demands: Healthy Lighting in an Office Environment**
Myriam Aries

nr 95
**A Spatial Decision Support System for the Provision and Monitoring of Urban Greenspace**
Claudia Pelizaro

nr 96
**Leren Creëren**
Adri Proveniers

nr 97
**Simlandscape**
Rob de Waard

nr 98
**Design Team Communication**
Ad den Otter

nr 99
**Humaan-Ecologisch Georiënteerde Woningbouw**
Juri Czabanowski

nr 100
**Hambase**
Martin de Wit

nr 101
**Sound Transmission through Pipe Systems and into Building Structures**
Susanne Bron-van der Jagt

nr 102
**Het Bouwkundig Contrapunt**
Jan Francis Boelen

nr 103
**A Framework for a Multi-Agent Planning Support System**
Dick Saarloos

nr 104
**Bracing Steel Frames with Calcium Silicate Element Walls**
Bright Mweene Ng'andu

nr 105
**Naar een Nieuwe Houtskeletbouw**
F.N.G. De Medts

nr 106 and 107
*Niet gepubliceerd*

nr 108
**Geborgenheid**
T.E.L. van Pinxteren

nr 109
**Modelling Strategic Behaviour in Anticipation of Congestion**
Qi Han

nr 110
**Reflecties op het Woondomein**
Fred Sanders

nr 111
**On Assessment of Wind Comfort by Sand Erosion**
Gábor Dezsö

nr 112
**Bench Heating in Monumental Churches**
Dionne Limpens-Neilen

nr 113
**RE. Architecture**
Ana Pereira Roders

nr 114
**Toward Applicable Green Architecture**
Usama El Fiky

nr 115
**Knowledge Representation under Inherent Uncertainty in a Multi-Agent System for Land Use Planning**
Liying Ma

nr 116
**Integrated Heat Air and Moisture Modeling and Simulation**
Jos van Schijndel

nr 117
**Concrete Behaviour in Multiaxial Compression**
J.P.W. Bongers

nr 118
**The Image of the Urban Landscape**
Ana Moya Pellitero

nr 119
**The Self-Organizing City in Vietnam**
Stephanie Geertman

nr 120
**A Multi-Agent Planning Support System for Assessing Externalities of Urban Form Scenarios**
Rachel Katoshevski-Cavari

nr 121
**Den Schulbau Neu Denken, Fühlen und Wollen**
Urs Christian Maurer-Dietrich

nr 122
**Peter Eisenman Theories and Practices**
Bernhard Kormoss

nr 123
**User Simulation of Space Utilisation**
Vincent Tabak

nr 125
**In Search of a Complex System Model**
Oswald Devisch

nr 126
**Lighting at Work: Environmental Study of Direct Effects of Lighting Level and Spectrum on Psycho-Physiological Variables**
Grazyna Górnicka

nr 127
**Flanking Sound Transmission through Lightweight Framed Double Leaf Walls**
Stefan Schoenwald

nr 128
**Bounded Rationality and Spatio-Temporal Pedestrian Shopping Behavior**
Wei Zhu

nr 129
**Travel Information: Impact on Activity Travel Pattern**
Zhongwei Sun

nr 130
**Co-Simulation for Performance Prediction of Innovative Integrated Mechanical Energy Systems in Buildings**
Marija Trčka

nr 131
*Niet gepubliceerd*

nr 132
**Architectural Cue Model in Evacuation Simulation for Underground Space Design**
Chengyu Sun

nr 133
**Uncertainty and Sensitivity Analysis in Building Performance Simulation for Decision Support and Design Optimization**
Christina Hopfe

nr 134
**Facilitating Distributed Collaboration in the AEC/FM Sector Using Semantic Web Technologies**
Jacob Beetz

nr 135
**Circumferentially Adhesive Bonded Glass Panes for Bracing Steel Frame in Façades**
Edwin Huveners

nr 136
**Influence of Temperature on Concrete Beams Strengthened in Flexure with CFRP**
Ernst-Lucas Klamer

nr 137
**Sturen op Klantwaarde**
Jos Smeets

nr 139
**Lateral Behavior of Steel Frames with Discretely Connected Precast Concrete Infill Panels**
Paul Teewen

nr 140
**Integral Design Method in the Context of Sustainable Building Design**
Perica Savanović

nr 141
**Household Activity-Travel Behavior: Implementation of Within-Household Interactions**
Renni Anggraini

nr 142
**Design Research in the Netherlands 2010**
Henri Achten

nr 143
**Modelling Life Trajectories and Transport Mode Choice Using Bayesian Belief Networks**
Marloes Verhoeven

nr 144
**Assessing Construction Project Performance in Ghana**
William Gyadu-Asiedu

nr 145
**Empowering Seniors through Domotic Homes**
Masi Mohammadi

nr 146
**An Integral Design Concept for Ecological Self-Compacting Concrete**
Martin Hunger

nr 147
**Governing Multi-Actor Decision Processes in Dutch Industrial Area Redevelopment**
Erik Blokhuis

nr 148
**A Multifunctional Design Approach for Sustainable Concrete**
Götz Hüsken

nr 149
**Quality Monitoring in Infrastructural Design-Build Projects**
Ruben Favié

nr 150
**Assessment Matrix for Conservation of Valuable Timber Structures**
Michael Abels

nr 151
**Co-simulation of Building Energy Simulation and Computational Fluid Dynamics for Whole-Building Heat, Air and Moisture Engineering**
Mohammad Mirsadeghi

nr 152
**External Coupling of Building Energy Simulation and Building Element Heat, Air and Moisture Simulation**
Daniel Cóstola

nr 153
**Adaptive Decision Making In Multi-Stakeholder Retail Planning**
Ingrid Janssen

nr 154
**Landscape Generator**
Kymo Slager

nr 155
**Constraint Specification in Architecture**
Remco Niemeijer

nr 156
**A Need-Based Approach to Dynamic Activity Generation**
Linda Nijland

nr 157
**Modeling Office Firm Dynamics in an Agent-Based Micro Simulation Framework**
Gustavo Garcia Manzato

nr 158
**Lightweight Floor System for Vibration Comfort**
Sander Zegers

nr 159
**Aanpasbaarheid van de Draagstructuur**
Roel Gijsbers

nr 160
**'Village in the City' in Guangzhou, China**
Yanliu Lin

nr 161
**Climate Risk Assessment in Museums**
Marco Martens

nr 162
**Social Activity-Travel Patterns**
Pauline van den Berg

nr 163
**Sound Concentration Caused by Curved Surfaces**
Martijn Vercammen

nr 164
**Design of Environmentally Friendly Calcium Sulfate-Based Building Materials: Towards an Improved Indoor Air Quality**
Qingliang Yu

nr 165
**Beyond Uniform Thermal Comfort on the Effects of Non-Uniformity and Individual Physiology**
Lisje Schellen

nr 166
**Sustainable Residential Districts**
Gaby Abdalla

nr 167
**Towards a Performance Assessment Methodology using Computational Simulation for Air Distribution System Designs in Operating Rooms**
Mônica do Amaral Melhado

nr 168
**Strategic Decision Modeling in Brownfield Redevelopment**
Brano Glumac

nr 169
**Pamela: A Parking Analysis Model for Predicting Effects in Local Areas**
Peter van der Waerden

nr 170
**A Vision Driven Wayfinding Simulation-System Based on the Architectural Features Perceived in the Office Environment**
Qunli Chen

nr 171
**Measuring Mental Representations Underlying Activity-Travel Choices**
Oliver Horeni

nr 172
**Modelling the Effects of Social Networks on Activity and Travel Behaviour**
Nicole Ronald

nr 173
**Uncertainty Propagation and Sensitivity Analysis Techniques in Building Performance Simulation to Support Conceptual Building and System Design**
Christian Struck

nr 174
**Numerical Modeling of Micro-Scale Wind-Induced Pollutant Dispersion in the Built Environment**
Pierre Gousseau

nr 175
**Modeling Recreation Choices over the Family Lifecycle**
Anna Beatriz Grigolon

nr 176
**Experimental and Numerical Analysis of Mixing Ventilation at Laminar, Transitional and Turbulent Slot Reynolds Numbers**
Twan van Hooff

nr 177
**Collaborative Design Support: Workshops to Stimulate Interaction and Knowledge Exchange Between Practitioners**
Emile M.C.J. Quanjel

nr 178
**Future-Proof Platforms for Aging-in-Place**
Michiel Brink

nr 179
**Motivate: A Context-Aware Mobile Application for Physical Activity Promotion**
Yuzhong Lin

nr 180
**Experience the City: Analysis of Space-Time Behaviour and Spatial Learning**
Anastasia Moiseeva

nr 181
**Unbonded Post-Tensioned Shear Walls of Calcium Silicate Element Masonry**
Lex van der Meer

nr 182
**Construction and Demolition Waste Recycling into Innovative Building Materials for Sustainable Construction in Tanzania**
Mwita M. Sabai

nr 183
**Durability of Concrete with Emphasis on Chloride Migration**
Przemysław Spiesz

nr 184
**Computational Modeling of Urban Wind Flow and Natural Ventilation Potential of Buildings**
Rubina Ramponi

nr 185
**A Distributed Dynamic Simulation Mechanism for Buildings Automation and Control Systems**
Azzedine Yahiaoui

nr 186
**Modeling Cognitive Learning of Urban Networks in Daily Activity-Travel Behavior**
Şehnaz Cenani Durmazoğlu

nr 187
**Functionality and Adaptability of Design Solutions for Public Apartment Buildings in Ghana**
Stephen Agyefi-Mensah

nr 188
**A Construction Waste Generation Model for Developing Countries**
Lilliana Abarca-Guerrero

nr 189
**Synchronizing Networks: The Modeling of Supernetworks for Activity-Travel Behavior**
Feixiong Liao

nr 190
**Time and Money Allocation Decisions in Out-of-Home Leisure Activity Choices**
Gamze Zeynep Dane

nr 191
**How to Measure Added Value of CRE and Building Design**
Rianne Appel-Meulenbroek

nr 192
**Secondary Materials in Cement-Based Products: Treatment, Modeling and Environmental Interaction**
Miruna Florea

nr 193
**Concepts for the Robustness Improvement of Self-Compacting Concrete: Effects of Admixtures and Mixture Components on the Rheology and Early Hydration at Varying Temperatures**
Wolfram Schmidt

nr 194
**Modelling and Simulation of Virtual Natural Lighting Solutions in Buildings**
Rizki A. Mangkuto

nr 195
**Nano-Silica Production at Low Temperatures from the Dissolution of Olivine - Synthesis, Tailoring and Modelling**
Alberto Lazaro Garcia

nr 196
**Building Energy Simulation Based Assessment of Industrial Halls for Design Support**
Bruno Lee

nr 197
**Computational Performance Prediction of the Potential of Hybrid Adaptable Thermal Storage Concepts for Lightweight Low-Energy Houses**
Pieter-Jan Hoes

nr 198
**Application of Nano-Silica in Concrete**
George Quercia Bianchi

nr 199
**Dynamics of Social Networks and Activity Travel Behaviour**
Fariya Sharmeen

nr 200
**Building Structural Design Generation and Optimisation including Spatial Modification**
Juan Manuel Davila Delgado

nr 201
**Hydration and Thermal Decomposition of Cement/Calcium-Sulphate Based Materials**
Ariën de Korte

nr 202
**Republiek van Beelden:**
**De Politieke Werkingen van het Ontwerp in Regionale Planvorming**
Bart de Zwart

nr 203
**Effects of Energy Price Increases on Individual Activity-Travel Repertoires and Energy Consumption**
Dujuan Yang

nr 204
**Geometry and Ventilation:**
**Evaluation of the Leeward Sawtooth Roof Potential in the Natural Ventilation of Buildings**
Jorge Isaac Perén Montero

nr 205
**Computational Modelling of Evaporative Cooling as a Climate Change Adaptation Measure at the Spatial Scale of Buildings and Streets**
Hamid Montazeri

nr 206
**Local Buckling of Aluminium Beams in Fire Conditions**
Ronald van der Meulen

nr 207
**Historic Urban Landscapes:**
**Framing the Integration of Urban and Heritage Planning in Multilevel Governance**
Loes Veldpaus

nr 208
**Sustainable Transformation of the Cities:**
**Urban Design Pragmatics to Achieve a Sustainable City**
Ernesto Antonio Zumelzu Scheel

nr 209
**Development of Sustainable Protective Ultra-High Performance Fibre Reinforced Concrete (UHPFRC):**
**Design, Assessment and Modeling**
Rui Yu

nr 210
**Uncertainty in Modeling Activity-Travel Demand in Complex Uban Systems**
Soora Rasouli

nr 211
**Simulation-based Performance Assessment of Climate Adaptive Greenhouse Shells**
Chul-sung Lee

nr 212
**Green Cities:**
**Modelling the Spatial Transformation of the Urban Environment using Renewable Energy Technologies**
Saleh Mohammadi

nr 213
**A Bounded Rationality Model of Short and Long-Term Dynamics of Activity-Travel Behavior**
Ifigeneia Psarra

nr 214
**Effects of Pricing Strategies on Dynamic Repertoires of Activity-Travel Behaviour**
Elaheh Khademi

nr 215
**Handstorm Principles for Creative and Collaborative Working**
Frans van Gassel

nr 216
**Light Conditions in Nursing Homes: Visual Comfort and Visual Functioning of Residents**
Marianne M. Sinoo

nr 217
**Woonsporen: De Sociale en Ruimtelijke Biografie van een Stedelijk Bouwblok in de Amsterdamse Transvaalbuurt**
Hüseyin Hüsnü Yegenoglu

nr 218
**Studies on User Control in Ambient Intelligent Systems**
Berent Willem Meerbeek

nr 219
**Daily Livings in a Smart Home: Users' Living Preference Modeling of Smart Homes**
Erfaneh Allameh

nr 220
**Smart Home Design: Spatial Preference Modeling of Smart Homes**
Mohammadali Heidari Jozam

nr 221
**Wonen: Discoursen, Praktijken, Perspectieven**
Jos Smeets

nr 222
**Personal Control over Indoor Climate in Offices: Impact on Comfort, Health and Productivity**
Atze Christiaan Boerstra

nr 223
**Personalized Route Finding in Multimodal Transportation Networks**
Jianwe Zhang

nr 224
**The Design of an Adaptive Healing Room for Stroke Patients**
Elke Daemen

nr 225
**Experimental and Numerical Analysis of Climate Change Induced Risks to Historic Buildings and Collections**
Zara Huijbregts

nr 226
**Wind Flow Modeling in Urban Areas Through Experimental and Numerical Techniques**
Alessio Ricci

nr 227
**Clever Climate Control for Culture: Energy Efficient Indoor Climate Control Strategies for Museums Respecting Collection Preservation and Thermal Comfort of Visitors**
Rick Kramer

nr 228
**Fatigue Life Estimation of Metal Structures Based on Damage Modeling**
Sarmediran Silitonga

nr 229
**A multi-agents and occupancy based strategy for energy management and process control on the room-level**
Timilehin Moses Labeodan

nr 230
**Environmental assessment of Building Integrated Photovoltaics: Numerical and Experimental Carrying Capacity Based Approach**
Michiel Ritzen

nr 231
**Performance of Admixture and Secondary Minerals in Alkali Activated Concrete: Sustaining a Concrete Future**
Arno Keulen

nr 232
**World Heritage Cities and Sustainable Urban Development:**
**Bridging Global and Local Levels in Monitoring the Sustainable Urban Development of World Heritage Cities**
Paloma C. Guzman Molina

nr 233
**Stage Acoustics and Sound Exposure in Performance and Rehearsal Spaces for Orchestras:**
**Methods for Physical Measurements**
Remy Wenmaekers

nr 234
**Municipal Solid Waste Incineration (MSWI) Bottom Ash:**
**From Waste to Value Characterization, Treatments and Application**
Pei Tang

nr 235
**Large Eddy Simulations Applied to Wind Loading and Pollutant Dispersion**
Mattia Ricci

nr 236
**Alkali Activated Slag-Fly Ash Binders: Design, Modeling and Application**
Xu Gao

nr 237
**Sodium Carbonate Activated Slag: Reaction Analysis, Microstructural Modification & Engineering Application**
Bo Yuan

nr 238
**Shopping Behavior in Malls**
Widiyani

nr 239
**Smart Grid-Building Energy Interactions: Demand Side Power Flexibility in Office Buildings**
Kennedy Otieno Aduda

nr 240
**Modeling Taxis Dynamic Behavior in Uncertain Urban Environments**
Zheng Zhong

nr 241
**Gap-Theoretical Analyses of Residential Satisfaction and Intention to Move**
Wen Jiang

nr 242
**Travel Satisfaction and Subjective Well-Being: A Behavioral Modeling Perspective**
Yanan Gao

nr 243
**Building Energy Modelling to Support the Commissioning of Holistic Data Centre Operation**
Vojtech Zavrel

nr 244
**Regret-Based Travel Behavior Modeling: An Extended Framework**
Sunghoon Jang

nr 245
**Towards Robust Low-Energy Houses: A Computational Approach for Performance Robustness Assessment using Scenario Analysis**
Rajesh Reddy Kotireddy

nr 246
**Development of sustainable and functionalized inorganic binder-biofiber composites**
Guillaume Doudart de la Grée

nr 247
**A Multiscale Analysis of the Urban Heat Island Effect: From City Averaged Temperatures to the Energy Demand of Individual Buildings**
Yasin Toparlar

nr 248
**Design Method for Adaptive Daylight Systems for buildings covered by large (span) roofs**
Florian Heinzelmann

nr 249
**Hardening, high-temperature resistance and acid resistance of one-part geopolymers**
Patrick Sturm

nr 250
**Effects of the built environment on dynamic repertoires of activity-travel behaviour**
Aida Pontes de Aquino

nr 251
**Modeling for auralization of urban environments: Incorporation of directivity in sound propagation and analysis of a framework for auralizing a car pass-by**
Fotis Georgiou

nr 252
**Wind Loads on Heliostats and Photovoltaic Trackers**
Andreas Pfahl

nr 253
**Approaches for computational performance optimization of innovative adaptive façade concepts**
Roel Loonen

nr 254
**Multi-scale FEM-DEM Model for Granular Materials: Micro-scale boundary conditions, Statics, and Dynamics**
Jiadun Liu

nr 255
**Bending Moment - Shear Force Interaction of Rolled I-Shaped Steel Sections**
Rianne Willie Adriana Dekker

nr 256
**Paralympic tandem cycling and handcycling: Computational and wind tunnel analysis of aerodynamic performance**
Paul Fionn Mannion

nr 257
**Experimental characterization and numerical modelling of 3D printed concrete: Controlling structural behaviour in the fresh and hardened state**
Robert Johannes Maria Wolfs

nr 258
**Requirement checking in the building industry: Enabling modularized and extensible requirement checking systems based on semantic web technologies**
Chi Zhang

nr 259
**A Sustainable Industrial Site Redevelopment Planning Support System**
Tong Wang

nr 260
**Efficient storage and retrieval of detailed building models: Multi-disciplinary and long-term use of geometric and semantic construction information**
Thomas Ferdinand Krijnen

nr 261
**The users' value of business center concepts for knowledge sharing and networking behavior within and between organizations**
Minou Weijs-Perrée

nr 262
**Characterization and improvement of aerodynamic performance of vertical axis wind turbines using computational fluid dynamics (CFD)**
Abdolrahim Rezaeiha

nr 263
**In-situ characterization of the acoustic impedance of vegetated roofs**
Chang Liu

nr 264
**Occupancy-based lighting control: Developing an energy saving strategy that ensures office workers' comfort**
Christel de Bakker

nr 265
**Stakeholders-Oriented Spatial Decision Support System**
Cahyono Susetyo

nr 266
**Climate-induced damage in oak museum objects**
Rianne Aleida Luimes

nr 267
**Towards individual thermal comfort: Model predictive personalized control of heating systems**
Katarina Katic

nr 268
**Modelling and Measuring Quality of Urban Life: Housing, Neighborhood, Transport and Job**
Lida Aminian

nr 269
**Optimization of an aquifer thermal energy storage system through integrated modelling of aquifer, HVAC systems and building**
Basar Bozkaya

nr 270
**Numerical modeling for urban sound propagation: developments in wave-based and energy-based methods**
Raúl Pagán Muñoz

nr 271
**Lighting in multi-user office environments: improving employee wellbeing through personal control**
Sanae van der Vleuten-Chraibi

nr 272
**A strategy for fit-for-purpose occupant behavior modelling in building energy and comfort performance simulation**
Isabella I. Gaetani dell'Aquila d'Aragona

nr 273
**Een architectuurhistorische waardestelling van naoorlogse woonwijken in Nederland: Het voorbeeld van de Westelijke Tuinsteden in Amsterdam**
Eleonore Henriette Marie Mens

nr 274
**Job-Housing Co-Dependent Mobility Decisions in Life Trajectories**
Jia Guo

nr 275
**A user-oriented focus to create healthcare facilities: decision making on strategic values**
Emilia Rosalia Catharina Maria Huisman

nr 276
**Dynamics of plane impinging jets at moderate Reynolds numbers – with applications to air curtains**
Adelya Khayrullina

nr 277
**Valorization of Municipal Solid Waste Incineration Bottom Ash - Chemical Nature, Leachability and Treatments of Hazardous Elements**
Qadeer Alam

nr 278
**Treatments and valorization of MSWI bottom ash - application in cement-based materials**
Veronica Caprai

nr 279
**Personal lighting conditions of office workers - input for intelligent systems to optimize subjective alertness**
Juliëtte van Duijnhoven

nr 280
**Social influence effects in tourism travel: air trip itinerary and destination choices**
Xiaofeng Pan

nr 281
**Advancing Post-War Housing: Integrating Heritage Impact, Environmental Impact, Hygrothermal Risk and Costs in Renovation Design Decisions**
Lisanne Claartje Havinga

nr 282
**Impact resistant ultra-high performance fibre reinforced concrete: materials, components and properties**
Peipeng Li

nr 283
**Demand-driven Science Parks: The Perceived Benefits and Trade-offs of Tenant Firms with regard to Science Park Attributes**
Wei Keat Benny Ng

nr 284
**Raise the lantern; how light can help to maintain a healthy and safe hospital environment focusing on nurses**
Maria Petronella Johanna Aarts

nr 285
**Modelling Learning and Dynamic Route and Parking Choice Behaviour under Uncertainty**
Elaine Cristina Schneider de Carvalho

nr 286
**Identifying indoor local microclimates for safekeeping of cultural heritage**
Karin Kompatscher

nr 287
**Probabilistic modeling of fatigue resistance for welded and riveted bridge details. Resistance models and estimation of uncertainty.**
Davide Leonetti

nr 288
**Performance of Layered UHPFRC under Static and Dynamic Loads: Effects of steel fibers, coarse aggregates and layered structures**
Yangyueye Cao

nr 289
**Photocatalytic abatement of the nitrogen oxide pollution: synthesis, application and long-term evaluation of titania-silica composites**
Yuri Hendrix

nr 290
**Assessing knowledge adoption in post-disaster reconstruction: Understanding the impact of hazard-resistant construction knowledge on reconstruction processes of self-recovering communities in Nepal and the Philippines**
Eefje Hendriks

nr 291
**Locating electric vehicle charging stations: A multi-agent based dynamic simulation**
Seheon Kim

nr 292
**De invloed van Lean Management op de beheersing van het bouwproces**
Wim van den Bouwhuijsen

nr 293
**Neighborhood Environment and Physical Activity of Older Adults**
Zhengying Liu

nr 294
**Practical and continuous luminance distribution measurements for lighting quality**
Thijs Willem Kruisselbrink

nr 295
**Auditory Distraction in Open-Plan Study Environments in Higher Education**
Pieternella Elizabeth Braat-Eggen

nr 296
**Exploring the effect of the sound environment on nurses' task performance: an applied approach focusing on prospective memory**
Jikke Reinten

nr 297
**Design and performance of water resistant cementitious materials– Mechanisms, evaluation and applications**
Zhengyao Qu

nr 298
**Design Optimization of Seasonal Thermal Energy Storage Integrated District Heating and Cooling System: A Modeling and Simulation Approach**
Luyi Xu

nr 299
**Land use and transport: Integrated approaches for planning and management**
Zhongqi Wang

nr 300
**Multi-disciplinary optimization of building spatial designs: co-evolutionary design process simulations, evolutionary algorithms, hybrid approaches**
Sjonnie Boonstra

nr 301
**Modeling the spatial and temporal relation between urban land use, temperature, and energy demand**
Hung-Chu Chen

nr 302
**Seismic retrofitting of masonry walls with flexible deep mounted CFRP strips**
Ömer Serhat Türkmen

nr 303
**Coupled Aerostructural Shape and Topology Optimization of Horizontal-Axis Wind Turbine Rotor Blades**
Zhijun Wang

nr 304
**Valorization of Recycled Waste Glass and Converter Steel Slag as Ingredients for Building Materials: Hydration and Carbonation Studies**
Gang Liu

nr 305
**Low-Carbon City Development based on Land Use Planning**
Gengzhe Wang

nr 306
**Sustainable energy transition scenario analysis for buildings and neighborhoods - Data driven optimization**
Shalika Saubhagya Wickramarachchi Walker

nr 307
**In-between living and manufactured: an exploratory study on biobuilding components for building design**
Berrak Kirbas Akyurek

nr 308
**Development of alternative cementitious binders and functionalized materials: design, performance and durability**
Anna Monika Kaja

nr 309
**Development a morphological approach for interactive kinetic façade design: Improving multiple occupants' visual comfort**
Seyed Morteza Hosseini

nr 310
**PV in urban context: modeling and simulation strategies for analyzing the performance of shaded PV systems**
Ádám Bognár

nr 311
**Life Trajectory, Household Car Ownership Dynamics and Home Renewable Energy Equipment Adoption**
Gaofeng Gu

nr 312
**Impact of Street-Scale Built Environment on Walking/Cycling around Metro Stations**
Yanan Liu

nr 313
**Advances in Urban Traffic Network Equilibrium Models and Algorithms**
Dong Wang

nr 314
**Development of an uncertainty analysis framework for model-based consequential life cycle assessment: application to activity-based modelling and life cycle assessment of multimodal mobility**
Paul Martin Baustert

nr 315
**Variable stiffness and damping structural joints for semi-active vibration control**
Qinyu Wang

nr 316
**Understanding Carsharing-Facilitating Neighborhood Preferences**
Juan Wang

nr 317
**Dynamic alignment of Corporate Real Estate to business strategies: An empirical analysis using historical data and in-depth modelling of decision making**
Howard Cooke

nr 318
**Local People Matter: Towards participatory governance of cultural heritage in China**
Ji Li

nr 319
**Walkability and Walkable Healthy Neighborhoods**
Bojing Liao

nr 320
**Light directionality in design of healthy offices: exploration of two methods**
Parisa Khademagha

nr 321
**Room acoustic modeling with the time-domain discontinuous Galerkin method**
Huiqing Wang

nr 322
**Sustainable insulating lightweight materials for enhancing indoor building performance: miscanthus, aerogel and nano-silica**
Yuxuan Chen

nr 323
**Computational analysis of the impact of façade geometrical details on wind flow and pollutant dispersion**
Xing Zheng

nr 324
**Analysis of urban wind energy potential around high-rise buildings in close proximity using computational fluid dynamics**
Yu-Hsuan Jang

nr 325
**A new approach to automated energy performance and fault detection and diagnosis of HVAC systems: Development of the 4S3F method**
Arie Taal

nr 326
**Innovative Admixtures for Modifying Viscosity and Volume Change of Cement Composites**
Hossein Karimi

nr 327
**Towards houses with low grid dependency: A simulation-based design optimization approach**
Zahra Mohammadi

nr 328
**Activation of demand flexibility for heating systems in buildings: Real-life demonstration of optimal control for power-to-heat and thermal energy storage**
Christian Finck

nr 329
**A computational framework for analysis and optimisation of automated solar shading systems**
Samuel B. de Vries

nr 330
**Challenges and potential solutions for cultural heritage adaptive reuse: a comparative study employing the Historic Urban Landscape approach**
Nadia Pintossi

nr 331
**Shared control in office lighting systems**
Tatiana Aleksandrovna Lashina

nr 332
**Comfort in Urban Public Spaces**
You Peng

nr 333
**Numerical modelling of metal soap formation in historical oil paintings**
Gerardus Johannes Anna Maria Eumelen

nr 334
**A transdisciplinary decision-making approach to food-water-energy nexus: A guide towards sustainable development**
Maryam Ghodsvali

nr 335
**Numerical modelling of transient low-frequency sound propagation and vibration in buildings**
Indra Sihar

nr 336
**Characterization of impact sound from lightweight joist floors**
Yi Qin

nr 337
**Cities for Children: Supporting Children and Caregivers in Participatory Urban Planning**
Özlemnur Ataol

nr 338
**Engaging the unengaged: Exploring citizen participation in nature-based solutions in China**
Li Dai

nr 339
**Municipal Solid Waste Incineration Residues: analysis, treatments, and applications**
Ekaterina Loginova

nr 340
**Enhancing the Uptake of Nature-Based Solutions in Urban Settings: An Information Systems Approach**
Shahryar Ershad Sarabi

nr 341
**Work Schedule Arrangements in Two-Adult Households with Children**
Bilin Han

nr 342
**Increasing awareness of urban cultural heritage using digital technologies: empirical design and analysis of a new multi-media web platform**
Benshuo Wang

nr 343
**Mechanical and physical properties of fibre-cement composites using alternative natural fibres**
Katerina Kochova

nr 344
**Numerical and experimental investigation of urban microclimate in a real compact heterogeneous urban area**
Nestoras Antoniou

nr 345
**Examining in-class activities to facilitate academic achievement in higher education: A framework for optimal indoor environmental conditions**
Henk W. Brink

nr 346
**High-temperature resistant geopolymers: composition, microstructure and performance**
Kinga Malgorzata Klima

nr 347
**Individual and household decision-making in shared parking**
Qianqian Yan

nr 348
**In-situ formation of LDHs in Alkali activated binders**
Tao Liu

nr 349
**Condition assessment of concrete sewer pipes through an integrated experimental-numerical approach**
Irene C. Scheperboer

nr 350
**In situ PU-based characterization of sound absorbing materials for room acoustic modeling purposes**
Baltazar Briere de La Hosseraye

nr 351
**Uncertainty analysis and management in building energy data mining: A bottom-up approach considering the temporal and spatial aspect of data**
Waqas Khan

nr 352
**Personalized Heating Control Systems to improve thermal comfort and reduce energy consumption**
Michal Veselý

nr 353
**Restorative value of the urban greenscape: Urban residential streets as restorative environments**
Robert P. van Dongen

nr 354
**Urban ventilation and the compact Mediterranean city: numerical investigations of the dynamic relationships between density, morphology and wind flow**
Olga Palusci

nr 355
**Data science for buildings: a multi-scale approach bridging occupants to smart-city energy planning**
Julien Leprince

nr 356
**Class Association Rule Models for Predicting Transportation Mode Choice**
Jiajia Zhang

nr 357
**Acceptance and use of autonomous vehicles**
Zhihui Tian

nr 358
**Consumer Acceptance of Crowdshipping Services**
Chenyu Wang

nr 359
**Determinants of habitual participation in leisure-time physical activity and active travel in life trajectories**
Xiaoyue Chen

nr 360
**Analysis of Citizens' Motivation and Intention Using Modern Information Technology in Urban Planning Public Participation**
Wenshu Li

nr 361
**Linking smart and physical port cities. Port-city interface areas: from obsolete/isolated to smart environments.**
Mercè de Miguel Capdevila

nr 362
**Assessment and improvement of indoor thermal comfort and energy demand of Chinese heritage apartment buildings under climate change**
Muxi Lei

nr 363
**Indoor airflow and heat transfer in a cross-ventilated generic building: wind tunnel experiments and computational fluid dynamics analyses**
Katarina Kosutova

nr 364
**A Robotic Construction Simulation Platform for Light-weight Prefabricated Structures.**
Aiyu Zhu

nr 365
**Lifetime prediction of vertical-axis wind turbines based on CFD simulations and high-cycle fatigue modeling**
Feiyu Geng

nr 366
**Computational modeling of convective heat transfer at building surfaces**
Samy Iousef

nr 367
**Numerical simulation of the atmospheric boundary layer with application to natural ventilation**
Raffaele Vasaturo

nr 368
**Bouwen zonder scrupules. De Nederlandse bouwnijverheid tijdens de bezetting en de eerste jaren van wederopbouw (1940-1950)**
Geert-Jan Mellink

nr 369
**Factors Promoting a Positive Experienced Neighborhood Public Space--A Virtual Environment-based analysis.**
Yuwen Zhao

nr 370
**Place quality making in high-speed railway station areas: Devising place quality indicators for urban design, beyond the transport-land use divide**
Jinglun Du

nr 371
**Sustainable Bio-based Adsorptive Concrete for Phosphorus Removal**
Fan Wu

nr 372
**The physical workplace as a resource for mental health: A salutogenic approach to a mentally healthy workplace design at home and at the office**
Lisanne Bergefurt

nr 373
**High-end application of basic oxygen furnace steel slag as sustainable building materials**
Muhammad Jawad Ahmed

nr 374
**Energy-Efficient Urban Rail Transit Operations: Models, Algorithms, and Applications**
Kang Huang

nr 375
**Household Energy Efficiency Adoption: Influencing Factors and Diffusion Interventions**
Hua Du

nr 376
**High-temperature resistant geopolymer-based materials out of industrial residuals.**
Yan Luo

nr 377
**A Simulation Approach Exploring the Impacts of Land Use Variables on Travel Behavior.**
Xiaoming Lyu

nr 378
**Understanding and modelling individual preferences for Mobility as a Service**
Valeria Caiati

nr 379
**Linking the physical and digital built environment - Enabling occupant-centric decision-making using cross-domain semantic digital twins**
Alex Donkers

nr 380
**Indoor Air Quality in Daycare Centers: Assessing and Mitigating Indoor Exposure on Young Children**
Hailin Zheng

nr 381
**A Data-Driven Approach to Understanding Visitors' Behavior to Reduce the Negative Effects of Tourism in Historical Cities**
Sezi Karayazi

nr 382
**Wind effects on internal depressurization for asbestos abatement**
Anjali Radhakrishnan Jayakumari

nr 383
**Spatiotemporal Graph Convolutional Neural Network for Robust and Accurate Traffic Flow Prediction**
Yutian Liu

nr 384
**Photo-responsive functional aluminosilicate cementitious materials - Design, Performance and Durability**
Daoru Liu

nr 385
**High-end applications of basic oxygen furnace slag as a cementitious binder. Phase Assemblage, Mechanical & Chemical Activation, Composites Application**
Winnie Franco Santos

nr 386
**Towards improved performance modelling of distributed PV systems in the built environment**
Bin Meng

nr 387
**Development of sustainable insulation materials. Design, performance and applications**
Alex Koh Chuen Hon

nr 388
**Simulations of Sandwich Panel Systems under Fire: Two-Scale Methods for Connections, Pyrolysis for Insulation, Experimental Validations**
Qingfeng Xu

nr 389
**Long-term Mechanical Performance of the Flax Fiber Reinforced Polymer Composites Considering the Environmental Effects**
Bowen Xu

nr 390
**Quality engineering and control for digital fabrication with concrete**
Derk Bos

nr 391
**Structural Engineering of 3D Printed Strain Hardening Cementitious Composites. From micro-scale analysis to application**
Karsten Nefs

nr 392
**Children's Outdoor Play in the Digital Age; The Role of Digital Interventions in Stimulating Children's Outdoor Play Behavior**
Avin Khalilollahi

nr 393
**Biophilic design and integrating nature in architecture: Guidelines for three-dimensional green spaces to innovate architectural typologies and create impact for sustainability**
Weijie Zhong

nr 394
**Crafting Smart Homes: Innovative Design Strategies to Enhance Housing Quality for Ageing Well**
Chuan Ma

nr 395
**Valorization of Natural Fibers and Municipal Solid Waste Incineration (MSWI) Bottom Ash in Building Composite**
Helong Song

nr 396
**Digital Placemaking and Healthy Ageing. A user-centric approach for empowering senior citizens in inclusive decision-making of future healthy ageing neighbourhoods**
Peyman Najafi

nr 397
**Optimizing aerodynamic performance in cycling. - Analyses of drafting strategies and skinsuit design through computational simulations and wind tunnel experiments**
Thijs Druenen

nr 398
**A simulation-based analytical framework for heat battery in residential use cases.**
Shuwei Wang

nr 399
**Design and performance of alternative cementitious materials using industrial solid wastes - carbonation and chemical activation**
Yanjie Tang

nr 400
**Valorization of industrial solid wastes as ingredients for construction materials: Design, Performance and Durability**
Xuan Ling

nr 401
**Towards Healthy Neighborhoods for Children –Analysis of Parental Perception of Child Friendliness and Children's Physical Activity**
Xiaoli Gong

nr 402
**Simultaneous large-scale modeling of individual and household life events**
Yajie Yang

nr 403
**Helical reinforcement in 3D printed concrete: Development and characterization of a novel reinforcement technique**
Lauri Hass

nr 404
**Advancing Sustainable Built Environment: Insights from stakeholder perspectives and decision support models**
Pei-Hsuan Lee

nr 405
**Children and urban green infrastructure in the digital age: children's perception and desires, and parents' attitudes, towards digitally-enabled interactions with urban green infrastructure**
Shengchen Yin

nr 406
**Exhibition Entanglements. The Department of Architecture at the Museo de Arte Moderno de Bogotá, 1983-1995**
Michael Forero Parra

nr 407
**Outdoor-to-indoor sound propagation models for noise exposure studies**
Michail Evangelos Terzakis

nr 408
**Conceptualising the relationship between the psychosocial and the physical learning environment. Towards an overarching theory, methodology and exploration of practices in innovative physical learning environments at a university of applied sciences**
Siebren Baars

nr 409
**Nano TiO2 hydrosols-based photocatalytic self-cleaning cementitious materials: FUNCTIONAL PERFORMANCES AND APPLICATIONS**
Zixiao Wang

nr 410
**Multi-Physics and Multi-Scale Investigations of the Temperature-Induced Response of Flax Fiber Reinforced Sandwich Footbridges with laboratory and field monitoring validation**
Marco Manconi

nr 411
**Flax Fiber Polyester Resin in Bridge Construction: Design, Modeling, and Long-Term Performance**
Ali Shahmirzaloo

nr 412
**Children's Mental Health and the Environment**
**Examining the role of activity patterns and environmental noise**
**exposure**
Maud Dohmen

nr 413
**Heterogeneous Human Mobility Analysis using Big DataCFD modeling of air pollution in an urban street canyon by car traffic emissions - Sensitivity analyses and recommendations**
Bin Zhang

nr 414
**CFD modeling of air pollution in an urban street canyon by car traffic emissions - Sensitivity analyses and recommendations**
Pen Qin

nr 415
**The spatial planning of urban green space – an empirical analysis and land-use modeling approach**
Jianfei Li

nr 416
**3D-printed mortars with carbon nanotubes for self-sensing applications**
Albanela Dulaj

nr 417
**A Framework for Modeling and Simulating Pedestrians' Affective Experiences, Perceptions, and Activities in Public Spaces**
Senqi Yang

nr 418
**High-rise living - Stimulating social interaction in high-rise apartment buildings**
Linh Nguyen

nr 419
**Enhancing activity-based models: dynamic scheduling and trip chain modeling**
Pim Labee

nr 420
**Built Environment, Active Travel, and Location-Based Outdoor Activity: Spatial and Temporal Perspectives**
Ting Zhou

nr 421
**In the Interplay of Acceptance of Crowd-Sourced Delivery and Transportation Mode Choice within a MaaS Service**
Qiang Qi

nr 422
**Spatial-Temporal Effects of Land-use on Food-Water Energy Nexus: A Case Study of Beijing-Tian Urban Agglomeration**
Ke Yang

nr 423
**Engaging Youth with Cultural Heritage in the Digital Age An Integrated Framework for Youth Digital Participation in Cultural Heritage Management**
Yingxin Zhang

nr 424
**E-bikes and the Built Environment. Cross-Sectional and Longitudinal Explorations of the Determinants of E-Bike Ownership and Use in the Netherlands**
Yushan Zhang

nr 425
**The fault-free case of low delta-T syndrome**
Alet van den Brink

nr 426
**The role of viewing behavior in simulating personal light conditions**
Myrta Gkaintatzi Masouti

nr 427
**Multi-scale analysis of the hygro-mechanical behaviour of oak wood. A numerical and experimental study**
Amin Livani

nr 428
**Ceiling and attic ventilation to improve the indoor thermal environment of residential buildings in hot-humid climates**
Mutmainnah

nr 429
**A multiscale approach to sustainable silica aerogels. Optimizing synthesis, waste valorization, and environmental analysis**
Marina Borzova

nr 430
**Smart and Hybrid Workplaces from the Perspective of Municipal Employees: Preferences and Experiences in Office- and Home-Workplaces**
Deniz Tuzcuoglu

Fire hazards in large-scale infrastructure, such as tunnels and long-span bridges, pose a significant risk to the safety of both structural systems and occupants. Although Ultra-High-Performance Concrete (UHPC) is known for its excellent mechanical strength and durability, its high vulnerability to explosive spalling at elevated temperatures limits its application in fire-prone environments. Meanwhile, Sprayed UHPC (SUHPC) offers great potential for rapid repair due to its formwork-free application and high early strength. However, challenges remain regarding its early-age workability, long-term performance, and fire resistance.

This dissertation addresses these challenges by optimizing the binder system and reinforcement strategy of SUHPC to achieve fire-resistant applications. The research is divided into two main parts. Part I focuses on UHPC, aiming to optimize its binder composition and investigate its spalling behavior after high-temperature exposure, with the goal of gaining deeper insight into its post-heating failure mechanisms. Part II centers on SUHPC and aims to design an optimized binder system to enhance both early-age and later-age performance, with a particular focus on improving resistance to explosive spalling under elevated temperatures. The overall objective of this thesis is to present a fire-resistant SUHPC tailored for rapid structural repair, building upon the fundamental understanding established through UHPC research.

**DEPARTMENT OF THE BUILT ENVIRONMENT**

TU/e EINDHOVEN UNIVERSITY OF TECHNOLOGY